Integrity of the stem cell niche in the developing brain – mechanisms shaping the neural tube

Inaugural-Dissertation

to obtain the academic degree
Doctor rerum naturalium (Dr. rer. nat.)

submitted to the Department of Biology, Chemistry, Pharmacy
of Freie Universität Berlin

by

Izabela Kowalczyk

Berlin, 2021

DECLARATION OF INDEPENDENCE

I, Izabela Kowalczyk, declare that this thesis has been composed solely by myself and has not been submitted for any other degree or qualification. The work was carried out from November 2017 to March 2021 under the supervision of **Dr. rer. nat. Annette Hammes-Lewin** at the Max Delbrück Center for Molecular Medicine in the Helmholtz Association, Berlin.

Part of the project was performed in collaboration with **Dr. rer. nat. Kerstin Feistel**, University of Hohenheim and any data generated by this group or others are specified in the text, cited and acknowledged.

First Reviewer: Prof. Dr. Thomas E. Willnow

The Max Delbrück Center for Molecular Medicine

Second Reviewer: Prof. Dr. Ursula Koch

Department of Biology, Chemistry, Pharmacy,

Freie Universität Berlin

Date of defense: **27.10.2021**

Individual publications

Part of this Ph.D. thesis has been published in the following manuscripts:

Kowalczyk I, Lee C, Schuster E, Hoeren J, Trivigno V, Riedel L, Görne J, Wallingford JB, Hammes A* and Feistel K* (2021). Neural tube closure requires the endocytic receptor Lrp2 and its functional interaction with intracellular scaffolds. Development 148: dev195008, DOI:10.1242/dev.195008

Mecklenburg N*, **Kowalczyk I***, Witte F*, Görne J, Laier A, Gonschior H, Lehmann M, Richter M, Sporbert A, Purfürst B, Hübner N, Hammes A. Identification of novel disease relevant genetic modifiers affecting the SHH pathway in the developing brain. Submitted to Development 2020, revision in progress. *joint first authors

Acknowledgements

Abstract

Neurulation is a complex morphogenetic process, requiring the integration of various molecular and cellular events in order to culminate in the development of sophisticated brain structures. Many mechanistic aspects of the regulatory cues, which pre-pattern the neural plate and further specification of the neuroepithelial stem cells, remain largely unknown. Nonetheless, understanding of the coordination between pivotal developmental processes is indispensable in successful prevention of congenital brain defects in human.

My Ph.D. work significantly contributed to understanding the mechanisms underlying the etiology of congenital brain disorders. I functionally characterized the potential genetic modifiers rendering mouse models with a higher predisposition to neural tube defects. Results from this work can further be extrapolated to human disease penetrance.

One of the key signaling molecules at the onset of neurulation is the morphogen SHH, which is required for ventral midline specification. Mice deficient for the LRP2, a SHH co-receptor in the ventral forebrain, suffer from insufficient SHH uptake by the neuroepithelium and develop holoprosencephaly (HPE) on C57BL/6N background. Congenic *Lrp2* mutants on FVB/N background, however, show normal SHH levels in the ventral forebrain and normal forebrain separation. We have identified new candidate modifier genes, *Pttg1* and *Ulk4,* that influence the capacity of SHH signaling pathway. Higher expression levels of *Pttg1* and *Ulk4* in developing brain of FVB/N mice are likely to contribute to advantageous cellular environment, which maintains the necessary SHH morphogen gradient in the ventral forebrain, independent of the receptor-mediated uptake, hence preventing HPE. The rational is that these novel, disease relevant, positive modulators of the SHH pathway make the early forebrain developmental processes less susceptible to disturbances in the SHH pathway.

Positive regulation of the SHH machinery is associated with efficient ciliogenesis. For the first time, I describe PTTG1 as a novel primary cilia component. I identified PTTG1 at the basal body – the primary cilia organizing center – and in the ciliary shaft. The variable localization of PTTG1 amongst different cilia suggested that it is not a structurally required component of the primary cilium, but may shuttle into the ciliary

shaft in a regulated fashion to support ciliary function and/or axoneme assembly, ultimately enhancing SHH signaling capacity.

Besides the ventral forebrain defect, there is a SHH-independent, dorsal phenotype in *Lrp2* mutant mice, reminiscent of neural tube closure defects (NTDs) affecting C57BL/6N and FVB/N mice. Combining mouse and *Xenopus* work from Kerstin Feistel's lab, we unraveled a conserved, novel function of the receptor, beyond its highly anticipated signaling scope. Neural plate bending and closure is a dynamic process involving cytoskeletal remodeling and apical constriction. We characterized LRP2-dependent apical membrane remodeling necessary for efficient upfolding of the neural plate. We documented for the first time in neuroepithelium, functional interaction of LRP2 with PDZ-containing adaptor proteins, which serve as a bridge to link LRP2 to the intracellular scaffold of neuroepithelial cells. Endocytic activity of the receptor facilitates apical membrane remodeling during apical constriction and simultaneously contributes to the apicobasal distribution of VANGL2, indicating a close interface between cell shape control and maintenance of planar cell polarity. Furthermore, I report the function of LRP2 goes beyond the neuroepithelium, and affects cranial neural crest, thus placing LRP2 in the context of multiple stem cell niches in the developing brain.

To conclude, on one hand, my work describes new aspects relevant for understanding the genetic modulation of signaling pathways and thus genetic predispositions to neural tube disorders. On other hand, we provide a detailed functional characterization of cell-autonomous mechanism in NTD etiology. LRP2 serves as a hub, orchestrating the signaling and endocytic pathways with cytoskeletal remodeling, at the periciliary compartment of the neuroepithelial stem cell. By this mechanism, LRP2 ensures homeostasis of neural stem cell niches and, simultaneously, facilitates the biomechanics of neural tube formation.

Zusammenfassung

Die Neurulation ist ein orchestrierter morphogenetischer Prozess, der die Integration verschiedener molekularer und zellulärer Ereignisse erfordert, um in der Entwicklung hochkomplexer Gehirnstruktur zu kulminieren. Viele mechanistische und regulatorische Aspekte der Vorstrukturierung der Neuralplatte sowie die genauen Grundlagen der weiteren Spezifikation der neuroepithelialen Stammzellen sind weitgehend unbekannt. Umso mehr sind weitere Erkenntnisse über die Koordination zentraler Entwicklungsprozesse für die erfolgreiche Prävention angeborener Hirndefekte beim Menschen unerlässlich.

Meine Doktorarbeit trägt wesentlich zum Verständnis der Mechanismen bei, die der Ätiologie angeborener Hirnerkrankungen zugrunde liegen. Im ersten Teil meiner Arbeit führte ich die funktionelle Charakterisierung potenzieller genetischer Modifikatoren in Mausmodellen mit einer ausgeprägten Veranlagung für Vorderhindefekte durch. Die Ergebnisse dieser Arbeit können durchaus auf die Penetranz und die Expressivität menschlicher kongenitaler Defekte der Gehirnentwicklung extrapoliert werden.
Eines der wichtigsten Signalmoleküle zu Beginn der Neurulation ist das Morphogen Sonic hedgehog (SHH), das für die ventrale Mittellinienspezifikation benötigt wird. Mäuse mit Verlust des low density lipoprotein receptor related protein 2 (LRP2), einem SHH-Co-Rezeptor im ventralen Vorderhirn, leiden unter einer unzureichenden SHH-Aufnahme und einem defekten Recycling des Morphogens durch das Neuroepithel und entwickeln eine Holoprosenzephalie (HPE) auf dem genetischen Hintergrund des C57BL/6N Mausstammes. Mäuse mit einer kongenen *Lrp2*-Mutationen auf einem FVB/N-Hintergrund zeigen jedoch eine normale *Shh* Expression im ventralen Vorderhirn sowie eine normale Trennung des Vorderhirnventrikels, das in normalen kortikalen Hemisphären resultiert. Mittels des Vergleichs von Transkriptomdaten konnten wir u.a. *Pttg1* und *Ulk4* als neue potenzielle genetische Modifikatoren identifizieren. Ich konnte in meiner Arbeit zeigen, das PTTG1 und ULK4 die Leistungsfähigkeit des SHH-Signalwegs positiv beeinflussen. Höhere Expressionsniveaus von *Pttg1* und *Ulk4* bei der Entwicklung des Gehirns von FVB/N-Mäusen, tragen wahrscheinlich zu einer vorteilhaften zellulären Umgebung bei, die den notwendigen SHH Morphogen Gradienten im ventralen Vorderhirn aufrechterhält,

trotz Verlust von LRP2. Durch diese Kompensation des Verlusts von LRP2 wird eine HPE verhindert. Wir postulieren, dass diese neu identifizierten, krankheitsrelevanten, positiven Modulatoren des SHH-Signalwegs die frühen Entwicklungsprozesse des Vorderhirns weniger anfällig für Störungen des SHH-Signalwegs machen.

Eine positive Regulierung der SHH-Maschinerie ist mit einer effizienten Ziliogenese verbunden. Tatsächlich identifizierte ich PTTG1 als eine neuartige Komponente des primären Ziliums. Ich konnte PTTG1 Protein am Basalkörper, dem primären Zilien-Organisationszentrum, und im Ziliarschacht nachweisen. Die variable Lokalisierung von PTTG1 im Vergleich verschiedener Zilien deutet darauf hin, dass es sich nicht um eine strukturell erforderliche Komponente des primären Ziliums handelt, sondern in regulierter Weise in den Ziliarschacht pendeln kann, um die Ziliarfunktion und/oder den Axonemaufbau zu unterstützen und damit letztlich die SHH-Signalkapazität zu verbessern.

Neben dem ventralen Vorderhirndefekt gibt es bei *Lrp2* mutierten Mäusen einen SHH-unabhängigen, dorsalen Phänotyp, der an Neuralrohrverschlussdefekte (NTDs) erinnert, die sowohl die Mutanten auf C57BL/6N als auch auf FVB/N Hintergrund betreffen. Durch die Kombination von Maus- und *Xenopus*-Arbeiten aus Kerstin Feistels Labor entdeckten wir eine konservierte, neuartige Funktion des LRP2-Rezeptors. Der Neuralrohrschluss ist ein dynamischer Prozess mit Umgestaltung des Zytoskeletts und apikaler Verengung der Zelloberfläche. Wir fanden heraus, dass die LRP2-abhängige apikale Membranumgestaltung für eine effiziente Auffaltung (Konvergenz) der Neuralplatte notwendig ist. Wir dokumentierten zum ersten Mal die funktionelle Wechselwirkung von LRP2 mit PDZ-haltigen Adapterproteinen im Neuroepithel, die als Brücke dienen und LRP2 mit dem intrazellulären subapikalen Gerüst von neuroepithelialen Zellen verlinkt. Die endozytotische Aktivität des Rezeptors unterstützt dabei die apikale Membranumbildung während der Konvergenz zum Neuralrohr. Gleichzeitig trägt diese zur apikobasalen Verteilung von VANGL2 bei, was auf eine enge Schnittstelle zwischen der Zellformkontrolle und der Aufrechterhaltung der planaren Zellpolarität hindeutet. Darüber hinaus berichte ich, dass die Funktion von LRP2 über die Spezifizierung des Neuroepithel hinausgeht und die Entwicklung der kranialen Neuralleisten beeinflusst, wodurch wir LRP2 Funktion im Kontext von multiplen Stammzellnischen im sich entwickelnden Gehirn definieren können.

Abschließend möchte ich sagen, dass meine Arbeit einerseits neue Aspekte beschreibt, die für das Verständnis der genetischen Modulation von Signalwegen und damit für die genetische Veranlagung von Neuralrohrschlussstörungen relevant sind. Auf der anderen Seite erarbeiteten wir eine detaillierte funktionelle Charakterisierung eines zellautonomen Mechanismus in der NTD-Ätiologie. LRP2 dient als Knotenpunkt, der die Signal- und Endozytosewege mit zytoskelettaler Umgestaltung im periziliären Kompartiment neuroepithelialer Stammzellen orchestriert. Dadurch gewährleistet LRP2 die Homöostase von neuronalen Stammzellnischen und unterstützt gleichzeitig die Biomechanik der Neuralrohrbildung.

Table of contents

List of abbreviations

LGE	Lateral ganglionic eminence	3
LRP2	Low-density lipoprotein Receptor-related Protein 2	12
MGE	Medial ganglionic eminence	3
MHP	Median hinge point	3
MKS	Meckel-Gruber Syndrome	26
ML	Mediolateral	6
MLC	Myosin light chain	6
MT	Microtubule	100
MTOC	Microtubule organizing center	100
MTOR	Mammalian target of rapamycin	77
NCC	Neural crest cell	4
NE	Neuroepithelium	1
NHERF1	Na+-H+ Exchanger Regulatory Factor 1	15
NP	Neural plate	1
NTC	Neural tube closure	1
NTD	Neural tube closure defect	1
OB	Olfactory bulb	8
ODF2	Outer dense fibre 2	103
OPC	Oligodendrocyte precursor cell	16
PBD	PDZ-binding domain	14
PBS	Phosphate-buffered saline	42
PCP	Planar cell polarity	5
PCR	Polymerase chain reaction	41
PDZ	Postsynaptic density 95, Disks large, Zona occludens-1	15
PrCP	Prechordal plate	3
P-S6RP	Phosphorylated ribosomal S6 protein	78
PTCH1	Patched 1	8
PTH	Parathyroid hormone	13
PTTG1	Pituitary tumor transforming gene	28
RA	Retinoic acid	8
RDVM	Rostral diencephalon ventral midline	3
RGC	Radial glial cell	77
RI	Refractive index	44
ROCK	Rho-associated kinase	6
RPGRIP1L	RPGR-Interacting Protein 1-Like Protein	26
RT	Room temperature	42
SCRB1	Scribble	6
SDA	Subdistal appendage	103
SDS	Sodium dodecyl sulfate	32
SDS-PAGE	SDS polyacrylamide gel electrophoresis	50
SEM	Scanning electron microscopy	51
SFOLR1	Soluble folate receptor 1	13
SHGB	Sex hormone binding globulin	13
SHH	Sonic hedgehog	2

List of figures

List of tables

I. INTRODUCTION

1 Complexity of brain development

The brain is the most sophisticated organ of the vertebrate body. The origin of brain structure and spinal cord begins at an early step in embryonic development through the process of neural tube closure (NTC), called neurulation (Colas and Schoenwolf, 2001; Schoenwolf and Smith, 1990). This fundamental process in embryogenesis consists of tightly coordinated morphogenetic changes that are in focus of the following sections.

Neurulation begins with a neural induction (Harland, 2000). This process determines the fate of dorsal embryonic ectodermal cells which acquire a neural fate and form a neural plate (NP) (Muñoz-Sanjuán and Brivanlou, 2002). Initially, the neuroepithelium (NE) is a flat sheet of cells, wide in the mediolateral and shorter in the rostrocaudal axis. Later it becomes thicker in the apicobasal axis where it acquires a pseudostratified, columnar character (Colas and Schoenwolf, 2001; Schoenwolf and Smith, 1990). Rostro-caudal elongation and specification of the embryo axis culminates with the formation of cranial region at the anterior neuropore and spinal region at the posterior end.

The hallmark of NTC is the bending and folding of the neural folds. This mechanical process is dependent on cell autonomous and tissue shape changes, which allow for elevation of the folds, culminating in a successful closure of the neural groove (Geelen and Langman, 1979; Nikolopoulou et al., 2017). Closure occurs gradually and is facilitated by 'zipping' from discrete closure points that initiate the fusion (Copp et al., 2003a). The first closure point is formed at the hindbrain/spinal cord level and allows for simultaneous fusion in anterior and posterior direction (Copp et al., 2003). Additional closing events at the cranial region start at the forebrain/midbrain boundary (closure 2) and at the rostral end of the anterior neuropore (closure 3) FIGURE 1 (Copp et al., 2003a). Interestingly, there is evidence that the position of closure 2 is polymorphic between inbred mice (Juriloff et al., 1991). A more rostral closure has been attributed to an increased susceptibility to develop cranial neural tube defects (NTDs) (Fleming and Copp, 2000). Additionally, limited reports from human embryology confirm the variable occurrence of closure 2 (Greene and Copp, 2009).
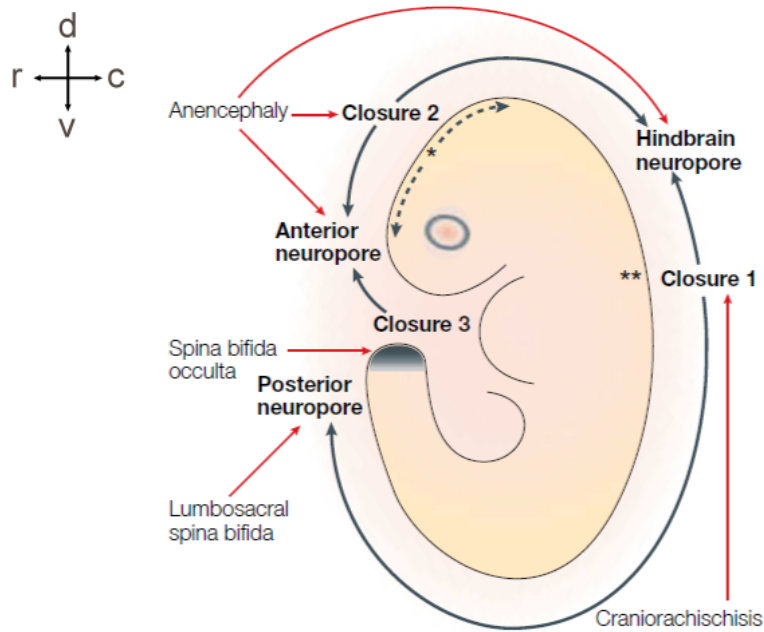
FIGURE 1: SCHEMATIC OF NEURULATION EVENTS DURING MOUSE DEVELOPMENT.
The closure of neural tube begins from closure 1, at the hindbrain/midbrain boundary at approximately 6-7 somites stage embryo, and continues in the rostral and caudal direction simultaneously. Cranial neural tube closure is facilitated by two additional closure sites: closure 2 at the forebrain/ midbrain boundary and closure 3 at the rostral end of the anterior neuropore. Black arrows indicate the directions of 'zippering'. Red arrows show the correlation between the closure points and specific NTC defects. Figure was adapted from (Copp et al., 2003a). d – dorsal, v – ventral, r – rostral, c – caudal.

The complexity of this fundamental embryonic morphogenesis has been the focus of many developmental studies, contributing to the understanding of many life-threatening congenital diseases (Greene and Copp, 2014).

1.1 Signaling pathways regulating forebrain patterning

Anterior-posterior patterning of the neural tube specifies forebrain, midbrain, hindbrain, and spinal cord regions. Additionally, complex signaling networks orchestrate the dorsoventral patterning (Gupta and Sen, 2016; Hoch et al., 2009). There are three, distinct organising centers established in developing forebrain FIGURE 2. Their key roles are maintenance of morphogens gradients and guidance of prospective brain structures development. The ventral midline (floor plate) is responsible for sonic hedgehog (SHH) signaling and ventral specification (Chiang et al., 1996). Anterior midline (anterior neural ridge, ANR) is a source of fibroblast growth factor (FGF) (Crossley et al., 2001). In contrast, the dorsal midline (roof plate) provides bone

morphogenetic protein (BMP) signaling (Furuta et al., 1997; Hébert et al., 2003)) and wingless-related integration site (WNT) signaling (Quinlan et al., 2009)), which serve as dorsalizing factors.
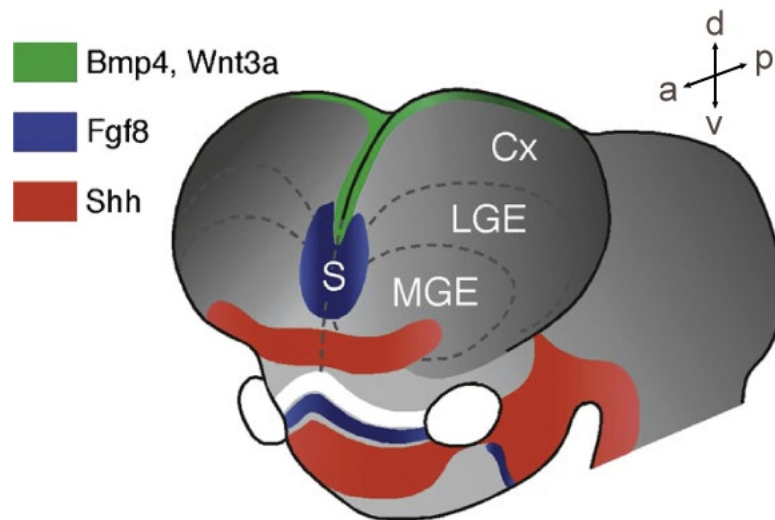
FIGURE 2: SIGNALING CENTERS GUIDING FOREBRAIN DEVELOPMENT.
Dorsoventral patterning of forebrain is regulated by four signaling centers: the dorsal midline (green) secretes WNTs and BMPs, the anterior center (blue) secretes FGFs, and the ventral midline secretes SHH. Figure was adapted from (Hoch et al., 2009). d – dorsal, v – ventral, a – anterior, p – posterior, S – septum, Cx – cortex, LGE – lateral ganglionic eminence, MGE – medial ganglionic eminence.

SHH signaling regulates both proliferation and specification of different cell types and their survival, and thusly is essential for the development of many organs, from brain and spinal cord to axial skeleton and limbs (Chiang et al., 1996). During onset of forebrain development, SHH takes part in ventral specification and acts on the rostral diencephalon ventral midline (RDVM). The morphogen SHH originates from the underlying prechordal plate (PrCP). It is internalized by membrane proteins and activates target genes via Glioma-associated oncogene homolog 1 (GLI) transcription factors (TFs) (Bertrand and Dahmane, 2006; Hoch et al., 2009). The induction of the ventral midline contributes to the median hinge point (MHP) formation, which is characterized by wedge-shaped cells with apically constricted surfaces. These cell shape changes facilitate initial bending of the neural folds (Greene and Copp, 2014; Placzek and Briscoe, 2005). Further into the forebrain development, SHH contributes to formation of lateral (LGE) and medial (MGE) ganglionic eminences, ventral telencephalic domains, and additionally plays a role in maintaining expression of FGF/BMP signals (Hayhurst et al., 2008; Hoch et al., 2009).

During gastrulation, FGF signaling initiates neural plate formation (Streit et al., 2000) and remains active through the early patterning of rostral telencephalon. Expression of FGF8, a key signaling molecule in this pathway, is found at the anterior neural ridge (ANR), which later becomes the rostral midline (Crossley et al., 2001). FGF8 regulates the proliferation, patterning of ventral progenitor cells, and overall size of the telencephalon (Theil et al., 2008) in coordination with SHH and BMP signals (Crossley et al., 2001). Interestingly, FGF signaling additionally depends on the correct cranial neural crest specification (Creuzet, 2009), indicating the cross-regulation between forebrain and neural crest cells (NCC) development.

BMP signaling is present at the gastrula ectoderm, and clearance of BMP ligands by inhibitors noggin and chordin coincides with neural induction and the onset of neurulation (Muñoz-Sanjuán and Brivanlou, 2002). BMP antagonism persists during neurulation and also contributes to the formation of dorsolateral hinge points (DLHPs) and neural folds bending, which brings dorsolateral ends together (Ybot-Gonzalez et al., 2007). Later in development, BMP signaling contributes to dorsal midline specification and the development of choroid plexus (Hébert et al., 2003). BMP factors are members of transforming growth factor beta (TGFβ) family and modulate SMAD (Mothers against decapentaplegic (DPP)) transcription factors via kinase receptors. BMP acts antagonistically to SHH and FGF signals, decreasing proliferative capacity of the tissue (Bertrand and Dahmane, 2006; Ohkubo et al., 2002).

WNT/ β-catenin signaling is a key regulator of initial developmental processes, from pre-implantation, germ layer growth, to body axis specification and neurogenesis. WNT glycoproteins function through frizzled receptors, and β-catenin, that interacts with T-cell factor (TCF)/ lymphoid-enhancer factor (LEF) transcription factors to drive transcription of target genes (Harrison-Uy and Pleasure, 2012; Marikawa, 2006). During neurulation, WNT promotes proliferation of the neuroepithelium and antagonizes the SHH and FGF signaling molecules. In forebrain patterning, cells receiving WNT signals adapt a dorsal identity, which contributes to roof plate specification and further choroid plexus and WNT-secreting cortical hem (Quinlan et al., 2009). While invagination separates two cerebral hemispheres, the dorsal structures form the hippocampus and the cerebral cortex (Gupta and Sen, 2016).

Additionally, the non-canonical, β-catenin independent, WNT/planar cell polarity (PCP) pathway has also been described during early development. WNT/PCP is responsible for the maintenance of polarity of the epithelial cells, which undergo dynamic morphogenetic changes, such as during neural tube closure (Seifert and Mlodzik, 2007; Wang et al., 2019a). WNT/PCP integrates the apico-basal distribution of different molecules in order to orchestrate the changes on the tissue plane level. This is discussed further in the following section (section 1.2).

Optimal balance between the signaling centers is required for the proper forebrain development *FIGURE 3*.
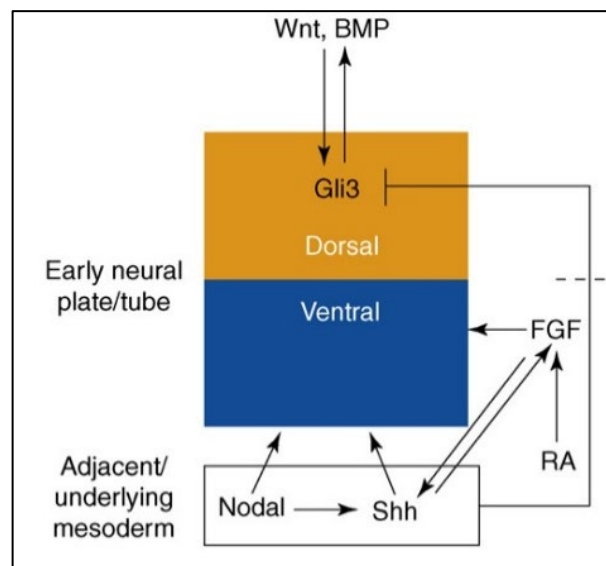
FIGURE 3: SIGNALING CROSSTALK DURING EARLY FOREBRAIN DEVELOPMENT.
Schematic depicting the interactions between signaling pathways occuring during early (E8.5 - E9.5) forebrain development. Arrows indicate the positive and T shape negative regulation. Figure was adapted from (Bertrand and Dahmane, 2006).

1.2   Mechanisms of neural tube morphogenesis

Neural tube formation and early forebrain patterning not only require signaling cues, but also mechanical forces to drive the cell shape changes, migration, intercalation, and tissue rearrangements to allow the simple neuroepithelial sheet to bend and fuse (Cearns et al., 2016; Colas and Schoenwolf, 2001; Nikolopoulou et al., 2017). The principal morphological processes are discussed in further detail below.

The hallmark of epithelial bending and tube formation is apical constriction, which allows cells to adapt a wedge-like shape with an expanded basal membrane and

narrowed apical surface. This cellular process is manifested by contraction of the apical actomyosin belt and finalizes with the reduction of the cell surface area (Suzuki et al., 2012). Central regulation of the apical constriction influences interaction of type II myosin motors with F-actin filaments and depends on phosphorylation of myosin light chain (MLC) by Rho-associated kinase (ROCK), a downstream effector of Rho/ROCK pathway (Barrett et al., 1997; Martin and Goldstein, 2014; Rolo et al., 2009). In consequence of apical constriction at the cellular level, hinge points are formed in precise locations across the tissue plane (Haigo et al., 2003; Schoenwolf and Smith, 1990). Thus, changes at the cellular level further drive furrow formation and bending of initially flat tissue.

Cytoskeletal rearrangements must be accompanied by cell membrane remodelling in order to guide lumen formation. The contraction of the apical plasma membrane has been linked to the apical endocytic pathways. Studies in *Drosophila* and *Xenopus* have shown that endocytosis facilitates the actomyosin contractility by removing excess membrane (Fabrowski et al., 2013; Lee and Harland, 2010). Only coordination of these processes allows for efficient cell shape changes, which, in consequence, leads to morphogenetic changes across the tissue plane.

Preceding the neural tube closure, the neural plate elongates, leaving the rostral (cranial) region widened and the caudal (spinal) region narrowed. According to current knowledge, the main driving force for these morphological changes is convergent extension (CE) (Wallingford et al., 2002). It consists of mediolateral (ML) convergence of neural and underlying non-neuronal mesodermal cells, which intercalate in the midline, leading to anterior-posterior (AP) lengthening of the neural plate (Keller et al., 2000).

Interestingly, studies on convergent extension and onset of neurulation performed on *Xenopus* and mice revealed the non-canonical WNT/PCP pathway plays a critical regulatory role in these processes (Darken et al., 2002; Sutherland et al., 2020a; Wallingford and Harland, 2002). Mutations in core WNT/PCP genes in mice are associated with CE phenotype and NTDs: Vang-like protein 2 (*Vangl2,* also *Ltap* or *Lpp1; loop-tail*) (Greene et al., 1998; Kibar et al., 2001; Montcouquiol et al., 2003), cadherin EGF LAG seven-pass G-type receptor 1 (*Celsr1*; *crash*) (Curtin et al., 2003; Nishimura et al., 2012), scribble (*Scrb1*; *circletail*) (Murdoch et al., 2003). Common

features of *Vangl2*, *Celsr1* and *Scrb1* mutant mice are: a widened neural plate and lack of well-defined median hinge points, which normally facilitates the bending of neural folds. Moreover, single, as well as double, mutants of these genes are lethal and documented with the most severe NTD – craniorachischisis – reminiscent of failure in closure 1, which culminates in an almost entirely open NT (Copp et al., 1994, 2003a; Murdoch et al., 2001).

Parallel to the neural tube formation, a new pluripotent population of cells, the neural crest cells (NCCs), arises from the dorsolateral neural folds. Although the process of delamination varies between the vertebrates, it has a close correlation to the neural tube closure and dorsalization of the forebrain regions (Creuzet, 2009; Creuzet et al., 2006). NCCs undergo epithelial to mesenchymal transition (EMT) and acquire migratory properties driving them to distinct embryonic regions in order to differentiate into various cell types (Mayor and Theveneau, 2013). EMT requires the loosening of cell-cell contacts on the border between the neuronal and non-neuronal ectoderm and may also facilitate the fusion of dorsal extensions of neural folds (Theveneau and Mayor, 2012a).

2 Impaired neural tube formation leads to congenital brain disorders

Congenital brain disorders affect development of the central nervous system (CNS) and they have been associated with many genetic and environmental risk factors. Variety of different animal models have been generated in order to better understand the normal course of development of complex brain structures and to analyse the consequences in abnormal situations. Due to their multifactorial origin and complexity of various morphogenetic processes that occur in the early stage of brain development, presently, the mechanisms of congenital brain disorders have not been well understood.

2.1 Holoprosencephaly (HPE) – the most common forebrain defect

Holoprosencephaly (HPE) statistically affects 1 out of every 250 human pregnancies, with most being lethal at early stage, bringing liveborn cases to around 1:10,000 - 20,000 (Muenke and Beachy, 2000). It develops due to genetic and environmental

disturbances, altering the primary neurulation occurring around week 4 of human gestation.

HPE is characterised by the failure of the forebrain (prosencephalon) to separate along the mid-sagittal axis into prospective right and left cerebral hemispheres (Cohen, 1989; Tekendo-Ngongang et al., 1993; Wallis and Muenke, 1999). Depending on the severity, it can lead to a drastic alobar HPE - characterized by a single brain ventricle lacking the corpus callosum and olfactory bulbs (OB). Semilobar HPE presents fusion of only frontal and parietal lobes, accompanied by absent or hypoplastic OB, while the least severe lobar HPE have mostly separated and developed brain structures. Structural brain anomalies are commonly accompanied by broad range of craniofacial malformations, from cyclopia, proboscis, cleft lip and/or palate, nasal defects, to milder ocular hypotelorism, single incisor and microcephaly (Geng and Oliver, 2009; Ming and Muenke, 2002; Tekendo-Ngongang et al., 1993; Wallis and Muenke, 1999).

Both genetic predisposition and environmental factors contribute to the complexity of HPE condition. Patient studies have shown that HPE can be mono-, di-, and oligogenic event, affecting chromosomes, with either autosomal dominant or recessive models of inheritance (Dubourg et al., 2018; Kim et al., 2019; Muenke and Beachy, 2000; Roessler and Muenke, 2010). Amongst primary, well-known, genetic mutations that have been identified in HPE patients are: *SHH* (Belloni et al., 1996; Roessler et al., 1996)*, Sine Oculis Homeobox-Like Protein 3* (*SIX3*) (Wallis et al., 1999)*, and Zinc Finger Protein Of The Cerebellum 2* (*ZIC2*) (Brown et al., 1998)*. Over the last few years, the range of genes important for forebrain development broadened by other, such as: *Patched 1* (*PTCH1*)*, GLI2, Forkhead Box H1* (*FOXH1*)*, TGFB Induced Factor Homeobox* (*TGIF*) (Wallis and Muenke, 1999)*, and more (Kim et al., 2019).

Additionally, maternal health status including diabetes, alcoholism, and prenatal exposure to drugs (retinoic acid (RA), cholesterol biosynthesis inhibitors), drastically increase the risk of HPE (Cohen and Shiota, 2002; Hong et al., 2020; Krauss and Hong, 2016). A combination of such a variety of factors culminates in a broad spectrum of clinical HPE manifestations, however, it does not fully explain the phenotypic variability observed between families, or, more strikingly, even between family members carrying the same mutation (Dubourg et al., 2018; Hong and Krauss, 2018; Solomon et al., 2010).

2.1.1 Defects in SHH signaling lead to HPE in human and mouse

Mouse models of HPE, based on human mutations, have elucidated mechanisms of HPE phenotypes, and they have proven to be instrumental in the progression of understanding human disease (Hayhurst and McConnell, 2003; Hong and Krauss, 2018). Often, single homozygous mouse mutants develop HPE features. While heterozygous mice appear normal, unless other mutations are introduced, or intriguingly, dependent on the congenic background (Geng and Oliver, 2009; Hong and Krauss, 2018). This supports a multigenic model of HPE, where co-occurrence of mutations in HPE-associated genes can lead to the phenotype and notably modulate its severity (Dubourg et al., 2018; Kim et al., 2019).

Interestingly, unlike in mice, homozygous variants of major HPE genes (*SHH, ZIC2, SIX3*) in human have not been documented, which can be explained by their critical function in the embryonic development (Dubourg et al., 2018; Geng and Oliver, 2009). Most likely, immediate lethality of such foetuses excludes them from clinical examinations. Following this line of evidences, an autosomal recessive model of inheritance in humans is a rare event and concerns less critical genes, in contrast to autosomal dominant (*de novo*) mutations (Dubourg et al., 2018).

According to clinical studies, most HPE-related mutations are linked to chromosome 7q36, where various SHH mutations, spanning the entire coding region, contribute to approximately 37% of all cases within autosomal dominant inheritance model of disease (Muenke and Beachy, 2000). SHH-deficient mouse embryos develop severe HPE phenotypes, represented by a loss of ventral forebrain structures, single brain vesicle, cyclopia, and proboscis. They also exhibit severe growth retardation, affecting the spinal cord and distal limbs (Chiang et al., 1996). Interestingly other components of SHH signaling have also been linked to the HPE phenotype in both human and mouse. Embryos deficient for *Dispatched RND Transporter Family Member 1* (*Disp1*) and *Smoothened* (*Smo*) also develop a single brain vesicle and cyclopia (Ma et al., 2002; Zhang et al., 2001). Lack of *Gli2* leads to ventral defects and craniofacial malformations, and, importantly, the single-allel-deficiency increases the severity of HPE after teratogenic factors (Heyne et al., 2016).

Despite enormous advances in the HPE field, the largest obstacle is to understand the bases of distinct clinical manifestations observed in human patients. Intriguingly,

independent studies report that the variability of HPE penetrance is reflected in mouse models, where it commonly depends on examined mouse strains (Anderson et al., 2002; Geng and Oliver, 2009; Geng et al., 2008; Hong and Krauss, 2018). Such results leave an open window for thorough investigation of new, disease relevant, strain dependent factors.

2.2 Neural tube closure defects (NTDs)

Neural tube defects (NTDs) arise from the failure of the neural tube to close during the first 3-5 weeks of pregnancy and are the most prevalent malformation among humans, after congenital heart defects (Zaganjor et al., 2016). An analysis of global and regional prevalence of NTDs reported that approximately 0.8 - 1 children in Europe to 3.2 in Southern Asia, per 1000 live births, suffer from NTDs. About 50% of the cases are subjected to pregnancy terminations, and 75% of infants die within 5 years (Blencowe et al., 2018).

Depending on the region of the neural tube which is affected, NTDs are classified into two categories: (1) NTDs related to anterior neuropore, which are usually lethal around birth, and (2) NTDs related to posterior neuropore, where individuals suffer from motor and sensory defects in legs, urinary and faecal problems, altered vertebrate curvature and hydrocephalus (Copp et al., 2003a; Greene and Copp, 2014). Exencephaly is a result of the open anterior neural tube and appears as transient enlargement of the neuropore, which, by late gestation, degenerates and results in anencephaly (Copp, 2005; Wood and Smith, 1984). A related cranial defect is encephalocele, where, despite proper closure of neural tube, part of the brain herniates through the altered skull. The most common defects affecting the posterior neuropore are the spinal closure defects, leading to spina bifida (myelomeningocele, myelocele) (Straaten et al., 1993). Failures in the upper spinal level result in craniorachischisis, where most of the brain and spinal cord remain open (Copp et al., 1994; Murdoch et al., 2001).

2.2.1 Risk factors for NTDs in human

High prevalence of NTDs correlates with a variety of risk factors that have been documented. Among the environmental causes are the maternal health status, such as obesity and diabetes, as well as continuous temperature instabilities and administration of teratogens, such as anticonvulsant drugs (Greene and Copp, 2014; Wallingford et al., 2013). The most recognized risk factor is nutrition, where low

maternal levels of vitamin B_9 (folate) have been correlated with high risk for affected pregnancy (Rosenquist and Finnell, 2001). However, up to 50% of NTDs are not susceptible to folate supplementation (Blom et al., 2006).

Despite mostly sporadic occurrence of pathology, there have been many genetic candidates from various signaling networks associated with NTDs, including those related to folate metabolism, glucose metabolism, DNA repair, retinoic acid signaling and the WNT/PCP pathway (Wallingford et al., 2013). Interestingly, the presence of additional environmental factors, such as maternal diabetes, have an increasing and detrimental influence on folate-impaired embryonic development (López-Escobar et al., 2019). Although some case studies implicate the possibility of a multifactorial poly- or oligogenic models of inheritance, it is difficult to assess because of a strong epigenetic and environmental influence on the disease expressivity (Juriloff and Harris, 2018).

Low folate levels result in an imbalance of amino acids required for nucleic acid biosynthesis, resulting in the accumulation of homocysteine due to methyl groups being unavailable for methylation, in order to transform homocysteine into methionine (Kang et al., 1987). In this vein, recent studies suggest the entirety of methylation metabolism, including B vitamins (B_2, B_6, B_9, B_{12}), methionine, and choline, influences the prevalence of NTDs (Blom et al., 2006; Imbard et al., 2013; Rosenquist et al., 2007). Overall, one-carbon (1C) metabolism is implicated as a critical link between parental nutritional environment and epigenetic regulation of embryonic development, and the alterations at this biochemical level translate into severe cellular malfunctions and a wide range of congenital defects (Clare et al., 2019; Renard et al., 2019; Steele et al., 2020). Mouse models serve as an invaluable tool to address the mechanistic foundations of NTDs. According to *Harris et al.,* the number of mouse models with NTDs exceeds 240, confirming the oligogenic occurrence and drawing attention to chromatin modifications and ciliopathies (Harris and Juriloff, 2007, 2010).

3 LDL Receptor Related Protein 2 - important player in embryogenesis

Low-density lipoprotein Receptor-related Protein 2, LRP2, also called gp330 or megalin, is a large 600-kDa cell-surface protein, belonging to the low-density lipoprotein (LDL) receptor gene family (Saito et al., 1994) *FIGURE 4*. Members of this family are evolutionarily conserved, and are found from nematodes and insects to vertebrates. Commonly, LRP family members are known as co-receptors for a vast variety of molecules from lipoproteins (Goldstein and Brown, 1979; Mineo, 2020), hormones (Hammes et al., 2005), vitamin carriers (Christensen et al., 1999; Kur et al., 2014; Nykjaer et al., 1999), and signaling proteins (Christ et al., 2012, 2015; Gajera et al., 2010; Tamai et al., 2000). They play a role in the modulation of ligand binding and cellular signal transduction (Herz and Strickland, 2001; Willnow et al., 2012). However, the driving force for delivery of the extracellular cargos and signals comes from the high endocytic capacity of these intracellular receptors (Nykjaer and Willnow, 2002; Schneider and Nimpf, 2003).
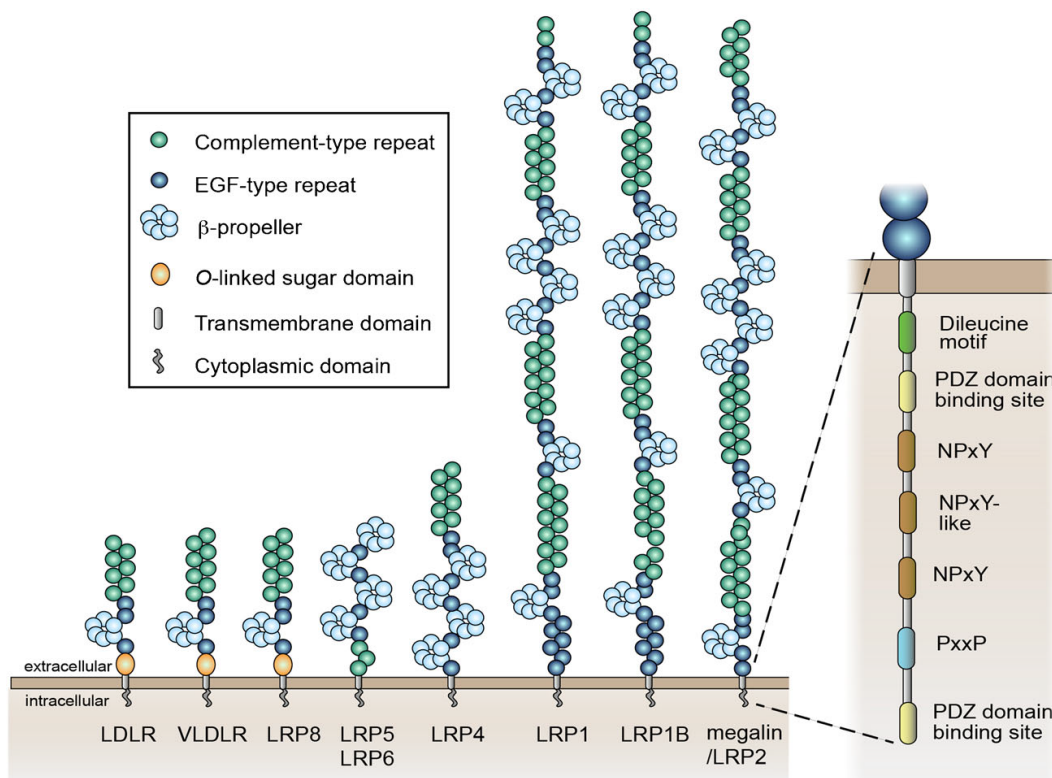
FIGURE 4 LRP2 IS A MEMBER OF THE LDL RECEPTOR GENE FAMILY.
Organisation of the mammalian LDL receptor gene family including structural differences between the members. Common elements of extracellular domains are described in the legend. The inset presents the functional motifs of cytoplasmic domain of LRP2. For further description, see section 3.1.1. Figure was adapted from (Willnow and Christ, 2017).

3.1 Plethora of LRP2 ligands

LRP2, as other LDL family members, is responsible for receptor-mediated endocytosis, which allows for the transport of macromolecules into cells and consequent signal transduction (Willnow and Christ, 2017). It is achieved either by direct binding of the molecules or by binding with the cargo proteins, and is facilitated by functional interactions of LRP2 with other multiligand epithelial receptors like cubilin (Assémat et al., 2005).

LRP2 regulates cellular uptake of a variety of molecules (Spuch et al., 2012). For example, it internalizes vitamins through binding their carriers: retinol-binding protein (RBP) (Christensen et al., 1999), vitamin D-binding protein (Nykjaer et al., 1999), and complex of transcobalamin – vitamin B_{12} (Moestrup et al., 1996). Additionally, a carrier for vitamin B_9 - folate binding protein (FBP), also known as soluble folate receptor 1 (sFOLR1), was detected to bind with LRP2 in kidney (Birn et al., 2005) and in developing brain (Kur et al., 2014).

The receptor binds also sex hormone binding globulin (SHGB), cargo for androgens and estrogens (Hammes et al., 2005) and parathyroid hormone (PTH) directly (Hilpert et al., 1999). It was reported to control renal insulin reabsorption (Orlando et al., 1998).

Furthermore, LRP2 acts as a scavenger for morphogens, and becomes a component of two critical signaling pathways in early embryogenesis: BMP (Spoelgen et al., 2005) and SHH (Christ et al., 2012; McCarthy et al., 2002).

The fate of the ligands differs. They either can be transported through polarized epithelia in the apico-basal axis or directed to lysosomes for degradation and retrieval of their amino acids, or recycled to the apical membrane (Willnow and Christ, 2017). The following sections provide more details on LRP2-dependent endocytosis.

3.1.1 LRP2 – receptor endowed with broad range of functional domains

LRP2 owes its physiological function to a large extracellular domain (ECD) responsible for ligand binding FIGURE 4. It is composed of four cysteine-rich complement-type ligand binding repeats, which are separated by β-propeller domains flanked by calcium-binding epidermal growth factor (EGF) homology modules (Marzolo and Farfán, 2011; Saito et al., 1994). EGF-like modules are assigned with a dual role:

facilitating proper receptor folding, as well as pH-dependent deposition of ligands into the acidic endosomal vesicles (Jeon et al., 2001). The transmembrane domain anchors the receptor in the cholesterol-rich apical plasma membrane of polarized epithelia (Marzolo et al., 2003), while the 209 amino acid residue intracellular domain (ICD) is necessary for the receptor trafficking.

The mechanisms of LRP2 internalization are associated with two conserved types of motifs present within the ICD. Two NPxY endocytic motifs serve as a recognition site for internalization of LRP2 in clathrin-coated pits found at the apical plasma membrane (Chen et al., 1990). A clathrin-dependent endocytosis occurs in visceral endoderm cells, supplying nutrients to the early embryo, and in renal epithelium (Gravotta et al., 2019; Maurer and Cooper, 2005; Saito et al., 2009). In contrast, a NPxY-like motif is responsible for the apical sorting of LRP2 (Takeda et al., 2003). Additionally, there is evidence for a clathrin-independent endocytosis in astrocytes, which involves caveolins, integral membrane proteins found in small membrane invaginations called caveolae (Bento-Abreu et al., 2009).

The second type of conserved sequences contributing to endocytic function of LRP2 are two PDZ-binding domains (PBD) present within ICD. They serve as indirect interaction sites between the receptor and the cytoskeletal and cytosolic scaffold (Gotthardt et al., 2000). The cytoplasmic tail of LRP2 also contains several phosphorylation motifs. One prominent and highly conserved proline-rich sequence (PPPSP) is constitutively phosphorylated by glycogen synthase kinase-3 (GSK3). This is a feature unique to LRPs and has been linked to the high recycling capacity of LRP2 (Yuseff et al., 2007).

3.1.2 Intracellular adaptor proteins for LRP2

The LRP2-dependent endocytic pathway is mediated by various functional interactions between the cytoplasmic tail and intracellular adaptor proteins (Gotthardt et al., 2000). One group of adaptor proteins for LRP2, are clathrin adaptors, such as adaptor protein 1 (AP-1) (Gravotta et al., 2019), AP-2 (Maurer and Cooper, 2005), Disabled-1 (DAB1) (Gotthardt et al., 2000), and DAB2, (Maurer and Cooper, 2005; Oleinikov et al., 2000). These adaptor proteins interact with LRP2 through binding to the NPxY endocytic motifs and assist in endocytosis and receptor trafficking by recruiting LRP2 to clathrin-coated

vesicles. Additionally, DAB2 can guide these coated endocytic vesicles through the actin cytoskeleton due to interaction with motor protein myosin 6 (Morris et al., 2002).

Another group of LRP2 interacting partners are PDZ-domain containing adaptor proteins. Postsynaptic density 95, Disks large, Zona occludens-1 (PDZ) domain is one of the common recognition sites for cellular trafficking and cytoskeletal interactions between proteins (Liu and Fuentes, 2019). LRP2 directly interacts with GAIP C-terminus-interacting protein 1 (GIPC1, also known as synectin/ TIP2/ GLUT1CBP/ SEMCAP-1) (Naccache et al., 2006) and Na^+-H^+ Exchanger Regulatory Factor 1 (NHERF1, also known as EBP50/ Slc9a3r1) (Slattery et al., 2011) in renal proximal tubule cells. GIPC1, in contrast to DAB2, recruits the myosin 6 to uncoated LRP2-mediated endocytic vesicles and also guide them through the actin meshwork (Aschenbrenner et al., 2003; Naccache et al., 2006).

Thanks to the diverse intracellular communication with adaptor proteins, LRP2 plays important, context-dependent physiological functions in various highly absorptive epithelia.

3.2 Manifestations of LRP2-deficiency in mouse model

Within mammals, LRP2 associates with specialized and highly absorptive epithelia of lung, brain, eye, kidney, and reproductive tissue. Various functions of the receptor have been extensively studied in mouse model and they are the subject of this section.

Newborn *Lrp2$^{-/-}$* mice die perinatally, most likely from respiratory complications, due to altered alveolar development (Willnow et al., 1996). They develop HPE, with a similar phenotype as in humans, resulting in affected forebrain - fusion of cortical hemispheres and craniofacial anomalies, such as shorter skull, midfacial clefting, and eye defects (Spoelgen et al., 2005; Willnow et al., 1996).

Another critical organ affected by loss of LRP2 is the heart (Baardman et al., 2016; Li et al., 2015). *Lrp2$^{-/-}$* mutant embryos develop with a common arterial trunk (CAT), in which the pulmonary artery and ascending aorta are fused. In some cases, the phenotype exhibits double-outlet right ventricle (DORV), characterised by both vessels connected to the right ventricle (Baardman et al., 2016; Mecklenburg et al., 2020). The molecular mechanisms for separate aorta and pulmonary trunk development were linked to the novel LRP2 function in the maintenance of the cardiac progenitor niche in

the anterior second heart field (SHF), a structure which contributes to outflow tract formation (Christ et al., 2020).

LRP2 is highly expressed in proximal tubular cells in the kidney (Willnow et al., 1996). Although, from a developmental point of view, the organ is mostly not altered, there is a mild decrease in the size and number of apical vesicles documented. Instead, LRP2-deficiency largely impairs essential renal functions - reabsorption of low-molecular weight proteins and vitamin carriers from glomerular filtrate (see section 3.1) (Birn et al., 2005; Christensen et al., 1999; Moestrup et al., 1996; Nykjaer et al., 1999). Analogical renal dysfunction affects human with renal Fanconi syndrome (Willnow and Christ, 2017). Interestingly, it has been shown that incomplete expression of LRP2 in neonatal kidneys of pre-termed infants is associated with vitamin A and D deficiencies (Charlton et al., 2019).

LRP2 contributes also to hormone dependent maturation of reproductive organs of both sexes by facilitating uptake of sex hormone binding globulin (SHBG), which transports androgens and estrogens (Hammes et al., 2005). LRP2 deficient mice were unable to efficiently respond to sex steroids.

Moreover LRP2 was reported to affect the morphology of the developing spinal cord, including the regulation of astrocyte and oligodendrocyte populations in this region (Wicher and Aldskogius, 2008). Additionally, the maturation of oligodendrocytes from oligodendrocyte precursor cells (OPCs) is also affected during optic nerve development (Ortega et al., 2012).

3.3 LRP2-related phenotypes in mice reflect severe human disorders

Independent patient studies documented *LRP2* pathogenic variants as genetic risk factors for developmental disorders affecting the brain and heart (Kozyraki and Cases, 2017).

Donnai-Barrow syndrome (DBS) or Faciooculoacusticorenal (FOAR) syndrome (DBS/FOAR) is a rare autosomal recessive disorder affecting, amongst others, brain and craniofacial structures. Clinical manifestations include agenesis of corpus callosum, enlarged anterior fontanelle, ocular anomalies, hearing loss, diaphragmatic hernia, proteinuria and intellectual disabilities (Longoni et al., 1993; Pober et al., 2009). *Kantarci* and colleagues were the first to associate DBS/FOAR syndrome to the 79-

exon-*LRP2* gene mapped to human chromosome 2q31.1. They used single nucleotide polymorphism (SNP) arrays to assess gene variants among affected patients (Kantarci et al., 2007). Analysis of coding and intron-exon fragments revealed various mutations, including: missense, nonsense, splice junction, and frameshifts within conserved sites of both alleles, encoding the extracellular domain of the receptor (Kantarci et al., 2007). Over the years, more case studies reported a *LRP2* association with DBS/FOAR (Kantarci et al., 2008; Ozdemir et al., 2019), with examples of inter- and intrafamilial variability in phenotypes (Khalifa et al., 2015; Pober et al., 2009). In addition, mutations in *LRP2* were reported in human cases diagnosed with HPE microforms (Rosenfeld et al., 2010), and, more recently, in severe HPE patients as well (Kim et al., 2019).

Some HPE and DBS/FOAR patients present characteristic craniofacial features, such as hypertelorism (widely spaced eyes) or severe cases of cyclopia, coloboma, short nose, midfacial clefting (Longoni et al., 1993; Tekendo-Ngongang et al., 1993). Such features are observed in patients with *LRP2* mutations as well (Kantarci et al., 2008). Interestingly, the LRP2 mouse model recapitulates the patients' phenotypes faithfully. *Lrp2* mutants, apart from brain defects, exhibit severe alterations in the maturation of craniofacial cartilage, manifested by shorter snout, midfacial clefting, eye anomalies, and cases of cyclopia as well (Mecklenburg et al., 2020; Willnow et al., 1996). However, until now, there are no published studies examining the role of LRP2 in the craniofacial development.

Additionally, congenital heart defects were documented in patients diagnosed with HPE and DBS/FOAR (Pober et al., 2009; Tekendo-Ngongang et al., 2020). Interestingly, an independent study on congenital heart defects in human listed *LRP2* amongst genes with *de novo* mutations (Zaidi et al., 2013). Whereas examination of patients with congenital hypoplastic left heart syndrome indicated function of *LRP2* in cardiomyocytes maturation (Theis et al., 2020).

Furthermore, *LRP2* SNPs appeared amongst the candidate genetic risk factors for neural tube defects in human (Pangilinan et al., 2012). However, there was no direct link for its causative effect until *Kur et al*. recently described the role of LRP2 in folate uptake in developing mouse brain (Kur et al., 2014). The first clinical evidence of pathogenic *LRP2* gene variants in human NTDs was reported much later and indicated a strong correlation between *LRP2* mutations and risk of NTDs, including altered folate

and active-B$_{12}$ (holotranscobalamin) serum levels (Prasoona K. et al., 2018). Another genetic study, based on exome sequencing, confirmed the association of *SHH* related genes, including *LRP2,* with risk of developing NTD in humans (Renard et al., 2019).

4 Understanding the LRP2 function in neurodevelopmental disorders

LRP2 mouse models have been critical in understanding human forebrain development (Spoelgen et al., 2005; Willnow et al., 1996). LRP2 is expressed broadly and uniformly on the apical surface of neuroepithelial cells and in the adjacent, non-neuronal ectoderm FIGURE 5, implicating an important role of the receptor during neurulation.
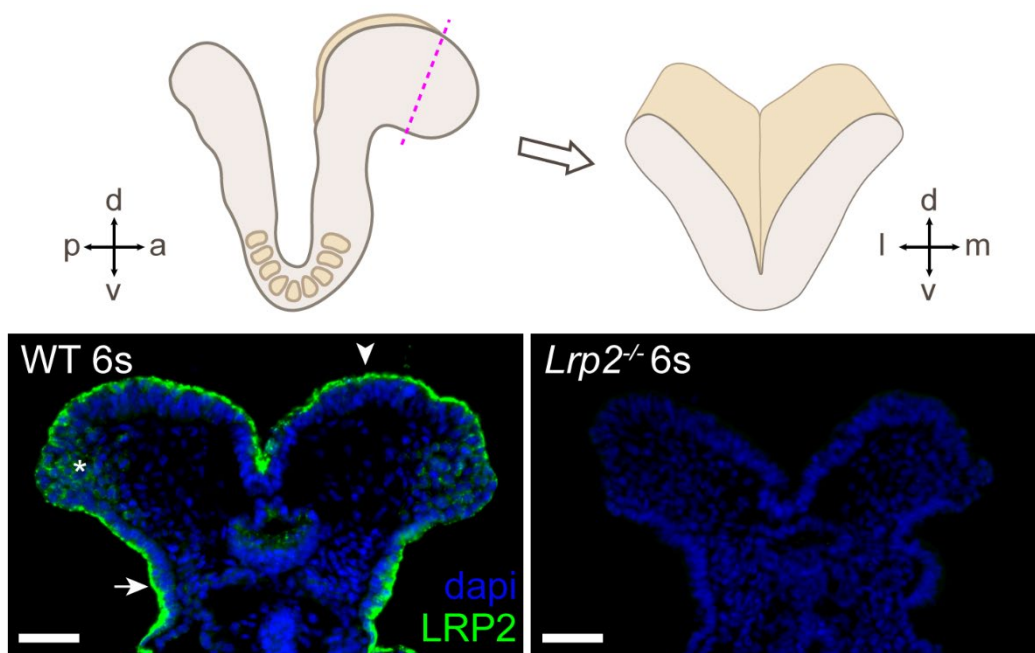
FIGURE 5 LRP2 EXPRESSION DURING NEURULATION.
From the top: schematic illustration of the E8.5 mouse embryo and coronal section through the anterior neural folds (magenta dashed-line). Immunofluorescence on coronal sections from wild-type (WT) and *Lrp2$^{-/-}$* mutant embryos at 6 somites (s). LRP2 is expressed on the apical surface of WT neuroepithelium (arrowhead), along the adjacent non-neuronal ectoderm (arrow). Note LRP2 expression in the dorsolateral neural folds (asterisk). d – dorsal, v – ventral, a – anterior, p – posterior, l – lateral, m – medial. Scale bar 50 µm.

4.1 LRP2 is necessary for SHH signaling in developing ventral forebrain

The balance between SHH and BMP4 morphogens is necessary for dorsoventral patterning. SHH is responsible for the ventral cell fates and BMP for dorsal cell fates, and they act antagonistically on each other (see section 1.1). LRP2 has the capability to bind both morphogens, and lack of LRP2 expression alters both early patterning centers (Spoelgen et al., 2005). However, *Christ et al.* showed the primary target of LRP2 activity during ventral forebrain specification is SHH signaling, since the BMP4 and FGF8 morphogens are not altered at this early time point (Christ et al., 2012). Of secondary consequence, BMP4 signaling was increased as well.
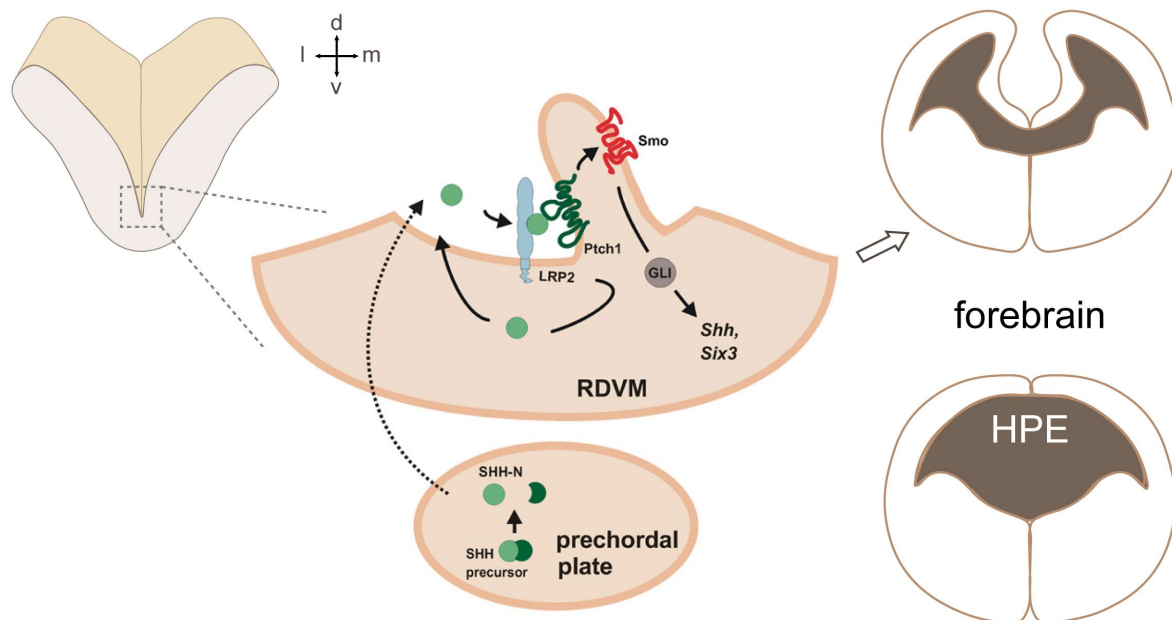
FIGURE 6 LRP2 FACILITATES SHH INTERNALIZATION IN THE VENTRAL MIDLINE.
SHH signaling associates with primary cilium of neuroepithelial cells. LRP2 acts as a co-receptor for Patched1 (Ptch1) and controls cellular uptake and recycling of SHH in the rostral diencephalon ventral midline (RDVM). SHH binding triggers Smoothened (Smo) activation and consequent GLI and target gene expression. Note, only a lipophilic, post-translationally modified SHH molecule with cholesterol moiety is internalized by LRP2 (McCarthy et al., 2002). Ventral midline induction results in proper division of cephalic hemispheres. In contrast, neuroepithelium deficient for LRP2 has impaired SHH signaling in the ventral midline resulting in holoprosencephaly (HPE). Figure was modified from (Christ et al., 2012). d – dorsal, v – ventral, l – lateral, m – medial.

During forebrain development, lack of LRP2 leads to a failure in the SHH signaling in the rostral diencephalon ventral midline (RDVM) during a critical time in forebrain specification. LRP2 acts as an important component of the SHH signaling machinery,

controling internalization of SHH/Patched 1 complexes *FIGURE 6* (Christ et al., 2012). This results in the activation of Smoothened and expression of target genes, and this activity is mediated through GLI transcription factors. The response to the morphogen is tissue specific, and, as a result of ventral midline induction, the proper division of cephalic hemispheres occurs. To strengthen the response and increase local morphogen concentrations, LRP2 and SHH enter the cellular recycling pathway. In *Lrp2* mutant mice, the ventral midline fails to receive inducing SHH signals, because cellular trafficking does not occur during the critical time window. As a consequence, ventral forebrain specification is defective and the HPE phenotype appears (Christ et al., 2012).

4.1.1   LRP2 acts as clearance receptor in context dependent manner

In contrast to increase the morphogen concentrations, LRP2 was also documented as a receptor responsible for endocytic clearance. Unlike in ventral midline induction, during eye development, LRP2 antagonizes SHH activity in the ciliary marginal zone (CMZ) of the prospective retina (Christ et al., 2015). This prevents the progenitor cells in the CMZ from proliferation and specification. Disrupted quiescent stage of cells in the LRP2-deficient mice leads to hyperproliferation of the embryonic CMZ and is associated with the large eye phenotype, buphthalmia, also affecting DBS patients (Christ et al., 2015).

4.2   Divergence between LRP2- and SHH- deficient phenotypes in mouse models

Comparison of *Lrp2* mutant mice to *Shh* mutant mice revealed intriguing discrepancies between the phenotypes. Apart from the altered ventral midline as the hallmark for HPE, a dilation of the neural tube in the dorsolateral region also was observed *FIGURE 7, B*. Moreover, approximately 30% of LRP2-deficient individuals exhibited additional cranial neural tube defects (NTDs), which potentially resulted in anencephaly *FIGURE 7, C* (Kowalczyk et al., 2020; Kur et al., 2014). These observations could not exclusively be explained by impaired SHH signaling *FIGURE 7, A*.

4.2.1 LRP2 receptor facilitates folate internalization

Neural tube disorders are correlated with folate metabolism in human and mouse (see section 2.2.1) (Rosenquist and Finnell, 2001; Wallingford et al., 2013). The folate receptor has been shown to be a functional binding partner of LRP2 in the neural tube, and it facilitates cellular uptake of folate during neurulation (Kur et al., 2014).

Interestingly, a recent mouse study on prevention of LRP2-related NTDs documented that a periconceptional intraperitoneal injection of folic acid, not a dietary supplementation, can reduce the incidence of NTDs (Sabatino et al., 2017). This highlighted the potential of LRP2 model to improve the understanding of NTDs susceptible to folate supplementation (Blom et al., 2006).
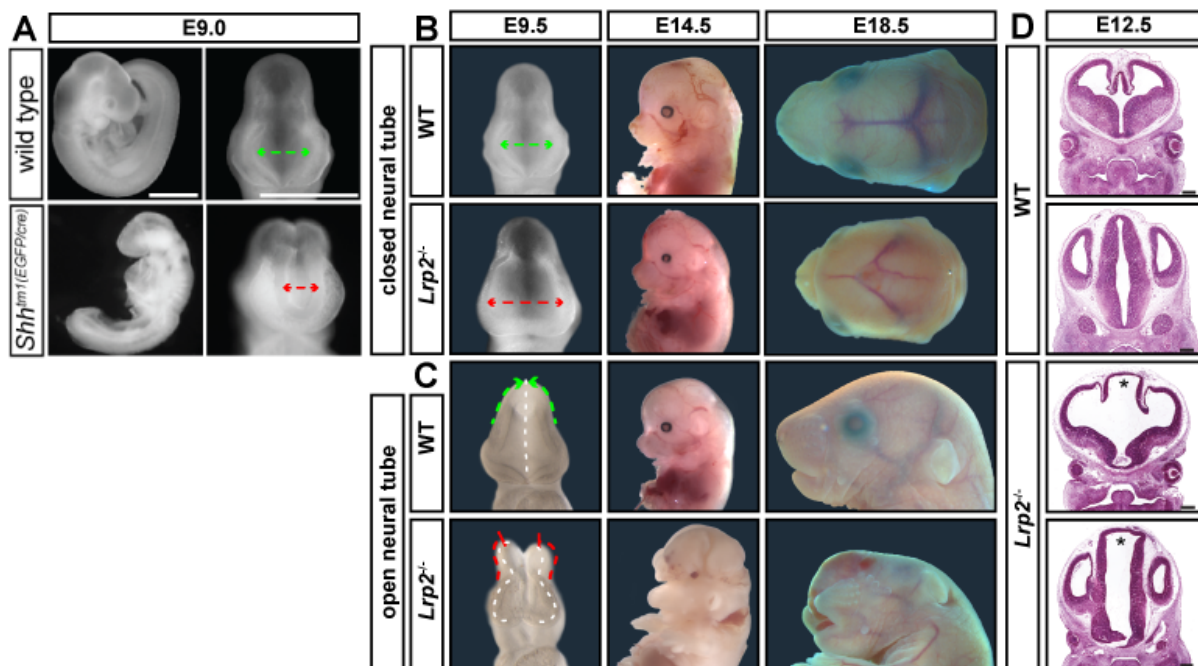
FIGURE 7 LRP2 PHENOTYPE IS DISTINCT FROM THE SHH-RELATED HPE PHENOTYPE.
(**A**) E9.0 embryos in lateral and frontal view. SHH-deficient embryos exhibit narrower telencephalic vesicle (red rashed line) compared to wild types (WT, green dashed-line). Forebrain phenotypes of *Lrp2^-/-* mice are distinct from SHH phenotype. E9.5 *Lrp2^-/-* embryos present a dilated neural tube (red dashed-line) (**B**) and, in about 35% cases (12 / 34), the NT fails to close (**C**). (**B**) The consequence of closed, but dilated, NT can potentially culminate in the mild NTD with enlarged fontanelle as presented for E14.5 and E18.5 embryos. (**C**) Open NTD results in the exencephaly (E14.5) and further anencephaly (E18.5). (**D**) H&E on coronal sections, through the closed NTs show the prominent dilation (asterisk) of the dorsal NT compared to WT. Figure (**A**) modified from (Kur et al., 2014), (**B-C**) modified from (Kowalczyk et al., 2021).

4.3 Rescue of the craniofacial and ventral midline phenotype in FVB/N mice

Despite many risk factors described, the variability in human manifestations of HPE (Dubourg et al., 2018) and DBS (Khalifa et al., 2015) remains incompletely understood. A growing number of mouse models, harbouring disease-relevant mutations found in humans, display phenotypic variability similar to human disease and confirm the multifactorial character of the diseases (Hong and Krauss, 2018). Interestingly, the genetic background of the mouse model strongly influences the penetrance of forebrain and craniofacial defects in *Lrp2* mutants. The craniofacial and brain malformations present in C57BL/6N LRP2-deficient mice are mostly rescued on congenic FVB/N strain background FIGURE 8, suggesting there is strong genetic modulation of the SHH pathway, which compensates for the loss of LRP2 activity (Mecklenburg et al., 2020).
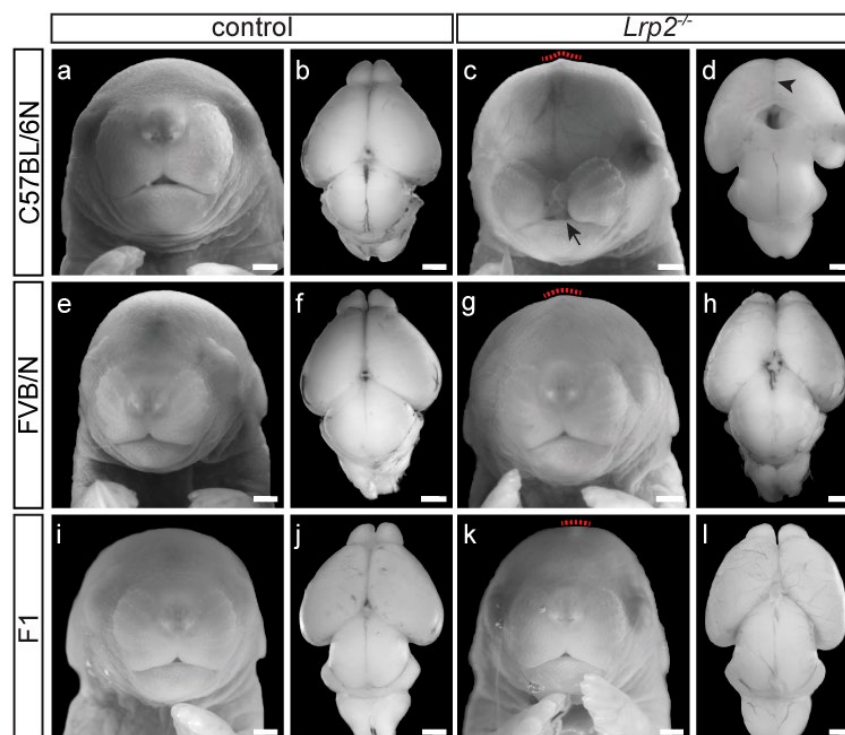
FIGURE 8 HPE AND CRANIOFACIAL PHENOTYPE OF *LRP2^-/-* C57BL/6N EMBRYOS IS RESCUED ON FVB/N BACKGROUND.
E18.5 embryonic heads, frontal view from *Lrp2^+/+* controls (a, e, i) and *Lrp2^-/-* mutants (c, g, k), as well as dorsal views on E18.5 brains, respectively. LRP2-deficient C57BL/6N embryos (**c**) present severe craniofacial defects: shortened snout, eye defects, and midfacial clefting (arrow). Brains present severe HPE phenotype (arrowhead) with absent olfactory bulbs (**d**). In contrast, congenic *Lrp2^-/-* FVB/N mice (**g**) as well as F1 mice (**k**) never display any form of HPE nor craniofacial malformations, and show normally developed forebrain hemispheres (**h, l**). The only common defect present in all *Lrp2^-/-* mice is a dorsal phenotype (red dashed-line) with enlarged fontanelle. Figure was modified from (Kowalczyk et al., 2021). Scale bars: 1 mm.

LRP2 function in ventral midline induction indicates the receptor is necessary to establish sufficient morphogen SHH level in the RDVM neuroepithelium during a critical (6 – 10 somites) time window. Failure of LRP2 action leads to the irreversible defects of RDVM specification culminating in HPE (Christ et al., 2012). Strikingly, analyses of the *Lrp2^-/-* mutant embryos on FVB/N background revealed a rescue of the forebrain and craniofacial defects F*IGURE 8* (Mecklenburg et al., 2020). Moreover, the rescue was also observed in the F1 generation from crossed C57BL/6N and FVB/N *Lrp2^+/-* mice. Detailed examination of the analogical stages of the embryos revealed that the morphogen SHH is present in sufficient levels in the ventral midline of FVB/N and F1 embryos, despite the lack of LRP2. Normal forebrain development in FVB/N mutants raised clear evidence that *Lrp2^-/-* FVB/N mice are resilient to SHH disturbances in the ventral midline. This result heavily implies an alternative mechanism, which can compensate for the loss of LRP2.

4.3.1 Defects in dorsal neural tube patterning are conserved in both mouse lines

Although the ventral specification of the neural tube is rescued in *Lrp2^-/-* FVB/N and F1 mice, they show dilated dorsal forebrain and enlarged fontanelle, reminiscent of NTD in *Lrp2^-/-* C57BL/6N mutants F*IGURE 8* (compare with F*IGURE 7*) (Mecklenburg et al., 2020). LRP2-related NTDs have been attributed to impaired folate uptake (see section 4.2.1) (Kur et al., 2014; Sabatino et al., 2017). Although the findings shed light on the mechanism by which LRP2 facilitates folate internalization (Kur et al., 2014), they neither address how folate internalization by LRP2 translates to the changes observed at the tissue level, nor do these results elucidate a mechanism of neural tube folding. The conserved dorsal phenotype between the mouse strains hinted towards a conserved, yet unknown function of LRP2 receptor in neural tube closure, which is independent of SHH signaling and etiology of holoprosencephaly (see section 4.2).

5 RNA sequencing as a tool to understand the HPE penetrance in mice

RNA sequencing is a powerful tool for analysing transcriptional changes, which underlie the revealed phenotypes in genetically manipulated animal models. *Mecklenburg et al.* performed RNA deep sequencing on the *Lrp2*$^{-/-}$ mutant and wild-type E9.5 embryonic heads on C57BL/6N and FVB/N background. The study included embryo samples from the F1 generation from crossed C57BL/6N and FVB/N *Lrp2*$^{+/-}$ mice to test whether FVB/N background provides a dominant rescue effect on the LRP2 loss of function phenotype (Mecklenburg et al., 2020). The results are discussed in further detail below.

5.1 The genotype dependent transcriptome comparison

Comparison of the RNAseq datasets from *Lrp2*$^{-/-}$ mutant samples against the *Lrp2*$^{+/+}$ wild-type samples, indicated various molecular pathways affected by *Lrp2* mutation. Differences in the transcriptome were the most prominent for the C57BL/6N background, in which the most severe HPE phenotype occurs F$_{IGURE}$ 9 (see also F$_{IGURE}$ 8) (Mecklenburg et al., 2020).
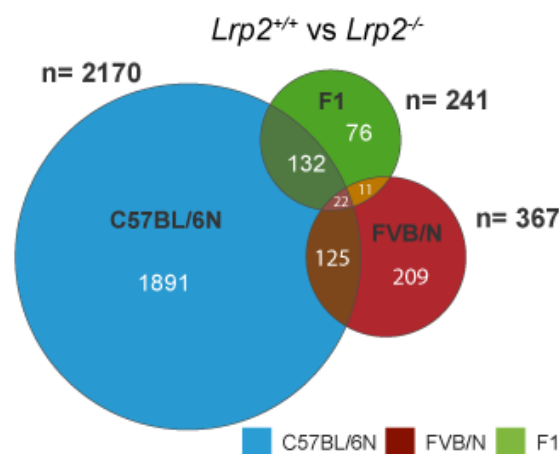
F$_{IGURE}$ 9 G$_{ENOTYPE}$ $_{DEPENDENT}$ $_{TRANSCRIPTOME}$ $_{COMPARISON}$ $_{FOR}$ C57BL/6N, FVB/N,F1 Venn diagram comparing *Lrp2*$^{+/+}$ and *Lrp2*$^{-/-}$ samples on a C57BL/6N, FVB/N and F1 background. The presentation of distinct and overlapping numbers of DEGs from the three strain specific comparisons. Figure was adapted from (Mecklenburg et al., 2020).

Among the most altered sets of genes were components of WNT signaling, primary cilia-related genes, and, interestingly, polarity and neural crest-related genes. These

novel results revealed differentially regulated pathways that have not been in the focus of the LRP2 studies before. However, they are closely correlated with the dorsal phenotype and dilation of the neural tube, as well as craniofacial phenotypes observed in *Lrp2* mutants. Both polarity and WNT signaling play a crucial role in the regulation of neural tube morphogenesis (see section 1.2) (Wallingford et al., 2002; Wang et al., 2019a). Moreover, development of craniofacial structures is tightly related by neural crest cells (Santagati and Rijli, 2003). NCC, on the other hand, have been implicated in the proper neural tube closure as well (Creuzet, 2009).

5.2 Strain specific transcriptome analysis unravels differentially expressed genes (DEGs) that may influence the penetrance of HPE phenotype

Previously unpublished results from the lab unravelled that SHH signaling and congenital brain and heart defects (not shown), with the exception of a dorsal neural tube phenotype, are fully rescued on the FVB/N background (see section 4.3, *Figure 8*). The F1 generation resembled the FVB/N rescue phenotype, thus implicating a strong genetic modulation with a dominant effect from the FVB/N genome. Strain specific transcriptome analysis provided a dataset of differentially expressed genes (DEGs) between the C57BL/6N and FVB/N, as well as, C57BL/6N and F1 for *Lrp2*$^{-/-}$ and *Lrp2*$^{+/+}$ samples *Figure 10*. These datasets shaped the direction of my Ph.D. research project.
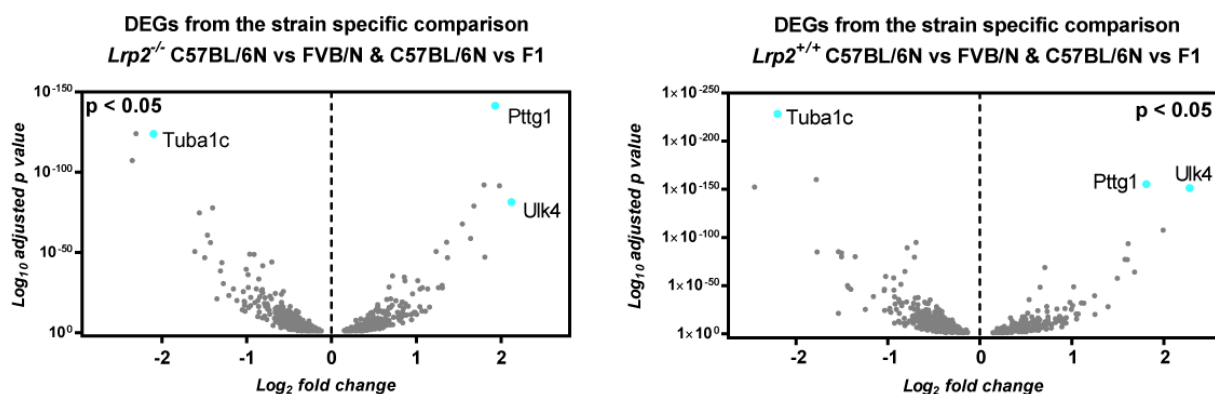
FIGURE 10 STRAIN SPECIFIC TRANSCRIPTOME ANALYSIS REVEALS COMMON DEGS FOR *LRP2*$^{-/-}$ AND *LRP2*$^{+/+}$ COMPARISONS.
Volcano plots present DEGs for *Lrp2*$^{-/-}$ and *Lrp2*$^{+/+}$ samples that were identified in both: C57BL/6N versus FVB/N and C57BL/6N versus F1 comparisons. Figure was adapted from (Mecklenburg et al., 2020).

SHH signaling presents the major cause of holoprosencephaly (Christ et al., 2012; Roessler et al., 1996) and is fully rescued on LRP2-deficient FVB/N background F*IGURE 8*. Following this line of thought, the initial focus from the Hammes lab was set on DEGs associated with SHH and primary cilia F*IGURE 11*. Dominant effects of the FVB/N background indicated a potential positive regulatory function of up-regulated genes in the FVB/N and F1 embryonic heads compared to C57BL/6N. Moreover, DEGs shared in both wild type and mutant comparisons, could potentially serve as strain dependent SHH modifying genes.

Amongst the filtered genes, *RPGR-Interacting Protein 1-Like Protein (Rpgrip1l or Ftm), Talpid3 (KIAA0586), and B9 domain-containing protein 1 (B9d1)* share many common features. TALPID3 is localized at the basal body (BB) (Yin et al., 2009), and B9D1/MKSR-1 and RPGRIP1L/MKS5 are present at both the BB and transition zone (TZ) of primary cilia (Garcia-Gonzalo et al., 2011; Vierkotten et al., 2007). They are necessary for ciliogenesis and facilitate efficient SHH signaling. Moreover, mutations in *RPGRIP1L, B9D1*, and *TALPID3* genes have been linked to human autosomal recessive multisystem ciliopathies with brain defects, including Meckel-Gruber (MKS) and Joubert syndrome (JBTS) (Bashford and Subramanian, 2019; Garcia-Gonzalo et al., 2011; Hopp et al., 2011). *Talpid3$^{-/-}$, Rpgrip1l$^{-/-}$ and B9d1$^{-/-}$* mutant mice share similar ciliopathy-related phenotypes resembling human JBTS/MKS syndromes and die perinataly (Andreu-Cervera et al., 2019; Bashford and Subramanian, 2019; Dowdle et al., 2011). They present neural tube patterning defects, like HPE, exencephaly, cleft lip/palate, and polydactyly, as well as renal and hepatic defects. Significant up-regulation of these genes in the transcriptome of FVB/N mice, supported by the evidence about their function in ciliogenesis and SHH signaling, suggest that regulation of the ciliogenesis can be an important aspect of HPE phenotype variability.
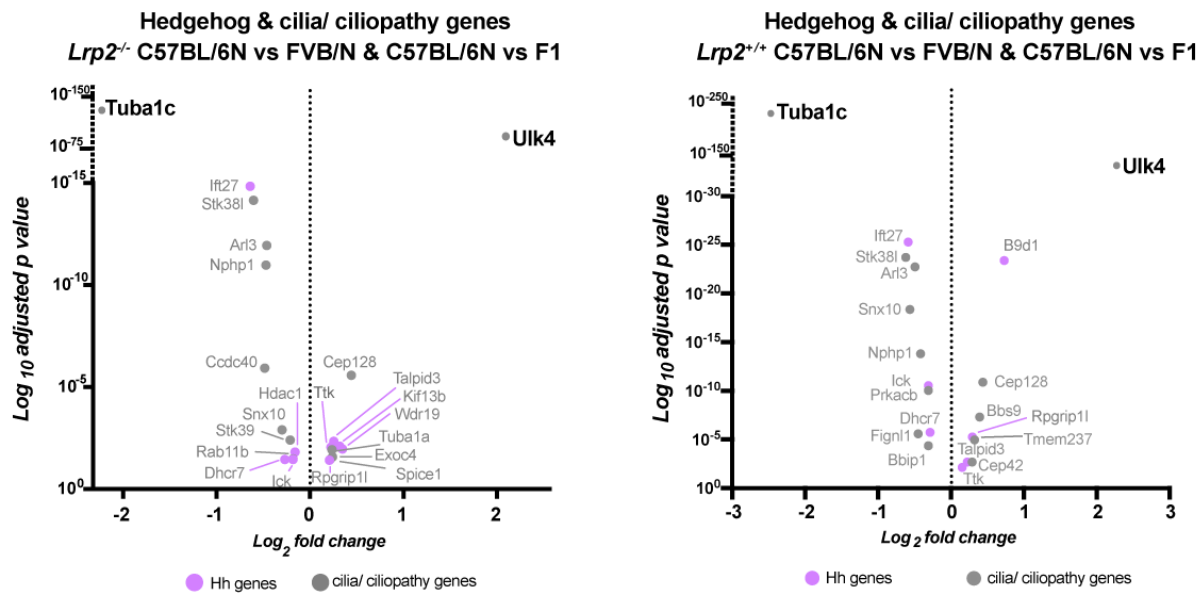
FIGURE 11 PRIMARY CILIA- AND SHH- ASSOCIATED DEGs CAN INFLUENCE HPE PHENOTYPE DEGs for *Lrp2⁻/⁻* and *Lrp2⁺/⁺* samples filtered for cilia, ciliopathy, and hedgehog signaling related genes according to (Breslow et al., 2018; Pusapati et al., 2018). Note: cilia/ciliopathy genes that are also HH-related genes are labeled in purple. Figure was adapted from (Mecklenburg et al., 2020).

5.2.1 Comparative transcriptomics – a source of novel SHH modifying genes?

Strikingly, the highest and most significantly regulated genes from unbiased RNAseq analysis are common in *Lrp2⁻/⁻* and *Lrp2⁺/⁺* datasets. Furthermore, they present novel target genes in the SHH field, implying the presence of uncharacterized regulatory factors in SHH signaling, that may be relevant for the strain dependent HPE phenotype *FIGURE 10*.

Unc-51-like kinase 4 (Ulk4), appeared as cilia-related gene *FIGURE 11*, highly up-regulated in FVB/N *Lrp2⁻/⁻* and *Lrp2⁺/⁺* embryonic heads compared to C57BL6/N. *Ulk4* is a serine/threonine kinase reported in the regulation of ciliogenesis of ependymal cells (Liu et al., 2016a). Inactivating and hypomorphic mutations of *Ulk4* in mice lead to deficits in cilia, hydrocephaly, dilated brain ventricles, and premature death (Liu et al., 2016a; Vogel et al., 2012). Additionally, the *ULK4* gene in humans has been associated with schizophrenia and other major psychiatric disorders (Lang et al., 2014, 2016).

Pituitary tumor transforming gene (Pttg1, also called *securin),* similar to *Ulk4,* was highly expressed in FVB/N *Lrp2$^{-/-}$* and *Lrp2$^{+/+}$* embryonic heads compared to C57BL6/N samples. However, unlike *Ulk4*, it previously had not been associated with cilia. *Pttg1* is known as an oncogene and has been mostly studied in context of various cancers (Genkai et al., 2006; Xiang et al., 2017). It exhibits transcriptional activity by directly binding DNA or through other binding factors and has been linked to DNA repair and apoptosis (Bernal et al., 2002; Tong and Eigler, 2009). Moreover, during mitosis, *Pttg1* controls sister chromatid separation by interaction with separase (Repo et al., 2017; Vlotides et al., 2007).

In contrast, *tubulin, alpha 1C (Tuba 1c)* was expressed significantly lower in both FVB/N *Lrp2$^{-/-}$* and *Lrp2$^{+/+}$* embryonic heads compared to C57BL/6N. *Tuba1c,* a component of tubulin, can be found in the ciliary genes database (van Dam et al., 2013; Pusapati et al., 2018), and is linked to the HH „OFF" state (Fabregat et al., 2018; Rothfels, 2014). However, its function within the cilia and SHH pathway has yet to be understood.

Applying complex comparative transcriptomics on *Lrp2$^{-/-}$* and *Lrp2$^{+/+}$* genotypes from all backgrounds, we investigated the LRP2-independent SHH signaling pathway modulation, contributing to the variability of HPE penetrance between the mouse strains.

Differential expression of signaling cascade components, as well as their different cellular organization could induce molecular changes during forebrain development. Thus, a deeper understanding of the existing correlations between signaling and cellular processes can lead to the more accurate interpretations of the phenotypic variabilities in animal models and, importantly, shed light on human disease.

II. AIMS OF MY STUDY

LRP2-deficient C57BL/6N mice suffer from holoprosencephaly caused by impaired SHH activity. These defects affecting the ventral neural tube are fully rescued on FVB/N background, indicating a strong influence of modifier genes. Applying comparative transcriptomics, the lab had identified strain-specific differentially regulated genes (DEGs), either highly down- or up-regulated in the rescue strain independent of the genotype. The aim of my work was to functionally analyse top regulated DEGs as potential candidate modifiers of the SHH pathway and therefore, modulators of the holoprosencephaly penetrance in LRP2-deficient mice. Towards this aim I applied *in vitro* assays in cell culture testing the potential impact of the candidate genes on the SHH induced signaling pathway, as well as further characterization of the candidate modifier genes in the mouse embryonic neural tube.

Based on the extensive phenotypic characterization of *Lrp2*−/− mouse embryos on C57BL/6N and FVB/N background, it became apparent that, besides the rescued ventral forebrain phenotype, a defect in dorsolateral neural tube patterning was conserved between strains, and independent of the SHH pathway. This result was strongly supported by our comparative transcriptome dataset indicating differences in the expression of genes relevant for dorsolateral patterning in mutants compared to controls from both strains. Therefore, my next aim was to elucidate a novel, SHH-independent function of LRP2 in dorsolateral neural tube specification and patterning. Additionally, loss of LRP2 lead to neural tube pattering defects in *Xenopus*, indicating a conserved role of the receptor in dorsal neural tube morphogenesis. In a collaborative project with Dr. Kerstin Feistel's lab using *Xenopus*, my work in the mouse model aimed at elucidating the mechanisms underlying the conserved function of LRP2 in the complex remodelling of the pseudostratified neuroepithelial cell layer during neural tube closure.

Dynamic neurulation processes are accompanied by specification and delamination of neural crest cells (NCCs), which later also contribute to craniofacial structures. Severe craniofacial malformations in LRP2-deficient mice, reminiscent of NC defects, were yet again supported in our transcriptome data set with NC specific genes highly

deregulated in *Lrp2* mutants. The function of the receptor in the population of cranial neural crest stem cells has hitherto not been investigated. Thus, the third objective of my thesis was to evaluate the presence of LRP2 in neural crest cells and the potential impact of the receptor on this important stem cell population.

The relevance of the study focused on LRP2 receptor refers to the patients with Donnai-Barrow syndrome, caused by autosomal recessive mutations in *LRP2* gene (Kantarci et al., 2007) and with neural tube closure defects (Prasoona K. et al., 2018; Renard et al., 2019). The understanding of mechanisms underlying early brain development can contribute to the understanding of etiology of congenital brain disorders, to better genetic counselling and to their successful prevention in the future.

III. HYPOTHESIS OF THE PROJECT

LRP2 coordinates pivotal developmental processes by integrating signaling pathways and morphogenetic events in tightly controlled spatiotemporal manner during neural tube formation.

IV. MATERIAL AND METHODS

1 Materials

1.1 Chemicals

TABLE 1 LIST OF CHEMICALS AND SUBSTANCES

Reagent	Supplier	Catalog number
Anti-digoxigenin(DIG)-AP	Roche	11093274910
Aqua Poly/Mount	Polysciences	18606-20
Blocking reagent	Roche	11096176001
BM Purple	Roche	11442074001
bromophenol blue	Merck	11746.0005
Bovine serum albumin (BSA)	Sigma-Aldrich	A9647
Cresol Red sodium salt	Sigma Aldrich	114480
Dako fluorescence mounting medium	Agilent	S302380-2
DIG RNA labeling kit	Roche	11277073910
DNAse I	Invitrogen	AM2222
dNTP ROTI®Mix PCR 3	Carl Roth	0179.2
Donkey serum	Biowest	S2170-500
Ethylenediaminetetraacetic acid (EDTA)	Carl Roth	8043.2
Formamide, deionized	Roth	P040.1
Gel 12% Tris-Glycine Gel	Invitrogen	XP0012C
GeneRuler™ DNA Ladder Mix	Thermo scientific	SM0331
Glycerol	Carl Roth	3783.1
Hydrogen Peroxide	Carl Roth	80702

β-mercaptoethanol	Carl Roth	4227.3
Methanol	Carl Roth	KK44.1
Nitrocellulose membrane 0.2 µm	Amersham Protran	10600006
O.C.T.™ Compound Tissue-Tek®	Sakura Finetek	sa-4583
PageRuler Plus Prestained Protein Ladder	LIFE Technologies	26619
Paraformaldehyde (PFA)	Sigma Aldrich	16005
ProLong Gold Antifade Mountant	Invitrogen	P36982
Proteinase K	Sigma	03115828001
RNAse Inhibitor	Roche	03335399001
Rneasy Mini Kit	Qiagen	74104
Roti®GelStain	Carl Roth	3865.1
Sodium dodecyl sulfate (SDS)	Serva	20765.03
Sheep Serum	Sigma Aldrich	S2263
Slow Fade Diamond Antifade Mountant	Invitrogen	S36963
SuperSignal West Dura	Life Technologies	34075
Taq Polymerase	NewEngland Biolabs	M0267L
ThermoPol® Buffer	NewEngland Biolabs	B9004S
Transcription kit SP6/T7	Roche	10999644001
Tris-HCl	Carl Roth	9090.5
Triton X-100	Carl Roth	3051.2
Tween-20	Carl Roth	9127.2
Other		
Coverslips 1.5 H	Carl Roth	LH25.1
HybriSlip™ Hybridization cover	Sigma	HS6024

Millicell Hanging Cell Culture Insert	Merck Millipore	MCEP06H48
Mini Gel Tank	Invitrogen	A25977
Secure-Seal Spacer	Invitrogen	S24737
sub-resolution TetraSpeck™ Microspheres	Invitrogen	T7280

TABLE 2 LIST OF THE CHEMICALS AND SOLUTIONS USED IN CELL CULTURE

Reagent	Supplier	Catalog number
Adenosine 5'-triphosphate, disodium salt (ATP)	ATP	A26209-1G
Aminophenyl methylbenzothiazole (APMBT)	Fluorochem	MFCD00005780
Cyclohexylenedinitrilo tetraacetic Acid (CDTA)	Carl Roth	1412.1
Coelenterazine	ZellBio	CZ2.5
Coenzyme A	Biomol	c7505-51.25
D-Luciferin, Potassium Salt	ZellBio	LUCK-100
DMEM, high glucose, GlutaMAX™ Supplement	Thermo Fisher	31966047
Dimethyl sulfoxide (DMSO)	Roth	47204
DPBS, no calcium, no magnesium	Thermo Fisher	14190250
1,4-Dithiothreitol (DTT)	Carl Roth	6908.1
Fetal Bovine Serum (FBS)	PAN-Biotech GmbH	P40-37500
Hepes	Carl Roth	9105.2
KAAD-cyclopamine	Calbiochem	239804
Lipofectamine3000	Invitrogen	L3000015
Magnesiumsulfat Heptahydrat (MgSO4 · 7 H2O)	Carl Roth	P027.1
Opti-MEM™ Medium	Thermo Fisher	31985062
Passive Lysis 5X Buffer	Promega	E1941

Penicillin-Streptomycin	Invitrogen	15140122
Sodium acetate (NaCH$_3$COO · 3 H2O)	Carl Roth	6779.2
Sodium pyrophosphate decahydrate (Na$_4$P$_2$O$_7$ · 10H$_2$O)	Fisher Scientific	221368-100G
Sodium sulfat (Na$_2$SO$_4$)	Carl Roth	8560.3
Other		
Nunc-Immuno(TM) MicroWell(TM) 96 well plates	Sigma	P8616-50EA
Nunc Lab-Tek II Chamber slides	Sigma	C6807

TABLE 3 LIST OF THE PRIMARY ANTIBODIES AND DILUTIONS

Antigen	Host	Supplier	Catalog number	Dilution IHC
acetylated α-Tubulin	mouse	Sigma Aldrich	T7451	1:1000
α-Tubulin	mouse	Merck Millipore	CP06	WB 1:2000
γ-Tubulin	mouse	Sigma Aldrich	T6557	1:200
ARL13b	rabbit	ProteinTech	17711-1-AP	1:1500
ARL13b	mouse	UC Davis/NIH NeuroMab	75-287	1:500
GIPC1	rabbit	Alomone	APZ-045	1:200
LRP2	sheep	Laboratory of Renata Kozyraki	N/A	1:5000
LRP2	rabbit	Abcam	ab76969	1:1000
NHERF1	rabbit	Alomone	APZ-006	1:500

Phalloidin A647	N/A	Invitrogen	A22287	1:20
p-S6RP	rabbit	Cell Signaling	2211s	1:200
PTTG1	rabbit	Abcam	ab79546	1:100 WB 1:5000
PTTG1	goat	LifeSpan Biosciences	LS-B5119-50	1:100
RAB11	mouse	BD Transduction Laboratories	610657	1:200
VANGL2	rabbit	Kindly provided by Mireille Montcouquiol	N/A	1:500
ZO-1	mouse	Invitrogen	33-9100	1:100

TABLE 4 LIST OF THE SECONDARY ANTIBODIES AND DILUTIONS

Antigen	Supplier	Catalog number	Dilution
DAPI	Invitrogen	62248	1:1000
Donkey anti-goat Alexa Fluor 647	Abcam	ab150131	1:500
Donkey anti-mouse Alexa Fluor 488	Abcam	ab150109	1:500
Donkey anti-mouse Alexa Fluor 555	Abcam	ab150106	1:500
Donkey anti-mouse Alexa Fluor 647	Abcam	ab150107	1:500
Donkey anti-mouse Alexa Fluor Plus 594	Invitrogen	A32744	1:200
Donkey anti-rabbit Alexa Fluor 488	Abcam	ab150073	1:500
Donkey anti-rabbit Alexa Fluor 555	Abcam	ab150074	1:500
Donkey anti-sheep Alexa Fluor 488	Abcam	ab150177	1:500
Goat anti-mouse IgG Fc (HRP)	Abcam	ab97265	1:20 000

Goat anti-rabbit IgG H&L (HRP)	Abcam	ab6721	1:20 000
Goat anti-rabbit - Gold 12nm	Dianova	111-205-144	1:20
Goat anti-rabbit ATTO647N	Active Motif	15038	1:200

TABLE 5 LIST OF THE PLASMIDS

Recombinant DNA	Supplier	Catalog number
B9d1 RIKEN cDNA clone	Source Bioscience	2810407E13
Firefly luciferase reporter (8 x 3'Gli-BSδ51LucII)	(Sasaki et al., 1997)	N/A
pBluescript SK+ control vector	Kindly provided by Niccolo Zampieri, MDC	N/A
pCMV6-Entry Tagged Cloning Vector	Origene	PS100001
Pttg1 cDNA	Origene	MR202008
Renilla luciferase reporter (pRL-TK)	Promega	E2241
Rpgrip1l RIKEN cDNA clone	Source Bioscience	1700047E16
Talpid RIKEN cDNA clone	Source Bioscience	2700049A03
Tuba1c RIKEN cDNA clone	Source Bioscience	2810407E13
Ulk4 cDNA	Origene	MR217918
In situ probe		
Sox10 riboprobe (plasmid pZL1/SX10 9.1.1.)	Kindly provided by Carmen Birchmeier, MDC	full length *Sox10*, (1-3022 bp), ORF 583-1981

1.2 Buffers and solutions

TABLE 6 COMPOSITION OF BUFFERS

Name	Technique	Composition
Basic reagent	DNA extraction	25 mM NaOH 0.2 mM EDTA Deionized dH_2O; pH 12

Neutralization buffer	DNA extraction	40 mM Tris-HCl Tween-20 dH_2O; pH 5
TAE 50x	agarose electrophoresis	2 M Tris 950 mM Acetic acid 50 mM EDTA pH 8 dH_2O; pH 8.3
PBS 10x	Immunohistochemistry	1.4 M NaCl 27 mM KCl 90 mM NaH_2PO_4 18 mM KH_2PO_4 dH_2O; pH 7.4
Firefly luciferase buffer (2xFLB) stock	Luciferase Assay	150 mM Hepes 8 mM $MgSO_4*7(H_2O)$ 40 mM DTT 0.2 mM EDTA 1.06 mM ATP dH_2O; pH 8, stored @-20°C
Firefly luciferase buffer (1xFLB with substrate)	Luciferase Assay	10 ml 1x FLB 270 µM CoA 200 µM Luciferin
Renilla luciferase buffer (2xRLB) stock	Luciferase Assay	30 mM $Na_4P_2O_7*10(H_2O)$ 15 mM NaAc 20 mM CDTA 800 mM Na_2SO_4 dH_2O; pH 5, stored @-20°C
Renilla luciferase buffer (1xRLB with substrate)	Luciferase Assay	10 ml 1x RLB 50 µM APMBT 2.2 µM Coelenterazine
Hybridization solution	*In situ* hybridization	50% Formamide 10% Dextran sulfate 1% Denhardt's solution 250 µg/ml tRNA 0.3 M NaCl 20 mM Tris-HCl pH 8 5 mM EDTA 10 mM Na_3PO_4 pH 8 1% Sarcosyl autoclaved dH_2O; @-20°C
MAB 5x	*In situ* hybridization	500 mM Malec acid 750 mM NaCl 950 mM NaOH dH_2O; pH 7.5
MABT	*In situ* hybridization	1x MAB-5x 0.1% Tween-20
MABT blocking	*In situ* hybridization	1x MAB-5x 2% blocking reagent 20% sheep serum 0.1% Tween-20
NTMT	*In situ* hybridization (ISH & WISH)	100 mM NaCl 100 mM Tris-HCl pH 9.5 50 mM $MgCl_2$ 0.1% Tween-20

SSC (20x)	*In situ* hybridization (ISH & WISH)	3M NaCl 0.3M Na$_3$Citrat autoclaved dH$_2$O; pH 4.5
Solution I	*In situ* hybridization (ISH & WISH)	50 % Formamide 4x SSC 1% SDS
Solution II	*In situ* hybridization (ISH & WISH)	50 % Formamide 2x SSC
Pre-hybridization solution	Whole mount *in situ* hybridization	50% Formamide 5x SSC pH 4.5 50 µg/ml Heparin 1 mg/ml tRNA100 50 µg/ml ssDNA 0.1%Tween-20
Hybridization solution	Whole mount *in situ* hybridization	50% Formamide 5x SSC pH 4.5 50 µg/ml Heparin 50 µg/ml ssDNA 0.1%Tween-20
SDS lysis buffer	SDS-PAGE/ western blotting	60 mM Tris-HCl pH 6.8 2% SDS 10% glycerol 0.01% bromophenol blue 1.25% β-mercaptoethanol
Running buffer 10x	SDS-PAGE/ western blotting	250 mM Tris 2.5 M Glycine 1% SDS
Transfer buffer 10x	SDS-PAGE/ western blotting	250 mM Tris 2.5 M Glycine

1.3 Technical equipment

TABLE 7 LIST OF THE TECHNICAL EQUIPMENT WITH SOFTWARE

Technical equipment	Software	Supplier
Centro XS³ LB 960 Microplate Luminometer	MikroWin 2000 4.41 Mikrotek Laborsysteme GmbH	Berthold Technologies
Cryostat CM1950	N/A	Leica
Leica MZ 10F stereomicroscope	LAS V4.9 software	Leica
Leica DM 5000C microscope	LAS X software	Leica
Leica TCS SP8 confocal microscope	LAS X software	Leica

Leica SP8 TCS STED microscope	LAS X software	Leica
Nanodrop spectrometer 2000	N/A	Thermo Fisher
Otimax 2010 X-Ray Film Processor	N/A	Protect
SEM, scanning electron microscope Gemini DSM 982	N/A	Zeiss
TEM, Morgagni electron microscope (80 kV), equipped with Morada CCD camera	iTEM software, EMSIS GmbH https://www.itemsoft.com/	Thermo Fisher

TABLE 8 LIST OF THE SOFTWARE FOR DATA ANALYSIS

Software	Supplier	Reference
Adobe Illustrator 2019	Adobe	https://www.adobe.com/products/illustrator.html#
Adobe Photoshop CC 2019	Adobe	https://www.adobe.com/products/photoshop.html
GraphPad Prism 7	GraphPad Software, Inc	https://www.graphpad.com/scientific-software/prism/
Huygens Professional 19.10	Scientific Volume Imaging	https://svi.nl/HomePage
ImageJ	Open source	http://imagej.nih.gov/ij/
IMARIS 9.3 and 9.5	Bitplane	https://imaris.oxinst.com/packages

1.4 Animal model

Experiments involving animals were performed according to MDC guidelines following approval by local authorities (licences X9005/12, G 0322/19).

1.4.1 Mouse strains

The generation of *Lrp2*$^{+/-}$ mice with targeted disruption of one allele of gene has been described in (Willnow et al., 1996). The *Lrp2* mutant mouse line used in the study was

crossed onto a pure C57BL/6NCrl background as described in (Spoelgen et al., 2005), and is referred as *Lrp2*^+/- C57BL/6N. Additionally, the *Lrp2*^+/- C57BL/6N line was back-crossed for more than 12 generations to obtain a congenic mouse line on a FVB/NCrl background (Mecklenburg et al., 2020), herein referred to as *Lrp2*^+/- FVB/N.

1.4.2   Cell culture

The murine NIH-3T3 and human HEK293T cell lines were obtained from T. Willnow (MDC) (Christ et al., 2012). Human SHHN-293 cells were originally kindly provided by M. Kato (Stanford School of Medicine) (Christ et al., 2012).

2 Mouse husbandry

Adult mice were housed in a 12-hours light-dark cycle with ad libitum food and water. We used mice older than 8 weeks of age for timed matings in order to collect embryos of defined developmental stages for the experiments. Females were checked for vaginal plugs and the day a vaginal plug was observed was defined as E0.5. Pregnant mice were sacrificed by cervical dislocation according to the German animal protection act. Embryos were classified into developmental stages by their number of somites.

Analyses of the congenital defects were carried out on *Lrp2*^-/- and on somite matched *Lrp2*^+/+ and/or *Lrp2*^+/- control littermates on a C57BL/6NCrl and FVB/NCrl background. Embryos having only one of the targeted *Lrp2* alleles (*Lrp2*^+/-, heterozygous) were phenotypically identical to wild-type embryos (*Lrp2*^+/+). Therefore, both genotypes were used as control embryos. For the generation of the F1 hybrid *Lrp2* mutant embryos, *Lrp2*^+/- FVB/NCrl females were crossed with *Lrp2*^+/- C57BL/6NCrl males (Mecklenburg et al., 2020) or *Lrp2*^+/- FVB/NCrl males with *Lrp2*^+/- C57BL/6NCrl females.

2.1   Genotyping

The genotyping was performed on genomic DNA isolated from yolk sac of E8.5 and E9.5 mouse embryos or from tail biopsies from older embryos. Genotyping of adult animals was performed on ear punches collected by animal caretakers.

The genomic deoxyribonucleic acid (DNA) was isolated using adapted Hot Sodium Hydroxide and Tris (HotSHOT) method (Truett et al., 2000). The samples were heated to 95°C for 30 minutes in the basic reagent TABLE 6 (20 µl for E8.5 embryos, 30 µl for older stage). Following DNA isolation, the solution was neutralized with the equal

volume of neutralization buffer *TABLE 6*. The DNA solution was stored at 4°C or directly used for the polymerase chain reaction (PCR) to genotype the transgenic *Lrp2* mice.

Specific primers *TABLE 9* were used in order to amplify the target sequences. A combination of the three primers validated the presence of genetically modified alleles. The 250 bp size of DNA product indicated *Lrp2+/+* (primers G20/G21), and 320 bp DNA product indicated the mutant *Lrp2-/-* (primers BPA/G21). Two bands of 250 bp and 320 bp size together indicated the heterozygote *Lrp2+/-*.

TABLE 9 PCR PRIMERS USED FOR GENOTYPING OF TRANSGENIC MICE

Oligonucleotides	Supplier	Sequence (5'-3')
Lrp2 PCR primer, targeted allele forward - BPA	Eurofins	GAT TGG GAA GAC AAT AGC AGG CAT GC
Lrp2 PCR primer, wild type and targeted allele reverse – G21	Eurofins	CAT ATC TTG GAA ATA AAG CGA C
Lrp2 PCR primer, wild type allele forward – G20	Eurofins	GAC CAT TTG GCC AGC CAA GG

TABLE 10 PCR REACTION AND THE PROTOCOL

Lrp2 (gp330)	stock concentration	final concentration
Buffer ThermoPol	10 x	1 x
cresol red	10 x	1 x
G20 (WT)	10 µM	0.25 µM
BPA (KO)	10 µM	0.25 µM
G21 (WT/KO)	10 µM	0.3 µM
dNTPs	10 mM	0.25 mM
Taq Polymerase	5 U/µl	0.03 U/µl
H$_2$0		Σ 20 µl/sample + 2 µl DNA

PCR protocol	
94°C	2 min.
95°C	30 sec.
56°C	40 sec.
72°C	35 sec.
cycles	40

The master mix for the PCR reaction was prepared according to the optimized protocol for the Taq polymerase and the reaction conditions are described in the TABLE 10.

The amplified DNA fragments were subjected to gel electrophoresis in Tris base, acetic acid, and EDTA (TAE) buffer TABLE 6, using 2.5% agarose gel in order to separate individual bands. The DNA was visualized, thanks to Roti Safe used in gel preparation, under ultraviolet (UV) light using Bio-Rad gel imaging system.

3 Histology

3.1   Whole mount embryo preparation

E8.5 embryos were dissected in ice-cold Phosphate-buffered saline (PBS) and the rostral neural tube was collected. The tissue was fixed with 4% PFA in PBS overnight, at 4°C, or 1 hour in room temperature (RT). Following the fixation, the embryos were washed two times in PBS and stored either at 4°C, or dehydrated through a series of methanol solutions in PBS: 25%, 50%, 75%, 100%, with 10 min for each step. The dehydrated samples were stored in 100% methanol at -20° until use.
For further PTTG1, NHERF1, GIPC1, VANGL2, or phalloidin staining, the embryos were one-hour-fixed and stored in PBS at 4°C, without methanol dehydration.

3.2   Tissue cryosections

The standard dissection procedure was performed as described above (section 3.1). The embryos stored in 100% methanol were rehydrated by subsequent methanol solutions 100%, 75%, 50%, 25%, back to PBS, following the infiltration in 15% and 30% sucrose in PBS. Next, the tissue was embedded in O.C.T. (Tissue-Tek®, Sakura Finetek) in embedding molds (10 mm x 10 mm x 5 mm). For quick freezing the samples with well-oriented specimens were placed on dry-ice-cold 100% methanol bath. Samples were stored at -20°C in plastic bags to avoid drying, or proceeded with cryostat sectioning into 10 µm coronal sections. Sections were stored at -20°C.

3.3   Mouse cephalic explants

Mouse cephalic explants were prepared analogically as described in (Echevarria et al., 2002). E9.5 mouse embryos were collected, and the neural tube was cut open along the dorsal midline, from the caudal to rostral direction, using an insect needle FIGURE 12. The neural folds were precisely cut above the heart and placed on the sterile filter

(Millipore), on the petri dish in the drop of PBS. The floor plate at the level of the cephalic flexure was pinched (*FIGURE 12*, red dashed-line) in order to unfold the tissue with the ventricular part facing up. The filter was placed in the 6-well plate containing DMEM/10% FCS and explants were incubated at 37°C, with 5% CO_2 and 95% humidity for 3-4 hours to flatten and recover. The explants were washed gently in PBS, fixed 1 hour in 4% PFA, and subjected to the standard immunofluorescence protocol described in (section 3.4.2).
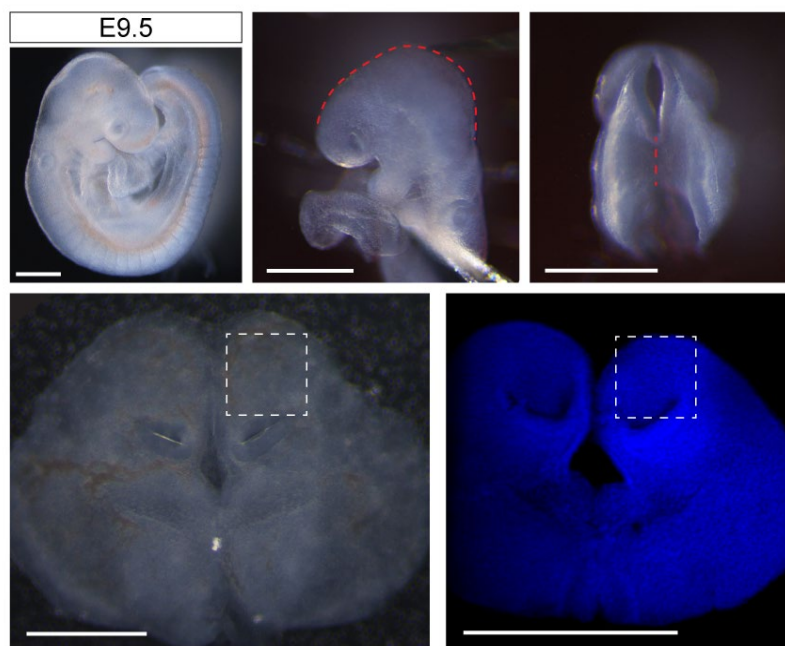
FIGURE 12 CEPHALIC EXPLANTS PREPARATION.
Cephalic explants, prepared from E9.5 embryos, served as a tool to examine the primary cilia of mouse neuroepithelium. The neural tube was cut and floor plate at the level of cephalic flexure was pinched (red dashed-lines) in order to unfold the tissue with the ventricular part facing up. Dashed-line squares indicate the forebrain region as the region of interest on the bright field and confocal image with dapi staining (blue). Scale bars: 500 µm.

3.4 Immunohistochemistry

3.4.1 Fluorescent immunohistochemistry on cryosections

Before standard immunohistochemical analysis, the cryosections (see section 3.2) were dried for 1 hour at RT and subsequently washed with PBST (0.1% Triton X-100 in PBS) 5 times for 7 minutes. Sections were blocked with blocking buffer (10% serum depending on the secondary antibody species in PBST) for 1 hour at RT. Next, tissue sections were incubated with primary antibodies diluted in the PBST with 1% serum, according to the *TABLE 3*, at 4°C overnight. The next day slides were washed with

PBST (5 x 7 minutes) and incubated with the secondary antibodies according to the *TABLE 4*, for 1 hour at RT. All samples were counterstained with DAPI. After washing the sections with PBST (5x 7 minutes), the slides were mounted with Dako Fluorescence Mounting Medium.

3.4.2 Fluorescent immunohistochemistry on whole mount embryos and explants

The whole mount embryos, or cephalic explants, were permeabilized with PBST (0.1% Triton X-100 in PBS) for 15 min and blocked with PBST containing 1% donkey serum and 2% BSA for 6 hours in RT. The procedure was performed using 2 ml Eppendorf tubes, by consequent changing of the solutions. Primary antibodies were incubated for 48 hours in 4°C, with the dilutions according to the *TABLE 3*. After two days, the samples were washed with PBST (5 x 1 hour) at RT. Incubation with secondary antisera conjugated with Alexa fluorophores *TABLE 4* was performed for 24 hours at 4°C in the dark. All the samples were counterstained with DAPI. The next day samples were washed with PBST (5 x 1 hour) at RT.

Explants were flat-mounted using Secure-Seal Spacer between two cover glasses. The whole mount neural tubes were mounted with the anterior side facing up, using Secure-Seal Spacer in order to keep the tissue in the original shape. The glycerol-based Slow Fade Diamond Antifade Mountant was used (RI 1.42) both in order to match the refractive index (RI) of the mountant and the immersion media of the glycerol objective (RI 1.45) and to prevent distortions of the specimens by pressure, shrinking, and hardening of the mountant.

3.5 Confocal microscopy and image processing

Confocal image acquisition and processing was carried out using Leica TCS SP8 confocal microscope equipped with a Leica LAS X software at the Advanced Light Microscopy (ALM) Platform at MDC, under supervision of Dr. Anje Sporbert and Matthias Richter.

3.5.1 Image acquisition – tissue sections

The tissue sections (see section 3.4.1) and cell samples (see section 6.4) were imaged using a HC PI Apo 20× NA 0.75 MultiIMM and HC PI Apo 63× NA 1.3 oil immersion objectives.

For all samples Alexa Fluor 488 was excited by a 488 nm laser (detection at 500 - 550 nm), Alexa Fluor 555 was excited by a 555 nm laser (detection at 570 - 620 nm), Alexa Fluor 647 was excited by a 633 nm or 647 nm laser (detection at 660 - 730 nm) with a pinhole set to 1 AU. DAPI was excited at 405 nm (detection at 420 - 450 nm).

3.5.2   Image acquisition – whole mount samples

The forebrain region of the explant (see section 3.4.2) samples was imaged en face FIGURE 12, using a HC Pl Apo 63× NA 1.3 glycerol immersion objective with a working distance (WD) of 0.3 mm to enable high-resolution imaging with minimal spherical aberrations of the thick specimen. High-resolution z-stack (60 nm pixel size, 12 bit, 0.2 µm z-step size) images of apical side of neuroepithelium were acquired with a z-piezo stepper.

The whole mount samples were imaged with a HC Pl Apo 20× NA 0.75 MultiIMM or HC Pl Apo 63× NA 1.3 glycerol immersion objectives. High-resolution z-stack (80 nm pixel size, 12 bit, 0.5 µm z-step size) images of anterior neural folds were acquired.

3.5.3   3D Data processing, deconvolution and correction

Confocal Z-stacks of explants and whole mount neural folds (see section 3.5.2) were subjected to a background correction and processed by deconvolution with the CMLE algorithm in order to obtain an improved signal to noise ratio and axial and spatial resolution, using Huygens Professional 19.10 software (Scientific Volume Imaging).

For optimal deconvolution of the explant samples, for further quantification of the primary cilia (see section 3.6.2), the experimental PSF was calculated with Huygens PSF Distiller by using sub-resolution TetraSpeck™ Microspheres, 0.2 µm embedded and acquired with analogical imaging conditions as the explant sample. The same deconvolved beads sample was used to estimate a chromatic aberration correction matrix (in x/y/z), which was used to correct the experimental sample data. To get isotropic voxel values, the aspect ratio of the deconvolved bead sample was changed. This new sampling value was applied to all image data with the IMARIS Software before doing further segmentation and analysis steps.

3.6   Immunofluorescence image analysis

All samples subjected to either qualitative or quantitative analysis were imaged under identical settings for laser power, detector, and pixel size.

3.6.1 PTTG1 immunofluorescence signal intensity - tissue sections

Z-stack images of the coronal sections (see section 3.4.1) were analyzed using ImageJ (Fiji, NIH). For the quantification of PTTG1 signals in the neuroepithelium, the full Z-stack was used. Region of interest (ROI) was manually outlined as shown in the FIGURE 20, and the mean fluorescent intensity was measured with the ROI manager. The average intensity for each animal was used in the final quantification, and an unpaired *t*-test statistical analysis was performed to assess the significance.

3.6.2 Immunofluorescence signal localization analysis - explants

Localization of the protein of interest (PTTG1) within the primary cilium of mouse neuroepithelium (see section 3.3 and 3.4.2) was assessed using IMARIS software (Imaris 9.3 and 9.5, Bitplane) after applying raw data corrections (see section 3.5.3). 3D rendering and surfaces reconstruction of individual cilia was performed with IMARIS XT module. Individual segmentation of channel with cilia marker (ARL13b) and channel with PTTG1, was performed. The classical object-based co-localization approach with voxel based co-localization was used. To visualize the precise spatial coexistence of the two proteins in individual cilia, views from different angles were created and transparent LUTs, as well as clipping planes were used to cut the 3D surfaces open to enable seeing inside cilia FIGURE 17. The total number of cilia in each sample was assessed during the same processing steps from the reconstructed surface of ARL13b signal and was given as number of cilia per area FIGURE 21.

3.6.3 Cell surface area quantification – whole mount neural folds

Anterior part of the matching somite stage wild-type and mutant neural folds was subjected to the cell surface area (CSA) analysis (see section 3.1 and 3.4.2). Four regions of interest (ROIs) of the same size were chosen per sample and cropped 3D in IMARIS (Bitplane) from the whole mount images. Using Z projection in Fiji they were transformed into a 2D view and analyzed further in IMARIS CELL. Cell detection algorithm was used, excluding the incomplete cells from the edges. Manual adjustment was performed, when necessary, and final cell surface area parameters were extracted. The complete dataset was subjected to the statistical analysis with unpaired *t*-test FIGURE 30.

3.7 Stimulated emission depletion (STED) microscopy

En face dual-color stimulated emission depletion (STED) microscopy imaging was performed on the mouse cephalic explants, which were prepared as described above (see section 3.3 and 3.4.2), with exception to the highly cross-absorbed secondary antibodies Alexa Fluor Plus 594 (Invitrogen), ATTO647N (Active Motif) TABLE 4 and ProLong Gold Antifade mountant (Invitrogen) which were used to obtain optimal resolution. STED microscopy images were taken with a Leica SP8 TCS STED microscope (Leica Microsystems) equipped with a pulsed white-light excitation laser (WLL; ~80 ps pulse width, 80 MHz repetition rate (NKT Photonics) and two STED laser for depletion at 592 nm and 775 nm. The system was controlled by the Leica LAS X software. Dual-color STED imaging was performed by exciting Alexa Fluor Plus 594 at 590 nm and Atto 647N at 647 nm. For emission depletion the 775 nm STED laser was used. Time gated detection was set from 0.3 – 6 ns. Two hybrid detectors (HyD) were used at appropriate spectral regions separated from the STED laser to detect the fluorescence signals. The emission filter was set for Alexa Fluor Plus 594 from 600 – 640 nm and for Atto 647N from 657 – 750 nm. Images were sequentially acquired with a HC PL APO CS2 100×/1.40 NA oil objective (Leica Microsystems), a scanning format of 1,024 × 1,024 pixels, 8-bit sampling, 16x line averaging, and 6x optical zoom, yielding a pixel size of 18.9 × 18.9 nm. Additionally, to every STED image, a confocal image with the same settings but just 1x line averaging was acquired.

All STED microscope images of the cilia within each independent experiment were acquired with equal settings. Single optical plane images were subjected to the cilia length quantification in ImageJ. Regions of interest (ROIs) were manually selected with the segmented line tool and the total lengths of single cilia were measured FIGURE 22. The average cilia lengths for both mouse lines were checked for the statistical significance using an unpaired *t*-test. The quantification was performed by student Jessica Görne, under my supervision.

3.8 *In situ* hybridization

3.8.1 Generation of Digoxigenin-labeled RNA probes

Probe synthesis was conducted with the components of the DIG RNA labeling kit. *Sox10* riboprobe was generated in the plasmid pZL1/SX10 9.1.1. and was kindly provided by Carmen Birchmeier TABLE 5. Firstly, the plasmid was linearized in order to

generate the anti-sense probe. The digestion was performed overnight, at 37°C, according to the reaction described below TABLE 11, followed by the heat inactivation of the restriction enzyme at 80°C for 20 minutes. The sample was subsequently used for the *in vitro* transcription to generate the Digoxigenin (DIG)-labeled riboprobe. The transcription reaction TABLE 11 was performed at 37°C for 3 hours. Afterwards, the DNAse I was added and incubated an additional 30 minutes, at 37°C. The riboprobes were purified using the RNeasy Mini Kit (Qiagen), following manufacturer's instruction, and eluted in RNase-free water. The concentration was determined using a Nanodrop spectrometer.

TABLE 11 DIGESTION AND *IN VITRO* TRANSCRIPTION

Plasmid digestion		In vitro transcription		
plasmid	10 µg	Linearized DNA	1 µg	
10x Buffer (3.1)	10 µl	DIG-labeling Mix	2 µl	
Enzyme (NcoI)	2 µl	Transcription buffer	2 µl	37°C, 3 hours
ddH$_2$O	final 100 µl	RNAse inhibitor	1 µl	
	37°C, O/N	RNA Polymerase (Sp6)	1 µl	
		DNase	2 µl	37°C, 30 min

3.8.2   *In situ* hybridization (ISH) on cryosections

In situ hybridization (ISH) protocol was adapted from (Jensen and Wallace, 1997). The cryosections (see section 3.2) were dried for one hour at RT and washed with autoclaved PBS (in DEPC water) for 5 – 10 minutes. The sections were post-fixed with 4% PFA (in PBS) for 10 minutes and then washed 3 times with PBS/DEPC for 5 minutes each. Next, the sections were permeabilized with Proteinase K (10 µg/mL) diluted (1:1000) in PBS for 6 minutes, washed 3x 5 minutes with PBS, post-fixed again with 4% PFA for 10 minutes, and finally washed 2x 8 minutes with PBS. Sections were dehydrated with 70% ethanol for 5 min and air-dried. For pre-hybridization, sections were incubated with hybridization buffer for 1 - 3 hours at 65°C in a humid chamber with 1:1 formamide/H$_2$O.

The riboprobes were prepared to a final concentration of 1 ng/µl in hybridization buffer and pre-incubated at 95°C for 5 min. The solution (150 µl/ slide) was applied, and slides were covered with the hybridization cover. The incubation was overnight, at 65°C, in the humid chamber. The next day, sections were washed with pre-heated Solution I (2x 30 minutes, 65°C), with Solution II (2x 30 minutes, 65°C), and with MABT (3x 10 minutes, RT). In order to reduce the unspecific binding, the sections were blocked for 2 - 4 hours at RT in MABT-blocking solution. Following the blocking, the anti-digoxigenin(DIG)-AP (Fab fragments) were diluted (1:5000) in blocking solution and applied on the slides (150 µl each) for overnight incubation at 4°C.

On the following day, the sections were washed with MABT (5x 20 minutes, RT) and with NTMT (10 minutes each). The final signal was developed using BM-Purple after 3 - 5 hours of incubation at RT, in dark. The sections were washed with PBS (3x 5 minutes, RT), followed by mounting in Aqua Poly/Mount. Slides were stored at 4°C. The composition of the solutions is summarized in the TABLE 6.

3.8.3   Whole mount *in situ* hybridization (WISH)

Whole mount *in situ* hybridization (WISH) protocol was adapted from (Hammes et al., 2001). The embryos (see section 3.1) stored in 100% methanol were rehydrated by graded methanol solutions to PBS, following by two washes with PBST (0.1% Tween-20 in PBS), 10 minutes each. The embryos were bleached in 6% H_2O_2 (in PBST), for 1 hour in darkness to reduce background, and then subsequently washed with PBST (2x 5 minutes). Next, the embryos were permeabilized for 8 minutes with Proteinase K (10 µg/mL) diluted (1:1000) in PBST, washed with PBST 5 minutes, and post-fixed with 4% PFA for 20 minutes. Finally, the embryos were washed 3x 5 minutes with PBST.

For pre-hybridization, embryos were incubated with pre-hybridization buffer for 3 hours at 65°C in 2 ml tubes. The riboprobes were prepared with the final concentration of 400 ng/ml in hybridization buffer and pre-incubated at 95°C for 5 min. Pre-hybridization solution was exchanged for 500 µl of hybridization solution and embryos were incubated overnight at 65°C. The next day, embryos were washed with pre-heated Solution I (2x 30 minutes, 65°C), with Solution II (2x 30 minutes, 65°C), and with PBST (3x 10 minutes, RT). In order to reduce unspecific binding, the embryos were blocked for 3 hours at RT in blocking solution containing 10% sheep serum and 1% BSA in

PBST. Following the blocking, the anti-DIG-AP was diluted (1:3500) in 500 µl blocking solution (with 1% sheep serum) per sample, and incubated overnight at 4°C.

On the following day, the embryos were washed with PBST (3x 5 minutes, RT), followed by another (10x 20 minutes, RT) PBST washes. Next, samples were washed with NTMT (2x 10 minutes) in order to equilibrate the pH. The final signal was developed using BM-Purple after 3 - 5 hours of incubation in RT, in the dark. Next, samples were washed with NTMT (2x 5 minutes), followed by a change of pH by overnight wash with PBST (pH 5.3) at 4°C. The following day, the samples were post-fixed with 4% PFA for 20 minutes and were washed with PBST (2x 10 minutes). The embryos were cleared in a glycerol gradient of 25%, 50%, and 80% in PBS and stored at 4°C. The imaging was done using a stereomicroscope. The composition of the solutions is summarized in the TABLE 6.

4 SDS-PAGE and western blotting

Whole E8.5 wild-type embryos from FVB/N, C57BL/6N, and F1 backgrounds were lysed in SDS lysis buffer TABLE 6. Samples were homogenized by pipetting and heated to 95°C for 10 min. Next, the samples were centrifuged 2 min at 13,200 rpm and stored at -20°C.

Equal amounts of protein samples were subjected to a SDS polyacrylamide gel electrophoresis (SDS-PAGE) using 12% Tris-Glycine gel. Samples were run at 90V in SDS-PAGE running buffer, and proteins separated according to their molecular mass. Next, proteins were transferred onto a nitrocellulose membrane (Amersham Protran 0.2 µm) using a wet electroblotting system (Bio-Rad Mini Protean II Cell) with transfer buffer at 100V for 1.5 hours.

The transfer was followed by immunoblotting. The membrane was blocked with 5% non-fat dry milk in TBST (0.1% Tween-20) for 1 hour at RT. Next, the membrane was incubated with the primary antibodies overnight, at 4°C. The antibodies were diluted in TBST as follows: rabbit anti-PTTG1 (Abcam, Cat. #ab79546, 1:5000), mouse anti-αTubulin (Merck Millipore, Cat. #CP06, 1:2000). The next day, the membrane was washed with TBST (3x 15 minutes) and incubated for one hour at RT, with peroxidase-conjugated secondary antibodies diluted in TBST TABLE 4. Next, membrane was

washed with TBST (3x 10 minutes). Signal was detected by SuperSignal West Dura (Life Technologies) with Otimax 2010 X-Ray Film Processor (PROTECT).

The result was quantified using ImageJ. The rectangle tool was used to select the bands, and the measurement of signal intensity was performed, following the subtraction of the analogically measured background signal. The PTTG1 signal intensity was normalized to αTubulin, and the relative protein level was calculated. Unpaired *t*-test statistical analysis was performed to assess the significance.

5 Electron microscopy

5.1 Scanning electron microscopy (SEM)

For scanning electron microscopy (SEM), E8.5 embryos were dissected and fixed in 0.1 M sodium cacodylate buffer (pH 7.3/7.4) containing 2.5% glutaraldehyde. The final sample preparation was performed by Mrs. Petra Schrade at Charite. The embryos were rinsed in cacodylate buffer and subjected to postfixation step in 2% OsO_4 for two hours. Samples were dehydrated in graded ethanol series, osmicated, dried in critical point apparatus Polaron 3000, coated with gold/palladium MED 020 (BAL-TEC), and examined by Nora Mecklenburg and myself, at the Zeiss scanning electron microscope (Gemini DSM 982).

5.2 Transmission electron microscopy (TEM)

Transmission electron microscopy (TEM) image acquisition was carried out in collaboration with Electron Microscopy Platform at MDC and by Dr. Bettina Purfürst. Thermo Fisher Morgagni electron microscope (80 kV), equipped with Morada CCD camera and the iTEM software was used. Sample preparation was done by Christina Schiel.

5.2.1 Average cell diameter analysis

The average cell diameter quantification was performed on the TEM images from ultrathin coronal sections from E9.5 embryos heads. The samples were already available in the lab and were prepared by Dr. Nora Mecklenburg and Dr. Bettina Purfürst according to the following protocol. Mouse embryos at E9.5 were fixed during dissection with 3% formaldehyde in 0.2 M HEPES buffer, pH 7.4, for 30 min at RT, followed by postfixation with 6% formaldehyde/ 0.1% glutaraldehyde in 0.2 M HEPES

buffer for 24 hours. Samples were stained with 1% OsO_4 for 2h, dehydrated in a graded ethanol series and propylene oxide, and embedded in Poly/Bed^R 812. Ultrathin sections were contrasted with uranyl acetate and lead citrate.

iTEM software was used to manually measure the size of the average cell diameter for *Lrp2$^{+/+}$* and *Lrp2$^{-/-}$* C57BL/6N mice. The quantification was performed by student Levin Riedel, under my supervision.

5.2.2 PTTG1 immunogold labeling

The head region of E9.5 mouse embryos was fixed with 3% freshly prepared formaldehyde/ 0.05% glutaraldehyde (EM-grade) in 0.1 M phosphate buffer for 1 hour at RT. After washing, samples were infiltrated with 2.3 M sucrose overnight at 4°C and frozen. Semithin sections were prepared to identify the region of the neuroepithelium. Ultrathin cryosections, according to Tokuyasu, were labeled with anti-PTTG1 antibody (Abcam, Cat. #ab79546, diluted 1:50) and 12 nm colloidal gold anti-rabbit secondary antibody (Dianova). Sections were contrasted and stabilized with a mixture of 3% tungstosilicic acid hydrate and 2.5% polyvinyl alcohol.

6 Cell culture

6.1 Maintenance

NIH-3T3 murine cells were maintained in DMEM (Invitrogen) with 10% Fetal Bovine Serum (FCS) and 1% Penicillin-Streptomycin (P/S) under sterile, humidified conditions with 5% CO_2, at 37°C TABLE 2. After reaching approximately 80% confluency, cells were passaged with a 1:10 dilution in order to maintain the cell culture. To detach, the cells were washed with DPBS and incubated 2-3 minutes with Trypsin/EDTA at 37°C. Next, cells were dissociated into a single-cell suspension, with warm growth medium, and seeded. For maintenance, 10 cm ⌀ cell culture dishes were used. Before every experiment, cells were counted using hemacytometer, and a precise number of cells was seeded on multi-well plates.

For cryopreservation, confluent cells were trypsinized, dissociated, and collected in 50 ml flacon tubes. Cells were centrifuged for 5 minutes at 1000 rpm at RT, and the medium was aspirated. Cells were re-suspended in the DMEM containing 20% FCS and 10% DMSO (approximately 2 ml of medium was used to re-suspend pellet from

1 confluent 10 cm ⌀ plate). Cells were frozen at -80°C in cryo-vials placed in the chamber with isopropanol. For longer-term storage, frozen cells were transferred to liquid nitrogen containers. After thawing the cells, the DMSO had to be removed by a quick change to regular growth medium.

6.1.1 SHH-conditioned medium preparation

SHH-conditioned medium was obtained from SHHN-293 cells, which were kindly provided by M. Kato (Stanford School of Medicine). SHHN-293 cells, thanks to the stable transfection with a SHH-N expression construct, are able to secret the lipid modified active SHH-Np protein. In order to collect the medium, cells were seeded onto a 15 cm ⌀ cell culture plate. After reaching about 80% confluency, the medium was changed to low-serum medium (DMEM with 2% FCS). Following a 48 hour incubation, the conditioned medium was collected and stored at -80°C in aliquots. The analogical procedure was performed with parental HEK293T cells, and the collected medium served as a control.

6.2 Transfection

Transient transfection of NIH-3T3 cells was performed with Lipofectamine™ 3000 Transfection Reagent (Invitrogen) according to the manufacturer's instructions. Cells were seeded the day before the transfection in order to reach 60-70% confluency. For 24-well plate, 4x10^4 NIH-3T3 cells were plated. The next day, prior to transfection, the medium was changed to antibiotic-free. Transfection reaction mix was prepared in Opti-MEM reduced serum medium, following the ration of 0.5 µg DNA/ 1 µl of P3000 Reagent / 1 µl of Lipofectamine 3000 Reagent. After pre-incubation of the reaction, the DNA-lipid complex was applied on the cells and incubated for 24 hours. The overexpression constructs used in the experiments are listed in the TABLE 5.

6.3 SHH luciferase reporter assay

NIH-3T3 cells, seeded in 24-well plates (4*10^4 cells/well), were transiently co-transfected with the gene of interest or proper empty plasmid, GLI-dependent *firefly* luciferase reporter (8 x 3'Gli-BSδ51LucII) (Sasaki et al., 1997), and a constitutive *renilla* luciferase reporter for normalization (pRL-TK; Promega) at a ratio 10:10:1 using Lipofectamine3000, as described in (section 6.2). After 24 hours, the medium was replaced with SHH-Np conditioned medium (see section 6.1.1) or control medium, at a 1:10 dilution, in DMEM containing 0.5% FCS. For control, inhibition study 50 nM

KAAD-cyclopamine (Calbiochem) or solvent (DMSO) were added to the conditioned medium with SHH-Np.

The luciferase assay was performed following a 48-hour stimulation. Cells were lysed in the 1x Lysis Buffer (Promega) (55 µl/well), frozen in order to facilitate the lysis, subsequently thawed and the lysate was aliquoted (10 µl) on the flat-bottom 96-well plate for the measurement. The reagents were prepared as described in TABLE 6. Luciferase activity was assayed with D-luciferin (in 1xFLB), and the results were normalized to the corresponding Renilla activity, assayed with coelenterazine (in 1xRLB). The measurements were performed using Berthold Luminometer, in biological triplicates, referring to three different wells assayed the same day, in minimum of three independent experiments, and results are presented as mean and standard deviation FIGURE 13. Statistical analyses was performed in Prism using Two-way ANOVA with Dunnett's multiple comparisons test.

6.4 Immunocytochemistry

For immunocytochemistry, NIH-3T3 cells were seeded in chamber slides (Sigma) in regular growth medium conditions with $5x10^4$ cells/well. After 24 h, cells were rinsed with PBS, fixed with 4% PFA for 15 min at RT, and permeabilized with PBST (0.25% Triton X-100 in PBS) for 20 min. In order to minimize the unspecific binding of antibodies, cells were blocking with 10% donkey serum in PBST for 1 hour at RT. Blocking was followed by a standard incubation with primary antibodies overnight and secondary antibodies for 1 hour, as described in immunohistochemistry section (section 3.4.1). The dilutions of antibodies were used as stated in TABLE 3 and TABLE 4. The walls surrounding the chambers were removed according to the manufacturer's instruction, and the samples were mounted with Dako Fluorescence mounting medium. Each experiment was repeated at least three times, in triplicates.

Additional validation of the endogenous PTTG1 levels in NIH-3T3 cells was performed using whole cell lysate and western blotting analysis (section 4) as well as using the siRNA approach (data are not included).

7 Statistical analysis

Statistical analysis on the datasets was performed with Prism 7 software (GraphPad). Unless otherwise stated, the unpaired Student's *t*-test was used, and the standard error of mean (SEM) is provided. The term significant was used if the p value of a result was less than 0.05 (p<0.05). Exact p values, n values and biological replicates are reported in the Figures or Figure legends. Final figures were prepared using Adobe Illustrator 2019 software.

V. RESULTS

1 Identification of novel candidate genetic modifier genes affecting the SHH pathway in the developing ventral forebrain

The initial hypothesis, based on the phenotypic characterisation of *Lrp2*^{-/-} mutant and wild-type mice on C57BL/6N and FVB/N congenic backgrounds FIGURE 8, implicated a dominant contribution of FVB/N background on the stability of SHH signaling (see introduction 4.3). The dominant effect manifested by the rescue of SHH-dependent phenotype in *Lrp2*^{-/-} FVB/N and F1 mutant mice. Following the transcriptome analysis described in the introduction (section 5.2, FIGURE 10), I started my Ph.D. work with a functional characterisation of differentially expressed genes (DEGs) that could potentially influence the SHH pathway and their observed phenotypes.

Based on the highest fold change and p-value, the top DEGs for the wild-type comparison were matching the top DEGs from analogical analysis performed only on the mutant samples FIGURE 10. This supported the hypothesis about the LRP2-independent but strain dependent modulation of SHH signaling. Amongst them were *Tuba1c*, *Ulk4,* and *Pttg1. Tuba1c* and *Ulk4* genes were simultaneously top DEGs within the filtered primary cilia and HH-related datasets FIGURE 11. However, direct function of *Tuba1c* and *Ulk4* in the SHH signaling was not clear (see introduction 5.2.1). Moreover, *Pttg1* has not hitherto been associated with primary cilia and SHH. This prompted us to test the functional potential of *Tuba1c*, *Ulk4,* and *Pttg1* in context of SHH signaling regulation.

In order to evaluate the potentially novel regulatory function of these genes on SHH signaling, I included DEGs previously associated with the SHH pathway (see FIGURE 11). Both *B9d1* (Dowdle et al., 2011) and *Rpgrip1l* (Andreu-Cervera et al., 2019; Vierkotten et al., 2007) were documented to decrease SHH pathway activation in a loss of function approach. In contrast, *Talpid3,* although never shown to modulate the SHH pathway, was shown to be essential for ciliogenesis (Yin et al., 2009).

B9d1, *Rpgrip1l*, and *Talpid3*, similarly to *Ulk4* and *Pttg1,* are upregulated in a more 'resilient' FVB/N mouse strain, in which SHH signaling is rescued in *Lrp2*^{-/-} mutant

embryos. For that reason, I examined their roles within the context of gain of function. In order to elucidate the potential positive modulatory effect on SHH signaling, I applied the *in vitro* Dual Luciferase Reporter Assay, a well-established assay in the SHH field (Christ et al., 2012; Taipale et al., 2000; Zhang et al., 2006). The assay is based on a *firefly* luciferase reporter construct with SHH-responsive GLI-binding sites (Sasaki et al., 1997), and it serves as a readout for activated SHH signaling, with a second constitutively active *renilla* luciferase reporter, serving as an internal control.

1.1 Candidate modifier genes increase cellular sensitivity to SHH

We asked whether shortlisted DEGs from the primary cilia and SHH-related dataset (*Ulk4, B9d1, Rpgrip1l, Talpid3, Tuba1c*) and unrelated (*Pttg1*) can positively regulate SHH signaling *in vitro*. In order to understand this better, I transiently co-transfected the NIH-3T3 cells with the luciferase reporter constructs, described above, with either test cDNA or a corresponding empty control vector (see methods 6.3). Next, cells were stimulated with either control media or media conditioned with SHH-Np – an active, double-lipid-modified SHH form with palmitic acid at N-terminus and cholesterol at C-terminus (Mann and Beachy, 2004; Porter et al., 1996) – in order to induce the SHH pathway. Following the stimulation, the bioluminescence was assessed and quantified FIGURE 13.

Overexpression of both *B9d1* and *Rpgrip1l* in transfected NIH-3T3 cells, treated with SHH-Np or control medium for 48 hours, resulted in a significant induction of relative GLI-driven luciferase levels compared to controls. In contrast, cells transfected with *Talpid3* and *Tuba1c* showed no induction of GLI1-based luciferase activity after SHH stimulation compared to controls. To prove that the observed activation of the SHH pathway is specific and signals through the canonical Smo activation, I used the HH pathway inhibitor, KAAD-cyclopamine (Taipale et al., 2000). The induction of firefly luciferase activity after overexpression with genes was inhibited after treatment with KAAD-cyclopamine. Taking these observations and the current state of knowledge together provided strong evidence that the established Luciferase Assay is sensitive to the canonical pathway modulation and is reliable and replicable.

Interestingly, both *Ulk4* and *Pttg1* overexpression appeared to influence the capacity of SHH signaling in NIH-3T3 cells as well. I observed significantly higher activation of the GLI luciferase reporter after SHH stimulation in *Ulk4* and *Pttg1* overexpressed cells,

compared to control vectors. This effect was inhibited by KAAD-cyclopamine. Summarizing, the results showed, for the first time, ULK4 and PTTG1 can positively modulate the SHH pathway *in vitro*. Additionally, these results support the idea that higher *Ulk4* and *Pttg1* expression levels in mouse embryos on a FVB/N background could contribute to more efficient SHH signaling. Importantly, it implicated *Pttg1* as a novel factor in the SHH field.
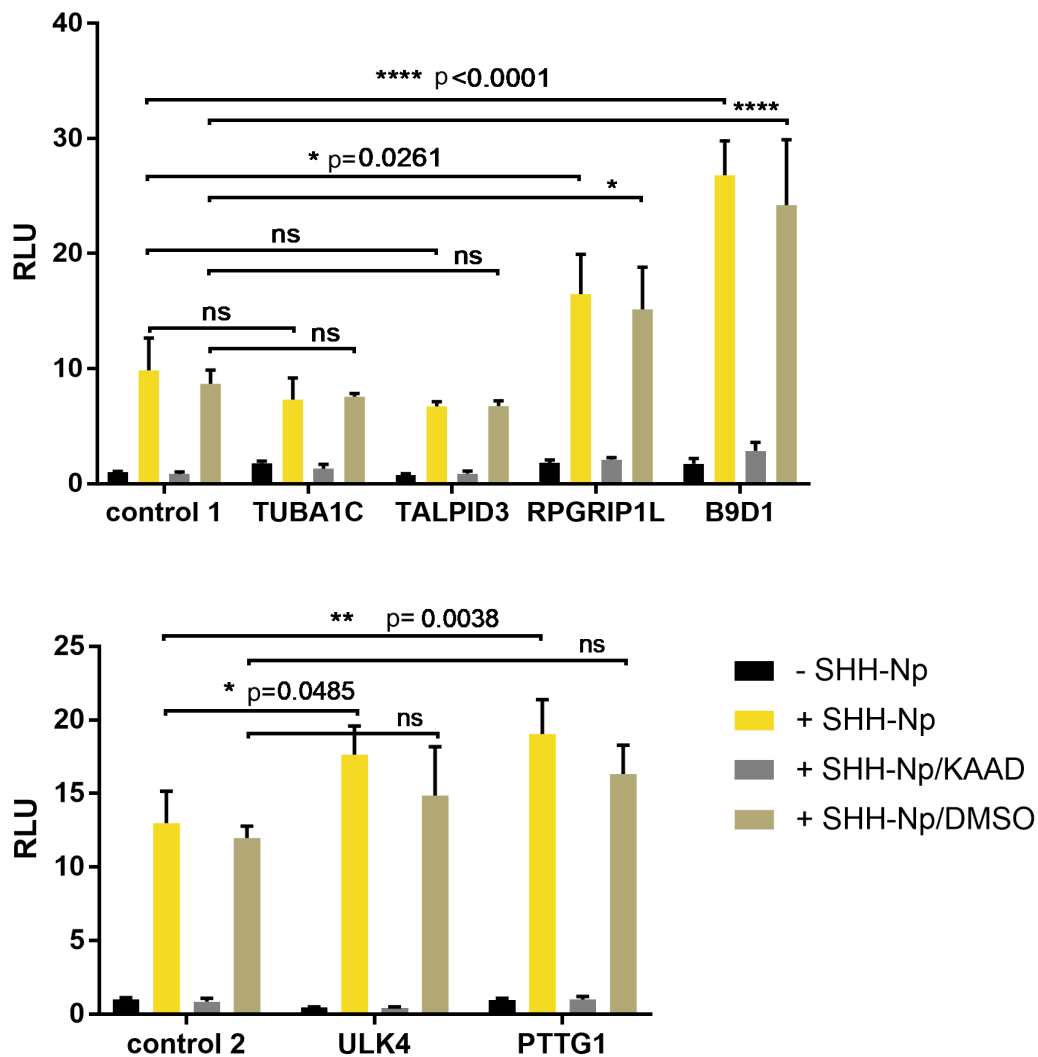
FIGURE 13 FUNCTIONAL CHARACTERISATION OF GENES IN A LUCIFERASE REPORTER ASSAY. Gli1-dependent luciferase reporter assay performed in NIH-3T3 cells verified the potential of candidate genes to modify the SHH signaling. Overexpression of *Rpgrip1l, B9d1*, *Ulk4,* and *Pttg1* resulted in significantly induced relative luciferase units (RLU) compared to controls. *Tuba1*c expression, referred to the SHH 'off' state, resulted in no induction, alike for *Talpid3*. NIH-3T3 cells were treated with medium containing SHH-Np (+SHH-Np) or control (-SHH-Np) medium. KAAD-cyclopamine was used to confirm the canonical response of SHH pathway. Two-way ANOVA was performed, and significance levels denoted as: * $p < 0.05$, ** $p < 0.001$, *** $p < 0.0001$, ns – not significant. Note: backbones of the used plasmids were different, thus control 1 and control 2 refer to respective control plasmids (see methods 6.3).

2 PTTG1 is a novel component of the primary cilium

B9D1 and RPGRIP1L are present at the basal body and transition zone of primary cilia (Garcia-Gonzalo et al., 2011; Vierkotten et al., 2007). In contrast, the current state of knowledge about PTTG1 reports it is degraded after cytokinesis (Hagting et al., 2002; Zur and Brandeis, 2001). Thus, I asked: how can PTTG1, in interphase, be a positive regulator of the SHH signaling pathway tightly linked to the primary cilium? In order to answer this question, I performed a thorough analysis of PTTG1 subcellular localization in NIH-3T3 cells (see methods 6.4).
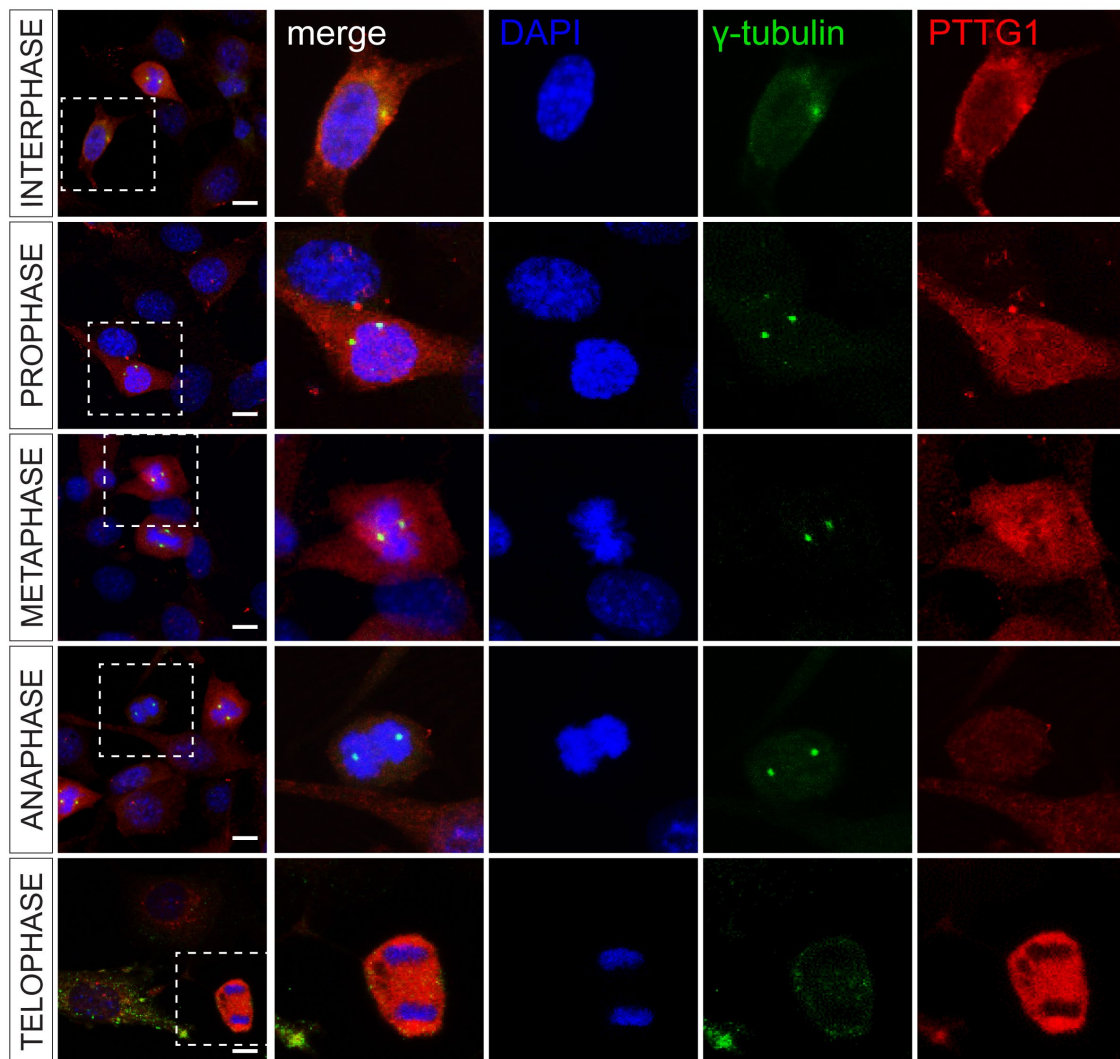
FIGURE 14 PTTG1 ASSOCIATES WITH THE NUCLEUS IN THE MITOTIC CELLS.
Confocal imaging detects immunofluorescence signals for PTTG1 in the perinuclear region of mitotic NIH-3T3 cells. Boxed, magnified insets present PTTG1 concentrated at the centrosomes positive for γ-tubulin and in the cytoplasm of dividing cells. Scale bar 10 um.

As it has already been well described in the context of metaphase-anaphase transition and control of premature separation of sister chromatids, we expected to find PTTG1 expression in the perinuclear region and centrosomes (Tong et al., 2008; Vlotides et al., 2007). Immunocytochemistry of NIH-3T3 cells, with γ-tubulin, as a marker for centrioles in mitotic cells, confirmed the expected co-localization with PTTG1 FIGURE 14. Some cells additionally showed a dispersed signal in the cytoplasm of dividing cells.

2.1 PTTG1 is present in primary cilia in subset of ciliated NIH-3T3 cells

A more comprehensive analysis of the immunofluorescence and cellular structures unraveled a new interesting finding. Some of the non-mitotic, ciliated cells were also positive for PTTG1. PTTG1 localized to a subset of primary cilia of NIH-3T3 cells, co-stained for acetylated tubulin (FIGURE 15, a, arrowheads). Interestingly, the localization pattern was diverse, with PTTG1 localizing either to the periciliary region (FIGURE 15, b), the proximal region of the primary cilium (FIGURE 15, c) or the entire ciliary shaft (FIGURE 15, d).

The cell cycle dependent variable localization of PTTG1 in the NIH-3T3 cells, at the centrosomes and in the primary cilia, challenged the current notion of ubiquitous degradation of PTTG1 by the anaphase-promoting complex (APC) at the end of metaphase (Vlotides et al., 2007; Zur and Brandeis, 2001). On the other hand, these observations, together with my functional approach, opened new, interesting questions about PTTG1. PTTG1 appeared to not only be not degraded, but also shuttled to the primary cilium under an unknown regulatory mechanism, possibly together with mother and daughter centrioles building the ciliary base. Moreover, the variable pattern within the cilium could indicate a supportive function in the cilium, potentially contributing to the positive regulation of signaling pathways, such as SHH.
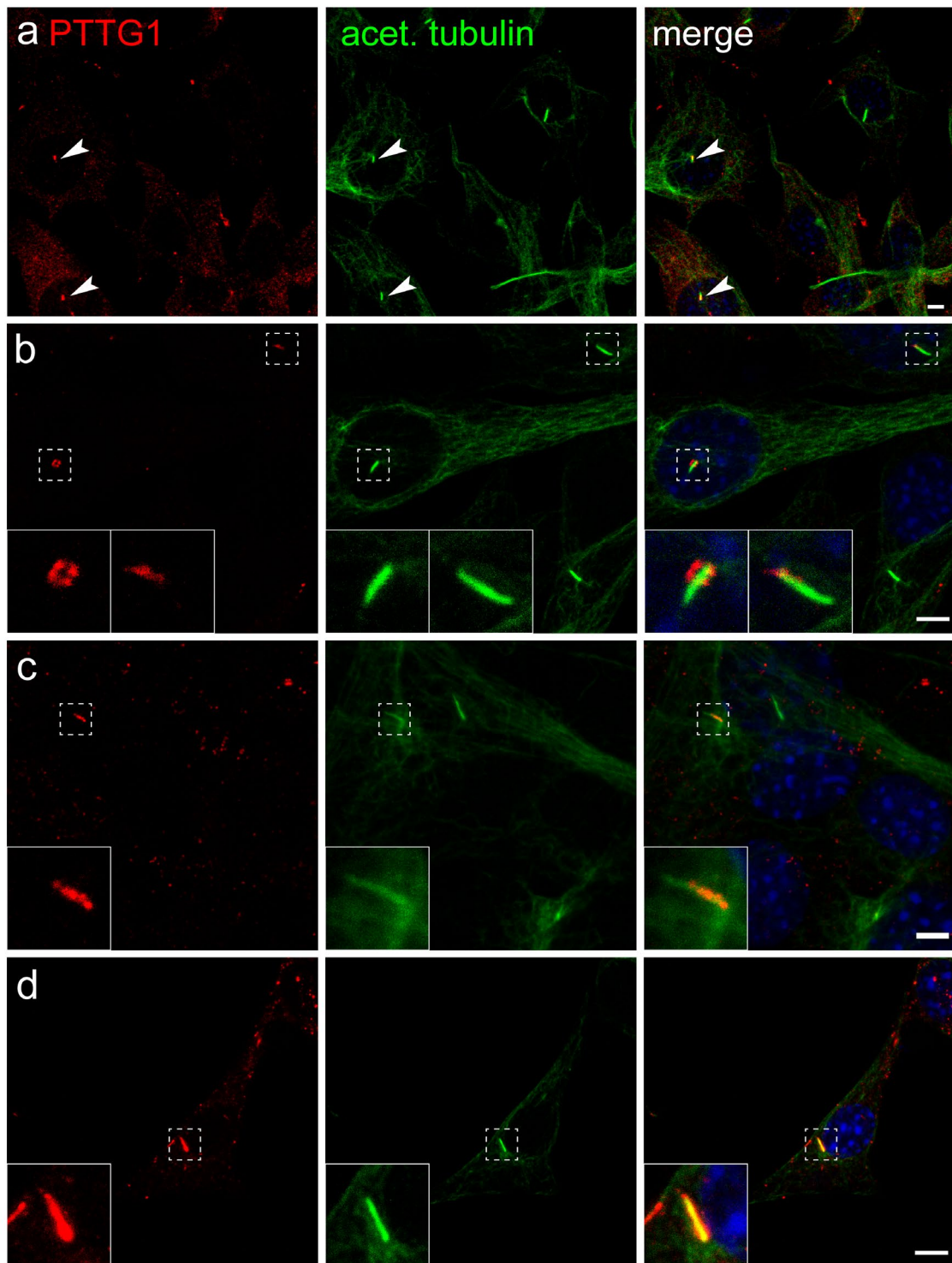
FIGURE 15 SUBCELLULAR LOCALIZATION OF PTTG1 IN THE CILIATED/QUIESCENT CELLS.
(**a**) Subset of interphase NIH-3T3 cells show PTTG1 localized to primary cilia stained with acetylated tubulin (arrowheads). PTTG1 expression pattern varies from periciliary region (**b**) to ciliary shaft, either at the proximal part (**c**) or along entire cilium (**d**). Insets show magnified primary cilia indicated by dashed-line squares. Scale bars: 1 µm. Figure was modified from (Mecklenburg et al., 2020).

2.2 PTTG1 localizes to a subset of primary cilia in mouse neuroepithelium

Interesting findings about the PTTG1 localization in the primary cilia in cell culture, prompted us to look into an *in vivo* model. For an en face view onto the forebrain polarized neuroepithelium, I prepared cephalic explants from FVB/N and C57BL6/N E9.5 wild-type mouse embryos (see methods 3.3, 3.4.2) FIGURE 12. These explants allowed me to examine the apical surface of neuroepithelium in high resolution. Confocal imaging of the forebrain neuroepithelium, as indicated by squares FIGURE 12 confirmed a subset of primary cilia is positive for PTTG1 (FIGURE 16, arrowheads) in both mouse lines.
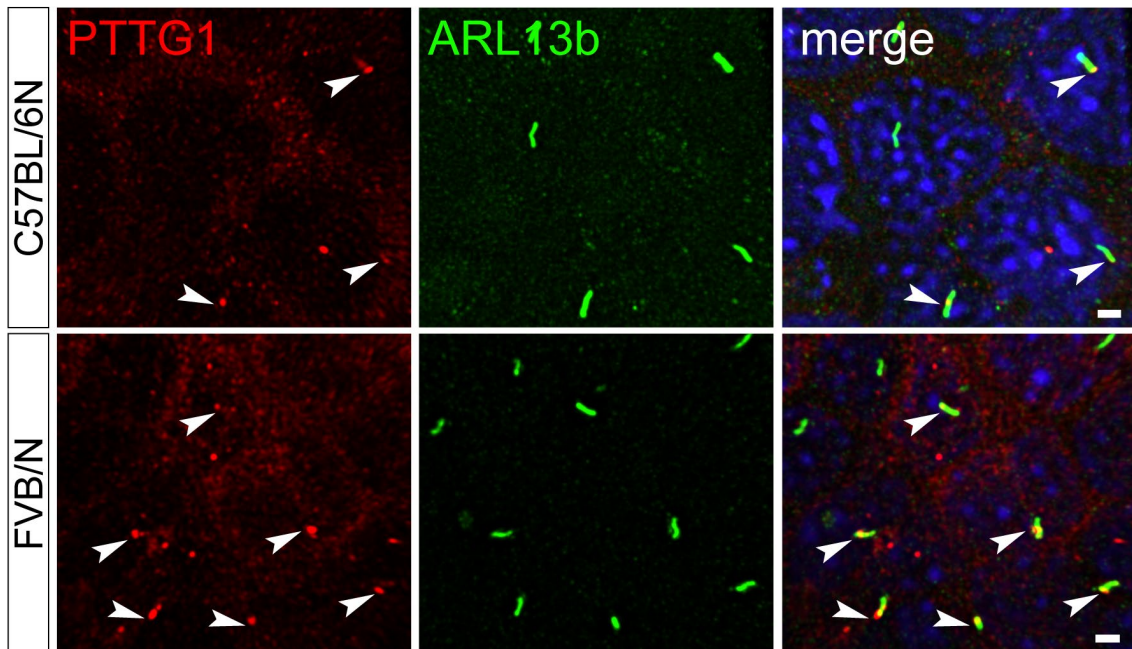
FIGURE 16 PTTG1 IN THE SUBSET OF PRIMARY CILIA OF NEUROEPITHELIAL CELLS. Immunofluorescence confocal microscopy on cephalic explants from E9.5 C57BL/6N and FVB/N embryos presented PTTG1 in the subset of primary cilia stained with ARL13b (arrowheads). Scale bars: 1 µm. Figure was adapted from (Mecklenburg et al., 2020).

In order to precisely asses the PTTG1 localization in the primary cilia of mouse explants, I applied complex raw data processing using imaging software (see methods 3.5.3). The images were subjected to deconvolution, chromatic shift correction, and 3D reconstruction of individual primary cilia stained for ciliary membrane marker ARL13b and PTTG1. Interestingly, the expression of PTTG1 perfectly recapitulated the observations from cell culture, showing a diverse pattern with PTTG1 covering

either the periciliary region (FIGURE 17, a, d), proximal parts (FIGURE 17, b, e), or the entire ciliary shaft (FIGURE 17, c, f) in both mouse lines. Segmentation of the single channels and detailed 3D analysis of the single primary cilia, presented in the insets, clearly show PTTG1 clearly localizes within the shaft of the primary cilium, although it does not colocalize with ARL13b.
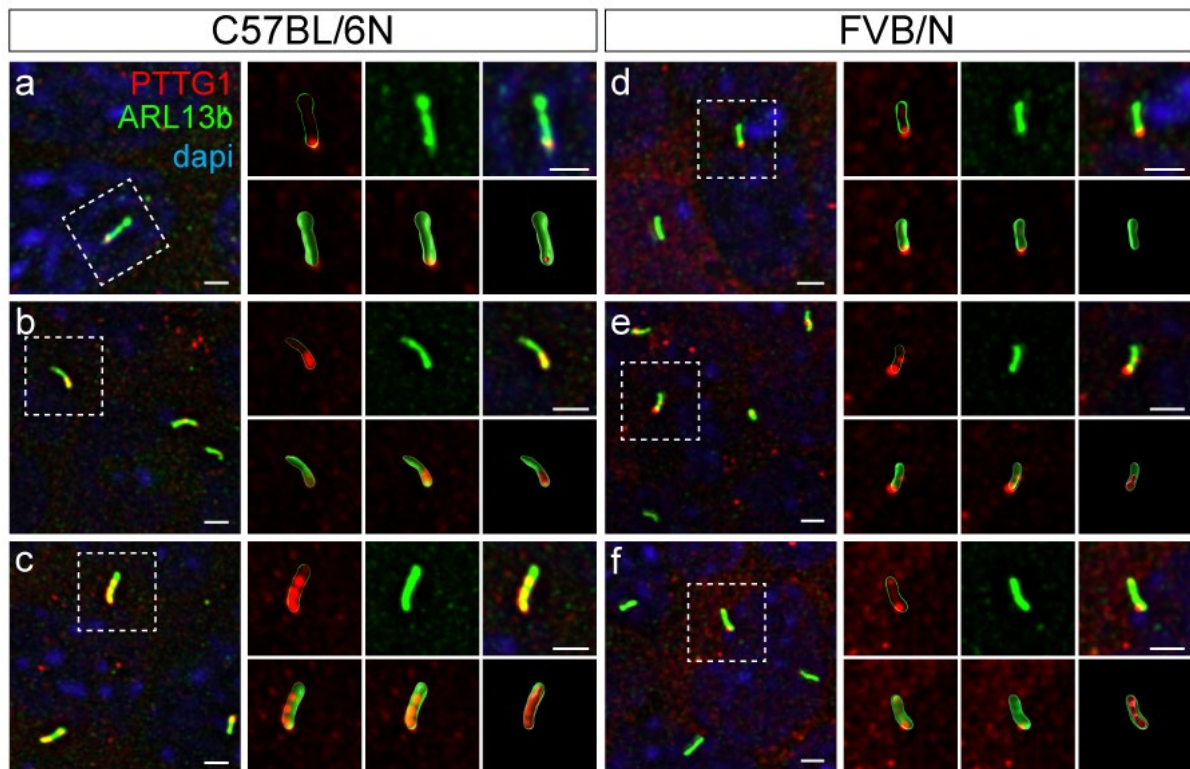
FIGURE 17 PTTG1 IS PRESENT IN THE CILIARY SHAFT IN THE FOREBRAIN NEUROEPITHELIUM. 3D reconstruction of primary cilia shows PTTG1 localized to the ciliary shaft. PTTG1 is present at the periciliary region (**a, d**) and in the ciliary shaft (**b, c** and **e, f**) for C57BL/6N and FVB/N embryos, respectively. Insets from the top panel (a' – f') magnify the chosen cilia (dashed-line squares) showing PTTG1 signals (with the outline of the cilium), ARL13b, and merge, respectively. Inserts from the bottom panel (a'' – f'') show the following: reconstructed ARL13b with non-reconstructed PTTG1 signal, the optical section through it, and reconstruction of both ARL13b and PTTG1. Note the difference in the cilia length between the backgrounds. Scale bars: 1 μm. Figure was adapted from (Mecklenburg et al., 2020).

Additional evidence for PTTG1 being present in the primary cilia of mouse neuroepithelial cells came from electron microscopy on immunogold labelled ultrathin tissue sections (see methods 5.2.2). The signal perfectly recapitulated the immunofluorescence observations, with PTTG1 present in the periciliary region (FIGURE 18, arrowheads), cytoplasm (FIGURE 18, asterisk), and microtubule-based ciliary shaft (FIGURE 18, boxed) for both mouse lines. There were also cilia without any

visible PTTG1 staining, confirming both the specificity of the assay and the immunocytochemistry in NIH-3T3 cells, where only subset of primary cilia is PTTG1 positive. Interestingly, we could also see PTTG1 associated with mother and daughter centrioles (*FIGURE 18*, arrows), building the basal body, indicating PTTG1 is indeed not degraded after mitosis, but rather participates during ciliogenesis.
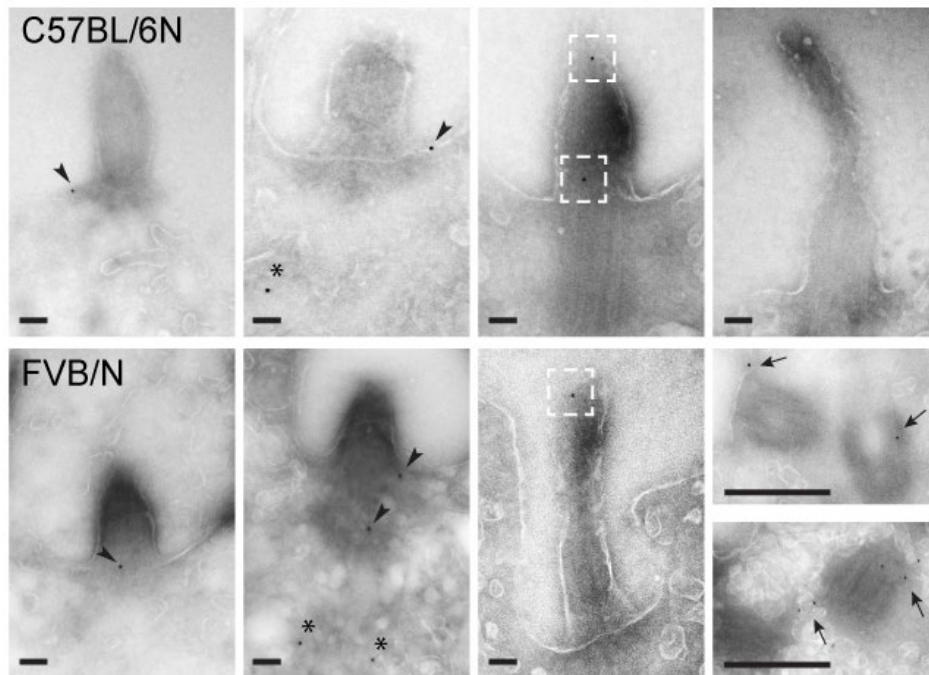
FIGURE 18 PTTG1 AT THE PRIMARY CILIUM – ULTRASTRUCTURAL TEM ANALYSIS. Immunogold labeling of PTTG1 - transmission electron microscopy (TEM) examination of the ultrathin coronal sections of E9.5 forebrain neuroepithelium from C57BL/6N and FVB/N embryos. Labeling confirmed the PTTG1 expression within a subset of primary cilia for both mouse strains. Protein was found at the periciliary region (arrowheads), ciliary shaft (dashed-line boxes), and in the cytoplasm (asterisks). Additionally, PTTG1 was found at the centrioles (arrows). Scale bar: 100 nm.

2.3 PTTG1 expression is significantly increased in the FVB/N neuroepithelium

Variable pattern of the PTTG1 localisation within the ciliary shaft made it difficult to quantitatively assess the protein level restricted to the primary cilia. C57BL/6N and FVB/N explants both presented similar expression pattern of PTTG1 within the primary cilia. However, indications from RNA deep sequencing about significantly higher *Pttg1*

transcripts for FVB/N and F1 mouse embryonic heads prompted us to validate the total protein level for the embryos (see methods 4).
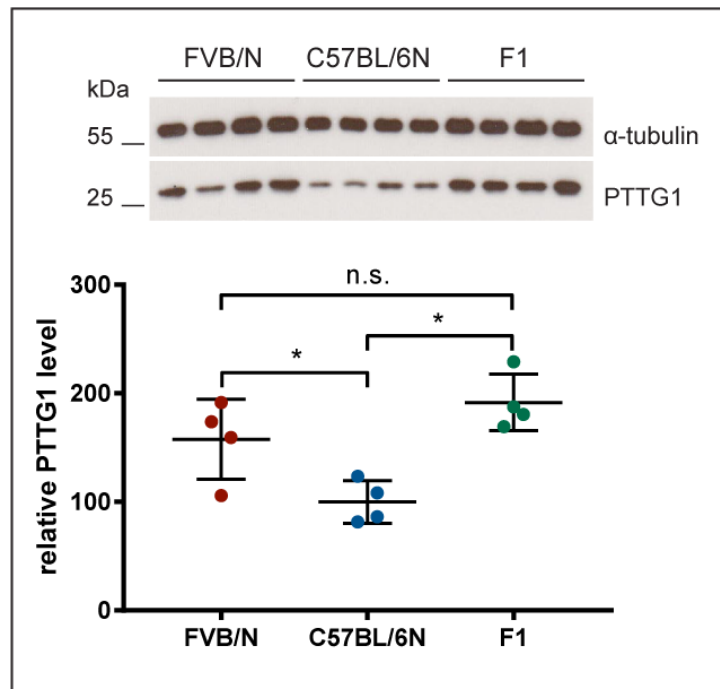
FIGURE 19 QUANTIFICATION OF TOTAL PTTG1 PROTEIN IN THE EMBRYONIC TISSUE.
Total PTTG1 protein levels from E8.5 (13 s) FVB/N, C57BL/6N and F1 embryonic heads were assessed by western blot. Significantly higher PTTG1 level was found in FVB/N and F1 embryos compared to C57BL/6N. PTTG1 signal (27 kDa) was normalized to α-tubulin (55 kDa). Note slightly decreased α-tubulin level for C57BL/6N. Unpaired *t-test*; * p < 0.05, ns – not significant. The experiment was performed with Nora Mecklenburg and the figure was adapted from (Mecklenburg et al., 2020).

Quantification of the relative PTTG1 level against α-tubulin showed significantly higher protein expression in FVB/N and F1 wild-type embryos compared to C57BL/6N FIGURE 19. A clear difference in PTTG1 level in the total embryonic tissue raised the question whether the difference can be specific to the neuroepithelium. Indeed, quantification of the relative fluorescence intensity (see methods 3.6.1) on the coronal sections of control 10 - 11 somites embryos from all three strains confirmed significantly increased PTTG1 protein in the neuroepithelium of the F1 and FVB/N embryos, with the latter being the highest FIGURE 20.
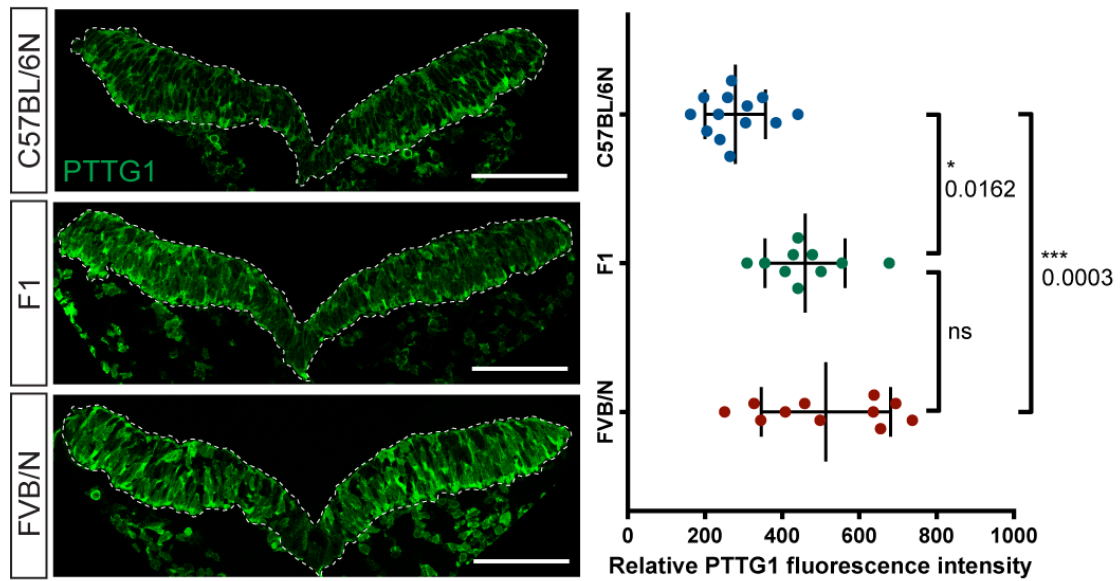
FIGURE 20 HIGHER PTTG1 PROTEIN LEVELS IN THE FVB/N NEUROEPITHELIUM.
Immunofluorescence intensity of PTTG1 was assessed in the neuroepithelium from E8.5 C57BL/6N, F1, and FVB/N control ($Lrp2^{+/+}$ and $Lrp2^{+/-}$) embryos. Neuroepithelium was manually delineated as depicted by dashed lines. A total of 3 coronal sections from each embryo (10 and 11 somites; C57BL/6N n = 5, F1 n = 3, FVB/N n = 4) were examined. Scale bars: 100 µm. Unpaired *t-test*; * p < 0.05, ** p < 0.001, *** p < 0.0001. Figure was modified from (Mecklenburg et al., 2020).

These results suggested that not only an *in vitro* system could show a positive modulation of the SHH pathway by PTTG1, but higher protein levels *in vivo* could analogically contribute to more efficient SHH signaling in developing FVB/N and F1 brains.

3 Strain-dependent differences in primary cilia of the forebrain region

Detailed analysis of the mouse cephalic explants from both mouse lines unravelled another interesting aspect about the neuroepithelial morphology (see methods 3.3, 3.6.2). Quantification of the cilia number per area revealed that the FVB/N anterior neural tube has a significantly higher number of cilia (645 cilia/mm^2 surface area) than C57BL/6N (425 cilia/mm^2 surface area) F$_{IGURE}$ 21. This result implicated a potential difference in the proliferative capacity of neuroepithelial cells and/or the cell cycle regulation between the mouse strains; however, it was not explored further in my project.
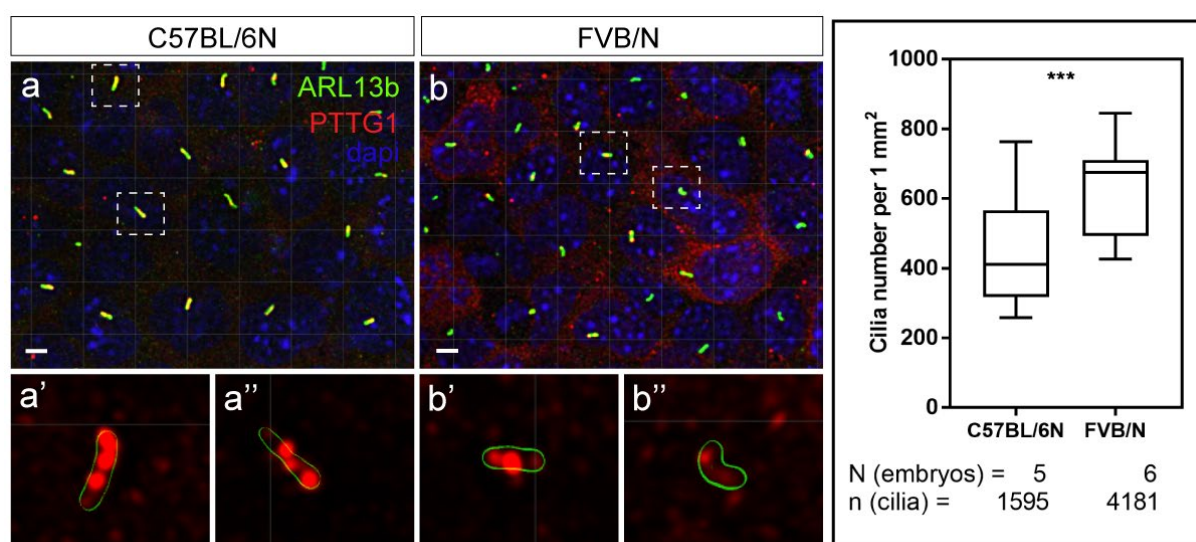
F$_{IGURE}$ 21 I$_{NCREASED}$ $_{NUMBER}$ $_{OF}$ $_{PRIMARY}$ $_{CILIA}$ $_{IN}$ $_{THE}$ $_{FOREBRAIN}$ $_{OF}$ FVB/N $_{EMBRYOS}$. Confocal microscopy images of the en face view on the neuroepithelium from *Lrp2*$^{+/+}$ C57BL/6N (**a**) and FVB/N (**b**) embryos presented differences in the cilia number. Two representative primary cilia for each strain are shown in higher magnification (**a', a''** and **b', b''**) and display PTTG1 within the ciliary shaft (ARL13b signal depicted as reconstructed mask showing the circumference of each cilium). Scale bar: 1 µm. The box plot represents the quantification of average cilia number per 1 mm^2 area with whiskers indicating minimal and maximal values. Unpaired *t-test*, *** p < 0.0001. Figure was modified from (Mecklenburg et al., 2020).

Screening hundreds of cilia also led us suspect cilia from FVB/N mice are shorter in length. En face single-color stimulated emission depletion (STED) microscopy imaging on the mouse cephalic explants labelled for the ARL13b validated these observations (see methods 3.7). Length measurements presented primary cilia of *Lrp2*$^{+/+}$ FVB/N to be 20% shorter (1.19 µm ± 0.011 SEM; n = 1068) compared to the primary cilia from

Lrp2⁺/⁺ C57BL/6N samples (1.49 µm ± 0.014 SEM; n = 908). The width of the primary cilia appeared to be comparable between FVB/N (0.272 µm ± 0.0012 SEM; n = 885) and C57BL/6N samples (0.271 µm ± 0.0014 SEM; n = 703) *FIGURE 22*.
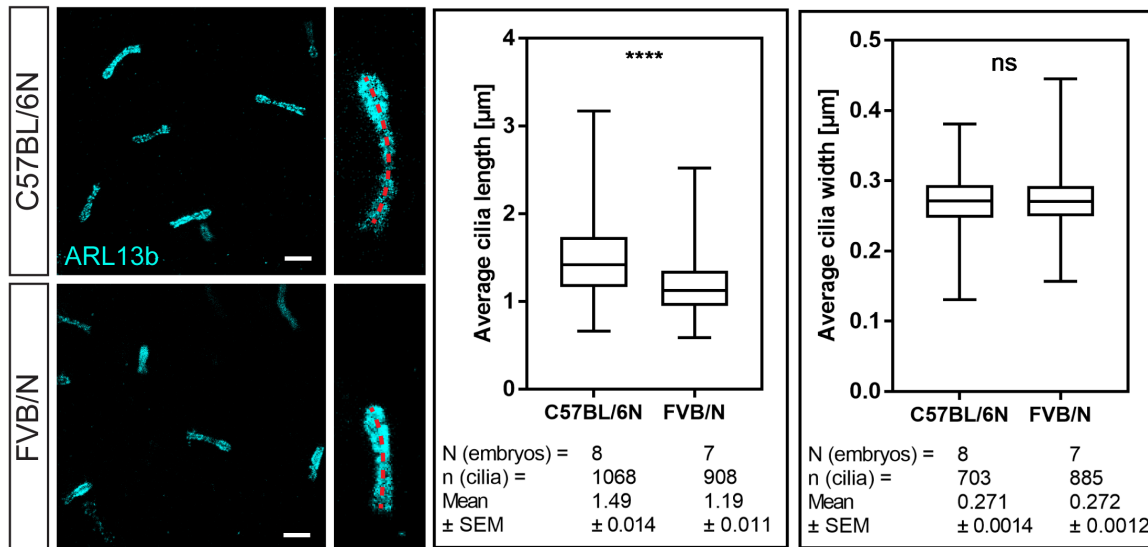
FIGURE 22 PRIMARY CILIA IN THE FVB/N FOREBRAIN ARE SHORTER THAN IN C57BL/6N.
Primary cilia, labeled with ARL13b, were imaged in the anterior region of E9.5 cephalic explants using STED microscopy. Primary cilia of *Lrp2*⁺/⁺ FVB/N embryos were 20% shorter compared to the cilia from *Lrp2*⁺/⁺ C57BL/6N. Ciliary width was comparable. Measurement of cilia length was performed as indicated by red dashed lines. The box plots represent the mean cilia length and width, with whiskers indicating minimal and maximal values. Unpaired *t*-test, **** p < 0.00001. Scale bar: 1 µm.

To summarize above results, I have shown that the presence of potential genetic modifiers, such as PTTG1 and ULK4, may compensate for the loss of LRP2 in FVB/N mice and lead to more resilient SHH signaling in the ventral midline of developing brain. Higher levels of these factors, dependent on the genetic background, may facilitate the signaling pathway during critical time points and allow for proper signal transduction. *Pttg1* and *Ulk4*, probably together with other modifying genes, could be responsible for the increase in the sensitivity of the cells to morphogens, and, as a consequence, they could trigger more efficient SHH pathway signaling at the primary cilium. I focused my interest on *Pttg1,* which not only regulates a cell cycle and mitosis, but, as suggested by above findings, also plays an important role in quiescent, ciliated cells, potentially by facilitating ciliogenesis, thereby making SHH signaling less susceptible to disturbances.

4 Mechanistic foundations of dorsal neural tube defects in *Lrp2* mutants

4.1 *Lrp2⁻/⁻* dorsal forebrain phenotype is independent of SHH signaling

C57BL/6N *Lrp2⁻/⁻* mutant mice exhibit cranial neural tube closure defects (Kur et al., 2014) (see introduction 4.2; FIGURE 7), with severe cases finalized in anencephaly (Kowalczyk et al., 2021). This dorsolateral phenotype cannot be explained by SHH signaling in the ventral midline. Despite rescue of the morphogen levels in both FVB/N and mixed F1 *Lrp2⁻/⁻* mutant mice, these mice still exhibit a conserved defect in dorsal forebrain, with enlarged fontanelle, reminiscent of NTDs observed in *Lrp2⁻/⁻* mutant C57BL/6N mice (FIGURE 8, red dashed-line). Furthermore, we documented the F1 generation presents range of NTDs, from mild indentations or enlarged fontanelle to exencephaly FIGURE 23.

Taking together these observations, we concluded there is a dorsal phenotype in *Lrp2⁻/⁻* mutant mice independent of the genetic background.
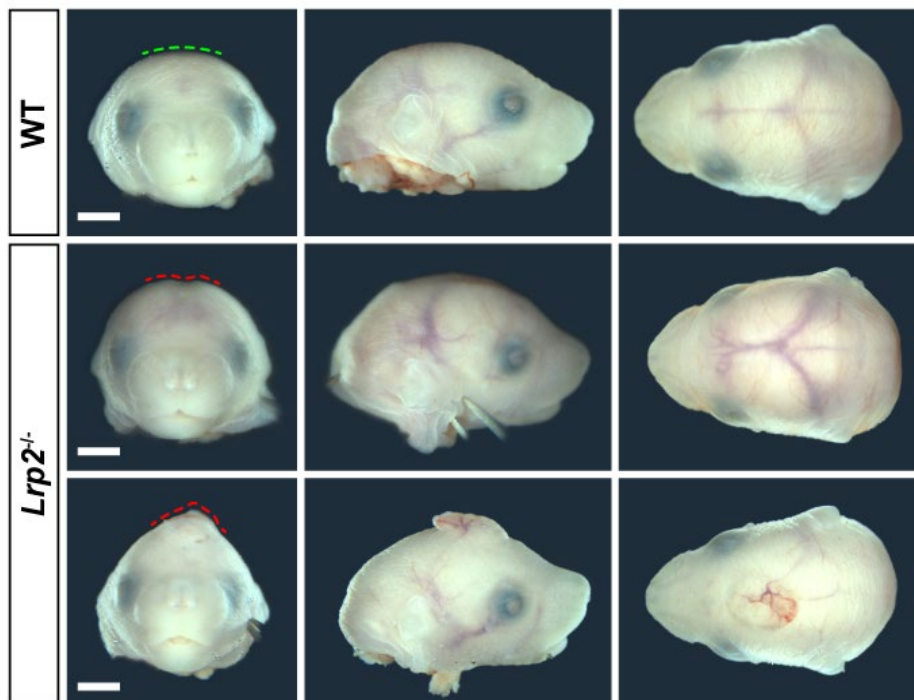
FIGURE 23 RANGE OF DORSAL PHENOTYPES IN *LRP2⁻/⁻* F1 HYBRIDS.
E18.5 embryonic heads from F1 generation presented in frontal, sagittal, and dorsal view. All *Lrp2⁻/⁻* F1 mutants show normal craniofacial features and no HPE (see FIGURE 8). However, they present range of dorsal phenotypes from mild indentations to exencephaly (red dashed-line). Scale bars present 2 mm.

4.2 Neural tube closure phenotype is conserved between mouse and *Xenopus*

Close collaboration with Kerstin Feistel's laboratory largely advanced the conceptualization of this project and significantly contributed to the understanding of LRP2-related etiology of NT defects. This collaboration documented that the dorsal neural tube closure phenotype is observed in *Xenopus laevis* FIGURE 24. Unilateral injection of translation-blocking morpholino oligomer targeting *lrp2*.L (*lrp2* MO) into the neural tissue of dorsal blastomeres led to impaired NP folding, compared to the control, uninjected side FIGURE 24. Bilateral injection led to more severe folding defects, while re-introduction of *lrp2* presented a rescue phenotype.
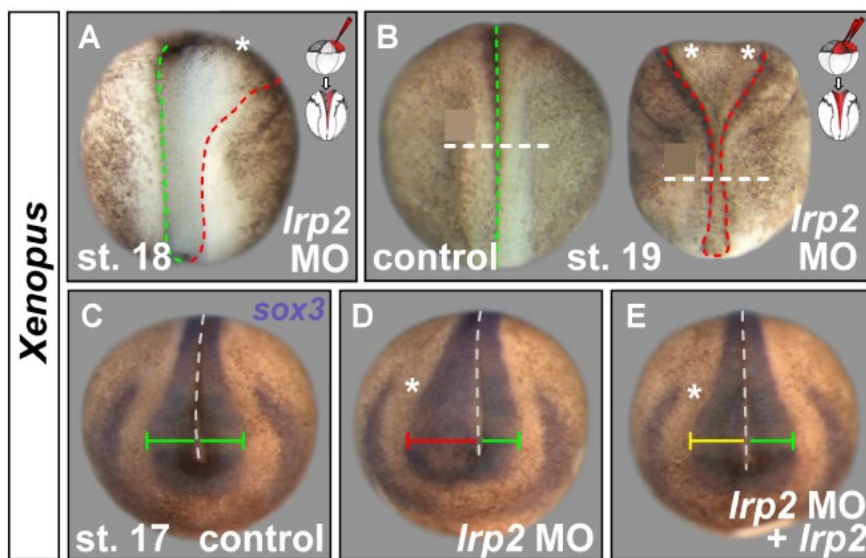
FIGURE 24 LRP2 IS REQUIRED FOR NEURAL TUBE CLOSURE IN *XENOPUS*.
Examination of neural plate (NP) morphology in *Xenopus*. (**A**) Unilateral injection of *lrp2*-targeted morpholino oligomer (*lrp2* MO) resulted in impaired folding of neural folds (asterisk). (**B**) Bilateral MO injection results in anterior and posterior NT folding (asterisks), comparing to closely apposed neural folds in control, at st. 19. (**C-E**) *In situ* hybridization for *sox3*; (**C**) normal neural plate (NP) width in control (green bar), (**D**) *lrp2* MO impairs NP narrowing (red bar), which is partially rescued by re-introduction of *lrp2* (**E,** yellow bar). Experiments were performed by Kerstin Feistel, and the figure was adapted from (Kowalczyk et al., 2021).

Findings in *Xenopus* from Dr. Feistel's lab encouraged us to elucidate the mechanism of LRP2-deficient neural tube defects by combining mouse and *Xenopus* models. This collaborative work significantly contributed to the understanding of bases of NT formation etiology, and it was summarized into a joined publication (Kowalczyk et al., 2021). In the following sections, I describe my experimental work performed in mouse

models. In order to decrease the mouse usage to the required minimum, we narrowed down this part of the study to the C57BL/6N mouse strain. Nevertheless, in the light of initial phenotypic analysis presented above we can confidently extrapolate the findings to the FVB/N and F1 mouse strains.

4.3 Early neural tube morphogenesis is altered in *Lrp2*$^{-/-}$ C57BL/6N mice

Polarity/PCP is one of the characteristics of epithelial morphology and is indispensable for morphogenetic changes during early development. Thus, instead of directly focusing on the transcriptional changes between the *Lrp2*$^{-/-}$ mutant and wild-type embryos, we first assessed the morphology at the onset of neural plate folding, one day before the anterior NTC occurs (see methods 5.1).

The scanning electron microscopy (SEM) imaging of the rostral neural folds, at three consecutive 6 – 8 somite stages of E8.5 embryos, allowed us to observe impaired neural tube folding in LRP2-deficient embryos (FIGURE 25, A). Mutant samples appeared to be smaller and substantially less developed. Comparison of matching somite stages during these dynamic morphological changes showed a clear delay in the folding of neural folds, which did not elevate in 8 s mutants as in control samples. Very prominent differences were located at the telencephalic invagination, where the optic sulcus emerges. In mutants, it was severely underdeveloped (FIGURE 25, A, mutant - red vs. control - green arrowheads). Interestingly we could also see a clear alteration in the ventral region, most likely related to the SHH signaling, and it was disturbed along the ventral midline induction. Approximately 60% of mutant neural folds did not fully separate at this stage (FIGURE 25, A).

A dorsal view of the neural folds confirmed a drastic delay in the folding process (FIGURE 25, B). It was especially prominent at 9 s embryos, where, in the controls, there was already a successful fusion of the dorsal neural tube. This was in contrast to still rounded, mutant neural folds at the same time point. These observations indicated the LRP2 receptor may have a significant impact on the maintenance and rearrangement of neuroepithelial cells during neural tube morphogenesis.
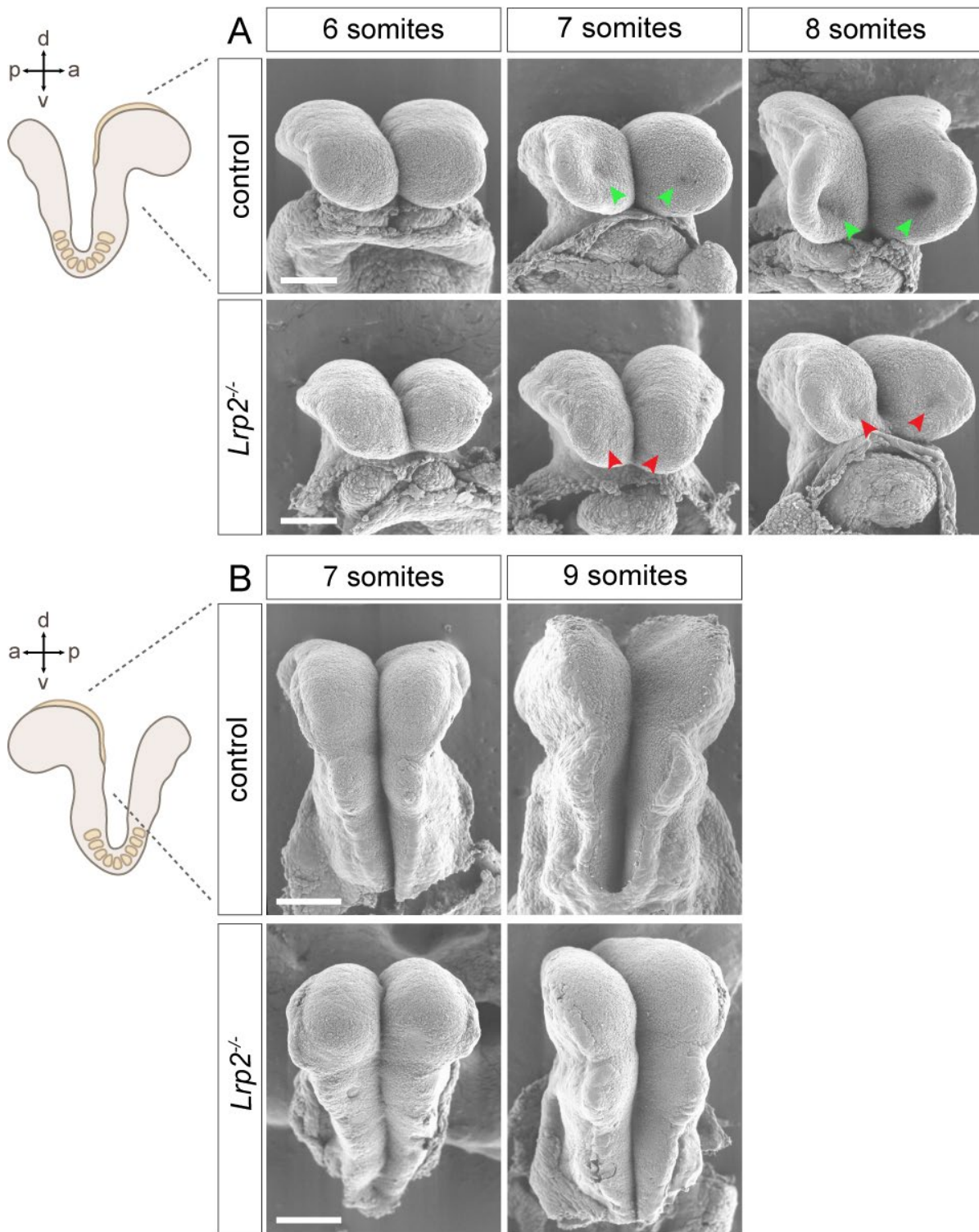
FIGURE 25 LRP2 IS REQUIRED FOR EARLY NEURULATION IN MICE.
Inspection of mouse neural folds (NFs) morphology by scanning electron microscope (SEM).
(**A**) Micrographs of anterior NFs from E8.5 control (*Lrp2*$^{+/+}$ and *Lrp2*$^{+/-}$, n = 20) and mutant (*Lrp2*$^{-/-}$, n = 22) embryos at 6, 7, and 8-somite stage. (**B**) Dorsal NFs from control (*Lrp2*$^{+/+}$ and *Lrp2*$^{+/-}$, n = 17) and mutant (*Lrp2*$^{-/-}$, n = 10) embryos at 7 and 9 s. Control NFs progressively elevate, the formation of optic evagination is initiated at 7 s (green arrowheads) and the closure point is visible at 9 s. Mutants present narrower NFs, delayed elevation and closure of NFs and impaired optic evagination (red arrowheads). (A) modified figure from (Kowalczyk et al., 2021). Scale bar presents 100 μm. d – dorsal, v – ventral, p – posterior, a – anterior.

Intrigued by prominent differences at the early neurulation, I took a closer look at the apical surface of the neuroepithelium *FIGURE 26*. Higher magnification on SEM images revealed additional interesting details about the organization of the cells. While the apical view on the cell layer of control samples seemed to be well organized and tightly packed with cells, which visibly constricted over the time, the view on the mutants appeared to be very irregular and full of excessive, protruding structures, sometimes almost completely covering the cells.

	anterior			posterior	
	6 somites	7 somites	8 somites	7 somites	9 somites
control					
Lrp2⁻ᐟ⁻					
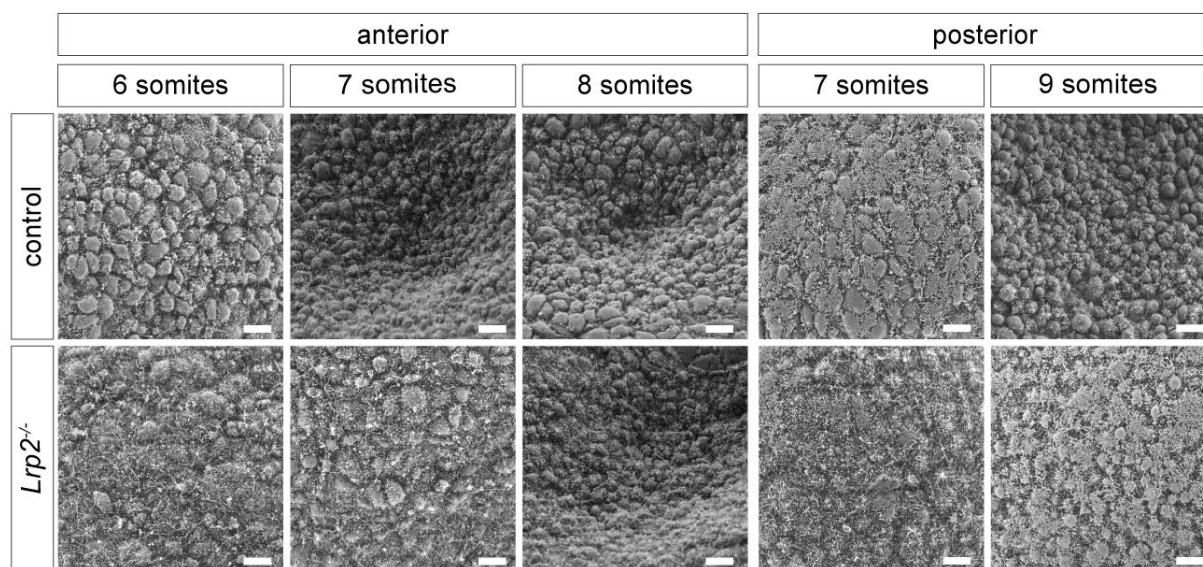
FIGURE 26 IMPAIRED MORPHOLOGY OF *LRP2⁻ᐟ⁻* MUTANT NEUROEPITHELIUM.
Scanning electron micrographs of mouse E8.5 neuroepithelium. Anterior views present the invaginating region. The surface of the mutant neuroepithelium is less structured, with prominent protrusions and single enlarged cells, compared to the unified and tightly packed surface of control neuroepithelium. Note the delay in process of invagination. A posterior view on the wild-type neuroepithelium shows a clear constriction of the cells between 7 and 9 s with reduced protrusions at 9 s. In contrast, mutant surfaces are lined with the protrusions. Scale bars present 5 µm.

Sectioning of the neural folds helped to more deeply examine the integrity of the neuroepithelium. Coronal sections were stained for the acetylated α-tubulin, a stabilized tubulin penetrating the pseudostratified cell layer in an apico-basal pattern (see methods 3.4.1). The alignment of the cells looking only by nuclei staining and by the distribution of tubulin was clearly disturbed in the mutant neuroepithelium *FIGURE 27*. Additionally, the sections confirmed that, from 8 to 10 s, at least, there is a continuous delay in elevation of the neural folds in mutants, which was previously observed in the SEM images *FIGURE 25*.
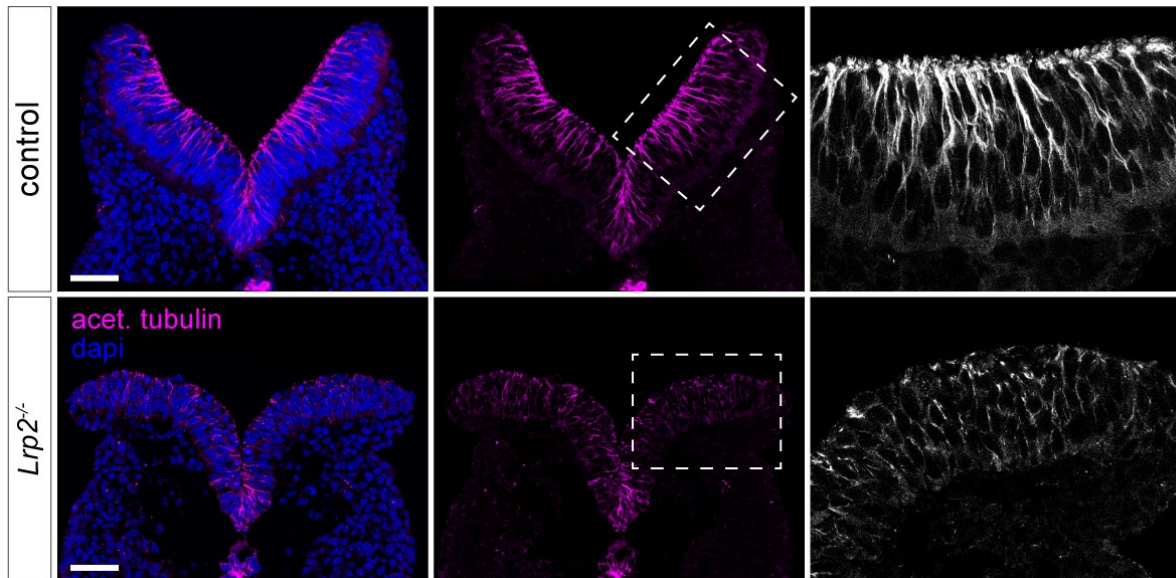
FIGURE 27 IMPAIRED CELL ALIGNMENT IN *LRP2⁻ᐟ⁻* MUTANT NEUROEPITHELIUM.
Immunofluorescence staining on coronal sections of 10 s control and *Lrp2⁻ᐟ⁻* mouse neural folds. Acetylated α-tubulin and nuclei staining present impaired apico-basal cell alignment. The neural folds of mutant embryos do not elevate, as in the controls. Scale bars represent 50 μm. Figure modified from (Kowalczyk et al., 2021).

5 LRP2 is necessary for apical constriction of neuroepithelial cells

To our knowledge, LRP2 expression was never assessed in the en face view of the entire anterior neural folds. As such, I performed whole-mount immunohistochemistry on the E8.5, 6 s embryos to identify how the expression of LRP2 correlates with the SEM observations (see methods 3.1, 3.4.2). As expected, LRP2 was detected across the entire neuroepithelium of the anterior neural folds and was not detected in the neuroepithelium of the mutants FIGURE 28. Co-staining of LRP2 with zona occludens-1 (ZO-1), a tight junction protein marking the cell borders, allowed us to better assess the distribution of the receptor on the cellular surfaces. LRP2 appeared to form one cluster per cell, however, the fluorescence signal varied depending on the region of the neural fold. Additionally ZO-1 staining confirmed smaller and more narrowed folds of the mutants.
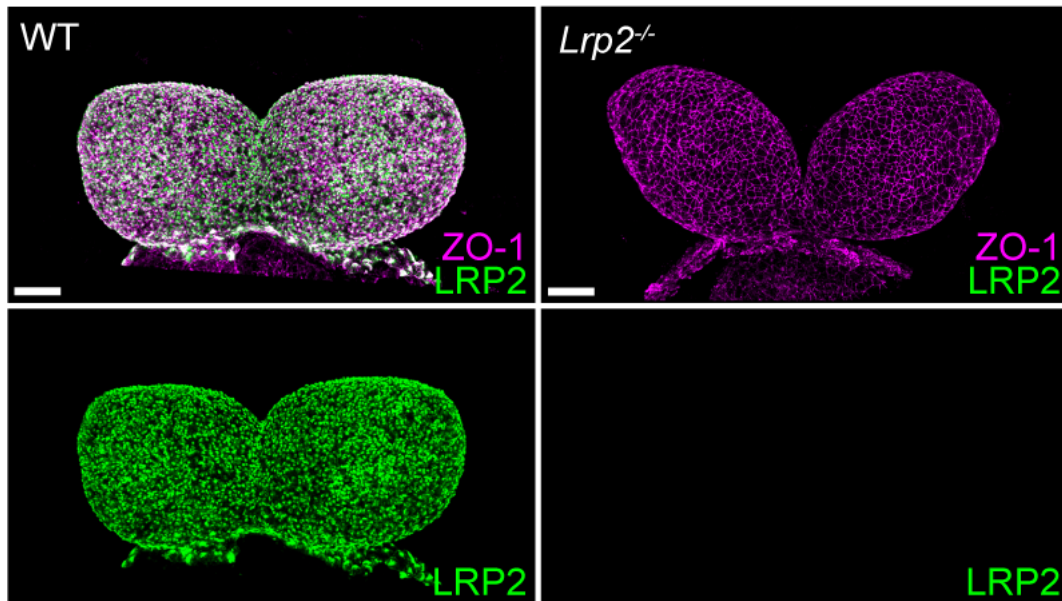
FIGURE 28 LRP2 EXPRESSION IN THE E8.5 MOUSE NEURAL FOLDS.
Immunofluorescence staining on whole-mount anterior neural folds from 6 s control and *Lrp2*-/- mutant embryos. LRP2 is detected apically throughout E8.5 control neural folds. ZO-1 marks cell boundaries. Scale bars represent 50 μm.

Looking at the 7 somite embryos clarified the LRP2 distribution. This stage is when evagination is initiated in control embryos, as presented on SEM images *FIGURE 25*. Interestingly, we could see a clear correlation between a more prominent LRP2 signal in the optic evagination (*FIGURE 29*, a''), where the cells undergo dynamic constriction, and more dorsal regions (*FIGURE 29*, a').

The high resolution imaging using Stimulated Emission Depletion (STED) microscopy, performed on the E9.5, wild-type cephalic explants (see methods 3.3, 3.7), showed precisely that LRP2 is concentrated in the highly endocytic, periciliary region surrounding the primary cilium *FIGURE 29*. This result confirmed the previously published LRP2 immunogold-TEM experiment (Christ et al., 2012). Moreover, co-staining with phalloidin again indicated the cells with smaller cell surfaces have more expression of LRP2, compared to the wide, non-constricting cells.
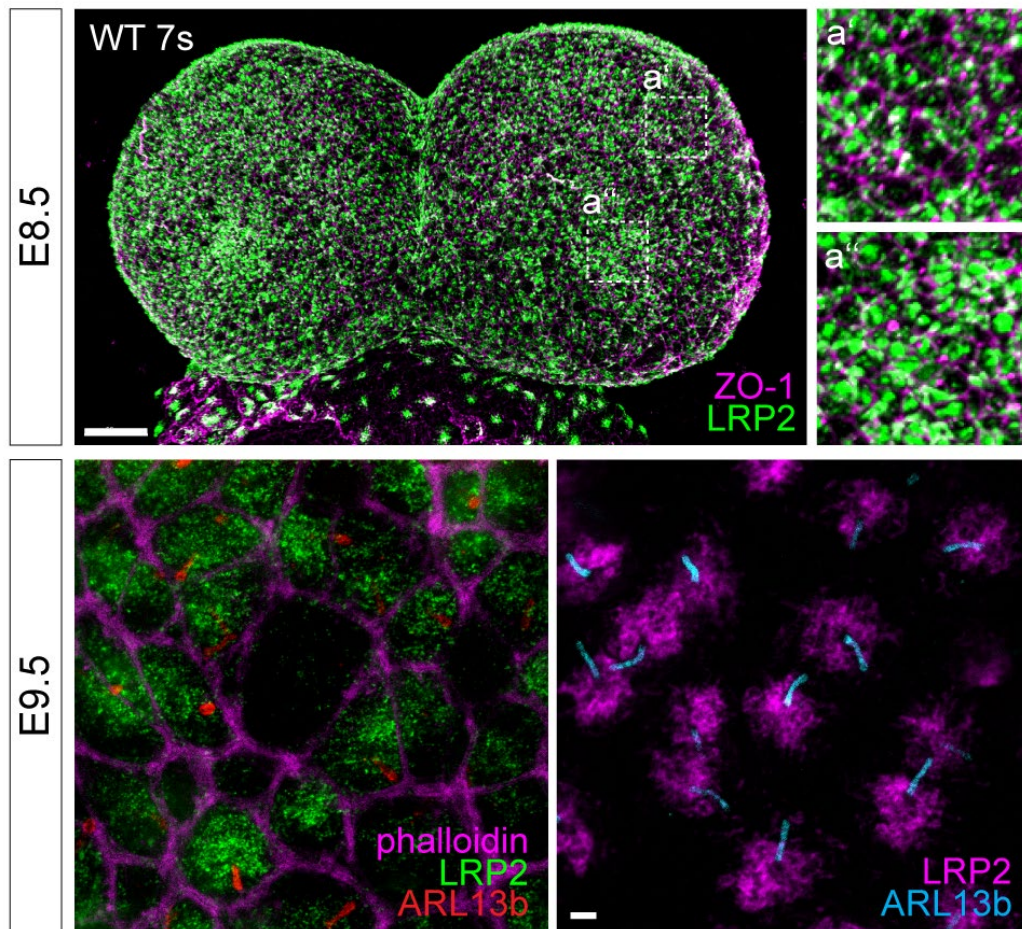
FIGURE 29 ENRICHED LOCALIZATION OF LRP2 IN THE CONSTRICTING NEUROEPITHELIAL CELLS
At E8.5, 7 s LRP2 protein is concentrated at the apically constricting region of optic evagination
(**a″**) in contrast to the dorsolateral region (**a′**). ZO-1 marks cell boundaries. STED imaging on
E9.5 cephalic explants presents LRP2 condensed around primary cilia labeled with ARL13b.
Phalloidin marks cell boundaries. Scale bars E8.5: 50 µm; E9.5: 1 µm.

5.1 Enlarged apical surface area of LRP2-deficient neuroepithelial cells

Neural tube closure is a very complex morphogenetic process, in which dynamic
rearrangements of the tissue and cells, such as autonomous changes like apical
constriction, take place. Differences within the progress of neurulation, observed using
electron microscopy, prompted us to look, in more detail at the neuroepithelial
architecture using whole mount immunohistochemistry.

To examine the apical cell layer of E8.5, 7s embryonic neuroepithelium, I used the
ZO-1 as a marker to delineate cell borders. Indications from SEM about lack of the
optic evagination at this stage were confirmed (*FIGURE 30*, arrowhead), but, more

strikingly, there were overall larger cell surfaces present in the mutants. Detailed semi-automated measurements using IMARIS software and mapping the cells using color-coding (see methods 3.5.3, 3.6.3) resulted in quantification confirming the significantly larger cell surface area (CSA) in neuroepithelium of LRP2-deficient embryos, compared to analogical regions in wild type. This data implicated the novel, formerly never addressed function of the LRP2 receptor in the apical constriction of neuroepithelial cells, which, in consequence, appears to facilitate proper NT morphogenesis and NTC.
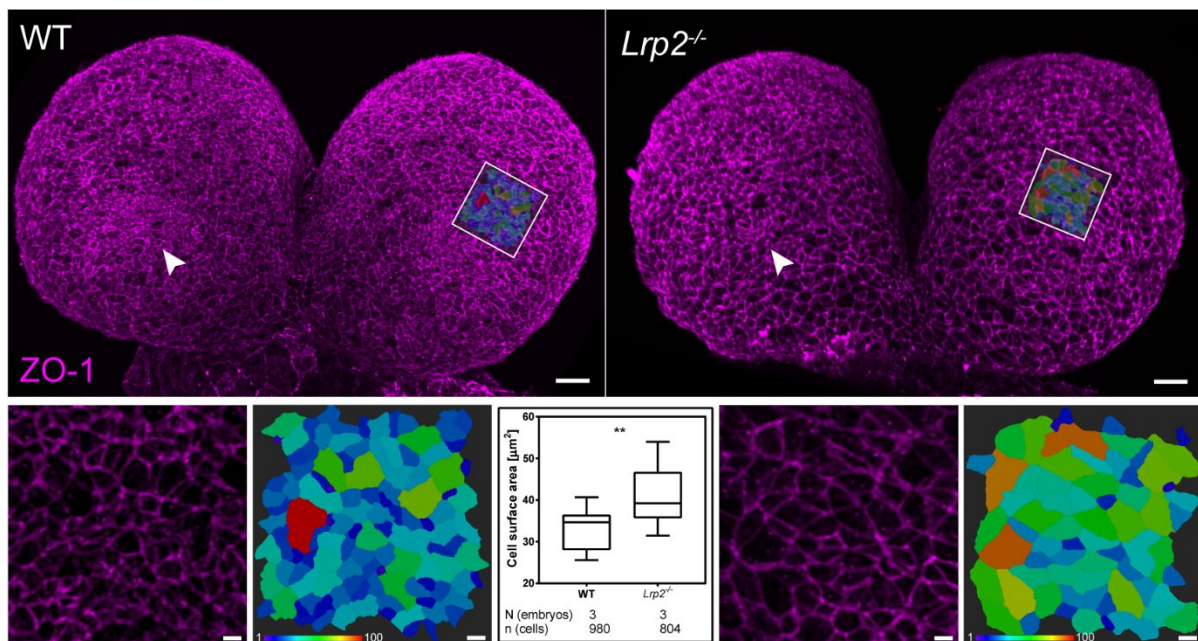
FIGURE 30 LRP2 IS REQUIRED FOR APICAL CONSTRICTION OF NEUROEPITHELIAL CELLS. Frontal views on developing forebrain from wild-type (WT) and *Lrp2*⁻ᐟ⁻ mouse embryos at E8.5, 7 s. Examination of cell surface area in the region of optic evagination (arrowheads). Mutants have significantly increased cell surface area compared to control embryos. Color-coded maps visualize differences. Box plot represents the mean cell surface area with whiskers indicating minimal and maximal values. Four areas per embryo were analyzed, unpaired *t*-test, ** p < 0.001. Scale bars present 20 μm and 3 μm for the inserts. Modified figure was published in (Kowalczyk et al., 2021).

Enlarged apical domains of radial glial cells (RGCs) in developing brain ventricles (Foerster et al., 2017), as well as increased size of collecting duct cells in polycystic kidney disease (Boehlke et al., 2010), have been explained by abnormal regulation of the mTORC1 pathway, due to cilia abrogation. mTORC1 is one of the two protein complexes of the mammalian target of rapamycin (mTOR) signaling pathway, which regulates cell metabolism, proliferation, and growth by integrating intra- and

extracellular signals (Laplante and Sabatini, 2009). The phosphorylated ribosomal S6 protein (p-S6RP) is a downstream target of mTORC1, and its expression was increased in enlarged mutant cells in both aforementioned studies. I, therefore, decided to test p-S6RP localization in the enlarged *Lrp2* mutant cells.
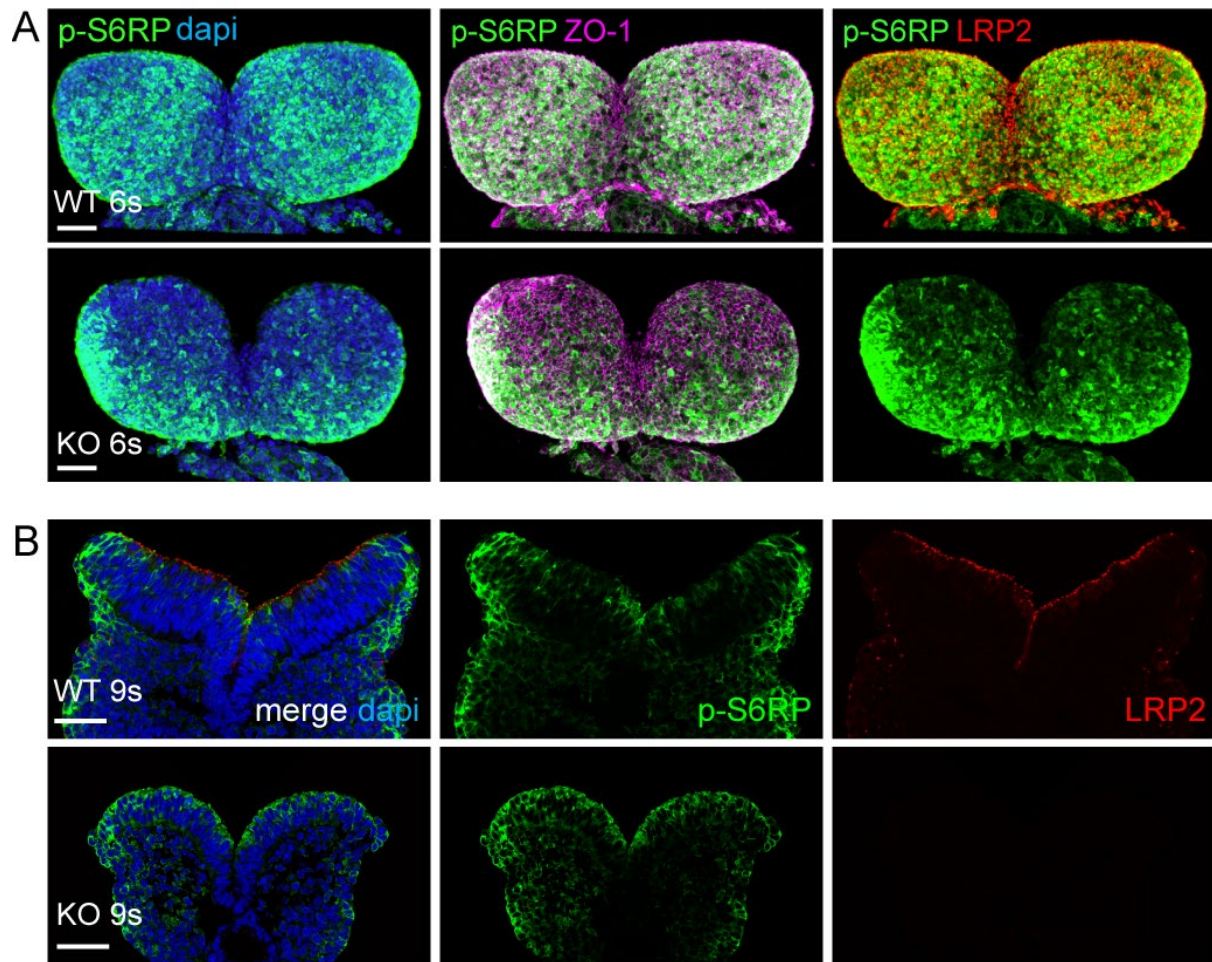
FIGURE 31 MTORC1 PATHWAY IS IMPAIRED IN MUTANT NEUROEPITHELIUM.
(A) Front view of immunofluorescence staining on whole-mount 6 s neural folds (NFs) from wild-type (WT) and *Lrp2*$^{-/-}$ mutant embryos. p-S6RP is detected in large, unconstricted cells which are present at this stage throughout the neuroepithelium. ZO-1 is used to mark cell boundaries. Co-staining with LRP2 indicates regional differences in proteins distribution. **(B)** Coronal sections of 9 s WT and *Lrp2*$^{-/-}$ NFs. p-S6RP is enriched at the elevated dorsolateral domains of controls, as well as along the non-neuronal ectoderm. In contrast, rounded mutant NFs express p-S6RP throughout the entire neuroepithelial surface. Scale bars present 50 μm.

I first looked at the 6 s neural folds (see methods 3.1, 3.4.2) to verify the en face p-S6RP distribution in the neuroepithelium (*FIGURE 31*, A). Larger cells for both mutant and wild-type embryos presented higher p-S6RP expression. At this stage, the neural plate stays flat and cells do not yet constrict intensively, which could explain overall

high activation of mTORC1. Interestingly, the signal in mutants was stronger at the boarders of the neural folds with significantly less signaling at the anterior surface.

Examination of 9 s coronal sections, when dynamic cell shape changes, constriction, and elevation of neural folds occurs in wild types, but not in the mutants, showed that the mutant neuroepithelial cells had more p-S6RP along the entire apical surface. In contrast wild types, presented condensed p-S6RP expression at the dorsal edges and at the boarder of neuronal and non-neuronal cells, but not in the neuroepithelium (FIGURE 31, B). Instead, there was a reversed correlation between high-LRP2 and low-p-S6RP in constricting wild-type neuroepithelium. These observations, in line with previous findings in RGCs and kidney cells, suggested that an enlarged CSA correlates with upregulation of the mTORC1 pathway in the neuroepithelium.

5.2 Impaired apical membrane remodeling in LRP2-deficient neuroepithelium

To further clarify our understanding of later embryonic stages and continuous dilation of the NT within the *Lrp2* mutants, we examined cellular morphology in the E9.5 embryos. Ultra-thin sections imaged on a transmission electron microscope (TEM) were used to quantify these observations (see methods 5.2.1). We found the average cell diameter in the mutants was significantly bigger, and it is consistent for both the ventral and dorsolateral domains of the neural tube FIGURE 32. In addition, we observed unusual bulging of the non-constricting cells in mutant samples, possibly indicating the increased tension from surrounding cells and a simultaneous defect in the plasma membrane remodeling.

Apical constriction is a driving force for tissue bending and folding during morphogenesis. Actomyosin contractility creates a tension on the plasma membrane. In order to change the cell shape, the excess has to be processed. The studies show this membrane can be re-distributed into filamentous protrusions, such as microvilli and spherical blebs, extending above the apical cell surface (Gauthier et al., 2012). The study in *Xenopus* (Lee and Harland, 2010) substantially extended this fact by showing efficient apical constriction requires endocytosis, which helps to remove the redundant, protruding membrane to finalize the constriction, conversely, impaired endocytosis resulted in NTDs.
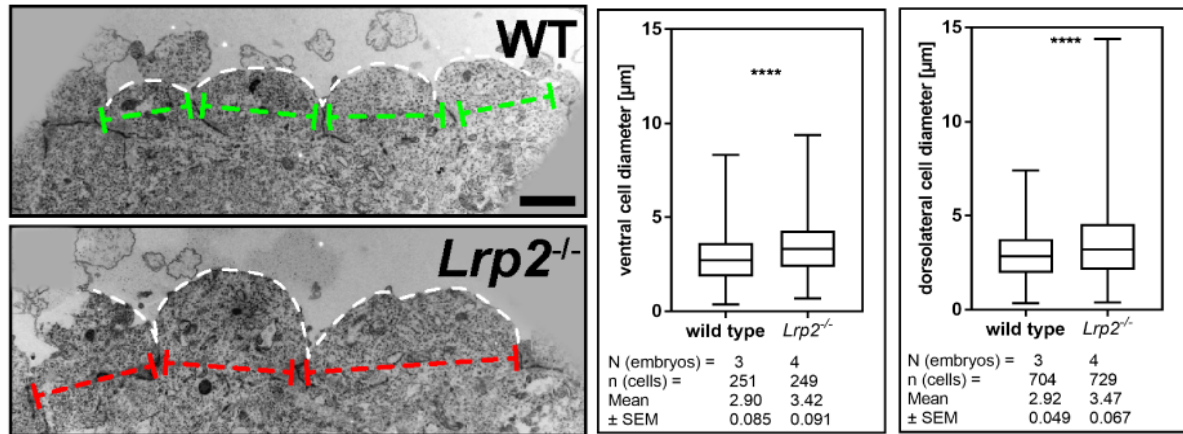
FIGURE 32 INCREASED CELL DIAMETER AND BULDGING OF *LRP2*^{-/-} NEUROEPITHELIAL CELLS. Transmission electron micrographs of E9.5 coronal ultrathin sections. Bulging of unconstricted *Lrp2*^{-/-} cells (red lines), compared to WT neuroepithelial cells with normal apical cell diameters (green lines). Independent quantification of ventral and dorsolateral cell diameters show significantly increased measurements in the mutants compared to WT. Student's *t*-test, **** $p < 0.00001$. Scale bar: 2 µm. Figure modified from (Kowalczyk et al., 2021).

Looking closer at the SEM images and neuroepithelial surfaces of wild types and *Lrp2* mutants (FIGURE 26, FIGURE 33), both presented the filamentous protrusions, suggesting these cells undergo the apical constriction. However, detailed analysis, in line with the above mentioned study from *Xenopus* (Lee and Harland, 2010), allowed us to see that mutant cells (9 s) are not able to retract the protrusions (FIGURE 33, D), in contrast to somite matched wild-type cells. Instead, the protrusions became denser in 9 s cells compared to 7 s cells, reminiscent of impaired endocytosis. The removal of excessive membrane in response to the continuous tension coming from actomyosin contractile forces was presumably impaired (Gauthier et al., 2012).
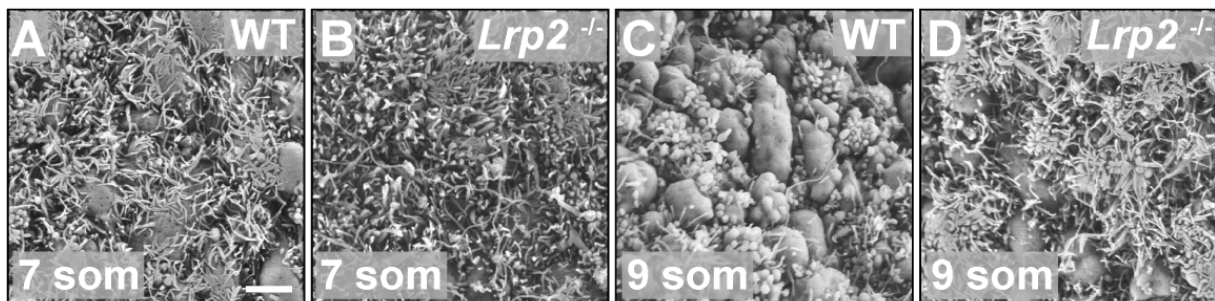
FIGURE 33 DEFECT IN MEMBRANE REMODELING IN LRP2-DEFICIENT NEUROEPITHELIAL CELLS. High magnification of neuroepithelial cell surfaces using SEM. Prominent filamentous protrusions on wild type (WT; A) neuroepithelium at 7 s are reduced in 9 s. In contrast to the LRP2-deficient situation (*Lrp2*^{-/-}; B and D). Scale bars: 2 µm. Figure was adapted from (Kowalczyk et al., 2021).

These data strongly indicated that endocytic receptor LRP2 has an important function in the process of eliminating surplus apical membrane, which is necessary for efficient apical constriction of neuroepithelial cells.

6 LRP2 loss impairs planar cell polarity of the neuroepithelium

Apart from the apical constriction and cell-autonomous shape changes, the neural plate undergoes dynamic cell movements and morphological changes in the tissue plane. Convergent extension (CE) movements play a role in the mediolateral and anteroposterior tissue growth and are necessary for the NTC to occur (see introduction 1.2). These dynamic changes, closure of the neural folds, are controlled by the non-canonical WNT/Planar cell polarity (PCP) pathway (Darken et al., 2002; Sutherland et al., 2020a; Wallingford and Harland, 2002). *Lrp2* mutant neural folds stay round and do not elevate compared to the control (FIGURE 25, FIGURE 27). Thus, we next asked whether the planar cell polarity is affected.

6.1 Subcellular localization of VANGL2 is impaired in *Lrp2* mutants

Vang-like protein 2 (VANGL2) is a core component of the PCP pathway and is known to be a regulator of apical constriction during *Xenopus* gastrulation and in NTC (Ossipova et al., 2014, 2015a). However, until now, function and distribution of VANGL2 in NTC was studied specifically in the more posterior NT (Ossipova et al., 2015b).

Immunofluorescence (see methods 3.4.1) on anterior neural folds presented VANGL2 in the apical neuroepithelium, for both wild-type and mutant embryos FIGURE 34. At 9 somites wild-type embryos VANGL2 was localized mainly to the apical plasma membrane, strikingly, with a prominent localization to the apical LRP2 (FIGURE 34, A'$_1$ and A'$_3$). These apical VANGL2/LRP2 signals clustered within RAB11-positive recycling endosomes (FIGURE 34, A'$_2$), reminiscent of apical accumulation of VANGL2 – RAB11 in the constricting *Xenopus* neuroepithelial cells (Ossipova et al., 2014). In contrast to wild types, *Lrp2* mutant neuroepithelium showed very extensive vesicular VANGL2 staining, mainly localized to the basolateral membrane (FIGURE 34, B'$_3$). Despite RAB11 still being present at the apical membrane (FIGURE 34, B'$_2$), LRP2

deletion clearly affected VANGL2 recruitment to the recycling endosomes, suggesting that, at least in context of anterior NP, LRP2 is required for the RAB11-dependent trafficking of VANGL2.
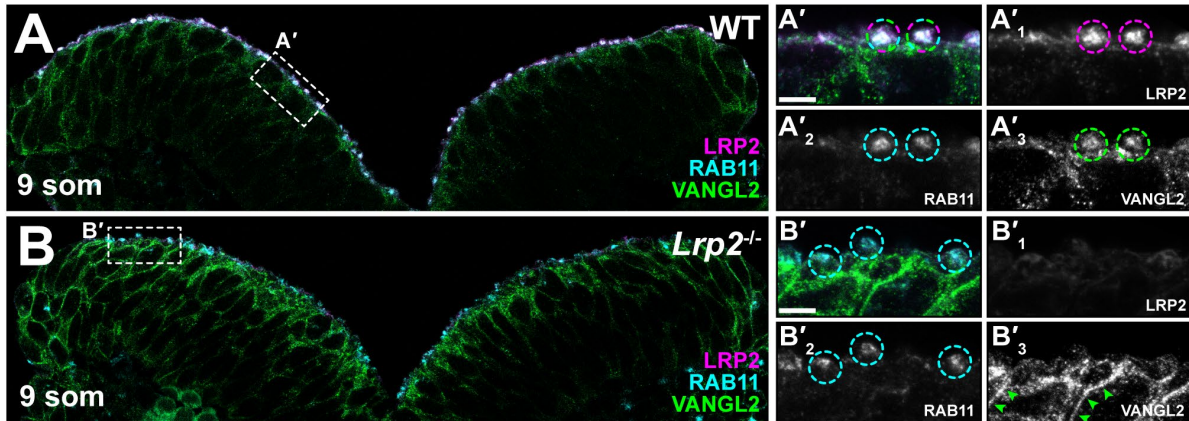
FIGURE 34 LRP2 REGULATES SUBCELLULAR LOCALIZATION OF VANGL2.
Immunofluorescence examination of VANGL2 distribution on coronal sections of 9 s wild-type (WT) and *Lrp2*^{-/-} neural folds. Magnifications from boxed areas (**A'**[1-3] and **B'**[1-3]) present single channels. Apical co-localization (dashed circles) of LRP2 and VANGL2 in RAB11-positive recycling endosomes in WT (**A**, **A'**) compared with absence of VANGL2 from RAB11-positive compartments in *Lrp2*^{-/-} cells (**B**, **B'**). VANGL2 localizes to basolateral membrane of mutant neuroepithelium (arrowheads in **B'**[3]). Scale bars present 5 µm. Figure modified from (Kowalczyk et al., 2021).

6.2 Subcellular CELSR1 distribution is not dependent on recycling endosomes

Intrigued by emerging LRP2 function in the proper apico-basal distribution of the PCP components during anterior neural folds morphogenesis and maintenance of the planar polarity of the neuroepithelium, I next asked whether other core components of PCP also are mislocalized in the LRP2-deficient neural plate. Cadherin EGF LAG seven-pass G-type receptor 1 (CELSR1), known PCP-regulating cadherin, was linked to the severe NTDs in human and mouse (Curtin et al., 2003; Lei et al., 2014). It is recruited to the adherens junctions (AJs) at the mediolateral (ML) axis of NP and was shown to contribute to the folding of the NP by integrating the PCP signals and contraction of actomyosin at the cellular edges associated with these AJs, consequentially leading to CE and bending of the tissue plane (Nishimura et al., 2012).

Interestingly, *Celsr1* is upregulated in *Lrp2* mutant embryos (RNAseq, data not shown), so I examined the protein distribution analogically as VANGL2. In 8 and 11 somites

wild-type and mutant embryos, CELSR1 was present along the NP, however, it did not show a clear distribution to the RAB11-positive vesicles FIGURE 35. Nevertheless, its expression was always next to these domains, along the basolateral membrane. As long as at the 8 somites stage there was no clear difference between the genotypes, at 11 somites, there was a pronounced increase in the CELSR1 signal at the apical junctions of mutant neuroepithelium FIGURE 35. This suggests there may be a compensatory function coming from the CELSR1, either for VANGL2 recruitment to cell-cell contacts (Lei et al., 2014) in order to maintain balance between PCP effectors, or forcing the mediolateral CE, while the cell-autonomous apical constriction and hinge point formation is perturbed.
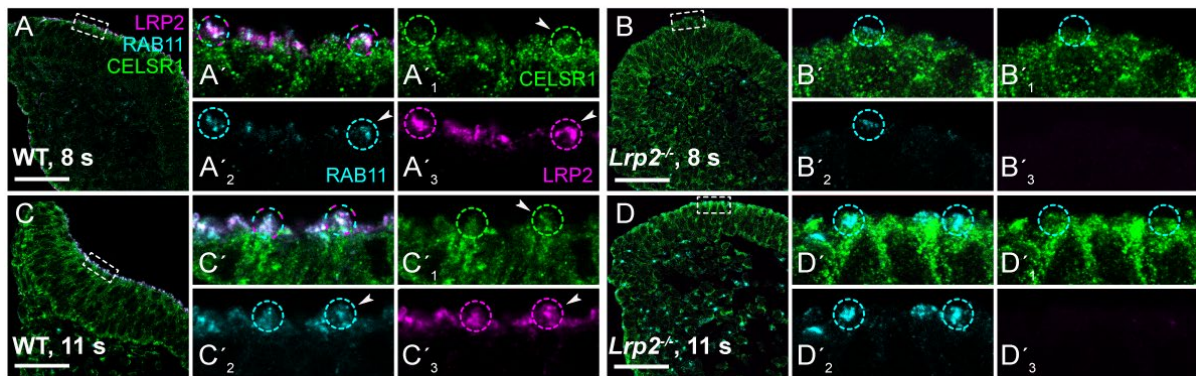
FIGURE 35 CELSR1 ACCUMULATION AT THE LATERAL MEMBRANE OF *LRP2* MUTANT CELLS. Immunofluorescence examination of CELSR1 distribution on coronal sections of 8 and 11 s wild-type (WT) and *Lrp2$^{-/-}$* neural folds. Magnifications from boxed areas (**A'$_{1-3}$** to **D'$_{1-3}$**) present single channels. Apical LRP2/RAB11 recycling endosomes (dashed circles) do not recruit CELSR1 in WT (**A**, **A'** and **C, C',** arrowheads). CELSR1 accumulates at the cell junctions of 11 s *Lrp2$^{-/-}$* cells (**D, D'**) compared to somite-matched WT (**C, C'**). Scale bars present 50 μm.

7 LRP2 mediates cell shape changes through intracellular adaptors

Endocytosis and efficient recycling of transmembrane receptors is tightly regulated in order to maintain cellular homeostasis. It is achieved by various adaptor proteins, which recognize their target receptors, and direct the endocytic vesicles along the intracellular scaffold (Liu and Fuentes, 2019).

LRP2 C-terminus harbors two PDZ-binding domains (PBD), which bind to a diverse set of intracellular adaptor scaffold proteins in highly absorptive tissues (see introduction 3.1.2) (Gotthardt et al., 2000; Marzolo and Farfán, 2011). However, this phenomenon has not been studied in context of neural tube formation and possible maintenance of tissue integrity. Taking into consideration all above discussed data, two promising hypotheses about new, distinct LRP2 functions emerged. Firstly, LRP2, as a highly endocytic receptor, performs intensive ligand-triggered endocytosis, internalizing morphogens, and other factors, which are necessary for neural tube development. Simultaneously, LRP2 participates in the removal of excessive plasma membrane, facilitating the constriction of the cells. Secondly, we could consider ligand independent function of the receptor, in which it serves as a component of a scaffolding complex, and, together with adaptor proteins, contributes to the cytoskeletal rearrangements and maintenance of neuroepithelial integrity. In order to verify these possibilities, we examined the role of two adaptor proteins that are known to be scaffolding partners for LRP2 in context of renal absorption: GIPC1 (Gotthardt et al., 2000; Naccache et al., 2006) and NHERF1 (Slattery et al., 2011). However, their role in the process of neurulation has been never investigated before.

NHERF1 contains two PDZ domains at the N-terminus, which allow for recognition of target receptors and C-terminal ezrin-radixin-moesin– (ERM) binding domain for actin cytoskeleton tethering (Treat et al., 2016; Weinman et al., 1998). It has been well characterized in the mammalian kidney, where it regulates endocytosis and ion transport (Shenolikar et al., 2002). Importantly, it was shown to directly bind to the proximal PDZ binding motif of LRP2, during albumin internalization in the proximal tubule cells (Slattery et al., 2011). Apart from the renal dysfunctions, studies in mouse and zebrafish additionally presented a hydrocephaly phenotype, with impaired organisation of ependymal motile cilia (Shenolikar et al., 2002; Treat et al., 2016). *Treat*

et al. analysed the underlying mechanism and showed NHERF1 acts as a promoting factor for the formation of Fzd4-VANGL2 complex, which enables efficient targeting of VANGL2 to the apical surface of ependymal cells. This was a novel function of NHERF1 in the PCP signaling (Treat et al., 2016). Following on these data, we asked whether NHERF1 could be a potential functional partner for LRP2 in the context of neural tube formation.

Indeed, immunohistochemistry on wild type 9 s coronal sections (see methods 3.4.1) detected NHERF1 at the apical surface of neuroepithelium, perfectly resembling the LRP2 expression pattern FIGURE 36. Strikingly, NHERF1 was completely lost in the *Lrp2* null mutant samples, indicating a direct interaction between LRP2 and NHERF1 in the neuroepithelium. This unveiled a new potential function of NHERF1/LRP2 scaffolding complex, responsible for the efficient endocytosis and establishment of apico-basal polarity, in consequence regulating NTC.
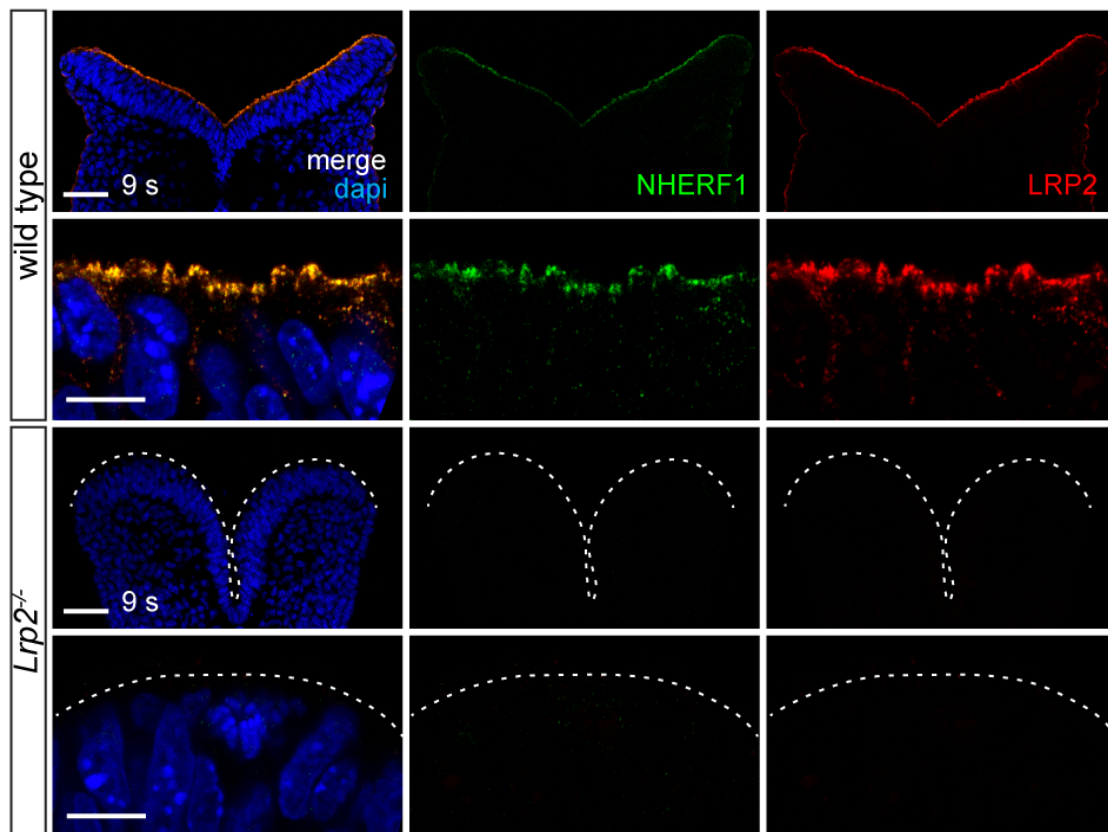
FIGURE 36 NHERF1 IS ABSENT FROM THE LRP2-DEFICIENT NEUROEPITHELIUM. Immunofluorescence on coronal sections of 9 s wild types reveals co-localization of LRP2 and adaptor protein NHERF1 in the neuroepithelium. In contrast, *Lrp2⁻/⁻* mutants lose both LRP2 and NHERF1 expression from the neural folds (delineated with dashed line). Merge, single channels and magnified images are presented; scale bars show 50 µm and 10 µm, respectively.

GIPC1 contains one, middle PDZ domain surrounded by a myosin VI (Myo6) binding domain at the C-terminus and N-terminal dimerizing region. Such composition allows GIPC1 to serve as a transporter of PDZ proteins in an actin-dependent manner (Aschenbrenner et al., 2003; Naccache et al., 2006; Reed et al., 2005; Shang et al., 2021). Importantly, GIPC1-cargo represents only endocytic trafficking, since Myo6 is a unique actin-based motor moving only from the actin-rich cell peripheries towards minus ends, oriented into the cell body (Wells et al., 1999).

GIPC1 functions during *Xenopus* gastrulation, where it is responsible for internalization of integrins and fibronectin assembly (Spicer et al., 2010). It binds with a distal PBD of LRP2 (see introduction 3.1.2), and the function of the complex has been examined in renal proximal tubules, where lack of the adaptor leads to proteinuria in mouse, mirroring the impaired trafficking of LRP2-mediated endocytosis (Gotthardt et al., 2000; Naccache et al., 2006). Additionally, GIPC1 is responsible for the trafficking of VANGL2 in the sensory epithelium of inner ear, and disruption of the cargo leads to defects in PCP signaling and maturation of the hair cells (Giese et al., 2012). These diverse, context-dependent functions of GIPC1 in cellular trafficking and direct binding with LRP2, prompted us to examine its localisation in neuroepithelium.

GIPC1 was expressed in the E8.5 mouse neuroepithelium and was localized mainly to the apical surface, sometimes overlapping with LRP2 FIGURE 37. In case of wild-type neural folds, progressive elevation of the dorsolateral domains was accompanied by increasing GIPC1 signals, also penetrating the cells in the apico-basal axis, leaving the highly constricted cells around the midline with less protein. This gradient localization of GIPC1 was not observed in the mutant neural folds, where apical expression was present along the entire neuroepithelium, and in the non-neuronal ectoderm.
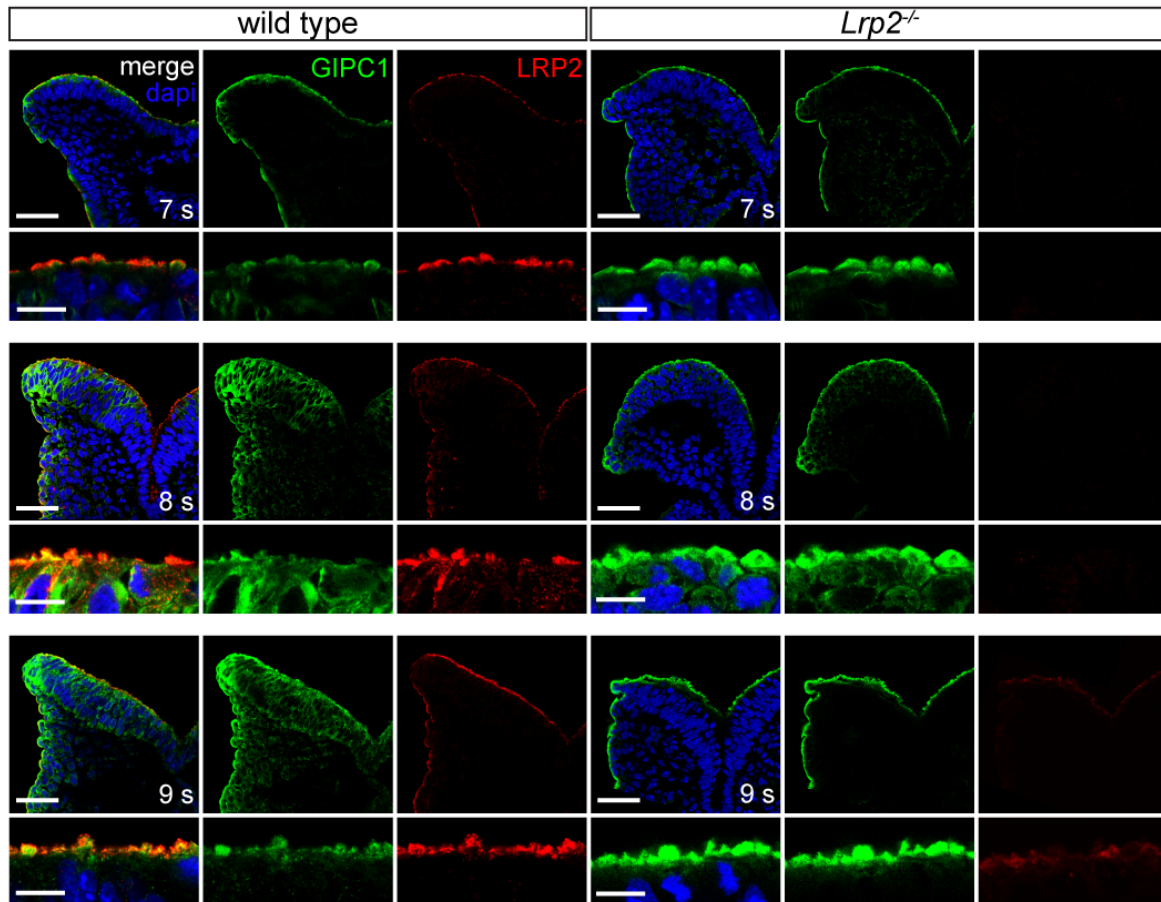
FIGURE 37 LRP2 ADAPTOR PROTEIN GIPC1 IS PRESENT IN THE NEUROEPITHELIUM.
Immunofluorescence examination of GIPC1 distribution on coronal sections of wild-type (WT) and *Lrp2^-/-* neural folds from 7 – 8 s embryos. GIPC1 is present in the neuroepithelium and partially localizes together with LRP2 (8, 9 s). Expression pattern exhibits stronger dorsolateral signal in the elevated WT neural folds, in contrast to unified expression along the LRP2-deficient neuroepithelium. Overall GIPC1 signal is stronger in mutant cells. Merge, single channels and magnified images are presented; scale bars show 50 µm and 10 µm, respectively.

Strikingly, GIPC1 expression seemed to be inversely correlated with the LRP2 expression which was highly enriched in the constricting regions. This was also observed in the whole mount immunostaining, at 7 s (see methods 3.4.2) FIGURE 38. However, there were single GIPC1-negative cells in 5 - 7 s wild-types that also had low LRP2 accumulation and were larger. Expression of GIPC1 in LRP2-deficient neuroepithelium appeared to be stronger overall, from one side more equally distributed, but on the other hand with more cells having low GIPC1 signal on the surface.
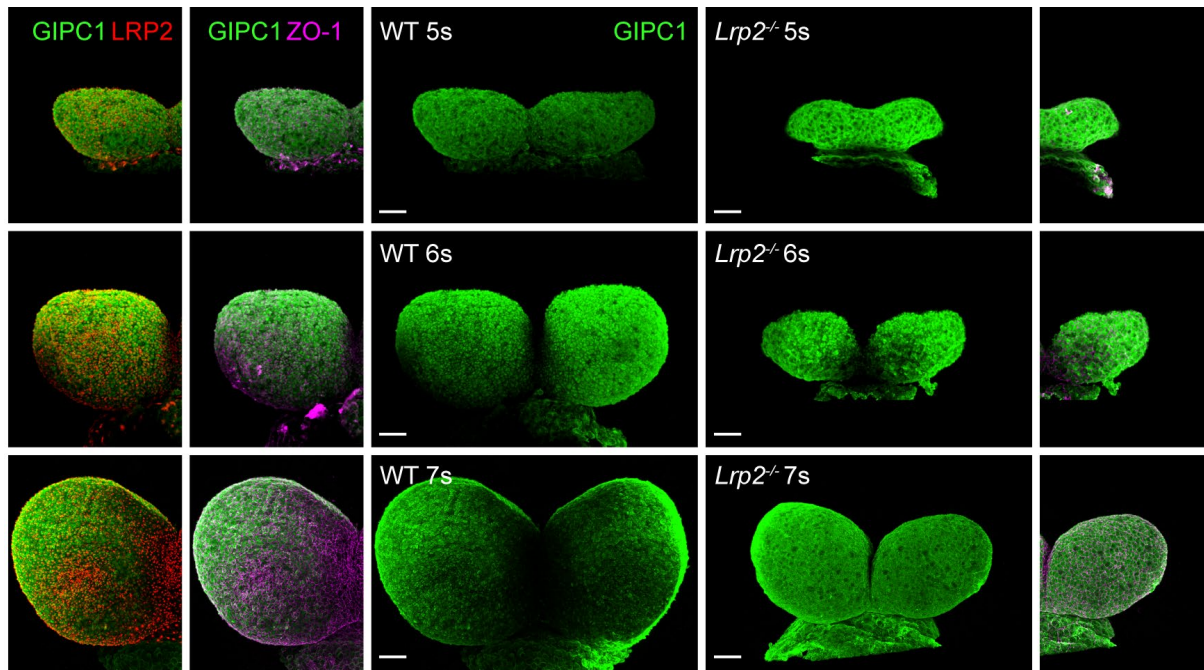
FIGURE 38 LRP2 MEDIATES APICAL CONSTRICTION THROUGH ADAPTOR PROTEIN GIPC1.
Whole-mount immunofluorescence on wild type (WT) and *Lrp2^-/-* mutant mouse neural folds at E8.5 (5 – 7 s), frontal views. Staining reveals differential enrichment of GIPC1 and LRP2 between constricted (optic evagination) and large cells (7 s). In contrast, homogenous GIPC1 expression is present within LRP2-deficient neuroepithelium. ZO-1 delineates cell borders. Scale bars present 50 μm.

To summarize, I demonstrated, for the first time, two adaptor proteins and known binding partners for LRP2 are present in the developing mouse neural folds, and their localization in the LRP2-deficient neuroepithelium is altered. These data suggest that LRP2 requires scaffolding partners to mediate its function in the maintenance of apico-basal polarity of the neuroepithelium, membrane remodeling via endocytosis, and in consequential apical constriction. All these processes have to be tightly regulated in spatiotemporal manner in order to allow for proper neural tube formation.

8 LRP2 is required for the cranial neural crest stem cell niche

Concomitantly with neurulation, a new population of cells emerge, vastly contributing to the development of the head. Neural crest cells (NCC) are transient, multipotent cells arising from the embryonic neuroepithelium with various patterns across the vertebrate species. They are induced at the neural plate border and undergo epithelial-to-mesenchymal transition (EMT), which facilitates the delamination from neighboring neuroepithelial cells and acquiring the migratory properties (Pla and Monsoro-Burq, 2018; Theveneau and Mayor, 2012a). For mammals, as well as *Xenopus,* delamination occurs before NTC from the lateral edges of neural folds. This contrasts with birds where it occurs after NTC is accomplished (Aybar and Mayor, 2002; Noden, 1975; Theveneau and Mayor, 2012a). Mouse neural crest EMT starts around 3-4 somites at the midbrain-hindbrain boundary, and cranial neural crest cells (CNCC) delaminate at 5-6 somites in a collective stream of cells (Nichols, 1981, 1987; Theveneau and Mayor, 2012a).

Despite the differences, NCC maturation is characterized by many common features. It requires extensive rearrangement of cytoskeleton, cell-cell and cell-matrix contacts, including loss of apico-basal polarity and high affinity tight- and adherens junctions in order to migrate and colonize the designated regions of the body (Ahlstrom and Erickson, 2009; Coles et al., 2006; Kalev-Altman et al., 2020; Theveneau and Mayor, 2012a). These changes are tightly controlled by environmental factors, gene regulatory networks, and various signaling pathways in order to fulfill the correct specification and final differentiation into broad spectrum of derivatives (Prasad et al., 2019; Sauka-Spengler and Bronner-Fraser, 2008).

Among three main populations: cranial, cardiac, trunk, the cranial neural crest cells emerge the earliest from the anterior neural folds and give rise to the most diverse derivatives – from ectodermal origin peripheral nerves to mesenchymal type skeletal bone, dentin, cartilage and smooth muscle. (Ishii et al., 2012; Santagati and Rijli, 2003) Additionally, studies in chicken neurulation and NCC have shown cephalic NCC are not only required for the craniofacial development, but also contribute to the correct FGF8 signaling at the ANR and NTC, and thusly to the proper forebrain and midbrain structures. After the depletion of early CNCC, NT closure failure and the exencephaly was observed (Creuzet, 2009; Creuzet et al., 2006; Etchevers et al., 1999).

Despite obvious craniofacial abnormalities present in *Lrp2* mutant mice (Willnow et al., 1996) (see introduction 4.3; FIGURE 8) as well as in humans (Kantarci et al., 2008), the potential mechanism of LRP2 in the NCC had not hitherto been investigated.

8.1 LRP2 is expressed in delaminating neural crest cells

Few studies over past years provided an indirect evidence that LRP2 is present in the neural crest cells of developing rats and mice (Assémat et al., 2005; Baardman et al., 2016). Additional contribution to the topic came from the Kozyraki group with the study on cubilin (Cubn), a multiligant endocytic receptor commonly spatially and functionally accompanied by LRP2 in developing epithelia. They demonstrated both Cubn and LRP2 co-express in the Tfap2α-positive CNCCs of E9.0 mouse embryo (Cases et al., 2013).

Transcription factor activation protein 2α (Tfap2α or AP-2α) is a retinoic acid-inducible transcription factor critical for the craniofacial development. It is expressed in the cranial NCC, and mice deficient for AP-2α die perinatally with severe craniofacial defects, anencephaly, and abdominoschisis (Schorle et al., 1996; Zhang et al., 1996). In humans mutations in *TFAP2A* are related to the developmental Branchio-oculo-facial syndrome (BOFS) (Milunsky et al., 2008; Min et al., 2020).

In order to verify the expression of LRP2 in early NCC, I performed immunohistochemistry on coronal sections of 6 s embryos for both genotypes (see methods 3.4.1). This is the stage when the cells delaminate and start migrating in mouse (Nichols, 1987; Theveneau and Mayor, 2012a). For both wild-type and mutant embryos, AP-2α-positive CNCC were present at the dorsal neural folds (FIGURE 39, a, b). Importantly, I demonstrated LRP2 is expressed in delaminating cranial NC cells (FIGURE 39, a') and in cells which already started to migrate. This result opened a possibility for another intriguing function of the LRP2 receptor and additionally expanded the range of cell types that may be regulated by the LRP2 in development to population of cranial neural crest cells.
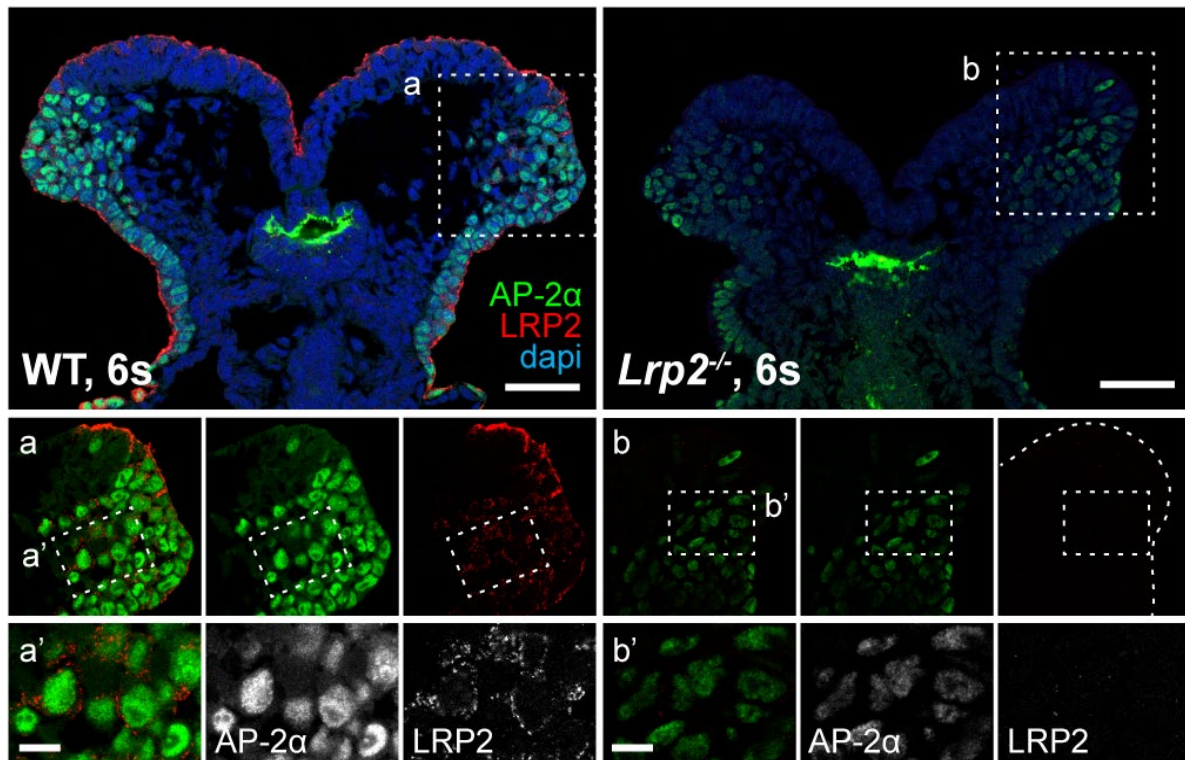
FIGURE 39 LRP2 IS PRESENT IN THE DELAMINATING CRANIAL NEURAL CREST CELLS.
Immunofluorescence on coronal sections from wild-type (WT) and *Lrp2*^{-/-} mutant embryos at
6 somites. LRP2 is expressed in the AP-2α-positive delaminating cranial neural crest cells
(CNCC) in the dorsolateral region of WT neural folds (**a**, **a'**; dashed-line boxes). Indicated
insets (dashed-line boxes) are presented in single channels (**a, b**) and grayscale (**a', b'**). Scale
bars show 50 μm and 10 μm (**a', b'**).

Analysis of consecutive somite stages in order to examine whether there are any
abnormalities in the early NCC population in the *Lrp2* mutant embryos resulted in
interesting observations. Firstly, a stream of migrating NCC was drastically expanded
in the LRP2-deficient neural folds at 8 s FIGURE 40, especially when the size difference
is taken into consideration (matching somite mutant neural folds are usually slightly
smaller). Strikingly, only in the case of mutant embryos we additionally observed
AP-2α-positive cells within the neuroepithelium (FIGURE 40, a', b', arrowheads). Taking
into account that cranial NC population of cells delaminates and moves away from
dorsal neural folds in a collective migratory stream, along the rostro-caudal body axis
towards the trunk (Theveneau and Mayor, 2011, 2012a), it was unexpected to see
NCCs in the neuroepithelium. Whether NCCs in *Lrp2* mutants receive wrong cues and
migrate in wrong direction, or the neuroepithelial cells acquire neural crest
characteristics, awaits further investigation; however, the environment depleted of
LRP2 clearly impairs early CNCC population.
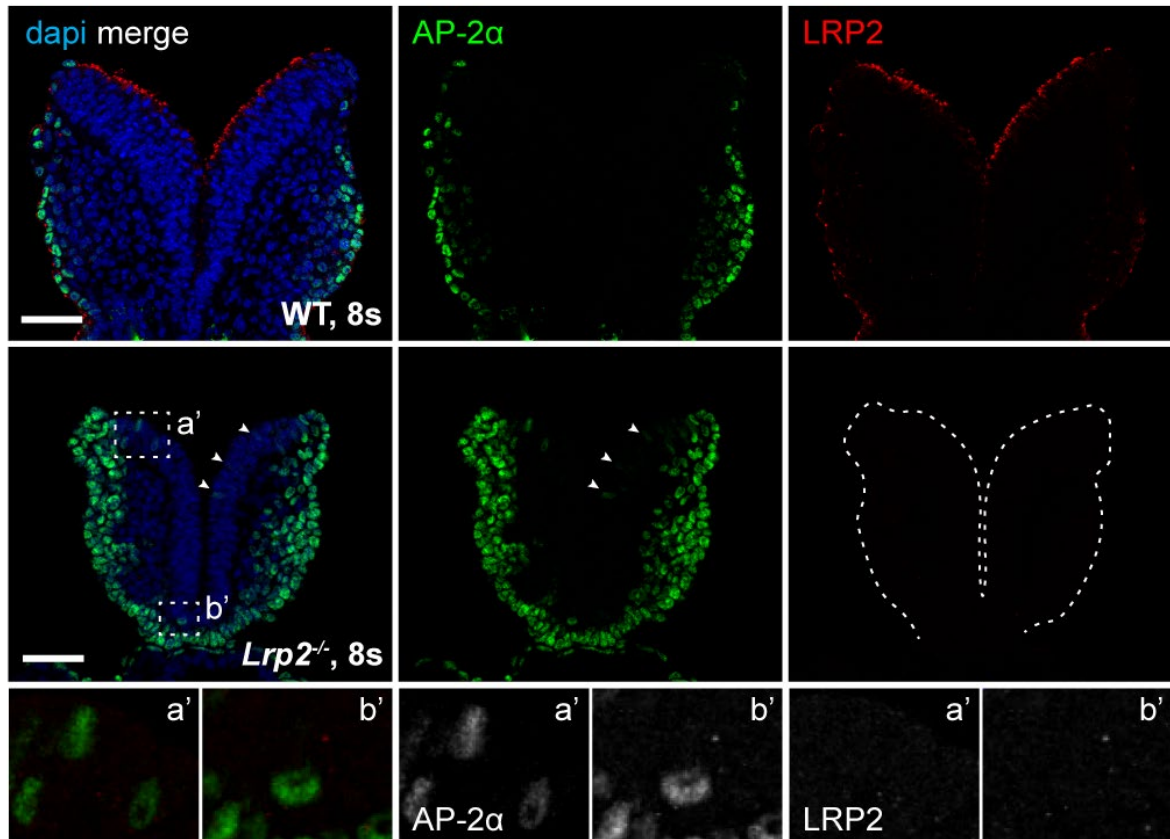
FIGURE 40 ABNORMAL NEURAL CREST CELLS PRESENT WITHIN *LRP2⁻ᐟ⁻* NEUROEPITHELIUM. Immunofluorescence examination of neural crest cells (NCC) on coronal sections from embryos at 8 somites. *Lrp2⁻ᐟ⁻* mutants present an expanded population of migrating AP-2α-positive NCC comparing to WT NCC. Additionally, aberrant AP-2α-positive cells are found within LRP2-deficient neuroepithelium (dashed line boxes and arrowheads). Single channels of magnified insets (**a'**, **b'**) are shown in grayscale. Scale bars present 50 μm.

Intriguingly, there was an interesting *in vitro* study on chicken neural tube explants in which the authors observed increased NCC outgrowth and migration after stimulation with homocysteine, recapitulating a low folate environment during pregnancy (Boot et al., 2003). Knowing both LRP2 is important for the folate uptake in the neuroepithelium (Kur et al., 2014) (see introduction 4.2.1) and it is expressed in NCC FIGURE 39, we preliminarily hypothesized this function may also influence the cranial NCC population.

8.2 Implications for aberrant migration of cranial NCC in *Lrp2* mutants

RNA deep sequencing data from C57BL/6N *Lrp2⁻ᐟ⁻* and *Lrp2⁺ᐟ⁺* samples (see introduction 5.1) again was a valuable source of deregulated genes, specifically in the context of neural crest TABLE 12. Severe craniofacial phenotypes of mutant embryos had a strong reflection at the transcriptomic level. Apart from upregulated *Tfap2α*, the most differentially expressed gene out of this population was *SRY-Box Transcription Factor 10* (*Sox10*) FIGURE 41.
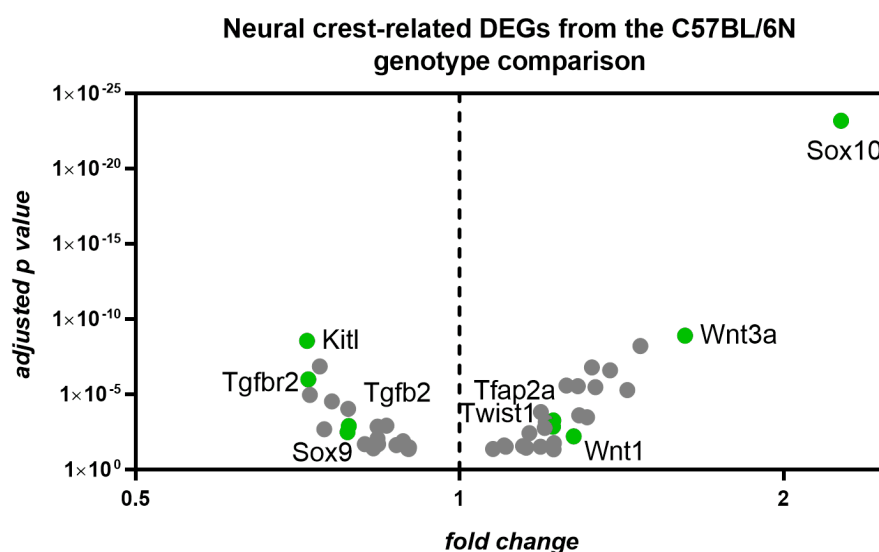
FIGURE 41 NEURAL CREST-RELATED DEGs FROM RNAseq ANALYSIS ON C57BL/6N.
Volcano plot presents DEGs for *Lrp2⁻ᐟ⁻* and *Lrp2⁺ᐟ⁺* C57BL/6N embryonic head samples which are related to neural crest (NC). The highest regulated gene is *Sox10.* Labels are provided for the genes indicated in green. The list of all the genes is attached as TABLE 12.

The SoxE transcription factor family (Sox8, Sox9, Sox10) is essential for development of NC population. Their expression at the neural plate boarder coincides with the NC induction, and Sox9 and Sox10 label the early cranial NCCs that migrate towards the pharyngeal arches. While both TFs initially maintain the multipotency of NCC, they, later during migration contribute to differentiation. Additionally, Sox9 can act as a *Sox10* activator (Aoki et al., 2003; Betancur et al., 2010; Cheng et al., 2000; Prasad et al., 2019).

SOX10 and SOX9 are also determinants of early NCC in humans (Betters et al., 2010), confirming the conserved pattern of these core NC markers, which allowed us to extrapolate from animal models to humans.
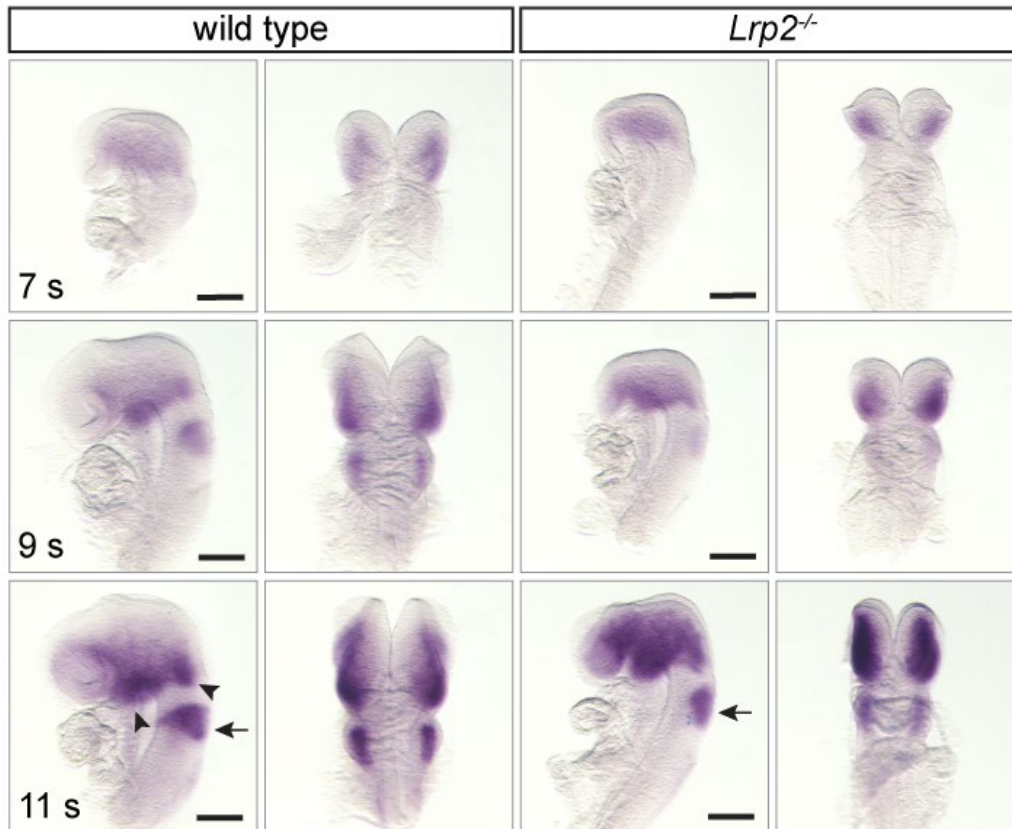
FIGURE 42 NEURAL CREST CELLS ACCUMULATE IN THE MUTANT TELENCEPHALON.
Whole-mount *in situ* hybridisation (WISH) for *Sox10* in the E8.5 wild-type (WT) and *Lrp2*-/-
mutant embryos at 7, 9, and 11 somites with lateral and posterior views. The *Sox10*-positive
migratory population of NCCs shows aberrant colonization of the embryonic domains, which
is prominently manifested at 11 s. In mutant embryos, *Sox10*-positive cells accumulate in the
telencephalic vesicle rather than into condensed domains at the 1st pharyngeal arch
(arrowheads) and rhombencephalon (arrows) as shown in WT. Scale bars present 200 µm.

Following this intriguing *Sox10* upregulation in E9.5 *Lrp2*-/- mutant embryos, we asked

whether significant transcriptomic changes already manifested at E8.5 embryos.

I performed a whole mount *in situ* hybridization (WISH; see methods 3.8.3) at different

somite stages for both genotypes in order to examine the early wave of migrating NCC

FIGURE 42. For 7 s, wild type and mutant *Sox10*-positive cells occupied the

telencephalic region of lateral neural folds with similar patterns, despite known

morphological differences of the neural folds (see FIGURE 25). Between 7 and 9 s, there

was a dynamic change in the NCC location – in wild type they condensed into the first

pharyngeal arch and colonized the rhombencephalon, which became even more

prominent for the 11 s embryos (FIGURE 42, arrowheads and arrow, respectively).

The matching somite mutant embryos exhibited a visible delay for the NCC to occupy the rhombencephalon (FIGURE 42, arrow). Instead, the entire prosencephalon and mesencephalon was *Sox10*-positive, without any domains emerging. The examination of early cranial NCC across 7 – 11 s indicated a progressive, aberrant migration pattern in the LRP2-deficient embryos. Additionally, there was an overall increase in NCC in the mutant forebrain region, which could consequentially contribute to the *Sox10* accumulation at the transcriptional level at E9.5 FIGURE 41.
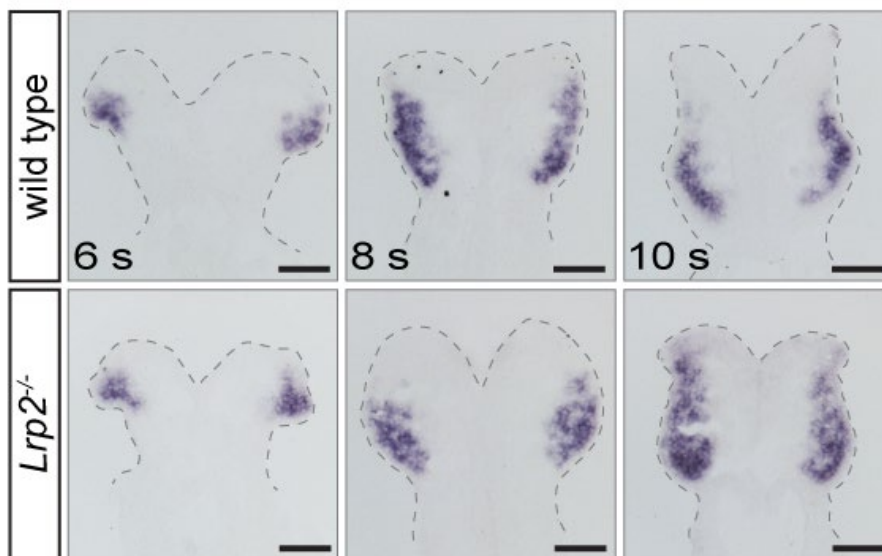
FIGURE 43 NCC POPULATION IS EXPANDED AND MISORIENTED IN *LRP2⁻/⁻* MUTANT EMBRYOS. *Sox10 in situ* hybridisation (ISH) on coronal sections from E8.5 wild-type (WT) and *Lrp2⁻/⁻* mutant embryos at 6, 8, and 10 somites. NCCs in mutant neural folds migrate in a less restricted stream (8, 10 s) comparing to WT, and they accumulate dorsally, incorrectly reaching towards the neuroepithelium (10 s). Dashed-lines delineate embryonic neural folds, underlying morphological differences between the somite-matched embryos. Scale bars present 75 µm.

In order to further evaluate the population of early CNCCs, I performed *Sox10* ISH on coronal sections across 6 – 10 s (see methods 3.8.2). Analogically to the AP-2α labelled CNCC at the 6 s coronal sections FIGURE 43, *Sox10*-positive cells were present at the dorsolateral aspects of neural folds FIGURE 43. Following the elevation of the neural folds in wild types, the migratory stream of cells at 8 – 10 s was directed caudally. In contrast, the population of mutant NCC seemed to accumulate rostrally, with a prominent signal at the neural plate border of 10 s embryos. This result supported the observations from the 11 s WISH FIGURE 42, where Sox10-positive cells clearly accumulated at the forebrain/midbrain region instead of migrating caudally.

Moreover, an overall widened migratory stream of cells recapitulated the AP-2α IHC on 8 s embryos.

Summarizing the characterization of the early CNCC population, we have clear evidence suggesting LRP2-deficient mouse embryos exhibit visible anomalies already at the initial developmental stage. Impaired migration and/or altered colonization of the specific domains may lead to misspecification of the NCC and importantly, this seems to be the origin of the future craniofacial defects observed in LRP2- deficient mice and humans.

Many genetic and cellular regulatory cues contribute to proper NCC development and migration (Prasad et al., 2019; Sauka-Spengler and Bronner-Fraser, 2008; Theveneau and Mayor, 2012b). Interestingly, an expanded stream of NCC was observed in the *laminin α5* mouse mutants, supporting the importance of the extracellular matrix (ECM) environment, which can specify the precise path of migratory stream of cells (Coles et al., 2006). Moreover, folate homeostasis is critical for the neural tube closure and appears to have a broader impact on NCC development, shown to increase *in vitro* at the expense of neuroepithelial cells (Boot et al., 2003).

Detailed analysis of LRP2-related phenotypes and their origin, unravel broader than expected function of this endocytic receptor in early embryonic development. The link between neuroepithelial integrity during neural tube closure and proper development and migration of neural crest cells, and how these processes are coordinated in order to build the vertebrate head, remains unknown. Interestingly, relying on above results, there is growing evidence suggesting that LRP2 plays an important role in the coordination of these embryonic stem cell niches. We hypothesize LRP2 facilitates the crosstalk between the signaling pathways which internalize the signaling factors, with the intracellular scaffolding complexes which contribute to the dynamic cell rearrangements during neurulation, and potentially cell migration.

VI. DISCUSSION

For many years, LRP2 has been recognized as a crucial component of the signaling pathways in the embryonic development. *Lrp2* loss of function mutations lead to severe forebrain development accompanied by craniofacial malformations (Christ et al., 2012; Spoelgen et al., 2005; Willnow et al., 1996), neural tube closure defects (Kur et al., 2014; Sabatino et al., 2017), and heart outflow tract anomalies (Baardman et al., 2016; Christ et al., 2020; Li et al., 2015). Importantly, mouse embryonic studies have their reflection in the human patients, where LRP2 has been listed as genetic risk factor for Donnai-Barrow syndrome, characterized amongst other symptoms by brain and craniofacial defects (Kantarci et al., 2007; Ozdemir et al., 2019; Pober et al., 2009). Furthermore, LRP2 was reported in clinical cases of holoprosencephaly (Kim et al., 2019; Rosenfeld et al., 2010), neural tube closure defects (Prasoona K. et al., 2018; Renard et al., 2019) and congenital heart defects (Theis et al., 2020).

Next to the environmental factors, genetic background strongly accounts for the spectrum of severity in congenital diseases in mouse models. A growing number of studies, including ours, present phenotype severity and penetrance dependent on the mouse genetic background (Gajera et al., 2010; Kooistra et al., 2011; Mecklenburg et al., 2020). The contribution of background dependent modifier genes is highly understudied, however, it could shed light on the variability in human disease (Leduc et al., 2017).

Our lab has shown that LRP2-dependent congenital brain and heart defects strongly manifest on C57BL/6N mouse background, but not on FVB/N background (Mecklenburg et al., 2020). My work focused on the brain defects, holoprosencephaly (HPE) and neural tube closure defects (NTDs), occurring in LRP2-deficient mice. I elucidated various mechanisms, which contribute to these distinct phenotypes in LRP2-deficient mice. First of all, I show that SHH-dependent development of the ventral midline can be highly modified by LRP2-independent mechanisms with new players in SHH- and primary cilia-biology, that are potential modulators of HPE penetrance. In addition, I characterised a novel, conserved function of LRP2 underlying the process of dorsal neural tube closure. Endocytic activity of LRP2 facilitates the

cytoskeletal remodelling of neuroepithelial cells and thus contributes to biomechanical changes during folding of the neural plate.

1 Novel, strain specific SHH signaling components capable to modulate cellular signaling capacity in the ventral midline

A fully penetrant HPE phenotype of *Lrp2* mutant mice on a C57BL/6N background is rescued on the FVB/N background F<small>IGURE</small> *8*, together with the causative insufficient SHH signaling in the ventral midline of the developing forebrain (Mecklenburg et al., 2020). Transcriptome analysis identified strain dependent changes in gene expression comparing the wild-type and mutant mice between C57BL/6N and FVB/N strains, including the F1 generation. These sets of genes serve as a valuable source of potential disease-relevant candidate modifier genes.

Functional *in vitro* examination of top DEGs from unbiased transcriptome analysis F<small>IGURE</small> *10* unraveled new, promising genetic players in the SHH biology and further in the understanding of complex modulation of disease penetrance. Intriguingly, the highest upregulated genes, *Ulk4* and *Pttg1*, listed for both wild-type and *Lrp2* mutant strain transcriptome comparisons, exhibited positive regulatory functions on the canonical SHH signaling *in vitro.* Importantly, to our knowledge, none of the genes have been associated with the SHH pathway before. However, *Ulk4* was shown to play a role in brain development and ciliogenesis in ependymal cells (Liu et al., 2016a). *Pttg1* expression was documented during murine and human brain development as well (Boelaert et al., 2003; Tarabykin et al., 2000), although its detailed function was never studied in this context previously. Instead, PTTG1 has been well documented within mitosis, where it inhibits separase from premature sister chromatid separation (Hagting et al., 2002; Tong et al., 2008; Zur and Brandeis, 2001). Additionally, it is well studied as an oncogene, promoting cell migration and tumorigenicity (Genkai et al., 2006; Xiang et al., 2017; Yan et al., 2015) and, in this context, was reported to regulate the *Gli1* expression by directly binding to its promoter (Feng et al., 2017).
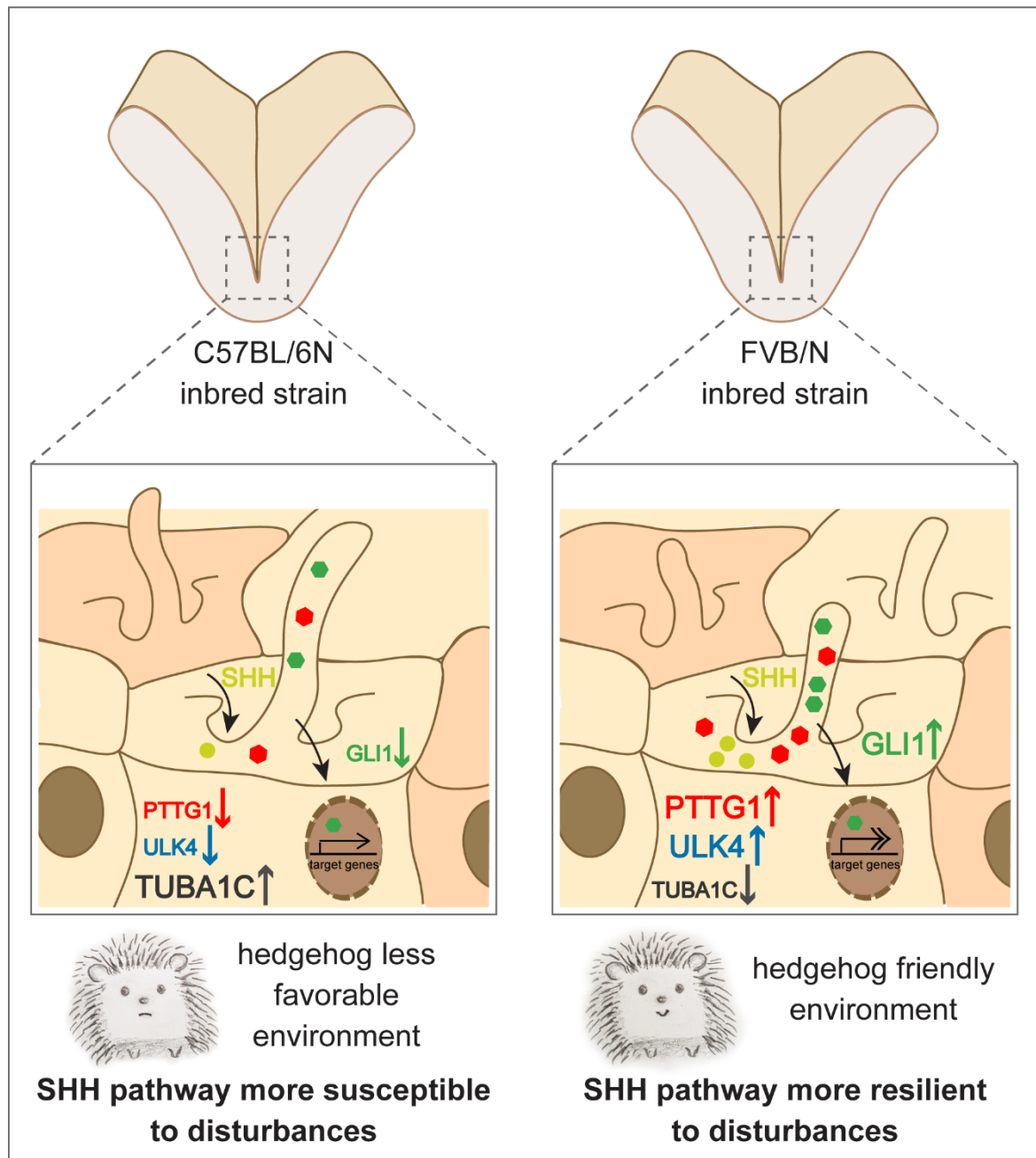
FIGURE 44 MODEL: DIFFERENCES IN THE STRAIN-DEPENDENT PRIMARY CILIA ENVIRONMENT. FVB/N neuroepithelial stem cells present higher *Pttg1* and *Ulk4* and lower *Tuba1c* expression, as well as enhanced SHH signaling, which is more resilient to disturbances. TUBA1c, ULK4, and PTTG1 are associated with microtubule function. Additionally, PTTG1 is localized at the primary cilium. The modifiers could enhance microtubule stabilization at the axoneme and thereby enhance SHH signaling. Shorter primary cilia could contribute to an overall advantageous environment for SHH in FVB/N, compared to C57BL/6N neuroepithelium. Figure was adapted from (Mecklenburg et al., 2020).

DISCUSSION

1.1 PTTG1 extends the list of centrosomal proteins found at the primary cilium

Interestingly, until now, PTTG1 was reported to undergo ubiquitous degradation by the anaphase promoting complex (APC) in order to facilitate anaphase and cell cycle progression (Hagting et al., 2002; Zur and Brandeis, 2001). Strikingly, we documented PTTG1 in primary cilia of post-mitotic or interphase, ciliated NIH-3T3 cells as well as of mouse neuroepithelial cells, implicating its function beyond the cell cycle control, likely in ciliogenesis. Ultrastructural immunogold analysis served as a strong argument for this hypothesis. Localization of PTTG1 to centrioles suggested the protein is shuttled together with mother and daughter centrioles to the cell membrane in order to facilitate primary cilia assembly. Moreover, variable localization of PTTG1 from periciliary region to the ciliary axoneme, together with the additive effect on SHH signaling capacity *in vitro*, supported a new function of PTTG1 in canonical SHH signaling regulation via primary cilia-associated mechanisms FIGURE 44.

1.2 Microtubule-stabilizing function as an emerging common denominator of candidate SHH modifying genes

Intriguingly, independent studies on *Pttg1* and *Ulk4*, the genes that we propose as candidate modifier genes in SHH biology, reported their association to microtubules. *Ulk4*, risk gene for schizophrenia, was documented as a regulator of post-translational modification of microtubules by controlling α-tubulin acetylation (Lang et al., 2014, 2016). Whereas PTTG1 was reported to play a role in cell division also outside of the nucleus, at the Golgi apparatus, where it participates in microtubule (MT) nucleation (Moreno-Mateos et al., 2011).

Centrosome-independent MT nucleation at the Golgi apparatus is well appreciated (Efimov et al., 2007; Martin and Akhmanova, 2018); however, the major microtubule organizing centers (MTOCs), anchoring the MT minus ends, are centrosomes. Centrosomes consist of a pair of centrioles and pericentriolar matrix (PCM) – protein complexes which participate in the MT nucleation (Woodruff et al., 2017). A growing number of studies implicates that defects in centrosomes, not only in primary cilia, lead to ciliopathies (Megraw et al., 2011; Nigg and Raff, 2009). In quiescent interphase cells, the centrosome serves as the building block for the primary cilium. The mother centriole forms the basal body, which nucleates the axonemal microtubules – core of

the ciliary shaft (Kim and Dynlacht, 2013; Kobayashi and Dynlacht, 2011), thus acts as organizing center for microtubules (MTOC) (Joukov and De Nicolo, 2019; Mirvis et al., 2018). Analogically to cytoplasmic MTs, the axonemal microtubules are dependent on the actin networks, and similarly, undergo posttranslational modifications (PTM) followed by dynamic de- and polymerization during cilia disassembly and ciliogenesis, respectively. Moreover, the regulation of centrioles - basal body transition and back remains under continuous investigation in context of cell cycle control. Recent studies consider PCM integrity as a predominant factor in correct primary cilia assembly (Joukov and De Nicolo, 2019; Jurczyk et al., 2004; Zebrowski et al., 2015). Therefore, biogenesis of the primary cilium is a very complex, tightly regulated process, dependent on the coordination of the cell cycle, cytoskeletal rearrangements and other cellular cues. However, it is still very understudied in the context of spatiotemporal extracellular signal transduction and the control of the signaling pathways' efficiency.

The primary cilium is an indispensable component of SHH machinery (He et al., 2017), thus ciliogenesis and microtubule polymerization following cell division is critical for the signaling. In light of these studies, we hypothesize *Ulk4* and *Pttg1,* candidate modifier genes enriched in the FVB/N mouse line, support the pericentriolar matrix (PCM) proteins in regulation of microtubule nucleation and efficient ciliogenesis, thereby enhancing robust SHH signaling. This, ultimately, leads to less susceptibility to disturbances such as LRP2 deficiency FIGURE 44.

1.3 More robust ciliogenesis in the forebrain of FVB/N mice is manifested by differences in primary cilia morphology

For the first time, I report differences in primary cilia morphology between wild-type mice on FVB/N and C57BL/6N background, which can potentially contribute to the subtle changes in the composition of primary cilia machinery and signal transduction on a baseline level (Gigante and Caspary, 2020; Nachury and Mick, 2019). Despite the clear classification of ciliopathies and some of their common manifestations, there is little understanding about the correlation between primary cilia morphology and composition in context of normal and abnormal function (Fliegauf et al., 2007; Gerdes et al., 2009; Wang and Dynlacht, 2018). Recent studies indicated that changes in both actin and microtubule cytoskeleton, can influence cilia length by regulating the availability of soluble tubulin (Sharma et al., 2011). Additionally, a genomic screen by *Kim et al.* highlighted the importance of endocytic recycling, which, in concert with the

actin dynamics, controls ciliogenesis and cilia length (Kim et al., 2010). The list of regulators also included prominin and ARL13b, membrane components of primary cilia (Jászai et al., 2020).

Intriguingly, the cell cycle regulator APC was reported to play a role in the maintenance of primary cilia length in addition (Wang et al., 2014). APC, found at the basal body, has the ability to destabilize axonemal microtubules by ubiquitin-mediated proteolysis and, in concert with other protein factors, regulates the resorption of the primary cilium, which precedes re-entry of quiescent cells to the cell cycle (Wang et al., 2014). Whether PTTG1 is a component of this machinery remains to be investigated. Nevertheless, PTTG1 is a known substrate for APC during cell cycle control (Hagting et al., 2002; Zur and Brandeis, 2001). Therefore, the study from *Wang* and colleagues strengthens our hypothesis about PTTG1 and its regulatory function in ciliogenesis. Ultimately it underscores that my results on PTTG1 localization to the primary cilium significantly contribute to the complex relationship between centrosomes and primary cilia - distinct organelles with a common centriole-based core (Joukov and De Nicolo, 2019).

1.4 Potential of other DEGs to contribute to more efficient primary cilia environment

It is important to mention that my study focused on the highest differentially expressed genes, which, until now, have not been associated with the SHH signaling. Nevertheless, transcriptome analysis of wild-type mice on FVB/N and C57BL/6N background is a powerful source of other DEGs that most likely together with *Ulk4* and *Pttg1* contribute to distinct, more resilient molecular environment of the primary cilia in FVB/N mice and therefore the canonical SHH pathway. I could show that B9D1 and RPGRIP1L proteins, known to be involved in ciliogenesis and SHH signaling (Andreu-Cervera et al., 2019; Dowdle et al., 2011; Garcia-Gonzalo et al., 2011; Vierkotten et al., 2007), also have the capability to increase the SHH signaling *in vitro.* Since both of them are the components of the basal body and transition zone of primary cilia, and are present at higher expression levels in FVB/N wild types as shown in our transcriptome data set, it is very tempting to assume that both may contribute to more efficient environment of primary cilia. This is supported by the evidence that RPGRIP1L plays role in the region-specific regulation of the SHH activity and GLI TFs expression in the mouse forebrain (Andreu-Cervera et al., 2019).

Interestingly, TALPID3, although not able to increase the SHH signaling capacity in my *in vitro* assay, in the light of recent studies (Wang et al., 2020; Yin et al., 2009), presents a candidate, which could indirectly influence the machinery. Studies on chicken have shown TALPID3, a centrosomal protein, is essential for proper docking of the mature basal body to the apical cell membrane and subsequent nucleation of ciliary axoneme, which is completely abolished in mutants (Yin et al., 2009). In contrast, another centrosomal protein involved in docking of the basal body – Outer dense fibre 2 (ODF2, known as cenexin) – was shown to influence the formation of appendages at the basal body, structures reminiscent of the maturation (Ishikawa et al., 2005), preceding the docking at the membrane. These two distinct processes guided by TALPID3 and ODF2, involved in the proper basal body anchoring and initiation of primary cilia assembly, clearly demonstrate the complexity and varying levels of regulation, which, when facilitated, may have a favourable contribution to efficient ciliogenesis. Intriguingly, a recent study of *Wang* and colleagues revealed TALPID3 is involved in the microtubule organisation in radial glial cells (RGCs) (Wang et al., 2020). This novel function was supported by the enriched localization of TALPID3 found at the mother centrioles of RGCs. Therefore, TALPID3, another upregulated gene from the FVB/N transcriptome appears to have a potential stabilizing impact on microtubules.

In the light of our hypothesis suggesting favorable microtubule environment of FVB/N mouse background, further experiments are required to correlate the transcriptional changes with the functional implications. Few recent studies performed independently unravel an interesting potential of centrosomal proteins, which are involved in ciliogenesis and microtubule regulation, to influence the signaling at the primary cilia. One of interesting examples is *Cep128* (*Centrosomal Protein 128*), upregulated in FVB/N. CEP128 was reported to regulate vesicular trafficking to the primary cilium and TGF-β/BMP signaling (Mönnich et al., 2018). Moreover, CEP128 was found at the subdistal appendages (SDA), where it is required for the SDA protein network assembly, consequently leading to stabilization of centriolar microtubules (Kashihara et al., 2019). This, as well as our study, highlights both the emerging crosstalk between the regulation of cell cycle and primary cilia biogenesis and how it is translated to effective signaling at the primary cilium. On one hand, the primary cilium serves as an interface between the extracellular cues and cytoplasmic microtubule network. This is achieved by the basal body of the primary cilium – a structure dependent on the

centrosome. On other hand, the basal body serves as an important MTOC, analog to the centrosome, and intracellular sensor of the cell cycle (Joukov and De Nicolo, 2019; Mirvis et al., 2018).

In conclusion, our study unravels a plausible explanation for the FVB/N congenic line being more resilient to SHH- and primary cilia- related developmental disorders comparing to C57BL/6N line (Mecklenburg et al., 2020). More efficient ciliogenesis, achieved by advantageous microtubule environment, most likely translates into overall higher SHH signaling capacity. This influences the disease penetrance in mouse models and provides relevant implications towards understanding human ciliopathies, which commonly demonstrate a variable spectrum of disorders.

2 Conserved dorsal neural tube phenotype in LRP2-deficient mice on different backgrounds and in *Xenopus*

Detailed phenotypic analyses of LRP2-deficient embryos on C57BL/6N, FVB/N, and mixed F1 backgrounds showed a full rescue of the SHH-dependent ventral midline specification, related to the etiology of holoprosencephaly; however, it did not rescue the dorsal phenotype of the developing brain. Instead, $Lrp2^{-/-}$ mutants on a FVB/N and F1 background develop a dilated dorsal forebrain, with incidents of more severe NTDs analogous to mutants on C57BL/6N background (FIGURE 8, FIGURE 23). This indicated a distinct, conserved function of LRP2 in dorsolateral forebrain development, which could not be explained by the SHH signaling deficiency, which is rescued in mutants on FVB/N and F1 background. Moreover, thanks to a close collaboration with Kerstin Feistel's laboratory, we observed a dorsal neural tube defect that is conserved as well in African Clawed Frog *Xenopus laevis* with LRP2 loss of function (LOF). Joining the mouse and *Xenopus* models, we elucidated a mechanism underlying the conserved LRP2 function in neural tube closure, which we published in (Kowalczyk et al., 2021). Importantly, for the purpose of this study, we focused on C57BL/6N background; however, based on the results, we can confidently extrapolate the findings to the FVB/N mouse strain with conserved dilation of the mutant neural tube. Additionally, dorsal phenotype and NTD of LRP2-deficient C57BL/6N mice was already investigated in context of co-receptor function and folate delivery (Kur et al., 2014). Here, we shed light on a novel function of the LRP2, beyond the signal transmission.

A well-established function of LRP2 in brain development is related to spatiotemporal control of morphogen gradient and vitamin uptake (Christ et al., 2012, 2015; Kur et al., 2014). However, this does not fully explain how the complex morphogenetic changes are executed after ligand stimulation and whether ligand stimulation is an absolute triggering factor. The driving force to deliver the extracellular cargos and signals comes from the high endocytic capacity of intracellular receptors (Schneider and Nimpf, 2003). I could show that function of LRP2 reaches beyond the canonical signal-transducing scheme. LRP2 serves as a critical component of a membrane scaffolding protein complex and orchestrates endocytic activity with apical constriction of neuroepithelial cells. This cellular function in individual cells further influences the planar cell polarity and convergent extension of the entire neuroepithelial sheet, an essential morphogenetic processes during conversion of the flat neural plate into a neural tube (Copp et al., 2003b; Wallingford et al., 2013).

2.1 Endocytic activity of LRP2 facilitates efficient apical constriction

Detailed scanning electron microscopy inspection of mouse neural folds revealed both disturbed neuroepithelial integrity in *Lrp2*$^{-/-}$ mutant embryos and impaired hinge points formation, which allow for consequent folding of the tissue (Colas and Schoenwolf, 2001). Contrarily, impaired elevation of the neural folds, present in *Lrp2*$^{-/-}$ mutants, is reminiscent of neural tube closure defects (Wallingford, 2005). Therefore, the phenotype affecting entire neuroepithelial structure seemed to be related to cell behavior and cytoarchitecture.

Neural tube closure is a very complex morphological phenomenon integrating various processes. It consists of apicobasal cell elongation, which precedes apical constriction and hinge points formation (Haigo et al., 2003; Hildebrand and Soriano, 1999; Martin and Goldstein, 2014; Suzuki et al., 2012), and proceeding tissue shape changes mediated by convergent extension and mediolateral cell intercalation (Keller et al., 2000; Sutherland et al., 2020b; Wallingford and Harland, 2002). Examination of LRP2 localization using confocal and super resolution microscopy revealed enriched protein distribution in constricting neuroepithelial cells at the hinge point formation.

Furthermore, LRP2 is localized at the pocket of primary cilia, which is characterized by high endocytic capacity (Molla-Herman et al., 2010).

Cell autonomous shape changes generate external forces driving tissue shape changes. Key cellular processes rely on dynamic actomyosin contractions, a hallmark of apical constriction in epithelial cells (Christodoulou and Skourides, 2015; Mason et al., 2016; Miao and Blankenship, 2020; Miao et al., 2019; Xie and Martin, 2015). Growing evidence indicates efficient apical constriction requires endocytosis in order to remove excess membrane (Lee and Harland, 2010) in addition to ensuring proper apicobasal and planar cell polarity (Ossipova et al., 2014, 2015a). However, how these processes are integrated in space and time remains unknown (Martin and Goldstein, 2014). We attempted to show that high endocytic capacity of LRP2 contributes to apical membrane remodeling, leading to a potential stabilization of the cell surface area during pulsatile actomyosin constriction (Martin et al., 2009; Miao et al., 2019). Based on live imaging and functional experiments performed in *Xenopus* (see (Kowalczyk et al., 2021)), we postulated mechanical initiation of actin dynamics is not impaired; however, a lack of LRP2-driven endocytosis hampers efficient apical constriction, leaving wide cell surfaces covered with membrane protrusions, reminiscent of impaired endocytosis (Fabrowski et al., 2013).

2.2 LRP2 serves as a hub that orchestrates apical constriction and PCP via direct interaction with adaptor proteins

Morphogenetic tissue changes reflect the organized cell rearrangements and convergence and extension movements. Underlying mechanisms have been associated with the WNT/PCP signaling and spatiotemporal distribution of the core PCP component VANGL2 (Nishimura et al., 2012; Wang et al., 2019a). VANGL2 is transported to the membrane in order to allow for cell polarization, and its asymmetric distribution initiates convergent extension (Roszko et al., 2015). Furthermore, VANGL2 trafficking from cytoplasm to apical cell surface has been associated with regulation of apical constriction (Ossipova et al., 2015a). Thus, endocytic pathways and intracellular trafficking of proteins greatly contribute to the maintenance of cell and tissue polarity during morphogenesis (Eaton and Martin-Belmonte, 2014; Ossipova et al., 2014). Our findings on LRP2-mediated endocytosis and trafficking strongly support this hypothesis

in context of anterior neurulation. Firstly, we demonstrate VANGL2 co-localization with LRP2 in the RAB11-positive recycling endosomes at the apical surface. Secondly, a lack of LRP2 leads to aberrant distribution of VANGL2 to basolateral membrane. Taken together, this indicates LRP2-mediated endocytosis, not only removes excessive plasma membrane, but, importantly, regulates recruitment and trafficking of critical PCP components in a precise spatiotemporal manner. Furthermore, growing evidence around functional correlation between apical constriction and planar cell polarity in NTC (McGreevy et al., 2015; Nishimura et al., 2012; Ossipova et al., 2014, 2015b) encouraged us to assume LRP2 is a common denominator for these two cellular processes in developing forebrain.

Cellular trafficking and cytoskeletal dynamics is mediated by PDZ proteins (Liu and Fuentes, 2019). These cytoplasmic adaptors act as scaffolds for protein complexes and integrate independent signaling pathways (Pawson and Scott, 2010). LRP2 contains two PDZ binding domains (PBDs) in the cytoplasmic domain (Gotthardt et al., 2000) and has been documented to functionally interact with PDZ-containing adaptor proteins GIPC1 and NHERF1 (Naccache et al., 2006; Slattery et al., 2011). However, none of the known adaptor proteins for LRP2 were studied in the developing neural plate and in context of NTC. I detected, for the first time, the GIPC1 and NHERF1 expression in the early neuroepithelium. Additionally, the results presented that localization of NHERF1 and GIPC1 is dependent on LRP2 expression, highlighting the new functional interaction of LRP2 and adaptor proteins in the developing forebrain.

Supported by LOF experiments in *Xenopus* (see (Kowalczyk et al., 2021)), we demonstrated a model with LRP2-based scaffolding complex orchestrating an apical constriction and PCP via direct interaction with adaptor proteins FIGURE 45. We reported that LRP2 binds to the PDZ domain of GIPC1 in neuroepithelium. Additionally, GIPC1 is able to dimerize (Reed et al., 2005) and transport the protein complexes responsible for apical constriction, followed by LRP2-induced apical membrane removal. Thus, both processes are integrated by binding to GIPC1 adaptor protein, which directs endocytic vesicles along the actin network via interaction with myosin VI (Aschenbrenner et al., 2003; Naccache et al., 2006) FIGURE 45.
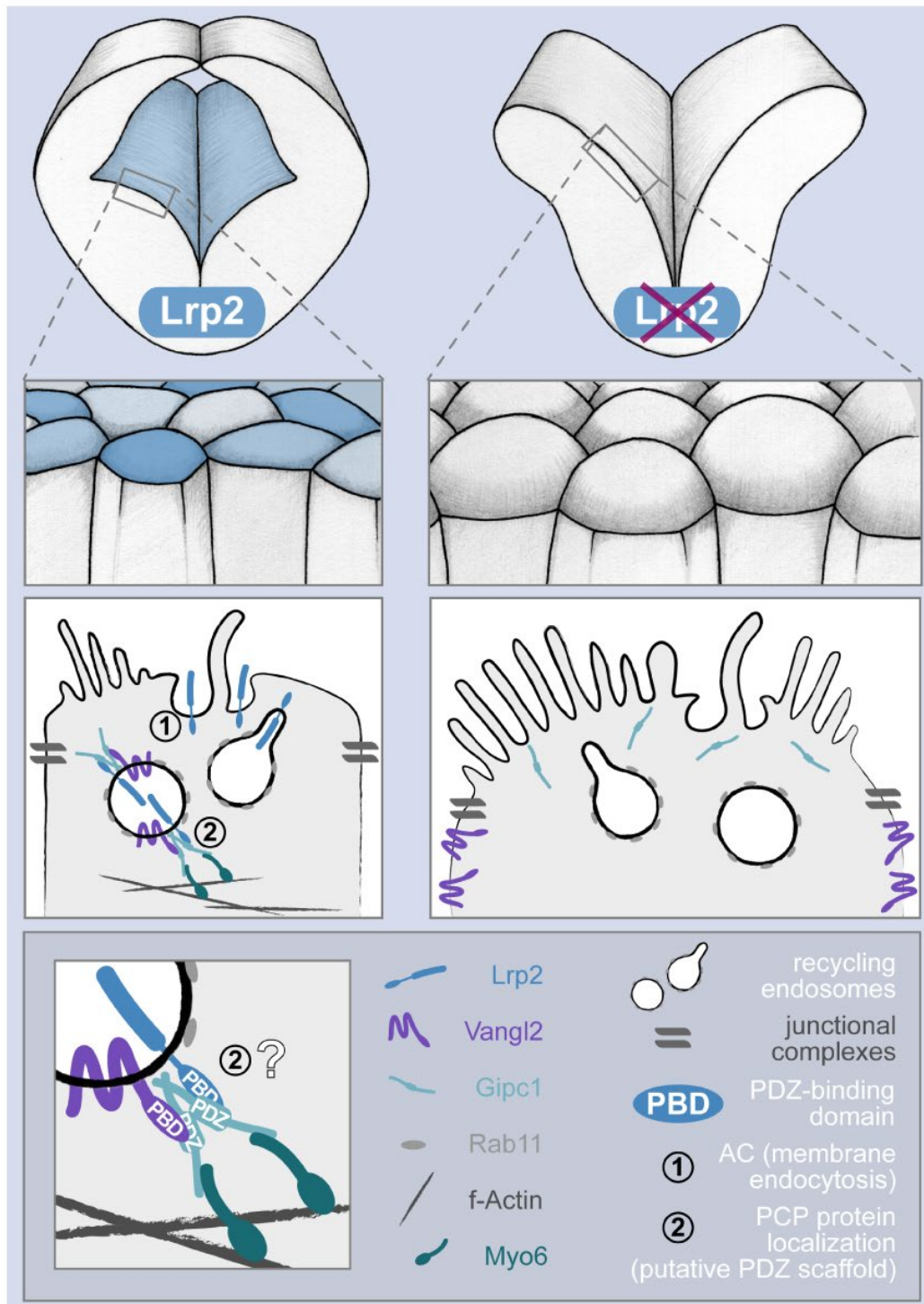
FIGURE 45 MODEL PRESENTING THE SCAFFOLDING FUNCTION OF LRP2 IN NEUROEPITHELIUM.
LRP2 facilitates the apical constriction by endocytic removal of excessive cell membrane (1).
The function is mediated by interaction of LRP2 with PDZ-adaptor proteins (GIPC1) that
connect to actin cytoskeleton. LRP2/RAB11 recycling endosomes, guided by GIPC1
associated with myosin 6 motor, regulate the spatiotemporal localization of VANGL2 (2).
Neuroepithelium deficient for LRP2, presents impaired apical constriction, due to defective
endocytosis, and mislocalization of PCP components, which culminates in neural tube closure
defect. Figure was adapted from (Kowalczyk et al., 2021).

In consequence of proper apical constriction and hinge points formation, a consecutive process towards NTC is PCP-mediated CE (Suzuki et al., 2012). Our results propose that succession of apical constriction and planar cell polarity changes could potentially be controlled by GIPC1-mediated scaffolding complex. GIPC1 was reported to bind VANGL2 via PDZ domain and control asymmetric localization at the apical membrane (Giese et al., 2012). VANGL2 intracellular distribution, on the other hand, is dependent on apical constriction and PCP (Ossipova et al., 2014, 2015a). We demonstrated VANGL2 colocalizes with LRP2 in recycling endosomes, confirming recruitment of VANGL2 to the apical membrane during apical constriction. Consequently, asymmetric distribution of VANGL2 to the lateral plasma membrane, reminiscent of CE, was documented in *Xenopus* at a later stage. In contrast, lack of LRP2 led to mislocalization of VANGL2. These results indicated LRP2-mediated recycling endosomes facilitate the VANGL2 delivery to appropriate cellular compartments, in correct time. Furthermore, binding to GIPC1 adaptor by both proteins again facilitates the directional transport of the vesicles through the actin meshwork

Together, our findings from mouse and *Xenopus* unraveled a novel, conserved role of LRP2 in integrating essential morphogenetic process during neural tube closure. LRP2 acts as a hub, orchestrating efficient apical constriction through endocytic membrane removal, with intracellular distribution of PCP components in spatiotemporal manner. The function of LRP2 is manifested by its intracellular domain that selectively binds to the adaptor proteins forming subcellular scaffolding complexes dependent on the cellular context.

2.3 LRP2 scaffolding function can potentially mediate assembly of apical junctional complexes

Not surprisingly, there is growing evidence of the role of apical cell junctions in the morphogenetic transformations. Cell-cell contacts, such as tight junctions (TJ) and adherens junctions (AJ), are a hallmark of all types of epithelia. Junctions not only mechanically stabilize the tissue, but dynamic exchange of the junctions between neighboring cells allow for cell intercalations, the driving force of CE, as well as delamination and migration (Guillot and Lecuit, 2013). Additionally, cell junctions are reported to produce and sense the mechanical tensions during morphogenesis

(Gomez et al., 2011). A very promising correlation arises around the LRP2 adaptor protein NHERF1. I discovered NHERF1 is expressed in the neuroepithelium, and, surprisingly, its expression is abrogated in the LRP2 mutants. NHERF1, a PDZ scaffolding protein, was shown to regulate the organization of TJs and their permeability in epithelia (Castellani et al., 2012; Seidler et al., 2009). Concurrent with those findings, I speculate a LRP2-NHERF1 scaffolding complex can play an important role in organized assembly of TJ meshwork within the neuroepithelium of developing neural tube.

Impaired integrity of the LRP2-deficient mouse neuroepithelium, documented in my work, implicates weakened cell connections. Despite ZO-1, core TJ protein presence in mutant neuroepithelia, we cannot exclude that structure of TJs and/or AJs is malfunctional. Interestingly, a long time ago, scientists documented that the composition of TJs changes from open NP to closed NT (Aaku-Saraste et al., 1996). They reported the TJ-specific transmembrane protein occludin is initially present at the apical neuroepithelium; however, it disappears during NTC, although the TJs remains functional. A more recent study unravelled a direct role of other core TJ proteins - claudins - in regulation of actomyosin contraction and cell intercalation during NTC (Baumholtz et al., 2017). The authors of the study reported that removal of Cldn3, 4, and 8 leads to folate-resistant NTDs. This was explained by impaired trafficking of VANGL2 and phosphorylated myosin, partially reminiscent of phenotype we observe in LRP2-deficient neuroepithelium. Intriguingly, another study highlighted another important role of TJs in the apical constriction. They showed recruitment of microtubule-associated proteins to TJs promotes the correct assembly of actomyosin ring and consequently apical constriction (Yano et al., 2021). Summarily, a growing number of evidence indicates apical junctional complexes (AJCs) largely contribute to the control of the cortical development from neurulation to neurogenesis (Gamero-Estevez et al., 2018; Veeraval et al., 2020). Whether the scaffolding capacity of LRP2 contributes to stabilization of AJCs remains unknown; however, it is highly attractive to investigate.

2.4 LRP2 coordinates the extracellular and intracellular cues in a tightly controlled spatiotemporal manner

The principal question that emerges in context of multiplex LRP2 function is whether scaffolding and membrane remodeling activity is dependent on the ligand binding and extracellular signal transduction.

An intriguing computational model mirroring the neural tube formation argues for independent capacity of morphogenetic process to drive folding of the epithelium on its own (Nielsen et al., 2020). Physical simulations show cell intercalation or cell wedging, independently, is sufficient for bending and tube formation. Although *Nielsen et al.* admit a major limitation of performed simulations is lack of morphogen signals, reported power of independent mechanical forces in tissue morphogenesis is impressive. Nevertheless, biological systems always exhibit extreme complexity of simultaneously manifested process, thus crosstalk of morphogens and morphogenetic processes is well appreciated and rational, although still not well understood.

Correlation between LRP2-mediated folate uptake during neurulation (Kur et al., 2014) and overall importance of the folic acid metabolism in human and mouse NTDs (Imbard et al., 2013), implicates integration of extracellular-signaling and intracellular-scaffolding functions by LRP2 is highly plausible. This hypothesis is strongly supported by the recent study, which reported that cilia-dependent SHH signaling plays role in the control of directed cell remodeling during midbrain NTC (Brooks et al., 2020). *Brooks* and colleagues demonstrated that midline cells exposed to high SHH levels are short and apically expanded, in contrast to highly constricting, elongated cells in lateral folds, exposed to low SHH. This study, in light of our results, strongly implies LRP2 plays a key role in the titration of signaling molecules which trigger the context dependent cellular scaffolding function of the receptor. Strikingly, there is emerging indication from a *C. elegans* study that LRP2 may also act downstream of EGL-20/WNT (Minor and Sternberg, 2019), which opens yet a new perspective on the complex receptor activity, at the crossroad between the critical signaling pathways during development. It is strongly supported by our transcriptome dataset as well.

To summarize, we reported LRP2 deficiency deprives cells from a functional endocytic pathway, which, from one side, manifests in apical constriction defect, and, from the

other side, impairs planar cell polarity and convergent extension, thus affecting two essential morphogenetic processes during anterior neural tube closure.

3 Neural tube defects, craniofacial defects and neural crest cells

Along the neuronal stem cell niche, the neural crest stem cell niche arises during early embryonic development. This unique vertebrate population of cells owes its remarkable character to the extensive migratory capacity. Many studies investigate the neural crest (NC) in various animal models, from zebrafish, *Xenopus*, and chicken to mice and rabbits. However, there are intriguing discrepancies, especially in the mouse NC, that keep many questions open (Barriga et al., 2015). The most intriguing is still different succession of the events between neural tube closure, EMT, and delamination (Barriga et al., 2015; Theveneau and Mayor, 2012a).

Despite being distinct populations of cells, induced at different time points in embryogenesis, neuroepithelial and NC cells together build the vertebrate head. Moreover, many congenital brain defects, like HPE, are accompanied by the NCC-related craniofacial defects, suggesting at least part of the regulatory network of these two stem cell niches is common or tightly dependent on each other (Santagati and Rijli, 2003). Indeed, independent studies on chicken and mice have shown altered retinoic acid (RA) signaling leads to reduced SHH signaling, which not only affects the developing forebrain, but also leads to perturbed cranial neural crest cells (CNCC), consequentially contributing to abnormal facial development (Schneider et al., 2001; Wang et al., 2019b). Impaired RA and SHH signaling pathways manifest in decreased expression of NC markers *Sox10* and *Tfap2α,* and apoptosis of NCC.

3.1 Expansion of neural crest cells in LRP2-deficient mice

The field of neural crest clearly appreciates how NC induction requires the combination of key developmental signaling pathways, such as WNT, FGF, and BMP. However, in case of mouse studies, many direct evidences remain unknown and this is well emphasised in the recent review from *Prasad et al* (Prasad et al., 2019). Moreover, how this crosstalk is modulated between neuronal and neural crest stem cell niches requires further investigation. Interestingly, there is growing evidence for an

advantageous effect of folate, vitamin B$_9$, on these two populations of cells, with the emphasis on the homeostasis between folic acid and homocysteine in maternal blood (Boot et al., 2003; Rosenquist and Finnell, 2001). Recent studies suggest that entire methylation/1C metabolism, including vitamin B$_9$, B$_{12}$, choline, influence the prevalence of NTDs (Clare et al., 2019; Imbard et al., 2013; Rosenquist et al., 2007; Steele et al., 2020).

Low folate/high homocysteine environments are characteristics for occurrence of NTDs in human, and, *in vitro,* it was shown to affect the cranial and cardiac NCC, expanding their outgrowth in the expense of neuroepithelial cells (Boot et al., 2003). Whether our results about increased expansion of NCC population, and, strikingly, ectopic expression of NC marker within neuroepithelium, could be placed in the context of, the aforementioned, folate study requires further investigation. However, presence of the LRP2 receptor in both stem cell niches and its importance in folate metabolism (Kur et al., 2014) is supportive of this hypothesis. Additionally, aberrant transformation of neuroepithelial cells to NCC at the early embryonic development seems to be a plausible explanation for our results because of the initial temporo-spatial co-existence of both populations during development and common co-occurrence of neural tube and craniofacial defects in model organisms and human.

It is important to distinguish between the initial induction of the NC characteristics and the further requirement to maintain the identity of NC cells (Aybar and Mayor, 2002). Our observations from the *Lrp2* mutant mice, with what is currently known, implicate LRP2, thanks to its ability to modulate the concentration of morphogens and folate, could maintain the initial balance between the neuroepithelial- and neural crest- like identity at the early neurulation.

3.2 Neural crest cells lose the directional migration potential and wrongly colonize

Besides the NCC specification, the feature that defines the unique character of NCC is coordinated migration. I observed that NCC in the *Lrp2* mutant embryos show impaired colonization of specific embryonic compartments, such as pharyngeal arches. Moreover, the migratory stream is less restricted and organized, resembling the expansion of NC stream in the *laminin α5* null mice, where laminin α5 was suggested as the ECM factor restricting the migratory path (Coles et al., 2006).

Theveneau and Mayor addressed in detail the current knowledge about the migratory character of NCC. They revised the combination of chemoattractants, such as FGF2 and chemorepellents, such as ephrinB, EphB, which guide distinct streams of NC cells and maintain regions free of NCC, together with semaphorins (Theveneau and Mayor, 2012b). These regulators, together with the ECM architecture and repulsive contact inhibition of locomotion (CIL) between the colliding cells contribute to the establishment of a well-defined stream of cells with polarisation of the leading edge. Close vicinity of cells partially controlled by cadherins (Becker et al., 2013) and gap junctions facilitate chemotaxis and interpretation of external signals, allowing for collective cell migration along the precise pathways (Kuriyama and Mayor, 2008; Theveneau and Mayor, 2011, 2012c, 2012b). However, how all these distinct, parallel signals are integrated exactly in order to properly segregate the NCC and colonize the target zones requires further investigation.

Here, basing on preliminary data from LRP2-deficient mouse embryos, we can draw the conclusion that LRP2 could be one of these signal transmitters. Firstly, we demonstrated LRP2 plays an important role in the cytoskeletal remodelling of polarised neuroepithelial cells, thus there is a possibility that impaired neuroepithelial integrity may influence the optimal transition to and maintenance of the mesenchymal character of NCC. Secondly, there is one gripping evidence of LRP2 involved in the positive regulation of migration of oligodendrocyte precursor cells (OPCs) during optic nerve development (Ortega et al., 2012). *Ortega* and colleagues demonstrated LRP2 is selectively expressed in the neighbouring astrocytes, allowing for the SHH internalization. Subsequent release of SHH in the proximity of OPCs serves as chemoattractant for the migration and proliferation of OPCs (Ortega et al., 2012). Although it has been documented that LRP2 controls the SHH gradient in a spatiotemporal and context dependent manner during development, the above study was a first evidence for the possible transmission of migratory cues. Whether this is a unique context or LRP2 exhibits a similar function in the neural crest, presenting the external morphogen gradients to the migratory stream, remains a very attractive hypothesis which we want to address in further detail.

3.3 Hints towards the imbalanced regulation between neuroepithelial and neural crest stem cell populations in LRP2-deficient mice

Studies on models, where neural tube closure occurs after CNCC delamination, present strong argumentation towards a hypothesis with a positive feedback loop between these two distinct processes. One good example comes from the mouse, where *Tfap2α–Irf6–Grhl3 (Transcription Factor Activation Protein 2α – Interferon Regulatory Factor 6 – Grainy Head-Like 3)* combination of genes is necessary for neurulation (Kousa et al., 2019). Mutations in any of them contribute to rostral and caudal NTDs commonly accompanied with neural crest-related orofacial clefting disorders in mouse and human (De Castro et al., 2018; Kousa et al., 2019; Schorle et al., 1996).

Especially intriguing for our study was *Tfap2α,* one of the upregulated genes in the *Lrp2* mutant mice compared to wild types. It presents ectopic expression within neuroepithelial cells. Interestingly, a study by *Dimitrova et al.*, added *Tfap2α* to the list of main TFs involved in the regulation of EMT in context of cancer in mice and humans (Dimitrova et al., 2017). They demonstrated overexpression of *Tfap2α* promotes an EMT phenotype by increasing the expression of TFs initiating EMT. Although EMT regulation in cancer shares many similarities with the EMT in development and NC (Thiery et al., 2009), until now, there has been no direct study confirming that *Tfap2α* specifically regulates EMT in NCC. The only clue comes from the epigenomic chromatin profiling on human embryonic stem cells-derived NCC (hNCC), where TFAP2α is a major TF found in hNCC enhancer regions (Rada-Iglesias et al., 2012) This suggests a powerful role of TFAP2α in the regulation of gene expression in transient population of developing neural crest cells.

Following the general concept that EMT extends the potential of epithelial cells to gain stem cell properties (Mani et al., 2008) brings us to a very compelling question. Could LRP2 facilitate the balance between the 'stemness'-like character of neuroepithelial and neural crest stem cell niches during early development?

VII. OUTLOOK AND FUTURE PERSPECTIVES

The variable clinical manifestations of congenital brain disorders, such as holoprosencephaly and neural tube defects, with limited prevention and treatment, demonstrate there is a high demand on better understanding the disease etiology. LRP2-deficient mouse models are a valuable tool to examine the crosstalk between pivotal signaling pathways and the biomechanical changes taking place during neural tube morphogenesis. My Ph.D. work provided novel insights into understanding how cell intrinsic features may contribute to both effectiveness of the signaling and integration of the signaling and biomechanical changes. Nevertheless, many open questions about detailed control and cross-regulation of these processes remain.

1 Do we have different primary cilia? A milestone in primary cilia-related disease penetrance around the corner

Our study unraveled a plausible explanation for the resilience to SHH-related developmental disorders seen in FVB/N congenic mice compared to the C57BL/6N line (Mecklenburg et al., 2020). More efficient ciliogenesis, achieved by an advantageous microtubule environment, very likely translates into an overall higher SHH signaling efficiency. This result has a great relevance clinically, with further implications towards understanding of human ciliopathies which commonly present a variable spectrum of disorders.

Primary cilia are tiny cell organelles projecting from the cell surface and sense extracellular cues. Because of technical limitations, they have mostly been studied *in vitro*, providing easier access for genetic modifications of the ciliary components, as well as, for resolving their localization in super resolution microscopy. However, considering various primary cilia-related diseases, there is a great necessity for a thorough examination of the primary cilia *in vivo*. The intriguing differences in lengths of the primary cilia between the forebrain of the wild-type inbred FVB/N and C57BL/6N mice, are a milestone in the understanding of another layer of disease regulation, in context of variable penetrance of severe developmental defects of the brain. We show the canonical risk factors, such as the SHH signaling pathway, can be modulated at

the level of primary cilia biogenesis. Therefore, a detailed examination of the ciliogenesis between FVB/N and C57BL/6N mice using advanced fluorescence and electron microscopy techniques could provide us with additional insight into relevant disease mechanisms influencing primary cilia composition, their capacity of signal transduction, and the cellular readout coordinating morphogenetic changes in space and time. Furthermore, thorough examination if the changes in primary cilia morphology relate to truly postmitotic, quiescent cells, or whether they reflect the significant differences in cell cycle regulation between the strains is required. Detailed functional analysis of centrosomal proteins, such as PTTG1, which are found at the primary cilium, will shed light on this crucial issue (see Discussion 1.3).

Tremendous recent work performed by *Ma* and colleagues provided a super resolution, atomic map of the ciliary doublet microtubule (Ma et al., 2019). The group used cryo-electron microscopy (cryo-EM) on flagella isolated from *Chlamydomonas* and resolved the atomic structure of native axonemal doublet microtubule. Combining the structural data with the available genetic data allowed them to precisely interpret the association between the distribution of the proteins and their function. Acquiring analogical cryo-EM data on a mammalian primary cilium will be challenging, but incredibly valuable. Such thorough structural analysis, combined with a proteomic and mass spectrometric approach (Kohli et al., 2017; Ma et al., 2019) would provide a comprehensive dataset on primary cilia biology. Only understanding of the detailed architecture of the primary cilia, including the static and dynamic components, will elucidate the underlying complex function and consequences of the primary cilia defects in human ciliopathies.

When considering further analysis of transcriptomic differences between FVB/N and C57BL/6N, there are many hints suggesting a distinct ciliary composition between the strains. TMEM237 is significantly upregulated in the FVB/N wild types. Surprisingly, it is known to directly interact with B9D1 and RPGRIP1L in the transition zone of the primary cilium (Lambacher et al., 2016). Moreover, it is RPGRIP1L that anchors the TMEM proteins, including TMEM237, at the TZ. On the other hand, TMEM proteins regulate the Y-link connectors between axonemal doublet microtubules and ciliary membrane (Huang et al., 2011; Lambacher et al., 2016), and this was resolved with great specificity using electron microscopy on *C. elegans* (Huang et al., 2011). Thus, structural differences of primary cilia are likely to translate into a functional relevance.

Especially that there are studies indicating that some of the proteins which regulate the TZ composition, such as RPGRIP1L (Andreu-Cervera et al., 2019) and kinesin motor KIF13B (Schou et al., 2017), can directly regulate the ciliary trafficking and SHH signaling activity.

In context of the PTTG1, a novel primary cilia component I characterized in my dissertation, a live imaging would be a valuable approach. PTTG1 is expressed in the variable pattern in different compartments, thus dynamic tracking of labeled PTTG1, in correlation with the cell cycle progression, will provide a deeper understanding on how exactly PTTG1 contributes to a presumably more stable ciliary environment. The findings will translate on the understanding the complex regulation of the pivotal signaling pathways, such as SHH, and how the cellular and primary cilia composition contributes to an alternative regulation of the signaling pathways and resilience to disturbances.

An independent study on centrosomal Rab-interacting lysosomal proteins (Rilp-like), which, similar to PTTG1, are dynamically localized at the primary cilium, presented their function as regulators of signaling efficiency in the accumulation of the signaling proteins at the cilium (Schaub and Stearns, 2012). Defects in removal of signaling factors by Rilp proteins, lead to the retention of the signal at the primary cilium, and, in consequence, this was shown to affect the organization of the epithelial cells as well (Schaub and Stearns, 2012). An analogical assessment of the PTTG1 in the cultured cells, in high resolution, will likely be informative on its direct function in the regulation of the SHH signaling capacity. In light of the above study, not only a potential stabilizing function of PTTG1 on the axoneme microtubules may be critical for SHH signaling, but PTTG1, similarly as Rilp proteins, may contribute to the signal trafficking at the primary cilium.

2 Primary cilium as the interface between extracellular and intracellular signaling

The periciliary domain serves as an interface between non-cell autonomous, extracellular signaling and cell autonomous signaling through the cell cytoskeleton. Stable microtubule environment that presumably facilitates primary cilia biogenesis

may as well affect the entire cellular cytoskeleton and, in consequence, cellular polarity (Cearns et al., 2016). Studies supporting this hypothesis are those relevant for Bardet-Biedl and Joubert syndromes, which manifest with ciliary defects, hydrocephaly, and NTDs (Huang et al., 2011; Ross et al., 2005). They provide compelling evidence that basal bodies and transition zones are involved in the PCP regulation and disruption of BB and TZ proteins affects VANGL2 localization at the primary cilium (Ross et al., 2005) with a consequence of convergent extension defects as described for TMEM237 (Huang et al., 2011). Following this line of reason, a well-functioning pericentriolar matrix at the base of the primary cilium may be a prerequisite, not only for the proper ciliary assembly and signaling pathways, but also for the complex assembly of entire cellular cytoskeleton. This, in consequence, allows for correct distribution of the cellular components, including PCP proteins.

We show that LRP2 is a central hub coordinating both cilia-related signaling and intracellular trafficking. Thus, super resolution imaging techniques, such as STED and STORM, will resolve the LRP2 scaffolding network, consisting of adaptor proteins that guide the intracellular cargos (GIPC1) but also may potentially control the integrity of the neuroepithelium by assembly of apical junctions (NHERF1).

3 Different view on the regulation of stem cell niches

Origin of brain development initiates at the neural stem cell (NSC) pool; however, how this population of cells is regulated and maintained remains elusive in many aspects. LRP2 is expressed in the embryonic (Christ et al., 2012) and adult (Gajera et al., 2010) neural stem cell niches. In addition, I provide direct evidence for LRP2 expression in the neural crest stem cell pool. Complex functional activity of the receptor in signaling and cellular cascades at the earliest stages of development strongly suggests LRP2 may be involved not only in the neural stem cell behaviour, as reviewed by (Auderset et al., 2016), but also in the regulation and maintenance of the stemness per se. Although this is a very far-reaching hypothesis, the results of my work, especially in the context of balance between neural- and neural crest- stem cell pools (see Discussion 3.1 and 3.3)., are partially supportive.

Drastically impaired regulation of the stem cell populations underlies congenital disorders. In the case of *Lrp2* mutants, where, presumably, expansion of neural crest stem cell niche occurs in the expense of neural stem cell niche in low folate

environment (Boot et al., 2003) (see Discussion 3.1), we observed severely underdeveloped brain and craniofacial structures. However, such imbalance could be counteracted by a strain dependent, more robust neural stem cell niche environment, a scenario we likely have in the FVB/N mice.

Supportive evidence for more advantageous neural stem cell niche in FVB/N comes from the study on ULK4, which has been shown to regulate the cell cycle and neural stem cell pool, partially through regulation of WNT signaling (Liu et al., 2016b). ULK4 deficiency results in a dramatic reduction of embryonic NSC population, which continues during adult neurogenesis. Whether the overall neural stem cell population is increased in FVB/N mice, with higher ULK4 expression, remains elusive. However, an increased primary cilia number in the FVB/N neuroepithelium, compared to C57BL/6N mice, could hypothetically be the result of a more efficient expansion/cell cycle control of these cells. Following in this direction, a more robust neural stem cell niche could strongly counteract the defects in the neural crest niche upon loss of LRP2, allowing a rescue, not only the HPE phenotype, but also craniofacial defects.

Additionally, PTTG1 is a known EMT regulator during cancer (Feng et al., 2017) and it was described to have a regenerative capacity in rat liver (Akino et al., 2005). Thus, as another cell cycle regulator, PTTG1 could potentially contribute to the maintenance of neural stem cell pool as well.

Furthermore, canonical WNT signaling regulates the maintenance of embryonic stemness character (Osei-Sarfo and Gudas, 2014). Interestingly, WNT components constitute a large part of DEGs in the FVB/N and C57BL/6N transcriptomes. Therefore, it would be compelling to follow up on the potential regulation of the maintenance of stem cell niches in context of WNT signaling regulation between different mouse strains, as well as looking into the LRP2-dependent context comparing mutants and wild types. It is plausible to assume the resistance to disturbances in the FVB/N mouse strain is due to a better genetic predisposition to more effectively maintain the neural stem cell pool, thanks to the robust ULK4 and PTTG1 expression. On the other hand, LRP2 could potentially be a significant receptor organising the WNT signaling cues, thus, regulating the balance between neural- and neural crest- stem cell fate, based on its potential function in WNT cascade (Minor and Sternberg, 2019).

VIII. SIGNIFICANCE STATEMENT

Coordination of signaling pathways and cellular rearrangements is essential for organized cell behaviors to establish forebrain structures. The signaling pathways rely on primary cilia, which transduce extracellular signals. Ultimately, dysfunctions of primary cilia commonly lead to defects in tissue architecture and congenital disorders as well. We uncovered that differences in the primary cilia size and composition may contribute to the signaling capacity of the cells and to the disease penetrance. Moreover, a proper balance between the stem cell pools may be critical for the coordination of consecutive tissue patterning and differentiation. LRP2 is a multifunctional player in the neural stem cell niche, a critical regulator of both extracellular signal internalization and cellular remodeling. As such, LRP2 integrates the control of cell identity and cell morphology, culminating in the large-scale morphogenesis of neural tube.

IX. APPENDIX

TABLE 12 NEURAL CREST-RELATED DEGS FROM THE C57BL/6N GENOTYPE COMPARISON. DEGs from C57BL/6N *Lrp2$^{-/-}$* vs *Lrp2$^{+/+}$* comparison are sorted according to the fold change.

Gene	log2(FoldChange)	Fold Change	P-value	P-adj
Sox10	1.1778	**2.2623**	1.160E-27	6.310E-24
Wnt3a	0.6983	**1.6200**	3.710E-12	1.220E-09
Lhx5	0.5581	**1.4724**	2.010E-11	5.900E-09
Nkx6-2	0.5179	**1.4319**	5.780E-08	4.900E-06
Fgf15	0.4649	**1.3802**	1.690E-09	2.380E-07
Cbln1	0.4195	**1.3374**	3.200E-08	3.160E-06
Kcna5	0.4081	**1.3270**	1.020E-09	1.560E-07
Foxa2	0.3942	**1.3142**	1.060E-05	3.140E-04
Msx2	0.3697	**1.2921**	7.570E-06	2.400E-04
Tcof1	0.3655	**1.2883**	2.680E-08	2.700E-06
Wnt1	0.3524	**1.2767**	4.750E-04	5.820E-03
Lef1	0.3298	**1.2568**	2.480E-08	2.520E-06
Ppp1r13l	0.2918	**1.2242**	2.019E-03	1.642E-02
Nkx6-1	0.2905	**1.2230**	8.256E-03	4.354E-02
Tfap2a	0.2893	**1.2220**	2.080E-05	5.330E-04
Twist1	0.2883	**1.2212**	6.660E-05	1.330E-03
Frzb	0.2660	**1.2025**	2.810E-05	6.710E-04
Hras	0.2633	**1.2002**	8.840E-05	1.658E-03
Ldb1	0.2515	**1.1905**	4.080E-06	1.470E-04
Atf5	0.2505	**1.1896**	4.450E-03	2.873E-02
Abt1	0.2154	**1.1611**	2.460E-04	3.613E-03
Jag1	0.2055	**1.1531**	5.458E-03	3.299E-02
Rdh10	0.1961	**1.1456**	3.848E-03	2.581E-02
Mapk3	0.1429	**1.1041**	4.501E-03	2.896E-02
Tead2	0.1374	**1.0999**	3.408E-03	2.368E-02
Cfl1	0.1038	**1.0746**	7.820E-03	4.196E-02

Smad5	-0.1560	**0.8975**	5.207E-03	3.190E-02
Fzd3	-0.1561	**0.8970**	7.734E-03	4.170E-02
Tpm1	-0.1592	**0.8955**	7.020E-03	3.911E-02
Hif1a	-0.1741	**0.8863**	1.369E-03	1.240E-02
Nedd4l	-0.1952	**0.8735**	3.250E-03	2.288E-02
Kbtbd8	-0.2259	**0.8550**	5.710E-05	1.180E-03
Fzd6	-0.2516	**0.8400**	2.537E-03	1.930E-02
Ednra	-0.2531	**0.8391**	7.890E-04	8.467E-03
Bmpr1a	-0.2536	**0.8388**	6.580E-05	1.320E-03
Dll4	-0.2659	**0.8317**	6.583E-03	3.765E-02
Foxc2	-0.2921	**0.8167**	2.513E-03	1.916E-02
Tgfb2	-0.3415	**0.7892**	5.960E-05	1.212E-03
Dmd	-0.3434	**0.7882**	2.160E-06	8.950E-05
Sox9	-0.3454	**0.7870**	2.070E-04	3.180E-03
Dach1	-0.3939	**0.7611**	4.670E-07	2.770E-05
Cacna2d1	-0.4171	**0.7489**	1.150E-04	2.027E-03
Atp7a	-0.4314	**0.7415**	8.130E-10	1.320E-07
Pdgfra	-0.4620	**0.7260**	1.340E-07	1.040E-05
Tgfbr2	-0.4666	**0.7237**	8.410E-09	9.710E-07
Kitl	-0.4712	**0.7214**	8.590E-12	2.660E-09

X. REFERENCES

Aaku-Saraste, E., Hellwig, A., and Huttner, W.B. (1996). Loss of Occludin and Functional Tight Junctions, but Not ZO-1, during Neural Tube Closure—Remodeling of the Neuroepithelium Prior to Neurogenesis. Dev. Biol. *180*, 664–679.

Ahlstrom, J.D., and Erickson, C.A. (2009). The neural crest epithelial-mesenchymal transition in 4D: a `tail' of multiple non-obligatory cellular mechanisms. Development *136*, 1801–1812.

Akino, K., Akita, S., Mizuguchi, T., Takumi, I., Yu, R., Wang, X., Rozga, J., Demetriou, A.A., Melmed, S., Ohtsuru, A., et al. (2005). A Novel Molecular Marker of Pituitary Tumor Transforming Gene Involves in a Rat Liver Regeneration1. J. Surg. Res. *129*, 142–146.

Anderson, R.M., Lawrence, A.R., Stottmann, R.W., Bachiller, D., and Klingensmith, J. (2002). Chordin and noggin promote organizing centers of forebrain development in the mouse. Development *129*, 4975–4987.

Andreu-Cervera, A., Anselme, I., Karam, A., Laclef, C., Catala, M., and Schneider-Maunoury, S. (2019). The Ciliopathy Gene Ftm/Rpgrip1l Controls Mouse Forebrain Patterning via Region-Specific Modulation of Hedgehog/Gli Signaling. J. Neurosci. *39*, 2398–2415.

Aoki, Y., Saint-Germain, N., Gyda, M., Magner-Fink, E., Lee, Y.-H., Credidio, C., and Saint-Jeannet, J.-P. (2003). Sox10 regulates the development of neural crest-derived melanocytes in Xenopus. Dev. Biol. *259*, 19–33.

Aschenbrenner, L., Lee, T., and Hasson, T. (2003). Myo6 Facilitates the Translocation of Endocytic Vesicles from Cell Peripheries. Mol. Biol. Cell *14*, 2728–2743.

Assémat, E., Châtelet, F., Chandellier, J., Commo, F., Cases, O., Verroust, P., and Kozyraki, R. (2005). Overlapping expression patterns of the multiligand endocytic receptors cubilin and megalin in the CNS, sensory organs and developing epithelia of the rodent embryo. Gene Expr. Patterns *6*, 69–78.

Auderset, L., Landowski, L.M., Foa, L., and Young, K.M. (2016). Low Density Lipoprotein Receptor Related Proteins as Regulators of Neural Stem and Progenitor Cell Function. Stem Cells Int. *2016*.

Aybar, M.J., and Mayor, R. (2002). Early induction of neural crest cells: lessons learned from frog, fish and chick. Curr. Opin. Genet. Dev. *12*, 452–458.

Baardman, M.E., Zwier, M.V., Wisse, L.J., Groot, A.C.G., Kerstjens-Frederikse, W.S., Hofstra, R.M.W., Jurdzinski, A., Hierck, B.P., Jongbloed, M.R.M., Berger, R.M.F., et al. (2016). Common arterial trunk and ventricular non-compaction in Lrp2 knockout mice indicate a crucial role of LRP2 in cardiac development. Dis. Model. Mech. *9*, 413–425.

Barrett, K., Leptin, M., and Settleman, J. (1997). The Rho GTPase and a Putative RhoGEF Mediate a Signaling Pathway for the Cell Shape Changes in Drosophila Gastrulation. Cell *91*, 905–915.

Barriga, E.H., Trainor, P.A., Bronner, M., and Mayor, R. (2015). Animal models for studying neural crest development: is the mouse different? Development *142*, 1555–1560.

Bashford, A.L., and Subramanian, V. (2019). Mice with a conditional deletion of Talpid3 (KIAA0586) – a model for Joubert syndrome. J. Pathol. *248*, 396–408.

Baumholtz, A.I., Simard, A., Nikolopoulou, E., Oosenbrug, M., Collins, M.M., Piontek, A., Krause, G., Piontek, J., Greene, N.D.E., and Ryan, A.K. (2017). Claudins are essential for cell shape changes and convergent extension movements during neural tube closure. Dev. Biol. *428*, 25–38.

Becker, S.F.S., Mayor, R., and Kashef, J. (2013). Cadherin-11 Mediates Contact Inhibition of Locomotion during Xenopus Neural Crest Cell Migration. PLOS ONE *8*, e85717.

Belloni, E., Muenke, M., Roessler, E., Traverse, G., Siegel-Bartelt, J., Frumkin, A., Mitchell, H.F., Donis-Keller, H., Helms, C., Hing, A.V., et al. (1996). Identification of Sonic hedgehog as a candidate gene responsible for holoprosencephaly. Nat. Genet. *14*, 353–356.

Bento-Abreu, A., Velasco, A., Polo-Hernández, E., Lillo, C., Kozyraki, R., Tabernero, A., and Medina, J.M. (2009). Albumin endocytosis via megalin in astrocytes is caveola- and Dab-1 dependent and is required for the synthesis of the neurotrophic factor oleic acid. J. Neurochem. *111*, 49–60.

Bernal, J.A., Luna, R., Espina, Á., Lázaro, I., Ramos-Morales, F., Romero, F., Arias, C., Silva, A., Tortolero, M., and Pintor-Toro, J.A. (2002). Human securin interacts with p53 and modulates p53-mediated transcriptional activity and apoptosis. Nat. Genet. *32*, 306–311.

Bertrand, N., and Dahmane, N. (2006). Sonic hedgehog signaling in forebrain development and its interactions with pathways that modify its effects. Trends Cell Biol. *16*, 597–605.

Betancur, P., Bronner-Fraser, M., and Sauka-Spengler, T. (2010). Genomic code for Sox10 activation reveals a key regulatory enhancer for cranial neural crest. Proc. Natl. Acad. Sci. *107*, 3570–3575.

Betters, E., Liu, Y., Kjaeldgaard, A., Sundström, E., and García-Castro, M.I. (2010). Analysis of early human neural crest development. Dev. Biol. *344*, 578–592.

Birn, H., Zhai, X., Holm, J., Hansen, S.I., Jacobsen, C., Christensen, E.I., and Moestrup, S.K. (2005). Megalin binds and mediates cellular internalization of folate binding protein. FEBS J. *272*, 4423–4430.

Blencowe, H., Kancherla, V., Moorthie, S., Darlison, M.W., and Modell, B. (2018). Estimates of global and regional prevalence of neural tube defects for 2015: a systematic analysis. Ann. N. Y. Acad. Sci. *1414*, 31–46.

Blom, H.J., Shaw, G.M., Heijer, M. den, and Finnell, R.H. (2006). Neural tube defects and folate: case far from closed. Nat. Rev. Neurosci. *7*, 724–731.

Boehlke, C., Kotsis, F., Patel, V., Braeg, S., Voelker, H., Bredt, S., Beyer, T., Janusch, H., Hamann, C., Gödel, M., et al. (2010). Primary cilia regulate mTORC1 activity and cell size through Lkb1. Nat. Cell Biol. *12*, 1115–1122.

Boelaert, K., Tannahill, L.A., Bulmer, J.N., Kachilele, S., Chan, S.Y., Kim, D., Gittoes, N.J.L., Franklyn, J.A., Kilby, M.D., and Mccabe, C.J. (2003). A potential role for PTTG/securin in the developing human fetal brain. FASEB J. *17*, 1631–1639.

Boot, M.J., Steegers-Theunissen, R.P.M., Poelmann, R.E., Van Iperen, L., Lindemans, J., and Gittenberger-de Groot, A.C. (2003). Folic acid and homocysteine affect neural crest and

neuroepithelial cell outgrowth and differentiation in vitro. Dev. Dyn. Off. Publ. Am. Assoc. Anat. *227*, 301–308.

Breslow, D.K., Hoogendoorn, S., Kopp, A.R., Morgens, D.W., Vu, B.K., Kennedy, M.C., Han, K., Li, A., Hess, G.T., Bassik, M.C., et al. (2018). A CRISPR-based screen for Hedgehog signaling provides insights into ciliary function and ciliopathies. Nat. Genet. *50*, 460–471.

Brooks, E.R., Islam, M.T., Anderson, K.V., and Zallen, J.A. (2020). Sonic hedgehog signaling directs patterned cell remodeling during cranial neural tube closure. ELife *9*, e60234.

Brown, S.A., Warburton, D., Brown, L.Y., Yu, C., Roeder, E.R., Stengel-Rutkowski, S., Hennekam, R.C.M., and Muenke, M. (1998). Holoprosencephaly due to mutations in ZIC2 , a homologue of Drosophila odd-paired. Nat. Genet. *20*, 180–183.

Cases, O., Perea-Gomez, A., Aguiar, D.P., Nykjaer, A., Amsellem, S., Chandellier, J., Umbhauer, M., Cereghini, S., Madsen, M., Collignon, J., et al. (2013). Cubilin, a High Affinity Receptor for Fibroblast Growth Factor 8, Is Required for Cell Survival in the Developing Vertebrate Head*,. J. Biol. Chem. *288*, 16655–16670.

Castellani, S., Guerra, L., Favia, M., Gioia, S.D., Casavola, V., and Conese, M. (2012). NHERF1 and CFTR restore tight junction organisation and function in cystic fibrosis airway epithelial cells: role of ezrin and the RhoA/ROCK pathway. Lab. Invest. *92*, 1527–1540.

Cearns, M.D., Escuin, S., Alexandre, P., Greene, N.D.E., and Copp, A.J. (2016). Microtubules, polarity and vertebrate neural tube morphogenesis. J. Anat. *229*, 63–74.

Charlton, J.R., Harer, M.W., Swan, C., and Nielsen, R. (2019). Immature megalin expression in the preterm neonatal kidney is associated with urinary loss of vitamin carrier proteins. Pediatr. Res. *85*, 405–411.

Chen, W.J., Goldstein, J.L., and Brown, M.S. (1990). NPXY, a sequence often found in cytoplasmic tails, is required for coated pit-mediated internalization of the low density lipoprotein receptor. J. Biol. Chem. *265*, 3116–3123.

Cheng, Y.-C., Cheung, M., Abu-Elmagd, M.M., Orme, A., and Scotting, P.J. (2000). Chick Sox10, a transcription factor expressed in both early neural crest cells and central nervous system. Dev. Brain Res. *121*, 233–241.

Chiang, C., Litingtung, Y., Lee, E., Young, K.E., Corden, J.L., Westphal, H., and Beachy, P.A. (1996). Cyclopia and defective axial patterning in mice lacking Sonic hedgehog gene function. Nature *383*, 407–413.

Christ, A., Christa, A., Kur, E., Lioubinski, O., Bachmann, S., Willnow, T.E., and Hammes, A. (2012). LRP2 Is an Auxiliary SHH Receptor Required to Condition the Forebrain Ventral Midline for Inductive Signals. Dev. Cell *22*, 268–278.

Christ, A., Christa, A., Klippert, J., Eule, J.C., Bachmann, S., Wallace, V.A., Hammes, A., and Willnow, T.E. (2015). LRP2 Acts as SHH Clearance Receptor to Protect the Retinal Margin from Mitogenic Stimuli. Dev. Cell *35*, 36–48.

Christ, A., Marczenke, M., and Willnow, T.E. (2020). LRP2 controls sonic hedgehog-dependent differentiation of cardiac progenitor cells during outflow tract formation. Hum. Mol. Genet. *29*, 3183–3196.

Christensen, E.I., Moskaug, J.Ø., Vorum, H., Jacobsen, C., Gundersen, T.E., Nykjær, A., Blomhoff, R., Willnow, T.E., and Moestrup, S.K. (1999). Evidence for an Essential Role of Megalin in Transepithelial Transport of Retinol. J. Am. Soc. Nephrol. *10*, 685–695.

Christodoulou, N., and Skourides, P.A. (2015). Cell-Autonomous Ca2+ Flashes Elicit Pulsed Contractions of an Apical Actin Network to Drive Apical Constriction during Neural Tube Closure. Cell Rep. *13*, 2189–2202.

Clare, C.E., Brassington, A.H., Kwong, W.Y., and Sinclair, K.D. (2019). One-Carbon Metabolism: Linking Nutritional Biochemistry to Epigenetic Programming of Long-Term Development. Annu. Rev. Anim. Biosci. *7*, 263–287.

Cohen, M.M. (1989). Perspectives on holoprosencephaly: Part I. Epidemiology, genetics, and syndromology. Teratology *40*, 211–235.

Cohen, M.M., and Shiota, K. (2002). Teratogenesis of holoprosencephaly. Am. J. Med. Genet. *109*, 1–15.

Colas, J.-F., and Schoenwolf, G.C. (2001). Towards a cellular and molecular understanding of neurulation. Dev. Dyn. *221*, 117–145.

Coles, E.G., Gammill, L.S., Miner, J.H., and Bronner-Fraser, M. (2006). Abnormalities in neural crest cell migration in laminin α5 mutant mice. Dev. Biol. *289*, 218–228.

Copp, A.J. (2005). Neurulation in the cranial region – normal and abnormal. J. Anat. *207*, 623–635.

Copp, A.J., Checiu, I., and Henson, J.N. (1994). Developmental Basis of Severe Neural Tube Defects in the loop-tail (Lp) Mutant Mouse: Use of Microsatellite DNA Markers to Identify Embryonic Genotype. Dev. Biol. *165*, 20–29.

Copp, A.J., Greene, N.D.E., and Murdoch, J.N. (2003a). The genetic basis of mammalian neurulation. Nat. Rev. Genet. *4*, 784–793.

Copp, A.J., Greene, N.D.E., and Murdoch, J.N. (2003b). Dishevelled: linking convergent extension with neural tube closure. Trends Neurosci. *26*, 453–455.

Creuzet, S.E. (2009). Neural crest contribution to forebrain development. Semin. Cell Dev. Biol. *20*, 751–759.

Creuzet, S.E., Martinez, S., and Douarin, N.M.L. (2006). The cephalic neural crest exerts a critical effect on forebrain and midbrain development. Proc. Natl. Acad. Sci. *103*, 14033–14038.

Crossley, P.H., Martinez, S., Ohkubo, Y., and Rubenstein, J.L.R. (2001). Coordinate expression of Fgf8, Otx2, Bmp4, and Shh in the rostral prosencephalon during development of the telencephalic and optic vesicles. Neuroscience *108*, 183–206.

Curtin, J.A., Quint, E., Tsipouri, V., Arkell, R.M., Cattanach, B., Copp, A.J., Henderson, D.J., Spurr, N., Stanier, P., Fisher, E.M., et al. (2003). Mutation of Celsr1 Disrupts Planar Polarity of Inner Ear Hair Cells and Causes Severe Neural Tube Defects in the Mouse. Curr. Biol. *13*, 1129–1133.

van Dam, T.J., Wheway, G., Slaats, G.G., Huynen, M.A., Giles, R.H., and SYSCILIA Study Group (2013). The SYSCILIA gold standard (SCGSv1) of known ciliary components and its applications within a systems biology consortium. Cilia *2*, 7.

REFERENCES

Darken, R.S., Scola, A.M., Rakeman, A.S., Das, G., Mlodzik, M., and Wilson, P.A. (2002). The planar polarity gene strabismus regulates convergent extension movements in Xenopus. EMBO J. *21*, 976–985.

De Castro, S.C.P., Hirst, C.S., Savery, D., Rolo, A., Lickert, H., Andersen, B., Copp, A.J., and Greene, N.D.E. (2018). Neural tube closure depends on expression of Grainyhead-like 3 in multiple tissues. Dev. Biol. *435*, 130–137.

Dimitrova, Y., Gruber, A.J., Mittal, N., Ghosh, S., Dimitriades, B., Mathow, D., Grandy, W.A., Christofori, G., and Zavolan, M. (2017). TFAP2A is a component of the ZEB1/2 network that regulates TGFB1-induced epithelial to mesenchymal transition. Biol. Direct *12*, 8.

Dowdle, W.E., Robinson, J.F., Kneist, A., Sirerol-Piquer, M.S., Frints, S.G.M., Corbit, K.C., Zaghloul, N.A., van Lijnschoten, G., Mulders, L., Verver, D.E., et al. (2011). Disruption of a Ciliary B9 Protein Complex Causes Meckel Syndrome. Am. J. Hum. Genet. *89*, 94–110.

Dubourg, C., Kim, A., Watrin, E., Tayrac, M. de, Odent, S., David, V., and Dupé, V. (2018). Recent advances in understanding inheritance of holoprosencephaly. Am. J. Med. Genet. C Semin. Med. Genet. *178*, 258–269.

Eaton, S., and Martin-Belmonte, F. (2014). Cargo Sorting in the Endocytic Pathway: A Key Regulator of Cell Polarity and Tissue Dynamics. Cold Spring Harb. Perspect. Biol. *6*, a016899.

Echevarria, D., Vieira, C., and Martinez, S. (2002). Mammalian neural tube grafting experiments: an in vitro system for mouse experimental embryology. Int. J. Dev. Biol. *45*, 895–902.

Efimov, A., Kharitonov, A., Efimova, N., Loncarek, J., Miller, P.M., Andreyeva, N., Gleeson, P., Galjart, N., Maia, A.R.R., McLeod, I.X., et al. (2007). Asymmetric CLASP-Dependent Nucleation of Noncentrosomal Microtubules at the trans-Golgi Network. Dev. Cell *12*, 917–930.

Etchevers, H.C., Couly, G., Vincent, C., and Douarin, N.M.L. (1999). Anterior cephalic neural crest is required for forebrain viability. Development *126*, 3533–3543.

Fabregat, A., Jupe, S., Matthews, L., Sidiropoulos, K., Gillespie, M., Garapati, P., Haw, R., Jassal, B., Korninger, F., May, B., et al. (2018). The Reactome Pathway Knowledgebase. Nucleic Acids Res. *46*, D649–D655.

Fabrowski, P., Necakov, A.S., Mumbauer, S., Loeser, E., Reversi, A., Streichan, S., Briggs, J.A.G., and De Renzis, S. (2013). Tubular endocytosis drives remodelling of the apical surface during epithelial morphogenesis in Drosophila. Nat. Commun. *4*, 2244.

Feng, W., Xiaoyan, X., Shenglei, L., Hongtao, L., and Guozhong, J. (2017). PTTG1 cooperated with GLI1 leads to epithelial-mesenchymal transition in esophageal squamous cell cancer. Oncotarget *8*, 92388–92400.

Fleming, A., and Copp, A.J. (2000). A genetic risk factor for mouse neural tube defects: defining the embryonic basis. Hum. Mol. Genet. *9*, 575–581.

Fliegauf, M., Benzing, T., and Omran, H. (2007). When cilia go bad: cilia defects and ciliopathies. Nat. Rev. Mol. Cell Biol. *8*, 880–893.

Foerster, P., Daclin, M., Asm, S., Faucourt, M., Boletta, A., Genovesio, A., and Spassky, N. (2017). mTORC1 signaling and primary cilia are required for brain ventricle morphogenesis. Development *144*, 201–210.

Furuta, Y., Piston, D.W., and Hogan, B.L. (1997). Bone morphogenetic proteins (BMPs) as regulators of dorsal forebrain development. Development *124*, 2203–2212.

Gajera, C.R., Emich, H., Lioubinski, O., Christ, A., Beckervordersandforth-Bonk, R., Yoshikawa, K., Bachmann, S., Christensen, E.I., Götz, M., Kempermann, G., et al. (2010). LRP2 in ependymal cells regulates BMP signaling in the adult neurogenic niche. J. Cell Sci. *123*, 1922–1930.

Gamero-Estevez, E., Baumholtz, A.I., and Ryan, A.K. (2018). Developing a link between toxicants, claudins and neural tube defects. Reprod. Toxicol. *81*, 155–167.

Garcia-Gonzalo, F.R., Corbit, K.C., Sirerol-Piquer, M.S., Ramaswami, G., Otto, E.A., Noriega, T.R., Seol, A.D., Robinson, J.F., Bennett, C.L., Josifova, D.J., et al. (2011). A transition zone complex regulates mammalian ciliogenesis and ciliary membrane composition. Nat. Genet. *43*, 776–784.

Gauthier, N.C., Masters, T.A., and Sheetz, M.P. (2012). Mechanical feedback between membrane tension and dynamics. Trends Cell Biol. *22*, 527–535.

Geelen, J.A.G., and Langman, J. (1979). Ultrastructural observations on closure of the neural tube in the mouse. Anat. Embryol. (Berl.) *156*, 73–88.

Geng, X., and Oliver, G. (2009). Pathogenesis of holoprosencephaly. J. Clin. Invest. *119*, 1403–1413.

Geng, X., Speirs, C., Lagutin, O., Inbal, A., Liu, W., Solnica-Krezel, L., Jeong, Y., Epstein, D.J., and Oliver, G. (2008). Haploinsufficiency of Six3 fails to activate Sonic hedgehog expression in the ventral forebrain and causes holoprosencephaly. Dev. Cell *15*, 236–247.

Genkai, N., Homma, J., Sano, M., Tanaka, R., and Yamanaka, R. (2006). Increased expression of pituitary tumor-transforming gene (PTTG)-1 is correlated with poor prognosis in glioma patients. Oncol. Rep. *15*, 1569–1574.

Gerdes, J.M., Davis, E.E., and Katsanis, N. (2009). The Vertebrate Primary Cilium in Development, Homeostasis, and Disease. Cell *137*, 32–45.

Giese, A.P., Ezan, J., Wang, L., Lasvaux, L., Lembo, F., Mazzocco, C., Richard, E., Reboul, J., Borg, J.-P., Kelley, M.W., et al. (2012). Gipc1 has a dual role in Vangl2 trafficking and hair bundle integrity in the inner ear. Development *139*, 3775–3785.

Gigante, E.D., and Caspary, T. (2020). Signaling in the primary cilium through the lens of the Hedgehog pathway. Wiley Interdiscip. Rev. Dev. Biol. *9*, e377.

Goldstein, J.L., and Brown, M.S. (1979). The ldl receptor locus and the genetics of familial hypercholesterolemia. Annu. Rev. Genet. *13*, 259–289.

Gomez, G.A., McLachlan, R.W., and Yap, A.S. (2011). Productive tension: force-sensing and homeostasis of cell–cell junctions. Trends Cell Biol. *21*, 499–505.

Gotthardt, M., Trommsdorff, M., Nevitt, M.F., Shelton, J., Richardson, J.A., Stockinger, W., Nimpf, J., and Herz, J. (2000). Interactions of the Low Density Lipoprotein Receptor Gene Family with Cytosolic Adaptor and Scaffold Proteins Suggest Diverse Biological Functions in Cellular Communication and Signal Transduction. J. Biol. Chem. *275*, 25616–25624.

REFERENCES

Gravotta, D., Perez Bay, A., Jonker, C.T.H., Zager, P.J., Benedicto, I., Schreiner, R., Caceres, P.S., and Rodriguez-Boulan, E. (2019). Clathrin and clathrin adaptor AP-1 control apical trafficking of megalin in the biosynthetic and recycling routes. Mol. Biol. Cell *30*, 1716–1728.

Greene, N.D.E., and Copp, A.J. (2009). Development of the vertebrate central nervous system: formation of the neural tube. Prenat. Diagn. *29*, 303–311.

Greene, N.D.E., and Copp, A.J. (2014). Neural Tube Defects. Annu. Rev. Neurosci. *37*, 221–242.

Greene, N.D.E., Gerrelli, D., Van Straaten, H.W.M., and Copp, A.J. (1998). Abnormalities of floor plate, notochord and somite differentiation in the loop-tail (Lp) mouse: a model of severe neural tube defects. Mech. Dev. *73*, 59–72.

Guillot, C., and Lecuit, T. (2013). Mechanics of Epithelial Tissue Homeostasis and Morphogenesis. Science *340*, 1185–1189.

Gupta, S., and Sen, J. (2016). Roof plate mediated morphogenesis of the forebrain: New players join the game. Dev. Biol. *413*, 145–152.

Hagting, A., den Elzen, N., Vodermaier, H.C., Waizenegger, I.C., Peters, J.-M., and Pines, J. (2002). Human securin proteolysis is controlled by the spindle checkpoint and reveals when the APC/C switches from activation by Cdc20 to Cdh1. J. Cell Biol. *157*, 1125–1137.

Haigo, S.L., Hildebrand, J.D., Harland, R.M., and Wallingford, J.B. (2003). Shroom Induces Apical Constriction and Is Required for Hingepoint Formation during Neural Tube Closure. Curr. Biol. *13*, 2125–2137.

Hammes, A., Guo, J.-K., Lutsch, G., Leheste, J.-R., Landrock, D., Ziegler, U., Gubler, M.-C., and Schedl, A. (2001). Two Splice Variants of the Wilms' Tumor 1 Gene Have Distinct Functions during Sex Determination and Nephron Formation. Cell *106*, 319–329.

Hammes, A., Andreassen, T.K., Spoelgen, R., Raila, J., Hubner, N., Schulz, H., Metzger, J., Schweigert, F.J., Luppa, P.B., Nykjaer, A., et al. (2005). Role of endocytosis in cellular uptake of sex steroids. Cell *122*, 751–762.

Harland, R. (2000). Neural induction. Curr. Opin. Genet. Dev. *10*, 357–362.

Harris, M.J., and Juriloff, D.M. (2007). Mouse mutants with neural tube closure defects and their role in understanding human neural tube defects. Birt. Defects Res. A. Clin. Mol. Teratol. *79*, 187–210.

Harris, M.J., and Juriloff, D.M. (2010). An update to the list of mouse mutants with neural tube closure defects and advances toward a complete genetic perspective of neural tube closure. Birt. Defects Res. A. Clin. Mol. Teratol. *88*, 653–669.

Harrison-Uy, S.J., and Pleasure, S.J. (2012). Wnt Signaling and Forebrain Development. Cold Spring Harb. Perspect. Biol. *4*.

Hayhurst, M., and McConnell, S. (2003). Mouse models of holoprosencephaly. Curr. Opin. Neurol. *16*, 135–141.

Hayhurst, M., Gore, B.B., Tessier-Lavigne, M., and McConnell, S.K. (2008). Ongoing sonic hedgehog signaling is required for dorsal midline formation in the developing forebrain. Dev. Neurobiol. *68*, 83–100.

He, M., Agbu, S., and Anderson, K.V. (2017). Microtubule Motors Drive Hedgehog Signaling in Primary Cilia. Trends Cell Biol. *27*, 110–125.

Hébert, J.M., Hayhurst, M., Marks, M.E., Kulessa, H., Hogan, B.L.M., and McConnell, S.K. (2003). BMP ligands act redundantly to pattern the dorsal telencephalic midline. Genesis *35*, 214–219.

Herz, J., and Strickland, D.K. (2001). LRP: a multifunctional scavenger and signaling receptor. J. Clin. Invest. *108*, 779–784.

Heyne, G.W., Everson, J.L., Ansen-Wilson, L.J., Melberg, C.G., Fink, D.M., Parins, K.F., Doroodchi, P., Ulschmid, C.M., and Lipinski, R.J. (2016). Gli2 gene-environment interactions contribute to the etiological complexity of holoprosencephaly: evidence from a mouse model. Dis. Model. Mech. *9*, 1307–1315.

Hildebrand, J.D., and Soriano, P. (1999). Shroom, a PDZ Domain–Containing Actin-Binding Protein, Is Required for Neural Tube Morphogenesis in Mice. Cell *99*, 485–497.

Hilpert, J., Nykjaer, A., Jacobsen, C., Wallukat, G., Nielsen, R., Moestrup, S.K., Haller, H., Luft, F.C., Christensen, E.I., and Willnow, T.E. (1999). Megalin Antagonizes Activation of the Parathyroid Hormone Receptor*. J. Biol. Chem. *274*, 5620–5625.

Hoch, R.V., Rubenstein, J.L.R., and Pleasure, S. (2009). Genes and signaling events that establish regional patterning of the mammalian forebrain. Semin. Cell Dev. Biol. *20*, 378–386.

Hong, M., and Krauss, R.S. (2018). Modeling the complex etiology of holoprosencephaly in mice. Am. J. Med. Genet. C Semin. Med. Genet. *178*, 140–150.

Hong, M., Christ, A., Christa, A., Willnow, T.E., and Krauss, R.S. (2020). Cdon mutation and fetal alcohol converge on Nodal signaling in a mouse model of holoprosencephaly. ELife *9*.

Hopp, K., Heyer, C.M., Hommerding, C.J., Henke, S.A., Sundsbak, J.L., Patel, S., Patel, P., Consugar, M.B., Czarnecki, P.G., Gliem, T.J., et al. (2011). B9D1 is revealed as a novel Meckel syndrome (MKS) gene by targeted exon-enriched next-generation sequencing and deletion analysis. Hum. Mol. Genet. *20*, 2524–2534.

Huang, L., Szymanska, K., Jensen, V.L., Janecke, A.R., Innes, A.M., Davis, E.E., Frosk, P., Li, C., Willer, J.R., Chodirker, B.N., et al. (2011). TMEM237 Is Mutated in Individuals with a Joubert Syndrome Related Disorder and Expands the Role of the TMEM Family at the Ciliary Transition Zone. Am. J. Hum. Genet. *89*, 713–730.

Imbard, A., Benoist, J.-F., and Blom, H.J. (2013). Neural Tube Defects, Folic Acid and Methylation. Int. J. Environ. Res. Public. Health *10*, 4352–4389.

Ishii, M., Arias, A.C., Liu, L., Chen, Y.-B., Bronner, M.E., and Maxson, R.E. (2012). A Stable Cranial Neural Crest Cell Line from Mouse. Stem Cells Dev. *21*, 3069–3080.

Ishikawa, H., Kubo, A., Tsukita, S., and Tsukita, S. (2005). Odf2-deficient mother centrioles lack distal/subdistal appendages and the ability to generate primary cilia. Nat. Cell Biol. *7*, 517–524.

Jászai, J., Thamm, K., Karbanová, J., Janich, P., Fargeas, C.A., Huttner, W.B., and Corbeil, D. (2020). Prominins control ciliary length throughout the animal kingdom: New lessons from human prominin-1 and zebrafish prominin-3. J. Biol. Chem. jbc.RA119.011253.

Jensen, A.M., and Wallace, V.A. (1997). Expression of Sonic hedgehog and its putative role as a precursor cell mitogen in the developing mouse retina. Development *124*, 363–371.

Jeon, H., Meng, W., Takagi, J., Eck, M.J., Springer, T.A., and Blacklow, S.C. (2001). Implications for familial hypercholesterolemia from the structure of the LDL receptor YWTD-EGF domain pair. Nat. Struct. Biol. *8*, 499–504.

Joukov, V., and De Nicolo, A. (2019). The Centrosome and the Primary Cilium: The Yin and Yang of a Hybrid Organelle. Cells *8*.

Jurczyk, A., Gromley, A., Redick, S., San Agustin, J., Witman, G., Pazour, G.J., Peters, D.J.M., and Doxsey, S. (2004). Pericentrin forms a complex with intraflagellar transport proteins and polycystin-2 and is required for primary cilia assembly. J. Cell Biol. *166*, 637–643.

Juriloff, D.M., and Harris, M.J. (2018). Insights into the Etiology of Mammalian Neural Tube Closure Defects from Developmental, Genetic and Evolutionary Studies. J. Dev. Biol. *6*, 22.

Juriloff, D.M., Harris, M.J., Tom, C., and MacDonald, K.B. (1991). Normal mouse strains differ in the site of initiation of closure of the cranial neural tube. Teratology *44*, 225–233.

Kalev-Altman, R., Hanael, E., Zelinger, E., Blum, M., Monsonego-Ornan, E., and Sela-Donenfeld, D. (2020). Conserved role of matrix metalloproteases 2 and 9 in promoting the migration of neural crest cells in avian and mammalian embryos. FASEB J. *34*, 5240–5261.

Kang, S.-S., Wong, P.W.K., and Norusis, M. (1987). Homocysteinemia due to folate deficiency. Metabolism *36*, 458–462.

Kantarci, S., Al-Gazali, L., Hill, R.S., Donnai, D., Black, G.C.M., Bieth, E., Chassaing, N., Lacombe, D., Devriendt, K., Teebi, A., et al. (2007). Mutations in *LRP2*, which encodes the multiligand receptor megalin, cause Donnai-Barrow and facio-oculo-acoustico-renal syndromes. Nat. Genet. *39*, 957–959.

Kantarci, S., Ragge, N.K., Thomas, N.S., Robinson, D.O., Noonan, K.M., Russell, M.K., Donnai, D., Raymond, F.L., Walsh, C.A., Donahoe, P.K., et al. (2008). Donnai–Barrow syndrome (DBS/FOAR) in a child with a homozygous LRP2 mutation due to complete chromosome 2 paternal isodisomy. Am. J. Med. Genet. A. *146A*, 1842–1847.

Kashihara, H., Chiba, S., Kanno, S.-I., Suzuki, K., Yano, T., and Tsukita, S. (2019). Cep128 associates with Odf2 to form the subdistal appendage of the centriole. Genes Cells Devoted Mol. Cell. Mech. *24*, 231–243.

Keller, R., Davidson, L., Edlund, A., Elul, T., Ezin, M., Shook, D., and Skoglund, P. (2000). Mechanisms of convergence and extension by cell intercalation. Philos. Trans. R. Soc. B Biol. Sci. *355*, 897–922.

Khalifa, O., Al-Sahlawi, Z., Imtiaz, F., Ramzan, K., Allam, R., Al-Mostafa, A., Abdel-Fattah, M., Abuharb, G., Nester, M., Verloes, A., et al. (2015). Variable expression pattern in Donnai-Barrow syndrome: Report of two novel LRP2 mutations and review of the literature. Eur. J. Med. Genet. *58*, 293–299.

Kibar, Z., Vogan, K.J., Groulx, N., Justice, M.J., Underhill, D.A., and Gros, P. (2001). Ltap , a mammalian homolog of Drosophila Strabismus/Van Gogh , is altered in the mouse neural tube mutant Loop-tail. Nat. Genet. *28*, 251–255.

Kim, S., and Dynlacht, B.D. (2013). Assembling a primary cilium. Curr. Opin. Cell Biol. *25*, 506–511.

Kim, A., Savary, C., Dubourg, C., Carré, W., Mouden, C., Hamdi-Rozé, H., Guyodo, H., Douce, J.L., Génin, E., Campion, D., et al. (2019). Integrated clinical and omics approach to rare diseases: novel genes and oligogenic inheritance in holoprosencephaly. Brain *142*, 35–49.

Kim, J., Lee, J.E., Heynen-Genel, S., Suyama, E., Ono, K., Lee, K., Ideker, T., Aza-Blanc, P., and Gleeson, J.G. (2010). Functional genomic screen for modulators of ciliogenesis and cilium length. Nature *464*, 1048–1051.

Kobayashi, T., and Dynlacht, B.D. (2011). Regulating the transition from centriole to basal body. J. Cell Biol. *193*, 435–444.

Kohli, P., Höhne, M., Jüngst, C., Bertsch, S., Ebert, L.K., Schauss, A.C., Benzing, T., Rinschen, M.M., and Schermer, B. (2017). The ciliary membrane-associated proteome reveals actin-binding proteins as key components of cilia. EMBO Rep. *18*, 1521–1535.

Kooistra, M.K., Leduc, R.Y.M., Dawe, C.E., Fairbridge, N.A., Rasmussen, J., Man, J.H.Y., Bujold, M., Juriloff, D., King-Jones, K., and McDermid, H.E. (2011). Strain-specific modifier genes of Cecr2-associated exencephaly in mice: genetic analysis and identification of differentially expressed candidate genes. Physiol. Genomics *44*, 35–46.

Kousa, Y.A., Zhu, H., Fakhouri, W.D., Lei, Y., Kinoshita, A., Roushangar, R.R., Patel, N.K., Agopian, A.J., Yang, W., Leslie, E.J., et al. (2019). The TFAP2A–IRF6–GRHL3 genetic pathway is conserved in neurulation. Hum. Mol. Genet. *28*, 1726–1737.

Kowalczyk, I., Lee, C., Schuster, E., Hoeren, J., Trivigno, V., Riedel, L., Görne, J., Wallingford, J.B., Hammes, A., and Feistel, K. (2020). Neural tube closure requires the endocytic receptor Lrp2 and its functional interaction with intracellular scaffolds. BioRxiv 2020.07.15.205252.

Kowalczyk, I., Lee, C., Schuster, E., Hoeren, J., Trivigno, V., Riedel, L., Görne, J., Wallingford, J.B., Hammes, A., and Feistel, K. (2021). Neural tube closure requires the endocytic receptor Lrp2 and its functional interaction with intracellular scaffolds. Development *148*.

Kozyraki, R., and Cases, O. (2017). Inherited LRP2 dysfunction in human disease and animal models. J. Rare Dis. Res. Treat. *2*, 22–31.

Krauss, R.S., and Hong, M. (2016). Gene-Environment Interactions and the Etiology of Birth Defects. Curr. Top. Dev. Biol. *116*, 569–580.

Kur, E., Mecklenburg, N., Cabrera, R.M., Willnow, T.E., and Hammes, A. (2014). LRP2 mediates folate uptake in the developing neural tube. J. Cell Sci. *127*, 2261–2268.

Kuriyama, S., and Mayor, R. (2008). Molecular analysis of neural crest migration. Philos. Trans. R. Soc. B Biol. Sci. *363*, 1349–1362.

Lambacher, N.J., Bruel, A.-L., van Dam, T.J.P., Szymańska, K., Slaats, G.G., Kuhns, S., McManus, G.J., Kennedy, J.E., Gaff, K., Wu, K.M., et al. (2016). TMEM107 recruits ciliopathy proteins to subdomains of the ciliary transition zone and causes Joubert syndrome. Nat. Cell Biol. *18*, 122–131.

Lang, B., Pu, J., Hunter, I., Liu, M., Martin-Granados, C., Reilly, T.J., Gao, G.-D., Guan, Z.-L., Li, W.-D., Shi, Y.-Y., et al. (2014). Recurrent deletions of ULK4 in schizophrenia: a gene crucial for neuritogenesis and neuronal motility. J. Cell Sci. *127*, 630–640.

Lang, B., Zhang, L., Jiang, G., Hu, L., Lan, W., Zhao, L., Hunter, I., Pruski, M., Song, N.-N., Huang, Y., et al. (2016). Control of cortex development by ULK4, a rare risk gene for mental disorders including schizophrenia. Sci. Rep. *6*, 31126.

Laplante, M., and Sabatini, D.M. (2009). mTOR signaling at a glance. J. Cell Sci. *122*, 3589–3594.

Leduc, R.Y.M., Singh, P., and McDermid, H.E. (2017). Genetic backgrounds and modifier genes of NTD mouse models: An opportunity for greater understanding of the multifactorial etiology of neural tube defects. Birth Defects Res. *109*, 140–152.

Lee, J.-Y., and Harland, R.M. (2010). Endocytosis Is Required for Efficient Apical Constriction during Xenopus Gastrulation. Curr. Biol. *20*, 253–258.

Lei, Y., Zhu, H., Yang, W., Ross, M.E., Shaw, G.M., and Finnell, R.H. (2014). Identification of Novel CELSR1 Mutations in Spina Bifida. PLOS ONE *9*, e92207.

Li, Y., Klena, N.T., Gabriel, G.C., Liu, X., Kim, A.J., Lemke, K., Chen, Y., Chatterjee, B., Devine, W., Damerla, R.R., et al. (2015). Global genetic analysis in mice unveils central role for cilia in congenital heart disease. Nature *521*, 520–524.

Liu, X., and Fuentes, E.J. (2019). Chapter Five - Emerging Themes in PDZ Domain Signaling: Structure, Function, and Inhibition. In International Review of Cell and Molecular Biology, L. Galluzzi, ed. (Academic Press), pp. 129–218.

Liu, M., Guan, Z., Shen, Q., Lalor, P., Fitzgerald, U., O'Brien, T., Dockery, P., and Shen, S. (2016a). Ulk4 Is Essential for Ciliogenesis and CSF Flow. J. Neurosci. Off. J. Soc. Neurosci. *36*, 7589–7600.

Liu, M., Guan, Z., Shen, Q., Flinter, F., Domínguez, L., Ahn, J.W., Collier, D.A., O'Brien, T., and Shen, S. (2016b). Ulk4 Regulates Neural Stem Cell Pool. STEM CELLS *34*, 2318–2331.

Longoni, M., Kantarci, S., Donnai, D., and Pober, B.R. (1993). Donnai-Barrow Syndrome. In GeneReviews®, M.P. Adam, H.H. Ardinger, R.A. Pagon, S.E. Wallace, L.J. Bean, K. Stephens, and A. Amemiya, eds. (Seattle (WA): University of Washington, Seattle), p.

López-Escobar, B., Wlodarczyk, B.J., Caro-Vega, J., Lin, Y., Finnell, R.H., and Ybot-González, P. (2019). The interaction of maternal diabetes with mutations that affect folate metabolism and how they affect the development of neural tube defects in mice. Dev. Dyn. *248*, 900–917.

Ma, M., Stoyanova, M., Rademacher, G., Dutcher, S.K., Brown, A., and Zhang, R. (2019). Structure of the Decorated Ciliary Doublet Microtubule. Cell *179*, 909-922.e12.

Ma, Y., Erkner, A., Gong, R., Yao, S., Taipale, J., Basler, K., and Beachy, P.A. (2002). Hedgehog-Mediated Patterning of the Mammalian Embryo Requires Transporter-like Function of Dispatched. Cell *111*, 63–75.

Mani, S.A., Guo, W., Liao, M.-J., Eaton, E.Ng., Ayyanan, A., Zhou, A.Y., Brooks, M., Reinhard, F., Zhang, C.C., Shipitsin, M., et al. (2008). The Epithelial-Mesenchymal Transition Generates Cells with Properties of Stem Cells. Cell *133*, 704–715.

Mann, R.K., and Beachy, P.A. (2004). Novel Lipid Modifications of Secreted Protein Signals. Annu. Rev. Biochem. *73*, 891–923.

Marikawa, Y. (2006). Wnt/β-catenin signaling and body plan formation in mouse embryos. Semin. Cell Dev. Biol. *17*, 175–184.

Martin, A.C., and Goldstein, B. (2014). Apical constriction: themes and variations on a cellular mechanism driving morphogenesis. Development *141*, 1987–1998.

Martin, M., and Akhmanova, A. (2018). Coming into Focus: Mechanisms of Microtubule Minus-End Organization. Trends Cell Biol. *28*, 574–588.

Martin, A.C., Kaschube, M., and Wieschaus, E.F. (2009). Pulsed contractions of an actin–myosin network drive apical constriction. Nature *457*, 495–499.

Marzolo, M.-P., and Farfán, P. (2011). New Insights into the Roles of Megalin/LRP2 and the Regulation of its Functional Expression. Biol. Res. *44*, 89–105.

Marzolo, M.-P., Yuseff, M.I., Retamal, C., Donoso, M., Ezquer, F., Farfán, P., Li, Y., and Bu, G. (2003). Differential Distribution of Low-Density Lipoprotein-Receptor-Related Protein (LRP) and Megalin in Polarized Epithelial Cells is Determined by Their Cytoplasmic Domains. Traffic *4*, 273–288.

Mason, F.M., Xie, S., Vasquez, C.G., Tworoger, M., and Martin, A.C. (2016). RhoA GTPase inhibition organizes contraction during epithelial morphogenesis. J. Cell Biol. *214*, 603–617.

Maurer, M.E., and Cooper, J.A. (2005). Endocytosis of megalin by visceral endoderm cells requires the Dab2 adaptor protein. J. Cell Sci. *118*, 5345–5355.

Mayor, R., and Theveneau, E. (2013). The neural crest. Development *140*, 2247–2251.

McCarthy, R.A., Barth, J.L., Chintalapudi, M.R., Knaak, C., and Argraves, W.S. (2002). Megalin Functions as an Endocytic Sonic Hedgehog Receptor*. J. Biol. Chem. *277*, 25660–25667.

McGreevy, E.M., Vijayraghavan, D., Davidson, L.A., and Hildebrand, J.D. (2015). Shroom3 functions downstream of planar cell polarity to regulate myosin II distribution and cellular organization during neural tube closure. Biol. Open *4*, 186–196.

Mecklenburg, N., Kowalczyk, I., Witte, F., Görne, J., Laier, A., Gonschior, H., Lehmann, M., Richter, M., Sporbert, A., Purfürst, B., et al. (2020). Identification of novel disease relevant genetic modifiers affecting the SHH pathway in the developing brain. BioRxiv 2020.11.03.366302.

Megraw, T.L., Sharkey, J.T., and Nowakowski, R.S. (2011). Cdk5rap2 exposes the centrosomal root of microcephaly syndromes. Trends Cell Biol. *21*, 470–480.

Miao, H., and Blankenship, J.T. (2020). The pulse of morphogenesis: actomyosin dynamics and regulation in epithelia. Development *147*.

Miao, H., Vanderleest, T.E., Jewett, C.E., Loerke, D., and Blankenship, J.T. (2019). Cell ratcheting through the Sbf RabGEF directs force balancing and stepped apical constriction. J. Cell Biol. *218*, 3845–3860.

Milunsky, J.M., Maher, T.A., Zhao, G., Roberts, A.E., Stalker, H.J., Zori, R.T., Burch, M.N., Clemens, M., Mulliken, J.B., Smith, R., et al. (2008). TFAP2A Mutations Result in Branchio-Oculo-Facial Syndrome. Am. J. Hum. Genet. *82*, 1171–1177.

Min, J., Mao, B., Wang, Y., He, X., Gao, S., and Wang, H. (2020). A Heterozygous Novel Mutation in TFAP2A Gene Causes Atypical Branchio-Oculo-Facial Syndrome With Isolated Coloboma of Choroid: A Case Report. Front. Pediatr. *8*.

Mineo, C. (2020). Lipoprotein receptor signalling in atherosclerosis. Cardiovasc. Res. *116*, 1254–1274.

REFERENCES

Ming, J.E., and Muenke, M. (2002). Multiple Hits during Early Embryonic Development: Digenic Diseases and Holoprosencephaly. Am. J. Hum. Genet. *71*, 1017–1032.

Minor, P.J., and Sternberg, P.W. (2019). LRP-2 likely acts downstream of EGL-20/Wnt. MicroPublication Biol. *2019*.

Mirvis, M., Stearns, T., and James Nelson, W. (2018). Cilium structure, assembly, and disassembly regulated by the cytoskeleton. Biochem. J. *475*, 2329–2353.

Moestrup, S.K., Birn, H., Fischer, P.B., Petersen, C.M., Verroust, P.J., Sim, R.B., Christensen, E.I., and Nexø, E. (1996). Megalin-mediated endocytosis of transcobalamin-vitamin-B12 complexes suggests a role of the receptor in vitamin-B12 homeostasis. Proc. Natl. Acad. Sci. *93*, 8612–8617.

Molla-Herman, A., Ghossoub, R., Blisnick, T., Meunier, A., Serres, C., Silbermann, F., Emmerson, C., Romeo, K., Bourdoncle, P., Schmitt, A., et al. (2010). The ciliary pocket: an endocytic membrane domain at the base of primary and motile cilia. J. Cell Sci. *123*, 1785–1795.

Mönnich, M., Borgeskov, L., Breslin, L., Jakobsen, L., Rogowski, M., Doganli, C., Schröder, J.M., Mogensen, J.B., Blinkenkjær, L., Harder, L.M., et al. (2018). CEP128 Localizes to the Subdistal Appendages of the Mother Centriole and Regulates TGF-β/BMP Signaling at the Primary Cilium. Cell Rep. *22*, 2584–2592.

Montcouquiol, M., Rachel, R.A., Lanford, P.J., Copeland, N.G., Jenkins, N.A., and Kelley, M.W. (2003). Identification of Vangl2 and Scrb1 as planar polarity genes in mammals. Nature *423*, 173–177.

Moreno-Mateos, M.A., Espina, Á.G., Torres, B., del Estal, M.M.G., Romero-Franco, A., Ríos, R.M., and Pintor-Toro, J.A. (2011). PTTG1/securin modulates microtubule nucleation and cell migration. Mol. Biol. Cell *22*, 4302–4311.

Morris, S.M., Arden, S.D., Roberts, R.C., Kendrick-Jones, J., Cooper, J.A., Luzio, J.P., and Buss, F. (2002). Myosin VI Binds to and Localises with Dab2, Potentially Linking Receptor-Mediated Endocytosis and the Actin Cytoskeleton. Traffic *3*, 331–341.

Muenke, M., and Beachy, P.A. (2000). Genetics of ventral forebrain development and holoprosencephaly. Curr. Opin. Genet. Dev. *10*, 262–269.

Muñoz-Sanjuán, I., and Brivanlou, A.H. (2002). Neural induction, the default model and embryonic stem cells. Nat. Rev. Neurosci. *3*, 271–280.

Murdoch, J.N., Rachel, R.A., Shah, S., Beermann, F., Stanier, P., Mason, C.A., and Copp, A.J. (2001). Circletail, a New Mouse Mutant with Severe Neural Tube Defects: Chromosomal Localization and Interaction with the Loop-Tail Mutation. Genomics *78*, 55–63.

Murdoch, J.N., Henderson, D.J., Doudney, K., Gaston-Massuet, C., Phillips, H.M., Paternotte, C., Arkell, R., Stanier, P., and Copp, A.J. (2003). Disruption of scribble (Scrb1) causes severe neural tube defects in the circletail mouse. Hum. Mol. Genet. *12*, 87–98.

Naccache, S.N., Hasson, T., and Horowitz, A. (2006). Binding of internalized receptors to the PDZ domain of GIPC/synectin recruits myosin VI to endocytic vesicles. Proc. Natl. Acad. Sci. *103*, 12735–12740.

Nachury, M.V., and Mick, D.U. (2019). Establishing and regulating the composition of cilia for signal transduction. Nat. Rev. Mol. Cell Biol. *20*, 389–405.

Nichols, D.H. (1981). Neural crest formation in the head of the mouse embryo as observed using a new histological technique. Development *64*, 105–120.

Nichols, D.H. (1987). Ultrastructure of neural crest formation in the midbrain/rostral hindbrain and preotic hindbrain regions of the mouse embryo. Am. J. Anat. *179*, 143–154.

Nielsen, B.F., Nissen, S.B., Sneppen, K., Mathiesen, J., and Trusina, A. (2020). Model to Link Cell Shape and Polarity with Organogenesis. IScience *23*, 100830.

Nigg, E.A., and Raff, J.W. (2009). Centrioles, Centrosomes, and Cilia in Health and Disease. Cell *139*, 663–678.

Nikolopoulou, E., Galea, G.L., Rolo, A., Greene, N.D.E., and Copp, A.J. (2017). Neural tube closure: cellular, molecular and biomechanical mechanisms. Development *144*, 552–566.

Nishimura, T., Honda, H., and Takeichi, M. (2012). Planar Cell Polarity Links Axes of Spatial Dynamics in Neural-Tube Closure. Cell *149*, 1084–1097.

Noden, D.M. (1975). An analysis of the migratory behavior of avian cephalic neural crest cells. Dev. Biol. *42*, 106–130.

Nykjaer, A., and Willnow, T.E. (2002). The low-density lipoprotein receptor gene family: a cellular Swiss army knife? Trends Cell Biol. *12*, 273–280.

Nykjaer, A., Dragun, D., Walther, D., Vorum, H., Jacobsen, C., Herz, J., Melsen, F., Christensen, E.I., and Willnow, T.E. (1999). An Endocytic Pathway Essential for Renal Uptake and Activation of the Steroid 25-(OH) Vitamin D3. Cell *96*, 507–515.

Ohkubo, Y., Chiang, C., and Rubenstein, J.L.R. (2002). Coordinate regulation and synergistic actions of BMP4, SHH and FGF8 in the rostral prosencephalon regulate morphogenesis of the telencephalic and optic vesicles. Neuroscience *111*, 1–17.

Oleinikov, A.V., Zhao, J., and Makker, S.P. (2000). Cytosolic adaptor protein Dab2 is an intracellular ligand of endocytic receptor gp600/megalin. Biochem. J. *347*, 613–621.

Orlando, R.A., Rader, K., Authier, F., Yamazaki, H., Posner, B.I., Bergeron, J.J., and Farquhar, M.G. (1998). Megalin is an endocytic receptor for insulin. J. Am. Soc. Nephrol. *9*, 1759–1766.

Ortega, M.C., Cases, O., Merchán, P., Kozyraki, R., Clemente, D., and Castro, F. de (2012). Megalin mediates the influence of sonic hedgehog on oligodendrocyte precursor cell migration and proliferation during development. Glia *60*, 851–866.

Osei-Sarfo, K., and Gudas, L.J. (2014). Retinoic acid suppresses the canonical Wnt signaling pathway in embryonic stem cells and activates the noncanonical Wnt signaling pathway. Stem Cells Dayt. Ohio *32*, 2061–2071.

Ossipova, O., Kim, K., Lake, B.B., Itoh, K., Ioannou, A., and Sokol, S.Y. (2014). Role of Rab11 in planar cell polarity and apical constriction during vertebrate neural tube closure. Nat. Commun. *5*, 1–8.

Ossipova, O., Chuykin, I., Chu, C.-W., and Sokol, S.Y. (2015a). Vangl2 cooperates with Rab11 and Myosin V to regulate apical constriction during vertebrate gastrulation. Development *142*, 99–107.

Ossipova, O., Kim, K., and Sokol, S.Y. (2015b). Planar polarization of Vangl2 in the vertebrate neural plate is controlled by Wnt and Myosin II signaling. Biol. Open *4*, 722–730.

REFERENCES

Ozdemir, H., Plamondon, J., Gaskin, P., Asoglu, M.R., and Turan, S. (2019). A prenatally diagnosed case of Donnai-Barrow syndrome: Highlighting the importance of whole exome sequencing in cases of consanguinity. Am. J. Med. Genet. A.

Pangilinan, F., Molloy, A.M., Mills, J.L., Troendle, J.F., Parle-McDermott, A., Signore, C., O'Leary, V.B., Chines, P., Seay, J.M., Geiler-Samerotte, K., et al. (2012). Evaluation of common genetic variants in 82 candidate genes as risk factors for neural tube defects. BMC Med. Genet. *13*, 62.

Pawson, C.T., and Scott, J.D. (2010). Signal integration through blending, bolstering and bifurcating of intracellular information. Nat. Struct. Mol. Biol. *17*, 653–658.

Pla, P., and Monsoro-Burq, A.H. (2018). The neural border: Induction, specification and maturation of the territory that generates neural crest cells. Dev. Biol. *444*, S36–S46.

Placzek, M., and Briscoe, J. (2005). The floor plate: multiple cells, multiple signals. Nat. Rev. Neurosci. *6*, 230–240.

Pober, B.R., Longoni, M., and Noonan, K.M. (2009). A review of Donnai-Barrow and facio-oculo-acoustico-renal (DB/FOAR) syndrome: Clinical features and differential diagnosis. Birt. Defects Res. A. Clin. Mol. Teratol. *85*, 76–81.

Porter, J.A., Young, K.E., and Beachy, P.A. (1996). Cholesterol Modification of Hedgehog Signaling Proteins in Animal Development. Science *274*, 255–259.

Prasad, M.S., Charney, R.M., and García-Castro, M.I. (2019). Specification and formation of the neural crest: Perspectives on lineage segregation. Genesis *57*, e23276.

Prasoona K., R., T., S., B., S., T., M.K., and A., J. (2018). LRP2 gene variants and their haplotypes strongly influence the risk of developing neural tube defects in the fetus: a family-triad study from South India. Metab. Brain Dis. *33*, 1343–1352.

Pusapati, G.V., Kong, J.H., Patel, B.B., Krishnan, A., Sagner, A., Kinnebrew, M., Briscoe, J., Aravind, L., and Rohatgi, R. (2018). CRISPR Screens Uncover Genes that Regulate Target Cell Sensitivity to the Morphogen Sonic Hedgehog. Dev. Cell *44*, 113-129.e8.

Quinlan, R., Graf, M., Mason, I., Lumsden, A., and Kiecker, C. (2009). Complex and dynamic patterns of Wnt pathway gene expression in the developing chick forebrain. Neural Develop. *4*, 35.

Rada-Iglesias, A., Bajpai, R., Prescott, S., Brugmann, S.A., Swigut, T., and Wysocka, J. (2012). Epigenomic Annotation of Enhancers Predicts Transcriptional Regulators of Human Neural Crest. Cell Stem Cell *11*, 633–648.

Reed, B.C., Cefalu, C., Bellaire, B.H., Cardelli, J.A., Louis, T., Salamon, J., Bloecher, M.A., and Bunn, R.C. (2005). GLUT1CBP(TIP2/GIPC1) Interactions with GLUT1 and Myosin VI: Evidence Supporting an Adapter Function for GLUT1CBP. Mol. Biol. Cell *16*, 4183–4201.

Renard, E., Chéry, C., Oussalah, A., Josse, T., Perrin, P., Tramoy, D., Voirin, J., Klein, O., Leheup, B., Feillet, F., et al. (2019). Exome sequencing of cases with neural tube defects identifies candidate genes involved in one-carbon/vitamin B12 metabolisms and Sonic Hedgehog pathway. Hum. Genet. *138*, 703–713.

Repo, H., Gurvits, N., Löyttyniemi, E., Nykänen, M., Lintunen, M., Karra, H., Kurki, S., Kuopio, T., Talvinen, K., Söderström, M., et al. (2017). PTTG1-interacting protein (PTTG1IP/PBF) predicts breast cancer survival. BMC Cancer *17*, 705.

Roessler, E., and Muenke, M. (2010). The molecular genetics of holoprosencephaly. Am. J. Med. Genet. C Semin. Med. Genet. *154C*, 52–61.

Roessler, E., Belloni, E., Gaudenz, K., Jay, P., Berta, P., Scherer, S.W., Tsui, L.-C., and Muenke, M. (1996). Mutations in the human Sonic Hedgehog gene cause holoprosencephaly. Nat. Genet. *14*, 357.

Rolo, A., Skoglund, P., and Keller, R. (2009). Morphogenetic movements driving neural tube closure in Xenopus require myosin IIB. Dev. Biol. *327*, 327–338.

Rosenfeld, J.A., Ballif, B.C., Martin, D.M., Aylsworth, A.S., Bejjani, B.A., Torchia, B.S., and Shaffer, L.G. (2010). Clinical characterization of individuals with deletions of genes in holoprosencephaly pathways by aCGH refines the phenotypic spectrum of HPE. Hum. Genet. *127*, 421–440.

Rosenquist, T.H., and Finnell, R.H. (2001). Genes, folate and homocysteine in embryonic development. Proc. Nutr. Soc. *60*, 53–61.

Rosenquist, T.H., Bennett, G.D., Brauer, P.R., Stewart, M.L., Chaudoin, T.R., and Finnell, R.H. (2007). Microarray analysis of homocysteine-responsive genes in cardiac neural crest cells in vitro. Dev. Dyn. *236*, 1044–1054.

Ross, A.J., May-Simera, H., Eichers, E.R., Kai, M., Hill, J., Jagger, D.J., Leitch, C.C., Chapple, J.P., Munro, P.M., Fisher, S., et al. (2005). Disruption of Bardet-Biedl syndrome ciliary proteins perturbs planar cell polarity in vertebrates. Nat. Genet. *37*, 1135–1140.

Roszko, I., Sepich, D.S., Jessen, J.R., Chandrasekhar, A., and Solnica-Krezel, L. (2015). A dynamic intracellular distribution of Vangl2 accompanies cell polarization during zebrafish gastrulation. Development *142*, 2508–2520.

Rothfels, K. (2014). Hedgehog "off" State. Reactome - Curated Knowledgebase Biol. Pathw. *50*.

Sabatino, J.A., Stokes, B.A., and Zohn, I.E. (2017). Prevention of neural tube defects in Lrp2 mutant mouse embryos by folic acid supplementation. Birth Defects Res. *109*, 16–26.

Saito, A., Pietromonaco, S., Loo, A.K., and Farquhar, M.G. (1994). Complete cloning and sequencing of rat gp330/"megalin," a distinctive member of the low density lipoprotein receptor gene family. Proc. Natl. Acad. Sci. *91*, 9725–9729.

Saito, A., Sato, H., Iino, N., and Takeda, T. (2009). Molecular Mechanisms of Receptor-Mediated Endocytosis in the Renal Proximal Tubular Epithelium. J. Biomed. Biotechnol. *2010*, e403272.

Santagati, F., and Rijli, F.M. (2003). Cranial neural crest and the building of the vertebrate head. Nat. Rev. Neurosci. *4*, 806–818.

Sasaki, H., Hui, C., Nakafuku, M., and Kondoh, H. (1997). A binding site for Gli proteins is essential for HNF-3beta floor plate enhancer activity in transgenics and can respond to Shh in vitro. Development *124*, 1313–1322.

Sauka-Spengler, T., and Bronner-Fraser, M. (2008). A gene regulatory network orchestrates neural crest formation. Nat. Rev. Mol. Cell Biol. *9*, 557–568.

Schaub, J.R., and Stearns, T. (2012). The Rilp-like proteins Rilpl1 and Rilpl2 regulate ciliary membrane content. Mol. Biol. Cell *24*, 453–464.

Schneider, W.J., and Nimpf, J. (2003). LDL receptor relatives at the crossroad of endocytosis and signaling. Cell. Mol. Life Sci. CMLS *60*, 892–903.

Schneider, R.A., Hu, D., Rubenstein, J.L.R., Maden, M., and Helms, J.A. (2001). Local retinoid signaling coordinates forebrain and facial morphogenesis by maintaining FGF8 and SHH. Development *128*, 2755–2767.

Schoenwolf, G.C., and Smith, J.L. (1990). Mechanisms of neurulation: traditional viewpoint and recent advances. Development *109*, 243–270.

Schorle, H., Meier, P., Buchert, M., Jaenisch, R., and Mitchell, P.J. (1996). Transcription factor AP-2 essential for cranial closure and craniofacial development. Nature *381*, 235–238.

Schou, K.B., Mogensen, J.B., Morthorst, S.K., Nielsen, B.S., Aleliunaite, A., Serra-Marques, A., Fürstenberg, N., Saunier, S., Bizet, A.A., Veland, I.R., et al. (2017). KIF13B establishes a CAV1-enriched microdomain at the ciliary transition zone to promote Sonic hedgehog signalling. Nat. Commun. *8*, 1–15.

Seidler, U., Singh, A.K., Cinar, A., Chen, M., Hillesheim, J., Hogema, B., and Riederer, B. (2009). The Role of the NHERF Family of PDZ Scaffolding Proteins in the Regulation of Salt and Water Transport. Ann. N. Y. Acad. Sci. *1165*, 249–260.

Seifert, J.R.K., and Mlodzik, M. (2007). Frizzled/PCP signalling: a conserved mechanism regulating cell polarity and directed motility. Nat. Rev. Genet. *8*, 126–138.

Shang, G., Brautigam, C.A., Chen, R., Lu, D., Torres-Vázquez, J., and Zhang, X. (2021). Structure analyses reveal a regulated oligomerization mechanism of the PlexinD1/GIPC/myosin VI complex. ELife *6*.

Sharma, N., Kosan, Z.A., Stallworth, J.E., Berbari, N.F., and Yoder, B.K. (2011). Soluble levels of cytosolic tubulin regulate ciliary length control. Mol. Biol. Cell *22*, 806–816.

Shenolikar, S., Voltz, J.W., Minkoff, C.M., Wade, J.B., and Weinman, E.J. (2002). Targeted disruption of the mouse NHERF-1 gene promotes internalization of proximal tubule sodium-phosphate cotransporter type IIa and renal phosphate wasting. Proc. Natl. Acad. Sci. *99*, 11470–11475.

Slattery, C., Jenkin, K.A., Lee, A., Simcocks, A.C., McAinch, A.J., Poronnik, P., and Hryciw, D.H. (2011). Na+-H+ exchanger regulatory factor 1 (NHERF1) PDZ scaffold binds an internal binding site in the scavenger receptor megalin. Cell. Physiol. Biochem. Int. J. Exp. Cell. Physiol. Biochem. Pharmacol. *27*, 171–178.

Solomon, B.D., Mercier, S., Vélez, J.I., Pineda-Alvarez, D.E., Wyllie, A., Zhou, N., Dubourg, C., David, V., Odent, S., Roessler, E., et al. (2010). Analysis of genotype–phenotype correlations in human holoprosencephaly. Am. J. Med. Genet. C Semin. Med. Genet. *154C*, 133–141.

Spicer, E., Suckert, C., Al-Attar, H., and Marsden, M. (2010). Integrin α5β1 Function Is Regulated by XGIPC/kermit2 Mediated Endocytosis during Xenopus laevis Gastrulation. PLOS ONE *5*, e10665.

Spoelgen, R., Hammes, A., Anzenberger, U., Zechner, D., Andersen, O.M., Jerchow, B., and Willnow, T.E. (2005). LRP2/megalin is required for patterning of the ventral telencephalon. Development *132*, 405–414.

Spuch, C., Ortolano, S., and Navarro, C. (2012). LRP-1 and LRP-2 receptors function in the membrane neuron. Trafficking mechanisms and proteolytic processing in Alzheimer's disease. Front. Physiol. *3*.

Steele, J.W., Kim, S.-E., and Finnell, R.H. (2020). One-carbon metabolism and folate transporter genes: Do they factor prominently in the genetic etiology of neural tube defects? Biochimie *173*, 27–32.

Straaten, H.W. van, Hekking, J.W., Consten, C., and Copp, A.J. (1993). Intrinsic and extrinsic factors in the mechanism of neurulation: effect of curvature of the body axis on closure of the posterior neuropore. Development *117*, 1163–1172.

Streit, A., Berliner, A.J., Papanayotou, C., Sirulnik, A., and Stern, C.D. (2000). Initiation of neural induction by FGF signalling before gastrulation. Nature *406*, 74–78.

Sutherland, A., Keller, R., and Lesko, A. (2020a). Convergent extension in mammalian morphogenesis. Semin. Cell Dev. Biol. *100*, 199–211.

Sutherland, A., Keller, R., and Lesko, A. (2020b). Convergent extension in mammalian morphogenesis. Semin. Cell Dev. Biol. *100*, 199–211.

Suzuki, M., Morita, H., and Ueno, N. (2012). Molecular mechanisms of cell shape changes that contribute to vertebrate neural tube closure. Dev. Growth Differ. *54*, 266–276.

Taipale, J., Chen, J.K., Cooper, M.K., Wang, B., Mann, R.K., Milenkovic, L., Scott, M.P., and Beachy, P.A. (2000). Effects of oncogenic mutations in Smoothened and Patched can be reversed by cyclopamine. Nature *406*, 1005.

Takeda, T., Yamazaki, H., and Farquhar, M.G. (2003). Identification of an apical sorting determinant in the cytoplasmic tail of megalin. Am. J. Physiol.-Cell Physiol. *284*, C1105–C1113.

Tamai, K., Semenov, M., Kato, Y., Spokony, R., Liu, C., Katsuyama, Y., Hess, F., Saint-Jeannet, J.-P., and He, X. (2000). LDL-receptor-related proteins in Wnt signal transduction. Nature *407*, 530–535.

Tarabykin, V., Britanova, O., Fradkov, A., Voss, A., Katz, L.S., Lukyanov, S., and Gruss, P. (2000). Expression of PTTG and prc1 genes during telencephalic neurogenesis. Mech. Dev. *92*, 301–304.

Tekendo-Ngongang, C., Muenke, M., and Kruszka, P. (1993). Holoprosencephaly Overview. In GeneReviews®, M.P. Adam, H.H. Ardinger, R.A. Pagon, S.E. Wallace, L.J. Bean, K. Stephens, and A. Amemiya, eds. (Seattle (WA): University of Washington, Seattle), p.

Tekendo-Ngongang, C., Owosela, B., Muenke, M., and Kruszka, P. (2020). Comorbidity of congenital heart defects and holoprosencephaly is likely genetically driven and gene-specific. Am. J. Med. Genet. C Semin. Med. Genet. *184*, 154–158.

Theil, T., Dominguez-Frutos, E., and Schimmang, T. (2008). Differential requirements for Fgf3 and Fgf8 during mouse forebrain development. Dev. Dyn. *237*, 3417–3423.

Theis, J.L., Vogler, G., Missinato, M.A., Li, X., Nielsen, T., Zeng, X.-X.I., Martinez-Fernandez, A., Walls, S.M., Kervadec, A., Kezos, J.N., et al. (2020). Patient-specific genomics and cross-species functional analysis implicate LRP2 in hypoplastic left heart syndrome. ELife *9*, e59554.

REFERENCES

Theveneau, E., and Mayor, R. (2011). Collective cell migration of the cephalic neural crest: The art of integrating information. Genesis *49*, 164–176.

Theveneau, E., and Mayor, R. (2012a). Neural crest delamination and migration: From epithelium-to-mesenchyme transition to collective cell migration. Dev. Biol. *366*, 34–54.

Theveneau, E., and Mayor, R. (2012b). Neural crest migration: interplay between chemorepellents, chemoattractants, contact inhibition, epithelial–mesenchymal transition, and collective cell migration. WIREs Dev. Biol. *1*, 435–445.

Theveneau, E., and Mayor, R. (2012c). Cadherins in collective cell migration of mesenchymal cells. Curr. Opin. Cell Biol. *24*, 677–684.

Thiery, J.P., Acloque, H., Huang, R.Y.J., and Nieto, M.A. (2009). Epithelial-Mesenchymal Transitions in Development and Disease. Cell *139*, 871–890.

Tong, Y., and Eigler, T. (2009). Transcriptional targets for pituitary tumor-transforming gene-1. J. Mol. Endocrinol. *43*, 179–185.

Tong, Y., Ben-Shlomo, A., Zhou, C., Wawrowsky, K., and Melmed, S. (2008). Pituitary tumor transforming gene 1 regulates Aurora kinase A activity. Oncogene *27*, 6385–6395.

Treat, A.C., Wheeler, D.S., Stolz, D.B., Tsang, M., Friedman, P.A., and Romero, G. (2016). The PDZ Protein Na+/H+ Exchanger Regulatory Factor-1 (NHERF1) Regulates Planar Cell Polarity and Motile Cilia Organization. PLOS ONE *11*, e0153144.

Truett, G. e., Heeger, P., Mynatt, R. l., Truett, A. a., Walker, J. a., and Warman, M. l. (2000). Preparation of PCR-Quality Mouse Genomic DNA with Hot Sodium Hydroxide and Tris (HotSHOT). BioTechniques *29*, 52–54.

Veeraval, L., O'Leary, C.J., and Cooper, H.M. (2020). Adherens Junctions: Guardians of Cortical Development. Front. Cell Dev. Biol. *8*.

Vierkotten, J., Dildrop, R., Peters, T., Wang, B., and Rüther, U. (2007). Ftm is a novel basal body protein of cilia involved in Shh signalling. Development *134*, 2569–2577.

Vlotides, G., Eigler, T., and Melmed, S. (2007). Pituitary Tumor-Transforming Gene: Physiology and Implications for Tumorigenesis. Endocr. Rev. *28*, 165–186.

Vogel, P., Read, R.W., Hansen, G.M., Payne, B.J., Small, D., Sands, A.T., and Zambrowicz, B.P. (2012). Congenital hydrocephalus in genetically engineered mice. Vet. Pathol. *49*, 166–181.

Wallingford, J.B. (2005). Neural tube closure and neural tube defects: Studies in animal models reveal known knowns and known unknowns. Am. J. Med. Genet. C Semin. Med. Genet. *135C*, 59–68.

Wallingford, J.B., and Harland, R.M. (2002). Neural tube closure requires Dishevelled-dependent convergent extension of the midline. Development *129*, 5815–5825.

Wallingford, J.B., Fraser, S.E., and Harland, R.M. (2002). Convergent Extension: The Molecular Control of Polarized Cell Movement during Embryonic Development. Dev. Cell *2*, 695–706.

Wallingford, J.B., Niswander, L.A., Shaw, G.M., and Finnell, R.H. (2013). The Continuing Challenge of Understanding, Preventing, and Treating Neural Tube Defects. Science *339*.

Wallis, D.E., and Muenke, M. (1999). Molecular Mechanisms of Holoprosencephaly. Mol. Genet. Metab. *68*, 126–138.

Wallis, D.E., Roessler, E., Hehr, U., Nanni, L., Wiltshire, T., Richieri-Costa, A., Gillessen-Kaesbach, G., Zackai, E.H., Rommens, J., and Muenke, M. (1999). Mutations in the homeodomain of the human SIX3 gene cause holoprosencephaly. Nat. Genet. *22*, 196–198.

Wang, L., and Dynlacht, B.D. (2018). The regulation of cilium assembly and disassembly in development and disease. Development *145*.

Wang, J., Li, T., Wang, J.-L., Xu, Z., Meng, W., and Wu, Q.-F. (2020). Talpid3-Mediated Centrosome Integrity Restrains Neural Progenitor Delamination to Sustain Neurogenesis by Stabilizing Adherens Junctions. Cell Rep. *33*, 108495.

Wang, M., de Marco, P., Capra, V., and Kibar, Z. (2019a). Update on the Role of the Non-Canonical Wnt/Planar Cell Polarity Pathway in Neural Tube Defects. Cells *8*, 1198.

Wang, Q., Kurosaka, H., Kikuchi, M., Nakaya, A., Trainor, P.A., and Yamashiro, T. (2019b). Perturbed development of cranial neural crest cells in association with reduced sonic hedgehog signaling underlies the pathogenesis of retinoic-acid-induced cleft palate. Dis. Model. Mech. *12*, dmm040279.

Wang, W., Wu, T., and Kirschner, M.W. (2014). The master cell cycle regulator APC-Cdc20 regulates ciliary length and disassembly of the primary cilium. ELife *3*, e03083.

Weinman, E.J., Steplock, D., Tate, K., Hall, R.A., Spurney, R.F., and Shenolikar, S. (1998). Structure-function of recombinant Na/H exchanger regulatory factor (NHE-RF). J. Clin. Invest. *101*, 2199–2206.

Wells, A.L., Lin, A.W., Chen, L.Q., Safer, D., Cain, S.M., Hasson, T., Carragher, B.O., Milligan, R.A., and Sweeney, H.L. (1999). Myosin VI is an actin-based motor that moves backwards. Nature *401*, 505–508.

Wicher, G., and Aldskogius, H. (2008). Megalin deficiency induces critical changes in mouse spinal cord development. NeuroReport *19*, 559–563.

Willnow, T.E., and Christ, A. (2017). Endocytic receptor LRP2/megalin—of holoprosencephaly and renal Fanconi syndrome. Pflüg. Arch. - Eur. J. Physiol. *469*, 907–916.

Willnow, T.E., Hilpert, J., Armstrong, S.A., Rohlmann, A., Hammer, R.E., Burns, D.K., and Herz, J. (1996). Defective forebrain development in mice lacking gp330/megalin. Proc. Natl. Acad. Sci. *93*, 8460–8464.

Willnow, T.E., Christ, A., and Hammes, A. (2012). Endocytic receptor-mediated control of morphogen signaling. Dev. Camb. Engl. *139*, 4311–4319.

Wood, L.R., and Smith, M.T. (1984). Generation of anencephaly: 1. Aberrant neurulation and 2. Conversion of exencephaly to anencephaly. J. Neuropathol. Exp. Neurol. *43*, 620–633.

Woodruff, J.B., Ferreira Gomes, B., Widlund, P.O., Mahamid, J., Honigmann, A., and Hyman, A.A. (2017). The Centrosome Is a Selective Condensate that Nucleates Microtubules by Concentrating Tubulin. Cell *169*, 1066-1077.e10.

Xiang, W., Wu, X., Huang, C., Wang, M., Zhao, X., Luo, G., Li, Y., Jiang, G., Xiao, X., and Zeng, F. (2017). PTTG1 regulated by miR-146a-3p promotes bladder cancer migration, invasion, metastasis and growth. Oncotarget *8*, 664–678.

REFERENCES

Xie, S., and Martin, A.C. (2015). Intracellular signalling and intercellular coupling coordinate heterogeneous contractile events to facilitate tissue folding. Nat. Commun. *6*, 7161.

Yan, H., Wang, W., Dou, C., Tian, F., and Qi, S. (2015). Securin promotes migration and invasion via matrix metalloproteinases in glioma cells. Oncol. Lett. *9*, 2895–2901.

Yano, T., Tsukita, K., Kanoh, H., Nakayama, S., Kashihara, H., Mizuno, T., Tanaka, H., Matsui, T., Goto, Y., Komatsubara, A., et al. (2021). A microtubule-LUZP1 association around tight junction promotes epithelial cell apical constriction. EMBO J. *40*, e104712.

Ybot-Gonzalez, P., Gaston-Massuet, C., Girdler, G., Klingensmith, J., Arkell, R., Greene, N.D.E., and Copp, A.J. (2007). Neural plate morphogenesis during mouse neurulation is regulated by antagonism of Bmp signalling. Development *134*, 3203–3211.

Yin, Y., Bangs, F., Paton, I.R., Prescott, A., James, J., Davey, M.G., Whitley, P., Genikhovich, G., Technau, U., Burt, D.W., et al. (2009). The Talpid3 gene (KIAA0586) encodes a centrosomal protein that is essential for primary cilia formation. Development *136*, 655–664.

Yuseff, M.I., Farfan, P., Bu, G., and Marzolo, M.-P. (2007). A Cytoplasmic PPPSP Motif Determines Megalin's Phosphorylation and Regulates Receptor's Recycling and Surface Expression. Traffic *8*, 1215–1230.

Zaganjor, I., Sekkarie, A., Tsang, B.L., Williams, J., Razzaghi, H., Mulinare, J., Sniezek, J.E., Cannon, M.J., and Rosenthal, J. (2016). Describing the Prevalence of Neural Tube Defects Worldwide: A Systematic Literature Review. PLOS ONE *11*, e0151586.

Zaidi, S., Choi, M., Wakimoto, H., Ma, L., Jiang, J., Overton, J.D., Romano-Adesman, A., Bjornson, R.D., Breitbart, R.E., Brown, K.K., et al. (2013). De novo mutations in histone-modifying genes in congenital heart disease. Nature *498*, 220–223.

Zebrowski, D.C., Vergarajauregui, S., Wu, C.-C., Piatkowski, T., Becker, R., Leone, M., Hirth, S., Ricciardi, F., Falk, N., Giessl, A., et al. (2015). Developmental alterations in centrosome integrity contribute to the post-mitotic state of mammalian cardiomyocytes. ELife *4*, e05563.

Zhang, J., Hagopian-Donaldson, S., Serbedzija, G., Elsemore, J., Plehn-Dujowich, D., McMahon, A.P., Flavell, R.A., and Williams, T. (1996). Neural tube, skeletal and body wall defects in mice lacking transcription factor AP-2. Nature *381*, 238–241.

Zhang, W., Kang, J.-S., Cole, F., Yi, M.-J., and Krauss, R.S. (2006). Cdo Functions at Multiple Points in the Sonic Hedgehog Pathway, and Cdo-Deficient Mice Accurately Model Human Holoprosencephaly. Dev. Cell *10*, 657–665.

Zhang, X.M., Ramalho-Santos, M., and McMahon, A.P. (2001). Smoothened Mutants Reveal Redundant Roles for Shh and Ihh Signaling Including Regulation of L/R Asymmetry by the Mouse Node. Cell *105*, 781–792.

Zur, A., and Brandeis, M. (2001). Securin degradation is mediated by fzy and fzr, and is required for complete chromatid separation but not for cytokinesis. EMBO J. *20*, 792–801.